Morphological Characterization of Conjugated Polymer Blends in Solid and Solution States Using Small Angle Scattering

Sage Charlie Scheiwiller

A dissertation

submitted in partial fulfillment of the

requirements for the degree of

Doctor of Philosophy

University of Washington

2024

Reading Committee:

Lilo D. Pozzo, Chair

David A. C. Beck

Cole A. DeForest

Program Authorized to Offer Degree:

Chemical Engineering

@ Copyright 2024
Sage Charlie Scheiwiller

University of Washington

Abstract

Morphological Characterization of Conjugated Polymer Blends in Solid and Solution States Using Small Angle Scattering

Sage Charlie Scheiwiller

Chair of Supervisory Committee:

Lilo D. Pozzo

Chemical Engineering

Conjugated polymers (CPs) are a subset of polymers with unique electronic properties and are found in the active layers of organic electronic devices, such as organic photovoltaics (OPVs), organic field-effect transistors (OFETs), organic LED's (OLEDs), and bioelectronics. In pure forms, CPs are often brittle and prone to environmental degradation, so to improve the durability and mechanical properties of organic electronics, CPs are often blended with mechanically favorable matrix polymers. The blending process often involves the application of heat, pressure, or solvents, and these processing variables can affect how the materials interact with each other. This, in turn, can affect the properties of the final product. A fundamental understanding of the morphology of conjugated polymer blends and how processing affects them is required to develop and optimize materials. In this work, we utilize neutron and X-ray

scattering techniques to determine the morphology of complex CP blends in both solution and solid states, under a variety of processing and sample conditions. We first explore a heat pressed elastomeric CP blend and determine how the phase structures of the matrix elastomer change and distort with the addition of a conjugated polymer. We also investigate how the heat pressing method, including variables such as solvent choice, pressing time, and pressing temperature, affect the structure and phases of the blended material. We continue our morphological characterization of complex blended systems with a high χ parameter copolymer and conjugated polymer in solution. This type of system has been proposed for use in Organic Mixed Ionic and Electronic Conductors (OMIECs), but a fundamental understanding of the structure of the system is required before optimization of desired properties is possible. We begin with solution-state analysis of the self-assembling high χ parameter copolymer and track the structural changes that result from polymer architecture and solvent quality. With an understanding of the structure of the matrix, we further identify how the addition of the conjugated polymer modifies the structure and extent of assembly in solution. Throughout these works, we emphasize the need to understand the morphology of complex CPs and how choices in materials and processing methods can affect the conformations of these blends.

Table of Contents

List of Figures

List of Tables

Chapter 1: Introduction

1.1 Conjugated Polymer Blends

Conjugated polymers (CPs) are a subset of polymers with unique electronic properties. They are found in the active layers of organic electronic devices, such as organic photovoltaics (OPVs), organic field-effect transistors (OFETs), organic LED's (OLEDs), and bioelectronics[2–5]. While conjugated polymers provide a useful electronic capability, there are some drawbacks to using pure forms of them. They are often thermally and environmentally sensitive, and can be physically brittle, making them difficult to incorporate into long lasting devices[5]. These undesirable physical properties can be mitigated through the use of polymer blends. To improve the durability and mechanical properties of organic electronics, researchers began to blend conjugated polymers with mechanically favorable commodity polymers, such as polystyrene. The addition of a commodity polymer does not greatly impact the electronic properties of the material, and with careful selection of the newly added matrix polymer, device performance could even be improved[6–8].

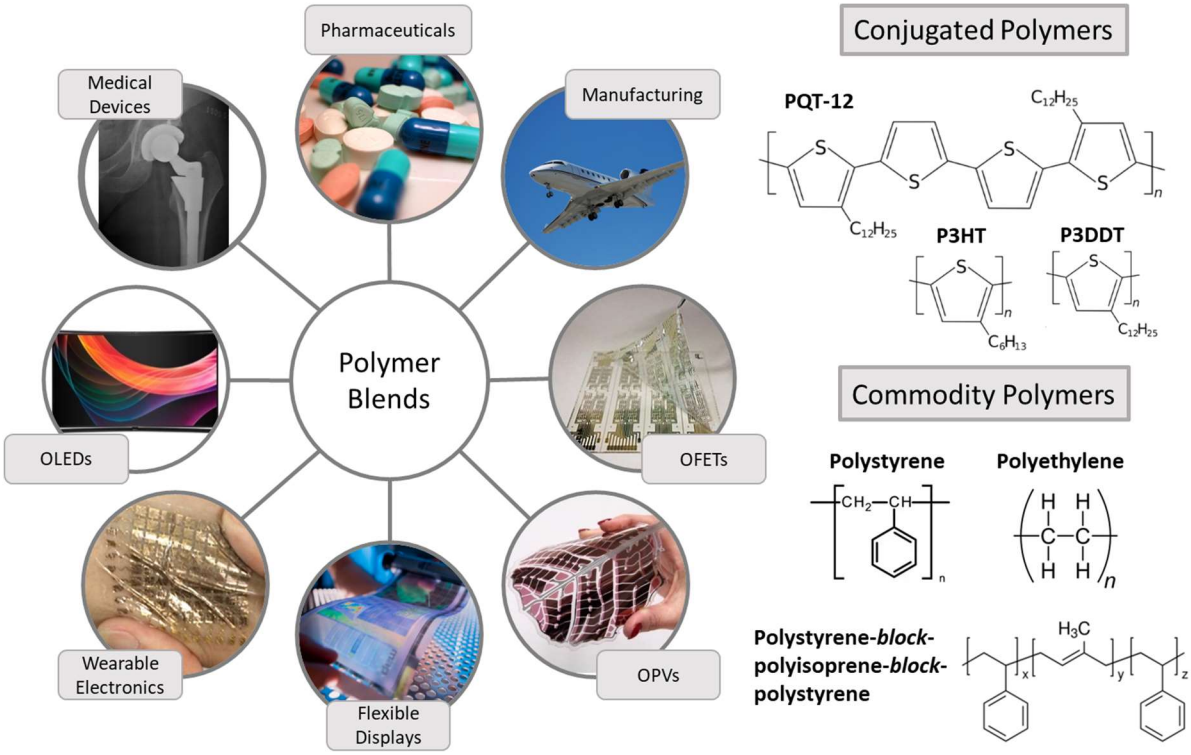

Figure 1.1: Polymer blend use cases and examples of common polymer blends components, with examples of both conjugated and commodity polymers.

These systems can be efficient as well; as Gu et al discussed, only a small amount of conjugated polymer is needed in a system to create desired charge carrying capabilities, and conductivity can reach peaks as low as 3 wt% (**Figure 1.2a**)[1,7]. During the last 50 years there have been many discoveries in the optimization of electronic properties with modifications of rings, subgroups, bonds, inclusion of dopants, and investigation into the intricacies of the conformation of the resulting solid-state product[9–12]. The unique conductive properties emerge due to the polymers conjugated backbone, with alternating single and double bonds that allow electron transport along the backbone and between chains through overlapping π-orbitals[13,14]. As discussed by Sirringhaus et al, a correlation between the direction of π-π stacking and charge mobility was identified, with improved alignment of π-orbitals resulting in increased charge mobility[15]. A mix of these methods of charge transport allows for a complex network of charge carrying structures, creating an electronic polymer (**Figure 1.2b**).

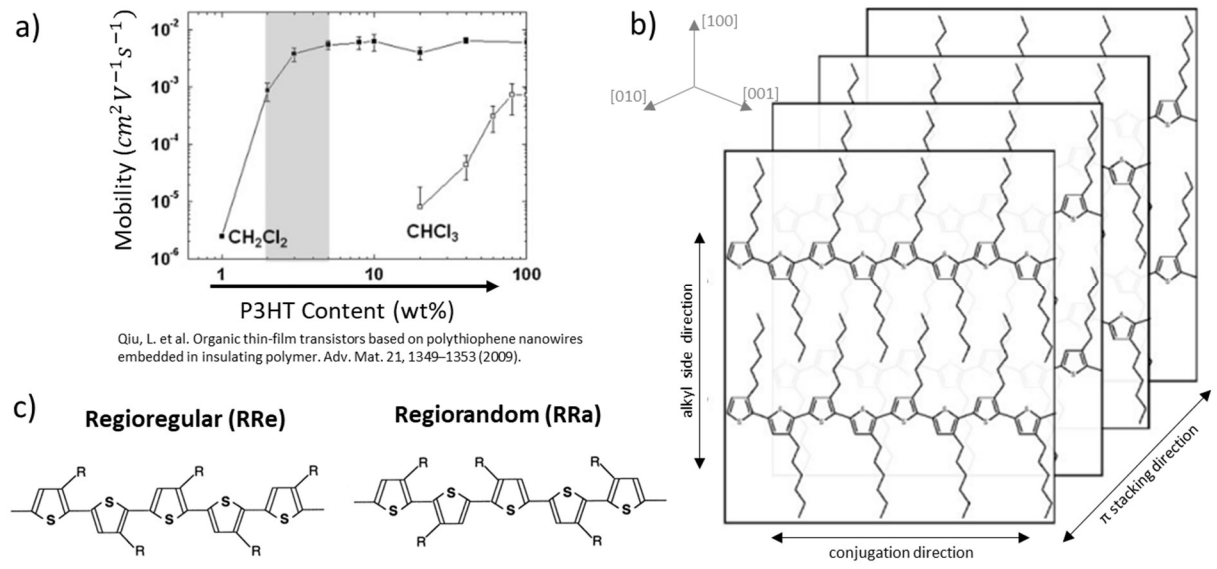

Figure 1.2: a) plot of conjugated polymer wt% and charge mobility from literature[7] showing a plateau in charge mobility in P3HT based devices around 3 wt% P3HT. This is an instance of high conductivity for lightly loaded blends, and no significant increase in charge mobility beyond this loading b) schematic of typical crystallization morphology with directions and methods of charge transport labeled, c) schematics of regioregular and regiorandom P3AT.

As investigated in previous works, crystallinity and regioregularity have a large impact on the electronic capabilities of the polymer[16]. In poly(3-hexylthiophene) (P3HT) films, the highest

charge mobilities were found in samples with the highest regioregularity, as well as those with the largest size of crystallite in plane with the direction of mobility[17]. Other researchers, such as Schwartz et al, echo these findings, emphasizing the importance of interchain transport facilitated by ordered π-π stacking[18]. Large crystal structures are formed when the CP has molecular structures that allow for orderly stacking. Regioregularity describes the ordering of the side chains along the backbone, with regioregular materials showing increased ordering over regiorandom materials. Example structures are shown in **Figure 1.2c**. In polymers where the side chains are consistently located, multiple chains can lie together nicely, creating an orderly crystalline structure which can quickly and efficiently allow for charge transport. In polymers where the side chains are 'randomly' oriented, the interaction between the side chains prevent orderly stacking, and leads to fully amorphous polymers with interference in the charge transport capabilities[17].

Many variables are involved in the creation of conjugated polymer blends, all of which impact the morphology and properties of the product. During processing, the materials used, steps taken, components added, and duration of processing variables all change the way the materials interact and can vastly change the final product[19–22]. Schwartz, in other collaborations, conducted experiments into the "memory" of the chain conformation in solution, through the processing stages, and into the final film. They were able to show visible differences in the final films which they proposed may be due to solution phase impacts[23]. These results are supported with multiple studies also suggesting a 'solution memory' that helps dictate the final blend conformation as the assembly in solution is carried through the casting process into the resulting film[24–26]. Vastly different products have also been observed from different components, with materials from the same family of polymers producing shapes and structures that are completely different. The complexity observed here allows for a vast array of variables to modify, pick and choose from, allowing researchers to investigate a multitude of systems that are tangentially related, in hopes of connecting and better understanding the entire field. This also allows for researchers to refine a polymer system to encourage specific structures, growth patterns, or properties[27,28].

1.2 Elastomers

Elastomers are a subset of commodity polymers with specific desirable mechanical properties. They are 'elastic polymers' defined as having increased stretchability and flexibility, or a polymer that displays rubber-like elasticity[29]. Elastomers are often used in devices that have a need for increased stretching and flexing, such as artificial skin, biosensors, solar windows, or

haptics[30–32]. The type of elastomer we focus on is a triblock copolymer, but blends made with other types of elastomers can also provide insight into our system. Block copolymers are complex polymers consisting of two or more sections of homopolymers that are bonded together in chunks. These sections have varying molecular weights and lengths, which allow for a large variety of polymers to be made. Block copolymers can vary greatly, with different repetition patterns and different ratios of concentrations of the homopolymer blocks, affecting and modifying the final product created[33].

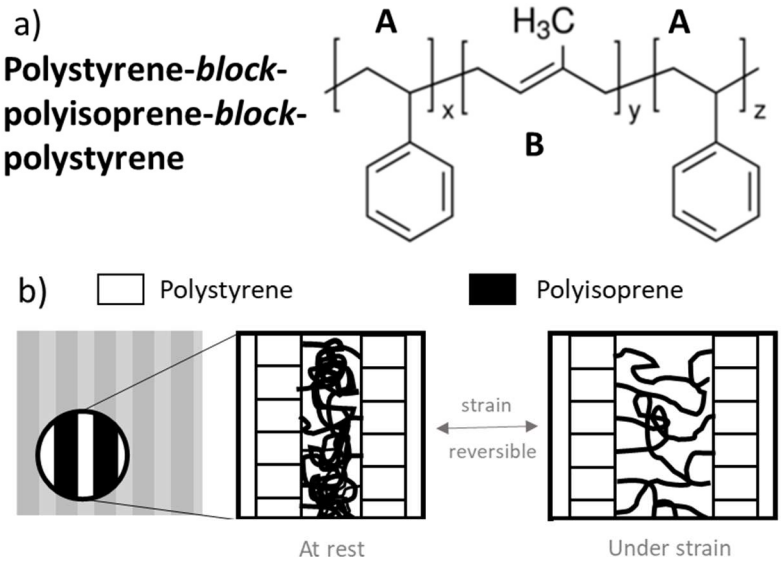

Figure 1.3: a) Tri-block elastomer polystyrene -block- polyisoprene-block-polystyrene (PS-PI-PS) structure, and b) schematic of PS-PI-PS film with lamellar structure at rest and under strain with extended polyisoprene chains

The specific version of block copolymer of interest to us in this work is a triblock copolymer with two sections of identical homopolymer sandwiching a third section of a different homopolymer in ABA pattern as shown in **Figure 1.3a**. When the "A" blocks are semi crystalline glassy blocks and the "B" blocks are amorphous rubbery blocks, then the resulting combination can create an elastomer. The glassy A blocks assemble into supportive structures linked by the rubbery "B" blocks, which stretch and deform when manipulated, but encourage the structure to return to the resting state once stresses are removed[33,34]. This restoring forcing seen in elastomers is driven by a mixture of enthalpy, the internal energy in the system due to interchain and intrachain interactions in the network, and entropy, resulting from changes in the configurations in the chain arrangement[35]. In experiments by Sharda and Tschoegl to isolate impacts from each component,

it was determined that most of the restoring forces in the elastomer of focus was due to entropy changes, but a significant contribution was made from internal energy changes[35]. Entropic changes occur during deformation, as some of the rubber chains are forced to shift, typically becoming linearly oriented, which causes an overall decrease in entropy in the rubber system[36]. This decreased entropy leads to a driving force to reestablish disorder in the system, leading to a restoring force. The specifics of the polymers, including material, block length, cross-linking specifics, as well as environmental factors such as temperature or extent of deformation will change the impact of both enthalpy and entropy, effecting the amount of restoring force present[35,36].

The mechanical properties of an elastomeric polymer make them useful for devices that will endure extreme or repetitive physical stresses. Traditional silicon devices are often brittle and have weakness in physical flexibility that makes them difficult to incorporate into biosimilar materials. For devices that are designed to mimic skin or sensorially 'disappear' when worn, having bulky, immobile materials is not ideal. By utilizing elastomers to build devices that can stretch and move along with the wearer or be placed on curved surfaces such as buildings or cars, a balance between form and function can be met. There are many different forms of elastomeric electronics that are currently being researched[37]. In the same vein as more traditional commodity polymers, elastomers can be used in blends with other materials to create a final device that has blended properties[38,39]. Researchers have cast electronic materials on or within an elastomeric mount, for instance, dispersing single-walled carbon nanotubes within a rubber gel, allowing for flexibility, delicate processing, and direct printing, all the while maintaining electronic properties[40]. Elastomeric mounted devices have been created using organic light diode displays made of organic transistors and organic light-emitting diodes sandwiched between two printed elastomeric sheets[41]. Conjugated polymer and elastomer blends have also been used, with block co-polymers consisting of a conjugated polymer component and a soft block polymer[42], or with refined processing techniques allowing rigid polymers to display flexible properties[43]. Research into this direction allows for the blending of desirable properties from each component, this time with a focus on mechanical elasticity alongside resilience, processing, and electronic capabilities.

1.3 OMIEC Materials

Organic Mixed Ionic Electric Conductive (OMEIC) materials are soft materials, typically polymers which can display conduction from both electrical and ionic methods[44–46]. Materials that

are currently in the forefront of OMIEC research were often initially developed without regard to their mixed properties. For example, the commonly focused upon poly(2,4-ethylenedioxythiophene): Poly (styrene sulfonate) (PEDOT: PSS) copolymer showed promises as an antistatic coating and conducting interlayer in optoelectronic devices[47]. As the requirements for materials shifted from purely conductive to more complex multi-layer, multi-functional devices, more interest was generated by the ionic conductivity as well. Current interest in OMIEC materials covers many fields including actuators[48], electronic devices [49,50], chemical sensors[51], ion pumps[52], and organic sensors for haptics and feedback[50,53–55]. OMIECS have found a particularly strong foothold in bioelectronics as the ability for the material to receive signals from the body's natural ionic output and translate that into electronic feedback makes these materials strong candidates for new devices[54].

OMIEC materials utilize three physical processes to balance their unique properties: ionic-electronic coupling, ionic transport, and electronic transport[44]. Ionic transport involves the movement of ions, while electronic transport relies on the movement of electrons or holes. Ionic-electronic coupling describes the mechanism for conversion between ionic and electric conductivity and the resulting feedback cycle which leads to improved material conductivity[56–58]. Each of these processes provide a form of conductivity and can be managed and utilized for specific device purposes. For example, storing energy in OMIEC batteries relies on ionic-electronic coupling, whereas charging rates are constrained by ion transport rates. In bioelectronic sensors the combination of ion transport and ionic-electronic coupling determine the response time of the sensor, whereas electronic transport and ionic-electronic coupling determine the transconductance[44]. In all devices OMIEC materials are used in, these three processes are interconnected and interdependent, creating a complex web of considerations for material design.

While the only requirement for OMIECs is to have both ionic and electronic conductivity capability, there are a multitude of materials that fall under these requirements. To help categorize these OMEICS, there are a few guidelines that help gather like materials. The first focuses on the ionic conductivity, separated into those which contain ionic charge within them, and those which do not[44]. The second categorization is between homogenous (ionic and electronic transport occurs within a single material) and heterogenous (ionic conductive-rich and electronic conductive-rich regions within the material) OMIECs. The heterogenous category is split into separate categories of a blended system or a single component co-polymer system. When these two categorizations

are applied, six separate categories emerge with various levels of copolymers and blends in the system. This categorization is shown in **Figure 1.4**[44]. Understanding the separate categories helps to narrow expectations and information for the system at hand. Each category will have slightly different needs for synthesis, development, and device creation, for example, if a material does not contain ions within its material, a doping agent is required in order for the device to work. These categories also help understand the complexity for a system, for example a blended or copolymer system will have polymer/polymer interactions on top of the solvent/polymer interactions.

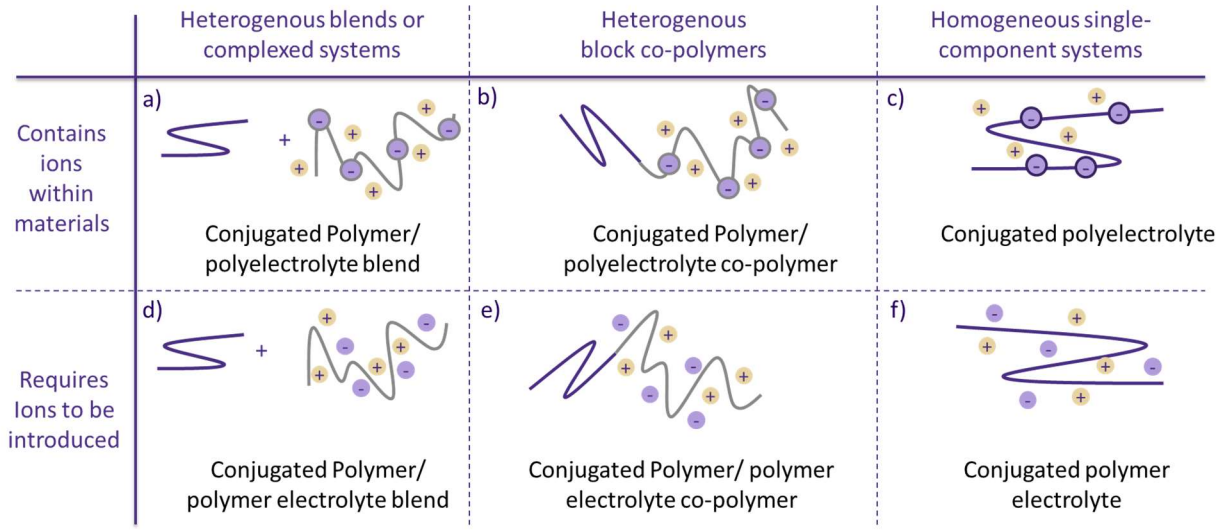

Figure 1.4: Schematic breakdown of OMIEC categorization, separating materials containing ions (a,b,c) and materials that require ions to be added (d,e,f) as well as mixed multiple component blended systems (a,d) and mixed single component systems with co-polymers (b,e) and single component system with a single homopolymer (c,f). Adapted from Paulsen et al Organic Mixed Ionic-Electronic Conductors[44]

A common trait of all the categories, and the cause for the mixed ionic and electronic capabilities, is the existence of a conjugated polymer component (electronic) and an electrolyte component (ionic). The property balance between the electronic and ionic component varies from category to category, but there are a few overarching trends that stay the same. The structural features that improve each property degrade the other, causing complications with balancing the two. Electric transport is improved through increased crystallization, rigidity, and regio-regularity, but ionic transport relies on flexibility, ion mobility and access to the backbone. These two sets of structural characteristics are directly competing and favoring one over the other will lead to an electronic-dominate or ionic-dominate system. This structural balance also underlies the need to

characterize and understand the structure and morphology of a system with respect to its properties, as refinement of properties will require change of structure through additives, processing changes, or material choice.

1.4 Small Angle Scattering

To fully characterize the polymer blend structure, we need to be able to measure features at a large array of length scales, as well as differentiate visually similar components in a system. Many common microscopy techniques cover a short range of lengths, typically in the tens to hundreds of microns and larger, with electron and x-ray microscopy techniques able to measure slightly smaller structures, but often requiring complex experimental set ups[59,60]. The use of Small Angle Scattering (SAS) techniques allows for the measurement of a large range of length scales, over many system relevant milestones **(Figure 1.5)**. Another advantage of using SAS for thick polymer films is the ability to measure buried bulk structures due to the high energy beam transmitting through the material and scattering on the entirety of the material thickness. Traditional microscopy can typically characterize surface structures but are unable to fully resolve internal bulk structures of thick films.

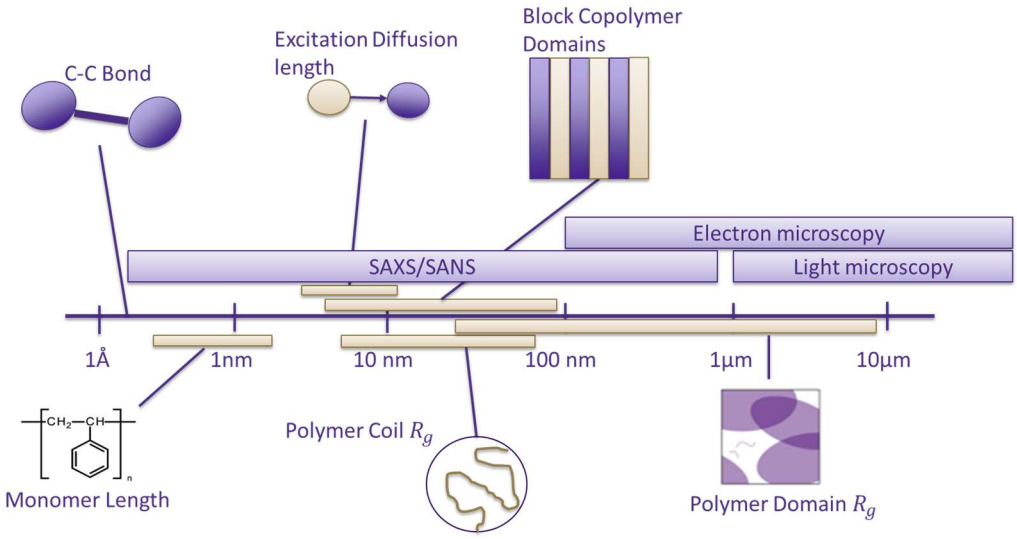

Figure 1.5: Schematic of measurable length scales of microscopy and scattering techniques, with reference to the length scales relevant to polymers

When studying polymers, interactions, and changes in the smallest structures, such as in bond distances (one to tens of angstroms) and monomer interactions (tens to hundreds of angstroms), are just as important as larger structures like aggregations or domains (tens of nanometers to microns)[61]. Using small angle scattering, we can utilize a single technique to

measure all the length scales of interest, reducing the error and sample variation which becomes possible when piecing information from different techniques together. SAS is a uniquely modifiable technique, allowing for refinable experiments to optimize the measurement of complex systems. For example, to fully understand polymer blend systems, we need to understand the morphology or physical structure of the blends throughout various steps in the processing method. With SAS instruments, both liquid and solid samples can be run with only changes to the sample holders. This allows us to track our samples through multiple stages of the processing timeline, observing how various structures are formed and destroyed throughout the process. SAS also allows us the capability to conduct complex experiments, such as dynamic time-resolved tracking of aggregations, or temperature dependent changes[60,62,63]. This variation in length scales, sample type, and experimental modifications make small angle scattering a powerful tool for this work.

1.5 Polymer Thermodynamics

In both the solid and liquid states, thermodynamics dictate the type, extent, and intensity of polymer movement and assembly. Tracking the thermodynamics of polymers over the processing states, from solution to solid films, aids us in anticipating how the system should work, and informs our understanding of the morphology of the resulting films. During the solution phase, there are a few metrics we must consider, the two of highest importance being solvent quality and χ parameters.

Solvent quality is a metric of the favorability of the interactions between the polymer and the solvent in question[64]. When considering solvent quality for a polymer of interest, there is not a single value that can describe the activity of a single polymer in all solvents, instead this metric is reliant on the relationship between the polymer and solvent in question (**Figure 1.6)**. When dissolved in a 'poor' solvent, it is more thermodynamically favorable for the polymer chains to interact with themselves than the solvent, causing the polymer to tightly coil into self-associated structures. For 'moderate' solvents, the polymer will be increasingly favorable to interactions with the solvent over itself and begin to spread out. This trend continues until the polymer is more favorable to the solvent than itself and forms a loose chain in a 'good' solvent[65]. A host of research has been conducted on polymer systems with respect to solvent quality, including work done on conjugated polymers in a single solvent, conjugated polymers in mixed solvents, and commodity polymers in solvent systems[66–68].

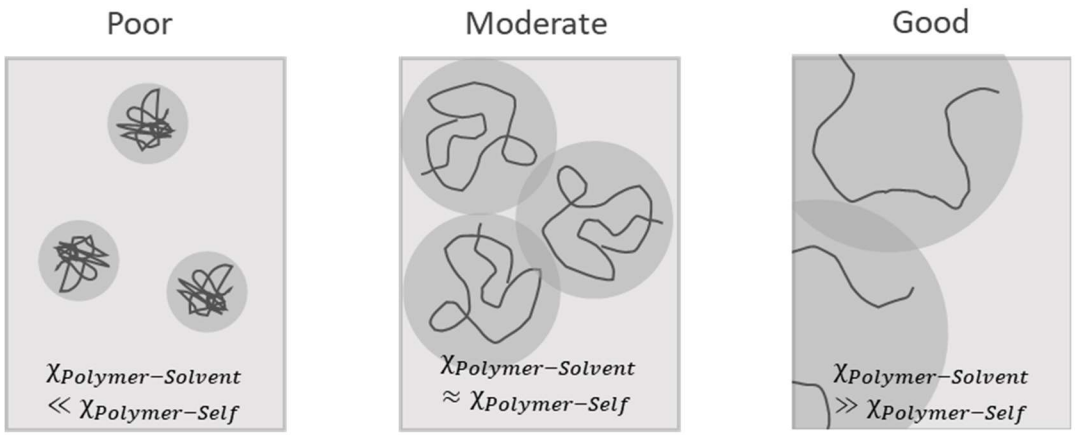

Figure 1.6: Schematic of effect of solvent quality on the spread of a polymer with poor, moderate, and good solvents with reference to χ parameters

Solvent quality in blended systems is more complicated, and researchers have been working on understanding the complex thermodynamic relationships between the solvent and each polymer and the polymers with each other[69,70]. In a blend, typically the solvent quality differs relative to each polymer. This means that although a solvent was added that is a 'good' solvent for one portion of the blend, it may be 'poor' for the other, applying uneven thermodynamic pressures across the system. This has effects on the final product as shown in work by Rivillon et al, looking at material properties of a blend of two polymers with varying interaction potential for the solvent and air interfaces[69].

Along with polymer/solvent interactions, in blends the polymer/polymer interactions come into play as well. A few different metrics are available to analyze the polymer/polymer interactions, but Flory Huggins parameters are widely used and available for most polymers. Flory Huggins theory expands traditional thermodynamic calculations into polymers and calculates the Gibbs free energy of mixing for polymer solutions[65,71]. This can be applied to interactions between a polymer and the solvent its dissolved in as well as between the polymers in a solution. While this is a useful and helpful metric, there are a series of assumptions that must be made before applying to complex polymer systems. We assume there is no volume change on mixing, we compute both entropy and enthalpy using random mixing, and we determine local concentration by the bulk average[71]. With these (and a few other) concessions in mind, the Flory Huggins Theory allows us to calculate χ parameters that quantify extent of favorability involved in the interaction of the systems, with lower χ values suggesting more favorable systems. The use of χ parameters allows

us to anticipate how the polymers will interact and assemble based on how each component reacts in the system.

In a solution phase, the system is assembled into a state that is most thermodynamically favorable for the experimental conditions, with consideration to the variables above. Once the solvent is removed from the system, the thermodynamic pressures change. This may include unfavorable impacts from poor solvents[66,69,70], drying times[72,73], processing conditions[74,75], and more. Oftentimes the equilibrium point that is thermodynamically most favorable was not reachable during the short time allowed during processing. This competition between kinetics and thermodynamics leaves materials with structures and arrangements that are often not at equilibrium. Once dried, the chains, depending on the glass transition and melting points, slowly move towards an equilibrium, and this movement can be encouraged through annealing[76,77]. Thermal annealing is a process of heating up a material, holding that temperature, and then slowly cooling. When annealing, the temperature must reach above the glass transition temperature in order to free the amorphous portions of the polymer, and above the melting point in order to free the crystalline structures. Once these components are free, they can slowly move and form energetically favorable structures over variable time periods. Annealing can be used in polymers in a variety of ways. It can change material properties, for example improving phase behavior of extruded blends, which are more easily extruded at cooler temperatures, but have lacking properties[78]. This post-processing technique can also be used to relieve stress in polymers with cooled locked-in stresses, such as after heat-molding or heavy pressing[79,80].

1.6 Chapter Overview and Goals

1.6.1: Chapter 2: Theory and Methods

Chapter 2 will cover the theory and the methods used in this work, focusing specifically on small angle scattering (both x-ray and neutron) and the data analysis used on scattering data.

1.6.2: Chapter 3: Solid Blends of Conjugated Polymer and Polystyrene

Chapter 3 will cover work conducted in collaboration with Dr. Caitlyn Wolf and Lorenzo Guio, including the initial foray into conjugated polymer blends and proposed work to investigate effects of the processing methods used previously with this system. This work utilizes contrast matched SANS, WAXS, and electronic property measurement techniques to understand solid film polythiophene and polystyrene blends.

1.6.3: Chapter 4: Blend Morphology of Conjugated Polymers and Elastomers in Solution and Solid States

Chapter 4 will expand the systems previously investigated by utilizing an elastomeric triblock copolymer as a commodity polymer matrix. The conjugated polymer additive of choice is P3HT, both semicrystalline and amorphous. With this work we look to understand a single complex system and investigate the morphology using SAXS.

1.6.4: Chapter 5: Processing Effects on Blends of Conjugated Polymers and Elastomers

Chapter 5 will continue the work conducted in Chapter 4, by investigating the effect of processing variables on the morphology and structure of the resulting blend. Variables analyzed in this work include pressing temperature, pressing time, solvent, intentional alignment, and post-processing annealing.

1.6.5: Chapter 6: High-χ Parameter Copolymers

Chapter 6 will explore an AB copolymer with blocks that are not thermodynamically compatible with each other in solution. These polymers are designed to encourage separation and aggregation, and an understanding of their assembly in solution can aid further experimentation with similar systems.

1.6.6: Chapter 7: OMIEC Blends with Conjugated Polymers

Chapter 7 will explore another conjugated polymer blend system using P3HT, explored in previous chapters, and the high-χ parameter copolymer investigated in isolation in Chapter 6. The system is designed to encourage separation and aggregation, with the goal of creating materials with both ionic and electronic conductivity.

1.6.7: Chapter 8: Conclusions and Outlook

Chapter 8 will summarize the work laid out in previous chapters and draw overarching conclusions on processing and polymer specificity.

1.6.8: Chapter 9: Appendix

Chapter 9 will cover projects worked on alongside those addressed in previous chapters as well as elastomer polymer blend dataset that is presented with a caveat. Pallicera is a startup that participated in multiple business competitions and accelerators which aimed to improve pediatric drug adherence by designing taste masked drug loaded solutions. Phase-IR is a low-cost hardware and software system developed from the ChemE data science capstone course to conduct high throughput phase identification using IR bolometry. A series of elastomer and conjugated polymer

blends were measured using APS USAXS in triplicate and show a unique peak shift that is not observed in that intensity in reproduced samples. This shift is interesting for incorporation and possible property repercussions but attempts to create samples with the observed shift have not been successful and insights provided by processing change experiments (Chapter 4 and 5) have not shown an obvious cause. Additional supplementary information and some solo run tensile samples are included to flesh out the work done on the elastomeric conjugated polymer system.

1.7 References

1. Gu, K. *et al.* Assessing the Huang-Brown Description of Tie Chains for Charge Transport in Conjugated Polymers. *ACS Macro Lett* **7**, 1333–1338 (2018).
2. Li, an, Chueh, C.-C. & K-Y Jen, A. Recent advances in molecular design of functional conjugated polymers for high-performance polymer solar cells. *Prog Polym Sci* **99**, 101175 (2019).
3. Pandey, M., Kumari, N., Nagamatsu, S. & Pandey, S. S. Recent advances in the orientation of conjugated polymers for organic field-effect transistors. *J Mater Chem C Mater* **7**, 13323–13351 (2019).
4. Gopalan, A.-I. *et al.* Functionalized conjugated polymers for sensing and molecular imprinting applications Nanostructuring Multicomponent Sensor Molecular imprinting. *Prog Polym Sci* **88**, 1–129 (2019).
5. Qiu, Z., Hammer, B. A. G. & Müllen, K. Conjugated polymers – Problems and promises. *Progress in Polymer Science* vol. 100 Preprint at https://doi.org/10.1016/j.progpolymsci.2019.101179 (2020).
6. Smith, J. *et al.* Solution-processed organic transistors based on semiconducting blends †. doi:10.1039/b921674j.
7. Qiu, L. *et al.* Organic thin-film transistors based on polythiophene nanowires embedded in insulating polymer. *Advanced Materials* **21**, 1349–1353 (2009).
8. Goffri, S. *et al.* Multicomponent semiconducting polymer systems with low crystallization- induced percolation threshold. *Nat Mater* **5**, 950–956 (2006).
9. Ocheje, M. U. *et al.* Amide-Containing Alkyl Chains in Conjugated Polymers: Effect on Self-Assembly and Electronic Properties. *Macromolecules* **51**, 1336–1344 (2018).
10. Meng, B. *et al.* Replacing Alkyl with Oligo (ethylene glycol) as Side Chains of Conjugated Polymers for Close π-π Stacking. *Macromolecules* **48**, 4357–4363 (2015).
11. Aubry, T. J. *et al.* Hydrophobic deep eutectic solvents as water-immiscible extractants. *Macromolecules* **3**, 1–20 (2019).
12. Mei, J. & Bao, Z. Side chain engineering in solution-processable conjugated polymers. *Chemistry of Materials* vol. 26 604–615 Preprint at https://doi.org/10.1021/cm4020805 (2014).
13. Wen, J., Luo, D., Cheng, L., Zhao, K. & Ma, H. Electronic Structure Properties of Two-Dimensional π-Conjugated Polymers. (2016) doi: 10.1021/acs.macromol.5b02572.
14. Wen, J., Luo, D., Cheng, L., Zhao, K. & Ma, H. Electronic Structure Properties of Two-Dimensional π-Conjugated Polymers. *Macromolecules* **49**, 1305–1312 (2016).
15. Sirringhaus, H. *et al. Two-Dimensional Charge Transport in Self-Organized, High-Mobility Conjugated Polymers*. *NATURE* vol. 401 www.nature.com (1999).
16. Wolf, C. M. *et al.* Blend Morphology in Polythiophene–Polystyrene Composites from Neutron and X-ray Scattering. *Macromolecules* (2021) doi: 10.1021/acs.macromol.0c02512.
17. Kim, H. J. *et al.* Solution-Assembled Blends of Regioregularity-Controlled Polythiophenes for Coexistence of Mechanical Resilience and Electronic Performance. *ACS Appl Mater Interfaces* **9**, 14120–14128 (2017).
18. Schwartz, B. J. CONJUGATED POLYMERS AS MOLECULAR MATERIALS: How Chain Conformation and Film Morphology Influence Energy Transfer and Interchain Interactions. *Annu. Rev. Phys. Chem* **54**, 141–72 (2003).

19. Heeley, E. L. *et al.* Effect of processing parameters on the morphology development during extrusion of polyethylene tape: An in-line small-angle X-ray scattering (SAXS) study. (2013) doi: 10.1016/j.polymer.2013.10.004.
20. Schneider, S. A. *et al.* Controlling Polymer Morphology in Blade-Coated All-Polymer Solar Cells. *Chemistry of Materials* **33**, 5951–5961 (2021).
21. Megelski, S., Stephens, J. S., Chase, D. B. & Rabolt, J. F. Micro-and Nanostructured Surface Morphology on Electrospun Polymer Fibers. (2002) doi:10.1021/ma020444a.
22. Søndergaard, R., Hösel, M., Angmo, D., Larsen-Olsen, T. T. & Krebs, F. C. Roll-to-roll fabrication of polymer solar cells. *Materials Today* **15**, 36–49 (2012).
23. Nguyen, T. Q., Doan, V. & Schwartz, B. J. Conjugated polymer aggregates in solution: Control of interchain interactions. *Journal of Chemical Physics* **110**, 4068–4078 (1999).
24. Nguyen, T.-Q., Martini, I. B., Liu, J. & Schwartz, B. J. Controlling Interchain Interactions in Conjugated Polymers: The Effects of Chain Morphology on Exciton-Exciton Annihilation and Aggregation in MEH-PPV Films. (2000) doi:10.1021/jp993190c.
25. Shi, Y., Liu, J. & Yang, Y. Device performance and polymer morphology in polymer light emitting diodes: The control of thin film morphology and device quantum efficiency. *J Appl Phys* **87**, 4254–4263 (2000).
26. Guo, T. F. & Yang, Y. In situ study on the reorientation of polymer chains in operating polymer diodes. *Appl Phys Lett* **80**, 148–150 (2002).
27. Park, Y. D. *et al.* Solubility-Induced Ordered Polythiophene Precursors for High-Performance Organic Thin-Film Transistors. doi:10.1002/adfm.200801763.
28. Meyer, D. L. *et al.* Side-Chain Engineering of Conjugated Polymers: Distinguishing Its Impact on Film Morphology and Electronic Structure. *Journal of Physical Chemistry C* **123**, 20071–20083 (2019).
29. Broekhoven, V., Song, H.-H. & Roe, R.-J.) Keller, A. In Polymers. *Liquid Crystals, and Low-Dimensional Solids* **16**, 575 (1987).
30. Kang, D. Y. *et al.* Scalable microfabrication procedures for adhesive-integrated flexible and stretchable electronic sensors. *Sensors (Switzerland)* **15**, 23459–23476 (2015).
31. Tsai, Y. S. *et al.* Multi-solution processes of small molecule for flexible white organic light-emitting diodes. *Thin Solid Films* **604**, 94–101 (2016).
32. Song, R. *et al.* Unveiling the Stress−Strain Behavior of Conjugated Polymer Thin Films for Stretchable Device Applications. (2020) doi: 10.1021/acs.macromol.9b02573.
33. Shi, W. *et al.* Morphology re-entry in asymmetric PS-PI-PS' triblock copolymer and PS homopolymer blends. *J Polym Sci B Polym Phys* **54**, 169–179 (2016).
34. Choi, M.-C., Kim, Y. & Ha, C.-S. Polymers for flexible displays: From material selection to device applications. *Prog. Polym. Sci* **33**, 581–630 (2008).
35. Sharda, S. C. & Tschoegl, N. W. The Elastic Restoring Force in Rubbers. *Macromolecules* **7**, 48 (1976).
36. Pal, S. *et al.* Origin of Rubber Elasticity. *Elasticity of Materials* (2023) doi:10.5772/INTECHOPEN.100205.
37. Sekitani, T. & Someya, T. Stretchable, large-area organic electronics. *Advanced Materials* vol. 22 2228–2246 Preprint at https://doi.org/10.1002/adma.200904054 (2010).
38. Wang, M., Baek, P., Akbarinejad, A., Barker, D. & Travas-Sejdic, J. Conjugated polymers and composites for stretchable organic electronics. *J Mater Chem C Mater* **7**, 5534–5552 (2019).
39. Savagatrup, S., Printz, A. D., Rodriquez, D. & Lipomi, D. J. Best of both worlds: Conjugated polymers exhibiting good photovoltaic behavior and high tensile elasticity. *Macromolecules* **47**, 1981–1992 (2014).
40. Sekitani, T. *et al.* A rubberlike stretchable active matrix using elastic conductors. *Science (1979)* **321**, 1468–1472 (2008).
41. Sekitani, T. *et al.* Stretchable active-matrix organic light-emitting diode display using printable elastic conductors. *Nat Mater* **8**, 494–499 (2009).
42. Stoyanov, H., Kollosche, M., Risse, S., Waché, R. & Kofod, G. Soft Conductive Elastomer Materials for Stretchable Electronics and Voltage Controlled Artificial Muscles. *Advanced Materials* **25**, 578–583 (2013).
43. Chen, J. Y. *et al.* Electrospinning-induced elastomeric properties of conjugated polymers for extremely stretchable nanofibers and rubbery optoelectronics. *J Mater Chem C Mater* **8**, 873–882 (2020).

44. Paulsen, B. D., Tybrandt, K., Stavrinidou, E. & Rivnay, J. Organic mixed ionic–electronic conductors. *Nature Materials* vol. 19 13–26 Preprint at https://doi.org/10.1038/s41563-019-0435-z (2020).
45. Tropp, J., Meli, D. & Rivnay, J. Organic mixed conductors for electrochemical transistors. *Matter* (2023) doi: 10.1016/j.matt.2023.05.001.
46. Tan, S. T. M. *et al.* Mixed Ionic–Electronic Conduction, a Multifunctional Property in Organic Conductors. *Advanced Materials* **34**, (2022).
47. Elschner Andreas, Kirchmeyer Stephan, Lövenich Wilfried, Merker Udo, R. K. *PEDOT Principles and Applications of an Intrinsically*. *Conductive Polymer* (CRC Press, 2011).
48. Smela, E. Conjugated polymer actuators for biomedical applications. *Advanced Materials* **15**, 481–494 (2003).
49. Tropp, J., Meli, D. & Rivnay, J. Organic mixed conductors for electrochemical transistors. *Matter* **6**, 3132–3164 (2023).
50. Li, G. PEDOT: PSS-based intrinsically soft and stretchable bioelectronics. *Soft Science* **2**, 7 (2022).
51. Jang, J., Ha, J. & Cho, J. Fabrication of water-dispersible polyaniline-poly(4-styrenesulfonate) nanoparticles for inkjet-printed chemical-sensor applications. *Advanced Materials* **19**, 1772–1775 (2007).
52. Isaksson, J. *et al.* Electronic control of Ca 2+ signaling in neuronal cells using an organic electronic ion pump. (2007) doi:10.1038/nmat1963.
53. Boehler, C., Aqrawe, Z. & Asplund, M. Applications of PEDOT in bioelectronic medicine. doi:10.2217/bem-2019-0014.
54. van de Burgt, Y. *et al.* A non-volatile organic electrochemical device as a low-voltage artificial synapse for neuromorphic computing. (2017) doi:10.1038/NMAT4856.
55. Kim, B. G. *et al.* Chronic neural recordings using silicon microelectrode arrays electrochemically deposited with a poly(3,4-ethylenedioxythiophene) (PEDOT) film. (2006) doi:10.1088/1741-2560/3/1/007.
56. Savva, A., Wustoni, S. & Inal, S. Ionic-to-electronic coupling efficiency in PEDOT: PSS films operated in aqueous electrolytes †. *J. Mater. Chem. C* **6**, 12023 (2018).
57. Keene, S. T., Rao, A. & Malliaras, G. G. The relationship between ionic-electronic coupling and transport in organic mixed conductors. (2023).
58. Panzer, M. J. & Frisbie, C. D. Exploiting ionic coupling in electronic devices: Electrolyte-gated organic field-effect transistors. *Advanced Materials* **20**, 3177–3180 (2008).
59. Van, B., Ku Leuven, M., Inoue, S., Yoshida, Y. & Perdigao, J. Microscopy investigations. Techniques, results, limitations. (2000).
60. Grunwaldt, J. D. & Schroer, C. G. Hard and soft X-ray microscopy and tomography in catalysis: bridging the different time and length scales. *Chem Soc Rev* **39**, 4741–4753 (2010).
61. Rubinstein, M. & Colby, R. H. Polymer Physics. 442 Preprint at (2003).
62. Endo, H. Study on multicomponent systems by means of contrast variation SANS. 682–684 (2006) doi: 10.1016/j.physb.2006.05.290.
63. Roe, R.-J. & Curro, J. J. Small-Angle X-ray Scattering Study of Density Fluctuation in Polystyrene Annealed below the Glass Transition Temperature. *P. N.; Sundelóf, L. O. Makromol. Chem* **51**, 871 (1947).
64. Riekel, C. & Vollrath, F. Spider silk fibre extrusion: combined wide-and small-angle X-ray microdiffraction experiments. *Int J Biol Macromol* **29**, 203–210 (2001).
65. Witten, T. A. *Polymer Solutions: A Geometric Introduction *. Typeset May* vol. 25 (1998).
66. Halperin, A., Kr€, M. & Zhulina, E. B. Colloid-Brush Interactions: The Effect of Solvent Quality. **44**, 3622–3638 (2011).
67. Nguyen, T. Q., Yee, R. Y. & Schwartz, B. J. Solution processing of conjugated polymers: The effects of polymer solubility on the morphology and electronic properties of semiconducting polymer films. *J Photochem Photobiol A Chem* **144**, 21–30 (2001).
68. Xi, Y., Wolf, C. M. & Pozzo, L. D. Self-assembly of donor–acceptor conjugated polymers induced by miscible 'poor' solvents. *Soft Matter* **15**, 1799–1812 (2019).

69. Rivillon, S., Monroy, F., Ortega, F. & Rubio, R. G. Dilational rheology of monolayers of a miscible polymer blend: From good-to poor-solvent conditions. *Eur. Phys. J. E* **9**, 375–385 (2002).

70. Broseta, D., Leibler, L. & Joanny, J.-F. Critical Properties of Incompatible Polymer Blends Dissolved in a Good Solvent. *Macromolecules* **20**, 1935–1943 (1987).

71. Nedoma, A. J., Robertson, M. L., Wanakule, N. S. & Balsara, N. P. Measurements of the Composition and Molecular Weight Dependence of the Flory-Huggins Interaction Parameter. doi:10.1021/ma800698r.

72. Higgins, J. S. & Cabral, J. T. A Thorny Problem? Spinodal Decomposition in Polymer Blends. *Macromolecules* vol. 53 4137–4140 Preprint at https://doi.org/10.1021/acs.macromol.0c00581 (2020).

73. Keum, J. K. *et al.* Solvent quality-induced nucleation and growth of parallelepiped nanorods in dilute poly(3-hexylthiophene) (P3HT) solution and the impact on the crystalline morphology of solution-cast thin film. *CrystEngComm* **15**, 1114–1124 (2013).

74. Liu, J., Arif, M., Zou, J., Khondaker, S. I. & Zhai, L. Controlling Poly(3-hexylthiophene) crystal dimension: Nanowhiskers and nanoribbons. *Macromolecules* **42**, 9390–9393 (2009).

75. Roesing, M., Howell, J. & Boucher, D. Solubility Characteristics of Poly(3-hexylthiophene). *J. Polym. Sci., Part B: Polym. Phys* **55**, 1075–1087 (2017).

76. Albalak, R. J., Thomas, E. L. & Capel, M. S. Thermal annealing of roll-cast triblock copolymer films. *Polymer (Guildf)* **38**, 3819–3825 (1997).

77. Liu, W., Zhang, L. & Wei, Y. The influence of annealing atmosphere, blending ratio, and molecular weight on the phase behavior of blend materials. *Processes* **9**, (2021).

78. Wach, R. A. *et al.* Enhancement of Mechanical Properties of FDM-PLA Parts via Thermal Annealing. *Macromol Mater Eng* **303**, 1800169 (2018).

79. Broutman, L. J. & Krishnakumar, S. M. Impact strength of polymers: 1. The effect of thermal treatment and residual stress. *Polym Eng Sci* **16**, 74–81 (1976).

80. So, P. & Broutman, L. J. Residual stresses in polymers and their effect on mechanical behavior. *Polym Eng Sci* **16**, 785–791 (1976).

Chapter 2: Theory and Methods

2.1 Small Angle Scattering

Information referenced in this chapter is heavily informed by the scattering textbook *Neutrons, X-rays and Light: Scattering Methods Applied to Soft Condensed Matter*[1] and the Sans Toolbox[2] reference document.

2.1.1 Fundamentals

Small angle scattering (SAS) is an instrumentation technique that includes neutron and X-ray scattering and is similar to commonly used diffraction and crystallography techniques.

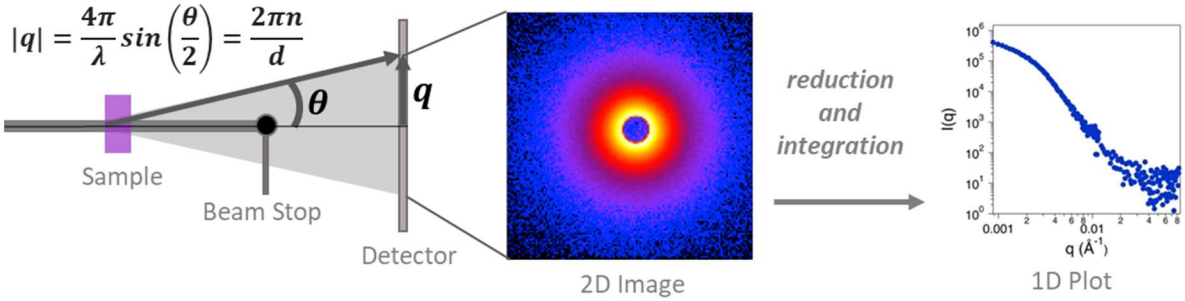

Figure 2.1: Schematic of a SAS experiment with 2D and 1D data representation

A schematic of the method is shown in **Figure 2.1** and involves a collimated beam of radiation, typically either neutrons or X-ray photons, originating from a source. After generation, the produced particles pass through various slits, rotors, or crystals which chop and refine the rough beam to produce an aligned and clean beam of specified wavelengths. The collimated beam is then directed at and passed through a sample. The sample allows a portion of the beam to pass through unobstructed, while the rest of the particles interact with the sample. The extent and methodology behind the interactions vary depending on the instrumentation and particle type and are addressed in more detail in the next few sections. Past the sample, the unobstructed beam and scattered particles enter a chamber where a series of detectors collect the radiation, and depending on the type of instrument, either collect or block the unobstructed beam. These detectors are excited by the scattered particles and record the number of particles hitting the detector at each location. The detector locations each correlate to a solid angle from the sample scattering point, and the number of particles hitting over a period of user set 'counting time' is calculated to be the intensity at that angle. Once the experiment is over, the number of counts per detector pixel can be

visualized in 2D images or transformed into a 1D plot of the intensity of photons or neutrons as a function of the wave-vector Q.

$$I(q) = n\Delta\rho^2 V^2 P(Q) S(Q) + background \quad (2.1)$$

For systems consisting of only one type of particle, the data can then be represented by equation 2.1. For more complex systems, this equation will need to be modified to express scattering from multiple types of particles, such as polydisperse assemblies, but it provides a solid starting point for analysis. This guiding equation can be used to plan experiments as well as analyze the data collected. For example, contrast $(\Delta\rho)^2$ is the variation in the scattering length density (SLD) of the components and when planning experiments, contrast must be considered to ensure there will be adequate or coherent scattering once conducted. The scattering length density is a material dependent property and reliant on the molecular makeup of the material and the type of instrument being used. It's important to note that the Δρ is squared, so if the difference between the SLDs is very low, then the contrast will typically be inadequate to collect clean data. In neutron systems, contrast can also be intentionally modified in a process called 'contrast matching' to improve the specificity of the experiment. The term P(Q) is the form factor, which corresponds to the scattering from the shape of a particle and can be fit to shape models to gain info on the form and size of the scatters in the material. There are a host of models available, with increasing complexity from basic spheres to complex aggregations of droplets[1,3]. The form factor can also be customized to fit complex systems that contain particles of multiple shapes through simultaneous fitting. The term S(Q) is the structure factor, which can be fit with equations that isolate particle-particle interactions. Fitting the structure factor can allow for analysis of interactions within the material, such as surface or interfacial information. Understanding the guiding equation and scattering theory aids the process of experimental refinement and analysis for data collected from small angle scattering.

2.1.2 Small Angle Neutron Scattering (SANS)

One technique in the SAS family utilizes a neutron source and encompasses specific measurements such as small angle neutron scattering (SANS) and ultra-small angle neutron scattering (USANS). Neutron sources vary, with two main categories: continuous (nuclear reactors, both thermal and cold sources) and pulsed sources (spallation source and a pulsed reactor in Russia). Continuous reactors utilize fission reactions and are similar to energy-focused reactors but use more compact cores and highly enriched fuel (over 90% uranium-235 opposed to 2-5% in

energy-focused) to achieve high neutron fluxes[2]. All of the neutron sources that have been used for this data are continuous sources. Pulsed sources can operate at higher flux and are better suited to specific instruments that can account for the time-of-flight mode of the source. Neutrons interact with the dense nucleus of the atoms, causing scattering length densities to vary across the periodic table. Nuclei-based interactions allows researchers to modify a material's SLD by utilizing isotopes with different nuclear densities, the most common being through the swapping hydrogen with deuterium, an isotope of hydrogen with a neutron in the nucleus. This can 'blend' some structures into the background scattering of the system, 'focusing' on structures that are experimentally desired for analysis[4–7].

Contrast matching and contrast variation is only possible in neutron systems, making these systems uniquely refinable for experimentation. Contrast variation is the process of refining an experiment in order to increase the scattering between the material of interest while reducing the contrast of the other components in the system as a whole[2]. When referring to the guiding equation of scattering the $(\Delta\rho)^2$ component incorporates the difference between the scattering length densities of the various materials with the dispersion media. With reference to the equations (2.2) and (2.3) below, we can parse apart important considerations.

$$SLD = \frac{\sum_i b_{ci}}{V_m} \tag{2.2}$$

Where b_{ci} represents bound coherent scattering of all 'i'-type atoms in the molecular part of the estimated volume, summed over all 'i' molecules in the system.

$$V_m = \frac{M_w}{dN_a} \tag{2.3}$$

Where the M_w is the molecular weight of the molecule, d is the density of the material and N_a is Avogadro's number. The distinction between the bound coherent scattering and total scattering is important. Total scattering is composed of bound coherent scattering (in phase sample specific scattering) and incoherent scattering (isotropic scattering not related to a Q direction contributing to background signal). Structural features of interest will cause the bound coherent scattering to rise above the background to be analyzed[2]. The estimated coherent scattering is then balanced with the estimated volume of the molecules in the system. By considering the coherent scattering from each molecule in the system weighted by the volume that molecule takes up, we can anticipate the scattering contrast and the intensity we can expect from experiments. The *b*

value is measured and known for all atoms and isotopes, so calculating the *b* value for a complex molecule can be done using the molecular formula. All values used in this work are derived from known literature values from the National Institute for Standards and Technology (NIST) through the use of their calculator[8].

With the scattering length density (SLD) of each molecule in the system determined, we can make informed decisions on experimental design. In a basic two-part system (solvent and solute) the contrast of the system is between the SLD of the solvent and the SLD of the solute. As shown in **Figure 2.2**, in a system where there is finite determined contrast, the solute and the solvent have different SLD's. Thus, when the beam interacts with the sample, it will scatter off the particles of solute and the interfaces between the structures[2]. If the contrast is zero (or the SLD's of the solute and solvent are equal) there is no discernable density difference between the two and there is no scattering[2]. In more complex systems where there are multiple components, the SLD of each component is considered. With an SLD difference between each solute and the solvent, as well as the difference between each solute, the intensity of each scattering source becomes hard to deconvolute. This is where contrast variation can be a useful tool. If the solvent can be modified molecularly so that the scattering length density is equal to one of the solutes (or the solute is modified to match the solvent), we can effectively remove the scattering contribution of those components. With this match made, we can effectively reduce a complex multicomponent system into a basic two-part system[5].

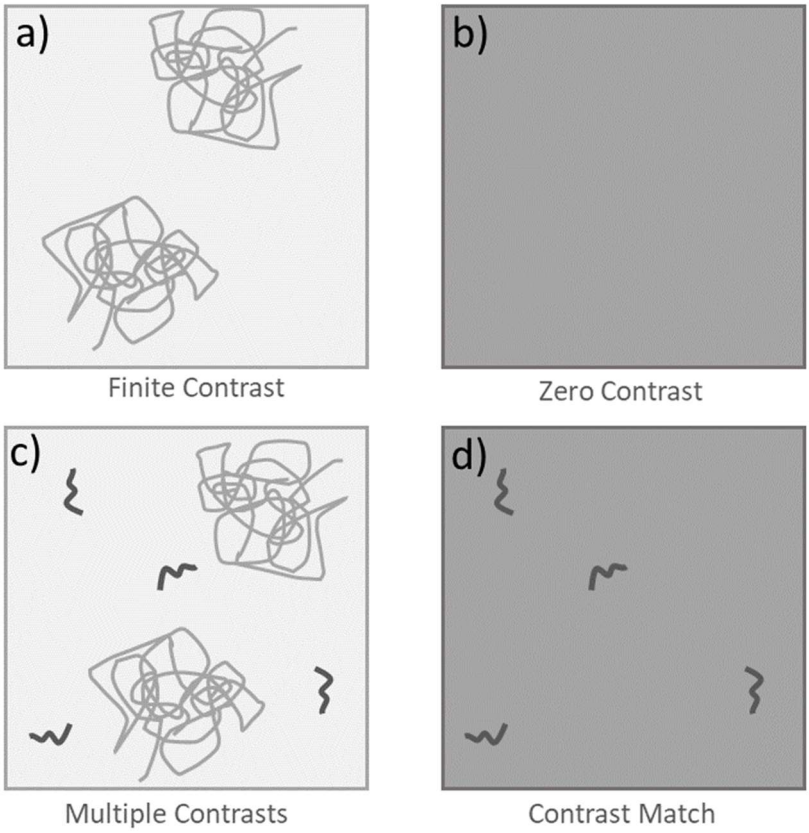

Figure 2.2: Schematic of contrast matching with respect to polymer systems with a) a polymer and a solvent with SLD differences b) a polymer and a solvent with matching SLDs c) two polymers and a solvent with different SLDs d) two polymers and solvent, where the solvent and one of the polymers have matching SLDs, leaving only one polymer 'visible'.

This technique is exceedingly useful in complex systems such as conjugated polymer blends, as it allows for the matrix commodity polymer to be deuterated and 'blended' into the background scattering, allowing the scattering from the conjugated polymer structures to dominate the system[4]. This method of contrast matching is possible for both solid and liquid systems, with solution state contrast matching allowing for hydrogenated and deuterated solvents to be mixed to achieve a desired SLD for the solvent[6,7].

2.1.3 Small Angle X-ray Scattering

The other technique that is used heavily throughout this work is small angle X-ray scattering (SAXS), which includes measurements in ultra-small angle X-ray scattering (USAXS) and wide-angle X-ray (WAXS) instruments. SAXS utilizes a collimated beam of X-ray photons which can be extracted from laboratory sources, such as copper or molybdenum-based X-ray tubes,

or from large scale sources, such as particle accelerators or synchrotrons[9]. The origin of the source can change the intensity and wavelength of the beam, allowing for different materials to be measured, as well as different Q ranges to be extracted. The use of an X-ray beam changes the way that contrast is calculated, as the photons interact with samples through the electron clouds. Due to the electron interaction, larger atoms with larger and denser electron clouds will scatter more intensely. This makes it more difficult to isolate the scattering from minute amounts of a molecules incorporated into mediums of compositionally similar molecules, but the technique can capture the structure of the system. For instance, in a polymer blend system with the addition of a small amount of a mostly hydrogen and carbon conjugated polymer into a much large amount of a matrix polymer that is also mostly hydrogen and carbon, the specific signal of the conjugated polymer is lost. The self-assembled structure of the large matrix polymer can dominate the signal over the sparse conjugated polymer and reduce the information that can be obtained directly about the structure of the additive. In these cases, we can still determine information about the structure of the blend as a whole and extract useful understandings through matrix conformation.

Due to the nature of X-rays, there are also some restrictions on the materials that can be used in the beam. For example, low energy X-ray photons are strongly absorbed by halogenated solvents, such as chloroform, chlorobenzene, and bromobenzene, so an extremely high energy source is needed to measure in these solvents. This is difficult for solution state measurements of the conjugated polymers used in this work, as halogenated solvents are the desired solvents, so SAXS measurements performed are on solid samples only. While high energy X-ray beams require complex sources such as a synchrotron or an accelerator, low energy sources are available for laboratory or university use, allowing increased access and ease of use.

2.2 SAS Data Analysis

2.2.1 Modeling Basics

Once scattering data has been collected, there are multiple avenues for analysis. Visual comparison between data in a set can be conducted, simply determining how features in either 2D or 1D data change or how intensity of features increase as the samples change. Data can be arithmetically processed to aid in comparisons by summing, scaling, or subtracting data sets from each other. This is most useful if the samples are collected with absolute intensity but can still be done to garner some information on the sample variation on samples with arbitrary intensity. Most often, to extract quantitative and comparable parameters from data, the samples are modeled.

Modeling uses equations associated with known features, structures, or properties to fit quantitative variables with algorithms intended to reduce the error between the data and the fits from the equation. The basis of scattering modeling comes from the fundamental equation for scattering discussed in previous sections and shown in equation 2.1. The two major opportunities for modeling in the fundamental scattering equation emerge in the structure, S(Q), and form factor, P(Q). For instance, the form factor, which describes the structure of isolated particles, can vary depending on size and shape, with a simple spherical system varying from solid spheres[10] to spheres with separated core and shell materials[11] to assemblies of multiple spheres in specific formations[12]. The structure factor can be modified to describe how the structures interact with each other. For example, if the scattered structures prevent overlap and do not interact, a hard sphere structure factor[13] may be adequate, but if the materials do not overlap but aggregate at close distances, a sticky hard sphere structure factor[14] may be more appropriate. Typically, modeling is approached by understanding the system and what structure is expected through kinetics, thermodynamics, and processing, before models are attempted on the data.

Models fit with this fundamental equation in mind are typically shape-dependent models that are looking to fit the data to a mathematical representation of how a specifically shaped population scatter. As a scattering system becomes more complex, the models required to fully describe it also become more complex. For instance, in a system with a single solute that forms a single monodisperse structure, a single form factor and structure factor may be adequate to fully understand the scattering. If there are multiple components in the system, or the solutes form a variety of structures, then multiple form factors to describe each shape's scattering impact may be necessary. When approaching shape dependent modeling, it is recommended to start from the most basic model before adding complexity. For instance, in a system that is known to have free chains, it's best to start by modeling chain-sized cylinders alone in solution before adding more complex structures. On the extreme end, shape dependent models for individual populations can be weighted and added together to form combined models that can accurately characterize, for example, a system that has free chains in solution and separate populations of assembled cylinders of various lengths. These complex models need to be approached carefully to ensure that the system is being accurately described. Common pitfalls with modeling include sample design that prevents accurate modeling of the data, multiple models that can fit the same data, and fits that do not converge because of local minima with fitted variables.

Understanding the sample and the system from a scattering perspective is the first step before modeling. In samples that have a low scattering length density difference, there is often not enough coherent scattering to separate the sample signal from the incoherent (SANS) or background (SAXS) signal. This can also result in high backgrounds which leads to a plateau at high-Q that prevents the analysis of weak coherent scattering signal at mid and high-Q. Another consideration that is important in designing samples to allow for cohesive modeling is the concentration of the system. In highly concentrated systems the particles may interact with each other, resulting in larger impact from the structure factor, possibly to a point where the shape is changed due to interactions. Dilute systems are typically low volume fraction solution samples, which allow for the scattering of a single particle to be considered in isolation. This removes the correlation between particles and allows for measurement and models to extract shape and form parameters.

Conventional modeling methods for SAS data is through least square optimization, which focuses on minimizing the square of the difference between the model and the data. There are many algorithms which utilize a least squares approach, including the Levenberg-Marquardt (LM) algorithm, which is known as a damped least-squares approach. The LM algorithm is better at finding a solution than previous iterations of least-square algorithm that would diverge completely but faces challenges with multiple available solutions. If the initial value provided is substantially different from the 'correct' value, the LM algorithm may find a local minimum of residuals and get 'stuck' in that well. This prevents the algorithm from correctly determining the global minimum and if not checked with outside sample information may lead to incorrect conclusions. This can also be fixed through a change in algorithm. Another algorithm utilized in the bumps fitting package, is the DREAM, or DiffeRential Evolution Adaptive Metropolis, algorithim[15]. This is a Markov Chain Monte Carlo method which generates new starting values for each iteration in the tens of thousands of iterations it runs. This prevents the algorithm from getting 'stuck' in a local minimum and increases the likelihood of achieving a reasonable set of variables. This generative method takes much longer to run but produces more consistent results.

The process of modeling for SAS data must be balanced with choices made during experimental design, theoretical understanding of the system, and specifics of the model itself. It is often an iterative process that requires much testing and adjustment. With proper constraints and

choices, the result is quantitative and comparable metrics of a system that can aid in the understanding of complex systems.

2.2.2 Broad Peak Model

The broad peak model is shape independent, meaning it is used to characterize the data trace features, and doesn't directly model the shape of the scattering populations. Many amorphous soft polymers including copolymers, polyelectrolytes, and multiphase blends have broad scattering peaks where this model is useful[16]. The model itself consists of a broad Lorentzian peak mixed with a power law decay fit (**Figure 2.3**), allowing for a peak that leads into an increasing slope that is common in aggregated soft samples.

$$I(Q) = \frac{A}{q^n} + \frac{C}{1 + (|Q - Q_0|\xi)^m} + B \tag{2.4}$$

Where A is the Porod law scale factor, n is the Porod exponent, C is the Lorentzian scale factor, m is the exponent of Q, ξ is the Lorentzian screening length, B is the flat background and Q_0 is peak position[16].

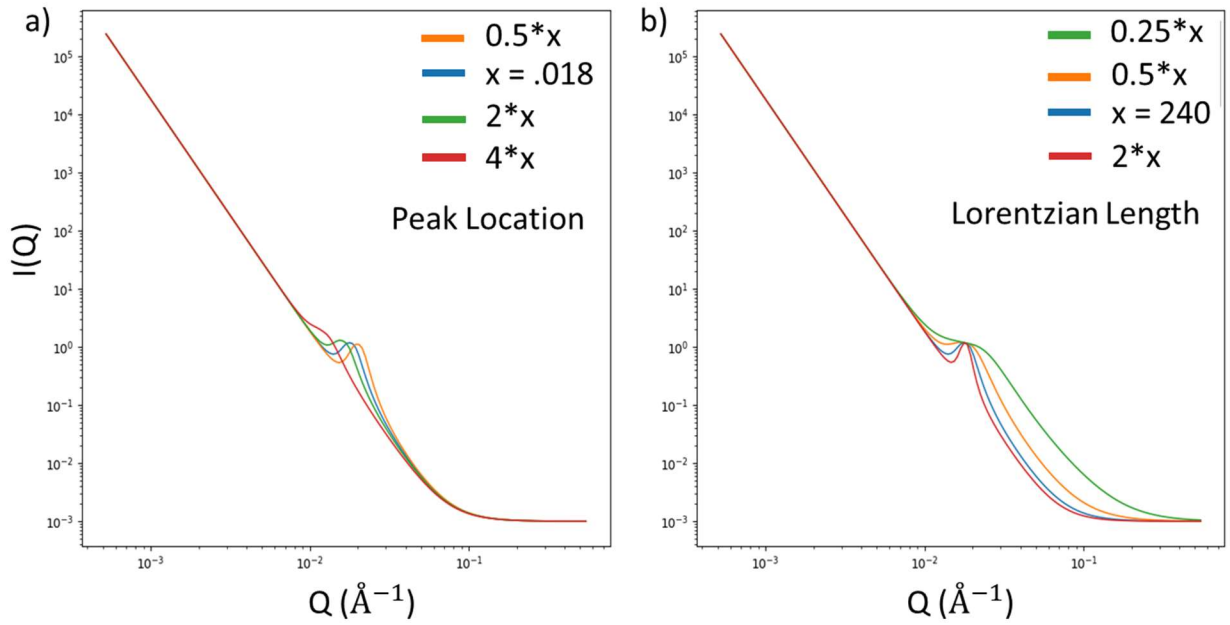

Figure 2.3: Examples of the broad peak model with a value typical of the data discussed in chapter 4 and 5 (scale = 1, peak location = 0.018, Lorentzian length = 240, Lorentzian exponent = 3.5, Lorentzian scale = 4, Porod exponent = 4, Porod scale = 1e-7). Variation in a) peak location and b) Lorentzian length is made to show the effect of the parameter on the model.

Peak position can be tracked to determine how the feature is changing as shown in **Figure 2.4a**. As a peak is shifted towards the low-Q region, the feature is increasing in size and when the peak is shifted towards high-Q the feature is decreasing in size. If the structure, shape, or phase is known through peak indexing or external information, then specific conversions are available convert the peak position into structure specific information. For example, if the phase is determined to be lamellar, then using equation 2.5, the spacing between the layers can be calculated from the peak position.[17]

$$Q_0 = \frac{2\pi}{d_0} \tag{2.5}$$

Other known phase formations have similar conversions, and another common phase seen in this work is hexagonally packed cylinders, with the distance between cylindrical neighbors calculated by equation 2.6[17].

$$d = \frac{4\pi}{\sqrt{3q_0}} \tag{2.6}$$

Lorentzian screening length (ξ) modifies the width of the peak and can be used as a proxy for peak width. Peak width for a feature correlates to the regularity of that feature and when a peak widens, the feature becomes more irregular as shown in **Figure 2.4b**. Irregularity can emerge in a multitude of ways: the spacing between structures or phases changes and encompasses a wider range of values, sections of a phase overlap and are disordered in their patterning, regions of a previously assembled structure disorders and form unstructured regions. In these cases, further analysis would be required in order to determine which forms of irregularity are present, but a general metric of system disorder can be seen in the Lorentzian length.

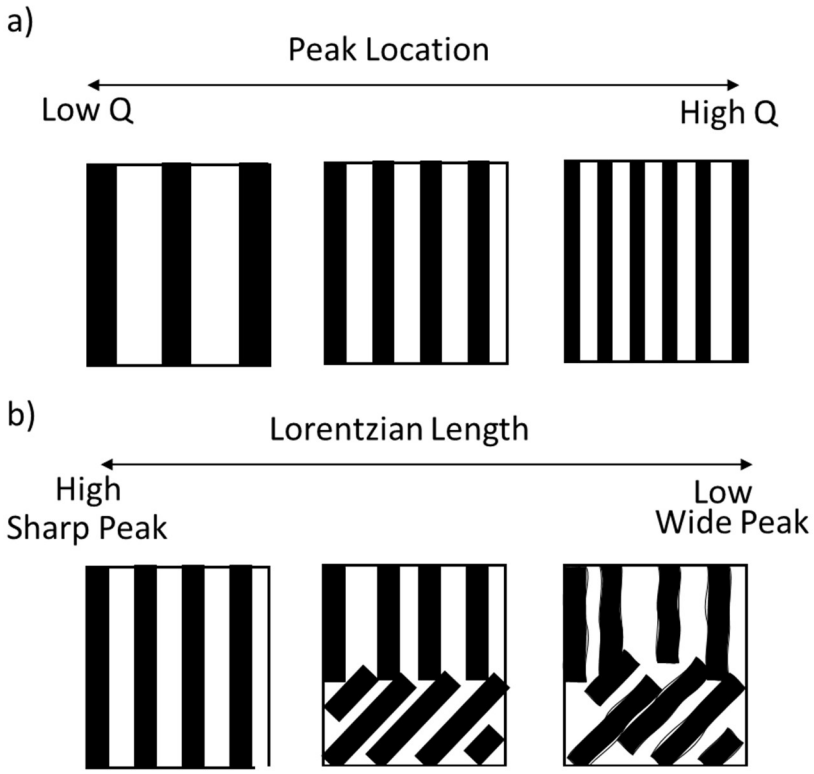

Figure 2.4: Schematics to describe the structural representation of variation in a) peak location and b) Lorentzian length in the broad peak model.

Another parameter of interest is the Porod exponent. The Porod portion of this model describes the linear section (on a log-log axis) that emerges towards the low-Q region of the peak. The exponent describes the interface between the structures and matrix displaying the feature. A Porod exponent of four describes a smooth interface between the materials, whereas lower values suggest the system has rougher interfaces and less of a clear differentiation between materials. In this work all of the materials are well described with smooth interfaces and so the Porod exponent has been set to 4.

2.2.3 Guinier-Porod Model

The Guinier-Porod model is another shape independent model utilized often for SAS data. This model can provide a general idea of the size and dimensionality (i.e., 1D, 2D or 3D) of a scattering population and can be fit directly to the data. The model is fit to data that has a 'hump' or feature in a power-law described region of data. The Porod portion of the model describes the power-law region, and the Guinier portion of the model describes the feature itself.

$$I(Q) = \frac{G}{Q^s}\exp\left[-\frac{Q^2R_g^2}{3-s}\right] when\ Q \le Q_1 \quad (2.7)$$

$$I(Q) = \frac{D}{Q^m} when\ Q \ge Q_1 \quad (2.8)$$

$$Q_1 = \frac{1}{R_g}\sqrt{\frac{(m-s)(3-s)}{2}} \quad (2.9)$$

$$D = \frac{G}{R_g^{m-s}}\exp\left[\frac{s-m}{2}\right]\left(\frac{(m-s)(3-s)}{2}\right)^{\frac{m-s}{2}} \quad (2.10)$$

Where G is a scale factor, R_g is the radius of gyration, m is the Porod Exponent, and s is the dimensionality variable in the range 0 to 2[18].

The dimensionality variable describes the general shape of the scattering population creating the feature. This variable is related to the dimensionality of the scattering objects, from s = 0 (3D symmetry, such as spheres or globules), s = 1 (2D symmetry, such as rods), and s = 2 (1D symmetry, such as plates)[18]. Observing the change in the dimensionality constant allows for a basic understanding of the shapes and complexity involved over the course of the sample set. Radius of gyration is a measure of the root mean square distance of a particle of the scattering population shape from its center of mass[2]. For large objects, the radius of gyration is larger. From the radius of gyration, information about radius can be extracted from shape dependent equations, if the exact shape of the scattering population is known. If unknown, the radius of gyration serves as a metric of size and can be tracked over the sample set.

2.2.4 Flexible Cylinder Model

This model is a shape dependent model that describes a flexible cylinder as described in equation 2.11[19,20].

$$S_{SB}(q,L,b) = S_{exv}(q,L,b) + C(\frac{L}{b})\left[\frac{4}{15} + \frac{7}{15u} - \left(\frac{11}{15} + \frac{7}{15u}\right)e^{-u}\right]\frac{b}{L} \quad (2.11)$$

where L is length of the cylinder, b is Kuhn length, and

$$u = \langle {R_g}^2\rangle_0 q^2 \quad (2.12)$$

$$S_{exv}(q,L,b) = w(qR_g)S_{Debye}(q,L,b) + \left[1 - w(qR_g)\right]\left[C_1(qR_g)^{-1/v} + C_2(qR_g)^{-2/v} + C_3(qR_g)^{-3/v}\right] \quad (2.13)$$

where $\langle {R_g}^2 \rangle_0$ is the ensemble average of the square of the radius of gyration and

$$w(qR_g) = \left[1 + \tanh\left((qR_g - C_4)/C_5\right)\right]/2 \quad (2.14)$$

$$S_{Debye}(q,L,b) = \frac{2[e^{-u} + u - 1]}{u^2} \quad (2.15)$$

Further individual parameter values and system dependent definitions are provided in the original derivation[20].

2.2.5 Spherical Micelles with Gaussian Chain Corona

The full equation describing scattering for a sphere with a self-associating core and a corona of gaussian chains surrounding the core is described in equation 2.16[21].

$$F_{mic}(q) = N^2{\beta_s}^2F_s(q) + N{\beta_c}^2F_c(q) + 2N^2\beta_s\beta_cS_{sc}(q) + N(N-1){\beta_c}^2S_{cc}(q) \quad (2.16)$$

Where N^2 is the number of chines in the micelle, $\beta_s$is the scattering length density of the sphere core, β_c is the scattering length density of the chains in the corona and all other factors are as follows.

The form factor for a sphere is described by $F_s(q)$ as a function of q and sphere radius (R)

$$F_s(q) = \Phi^2(qR) \quad (2.17)$$

$$\Phi^2(qR) = \frac{3[\sin(qR) - qR\cos(qR)]}{(qR)^3} \quad (2.18)$$

The form factor for the flexible chains in the corona are described as follows:

$$F_c(q) = \frac{2[e^{-x} - 1 + x]}{x^2} \quad (2.19)$$

where $x = {R_g}^2q^2$

The structure factor for the interactions between the sphere and each of the chains in the corona is shown in equation 2.15.

$$S_{sc}(q) = \Phi(qR)\psi(qR_g)\frac{\sin(q[R + dR_g])}{q[R + dR_g]} \quad (2.20)$$

where R is the radius of the core, R_g is the radius of gyration of the chains, and $\psi(qR_g)$ is shown in equation 2.21.

$$\psi(qR_g) = \frac{\left[1 - e^{-(qR_g)}\right]}{qR_g} \tag{2.22}$$

The structure factor for the interactions between each chain surrounding the core is given in equation 2.23.

$$S_{cc}(q) = \psi^2(qR_g)\left[\frac{\sin(q[R + dR_g])}{q[R + dR_g]}\right]^2 \tag{2.23}$$

Spectra with typical values of the parameters of interest, as well as a variation in an isolated parameter are shown in **Figure 2.5**.

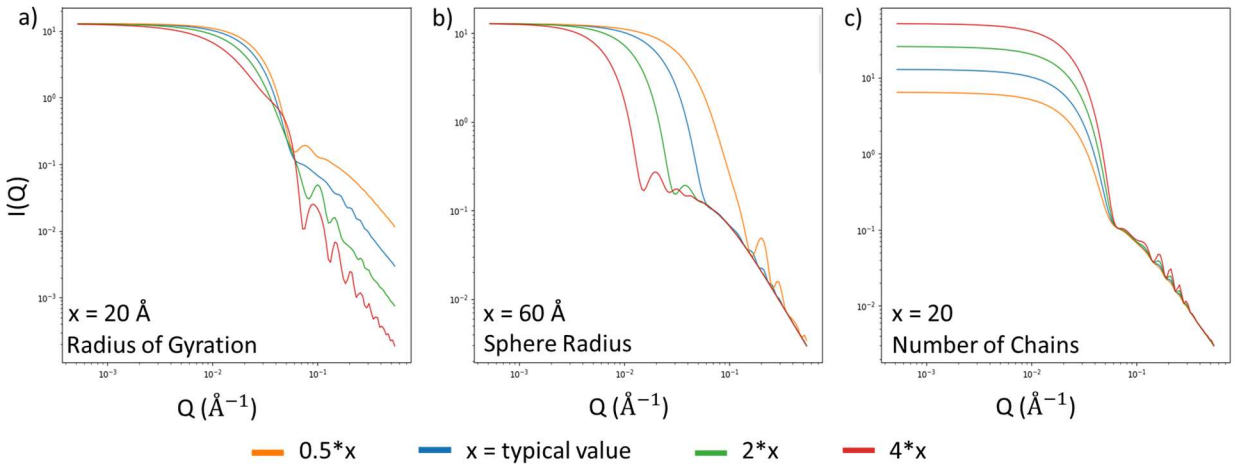

Figure 2.5: Examples of the spherical micelle model with a value typical of the data discussed in chapter 6 (scale = 1e-6, background = 0, volume of core = 13700 Å, volume of corona = 12200 Å, SLD solvent = 6.35e-6 Å^{-2}, SLD core = 1.85 Å^{-2}, SLD corona = 0.817 Å^{-2}, radius of core = 60 Å, radius of gyration = 20 Å, penetration distance = 1, number of chains = 20). Variation in a) radius of gyration. B) sphere radius, and c) number of chains are plotted to show the effect of each parameter on the model.

This equation assumes that the core is dry with the only volume and SLD contributions emerging from the polymer in the core, which in our case is the hydrophobic fluorinated polymer. We do not anticipate this to be the case and believe that the core is solvated and has a volume fraction (ϕ_{sol}) of solvent that is expanding the volume of the core. Similar systems have been addressed with similar solvated spheres, and fitting was approached by allowing both the radius of the core R_c and the number of chains in the micelle N_{agg} to be fit. The solvent volume fraction is then calculated using the volume of the polymer block in the core (V_{core}) and equation 2.24[22].

$$(1-\phi_{sol})\frac{4}{3}\pi {R_c}^3 = N_{agg}V_{core} \tag{2.24}$$

The volume of the polymer block in the core (V_{core}) and the volume of the poylmer block in the corona (V_{corona}) are fixed parameters calculated from polymer architecture and composition.

$$V_{core} = DOP_F * Conversion * \frac{\rho_F * Mw_F}{NA} \tag{2.25}$$

$$V_{corona} = DOP_{EG} * Conversion * \frac{\rho_{EG} * Mw_{EG}}{NA} \tag{2.26}$$

Where NA is Avogadro's number, ρ_i is the density of the monomer, Mw_i is the molecular weight of the monomer, conversion is 1e24 to convert from cm^3 to scattering relevant Å^3, and DOP_i is the degree of polymerization for the block of interest. These were set for each polymer and unchanged throughout fitting and calculations.

2.2.6 Phase Indexing

An additional technique that is used for SAS data is peak indexing for phase determination. In this case, phase is used to refer to the crystalline structure for a material (lamellar, hexagonally packed cylinders, face centered cubic, etc.), not the state of matter (gas, liquid, solid). Indexing derives from Bragg's law, which was pioneered by father-son scientist duo William Henry Bragg and Lawrence Bragg in 1913[23]. In experiments with X-ray scattering of crystalline solids they found that there was a pattern of reflected X-rays not typically seen in other more amorphous materials. With further work it was determined that the spacing of the planes of the crystal produced constructive and destructively interfering emissions which selectively produced specific patterns. This allowed for X-ray and neutron diffraction to be used to determine crystal structures of previously unknown materials. As further research was done on a variety of materials, more patterns were identified for other phases and a method for identifying phases based on a ratio of peaks (SAS) or 2D scattering pattern (**Figure 2.6b**).

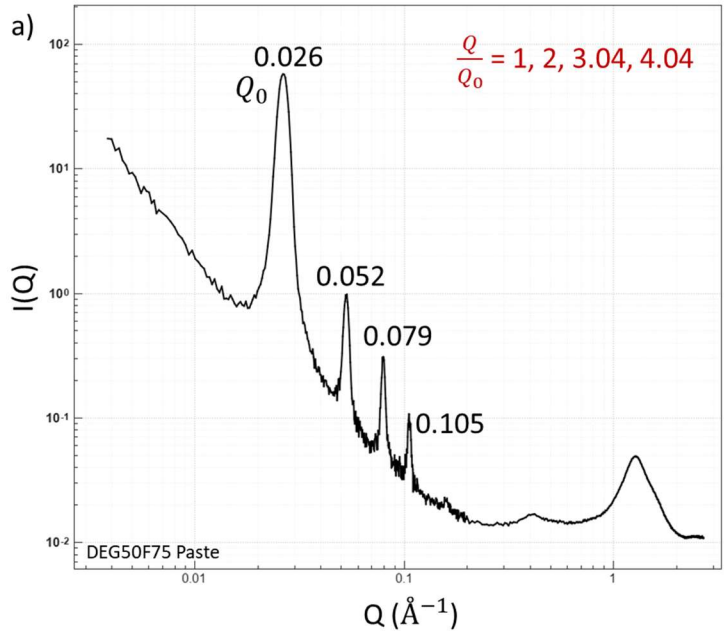

b) Known Peak Ratios

Lamellae	1,2,3,4,5
Hex Packed Cylinders	1,1.73,2.0,2.65,3.0
Face Centered Cubic (Spheres)	1,1.15,1.63,1.91,2,2.3
Body Centered Cubic (Spheres)	1,1.41,1.73,2,2.23
Gyroid	1,1.15,1.53,1.63,1.83
Close Packed Spheres	1, 1.06, 1.13, 1.46, 1.73

Figure 2.6: a) Example of a lamellar phase for a DEG50F75 polymer explored in depth in chapter 6 and 7, with peaks labeled and peak ratio calculated. b) table of a sample of known peak ratios, with the first few ratios listed

While this was identified for crystals and is still a common technique used for traditionally crystal structures, the peak ratios are maintained for semi-crystalline, or phase separated materials in organized structures. SAS allows for the differentiation between materials in a structure, and if that phase separated structure is crystalline in nature (with repeated units of material A in material B with enough clarity and regularity) then a series of peaks emerge. Indexing, or finding the Q value at the peak, can allow for phase identification, aid in the understanding of a material's morphology, and track changes within a sample set (**Figure 2.6a**). Indexing may be difficult if the system has mixed phases, as the peaks for each phase can overlap or smear out, or if the system has sufficient disorder in the phase. Disorder leads to wider, less coherent peaks or can cause multiple peaks to smear together, which can make indexing more difficult and the final result less confident. These results can still help flesh out a system, even with caveats provided to the phase integrity.

2.3 References

1. Linder, P. & Zemb, Th. *Neutrons, X-Rays and Light: Scattering Methods Applied to Soft Condensed Matter*. (Elsevier Science, 2002).
2. Hammouda, B. PROBING NANOSCALE STRUCTURES-THE SANS TOOLBOX.

3. Pedersen, J. S. Analysis of small-angle scattering data from colloids and polymer solutions: modeling and least-squares fitting. *Adv Colloid Interface Sci* **70**, 171–210 (1997).
4. Wolf, C. M. *et al.* Blend Morphology in Polythiophene–Polystyrene Composites from Neutron and X-ray Scattering. *Macromolecules* (2021) doi: 10.1021/acs.macromol.0c02512.
5. Endo, H. Study on multicomponent systems by means of contrast variation SANS. 682–684 (2006) doi: 10.1016/j.physb.2006.05.290.
6. Lee, Y. T., Li, D. S. & Pozzo, L. D. Kinetic Analysis of Ultrasound-Induced Oil Exchange in Oil-in-Water Emulsions through Contrast Variation Time-Resolved Small-Angle Neutron Scattering. *Langmuir* **35**, 15204–15213 (2019).
7. Lee, Y. T. & Pozzo, L. D. Contrast-Variation Time-Resolved Small-Angle Neutron Scattering Analysis of Oil-Exchange Kinetics Between Oil-in-Water Emulsions Stabilized by Anionic Surfactants. *Langmuir* **35**, 15192–15203 (2019).
8. Neutron Activation and Scattering Calculator. https://www.ncnr.nist.gov/resources/activation/.
9. Gommes, C. J., Jaksch, S. & Frielinghaus, H. Small angle scattering for beginners. *J Appl Crystallogr* **54**, 1832–1843 (2021).
10. sphere — SasView 5.0.6 documentation. https://www.sasview.org/docs/user/models/sphere.html.
11. core_shell_sphere — SasView 5.0.6 documentation. https://www.sasview.org/docs/user/models/core_shell_sphere.html.
12. raspberry — SasView 5.0.6 documentation. https://www.sasview.org/docs/user/models/raspberry.html.
13. hardsphere — SasView 5.0.6 documentation. https://www.sasview.org/docs/user/models/hardsphere.html.
14. stickyhardsphere — SasView 5.0.6 documentation. https://www.sasview.org/docs/user/models/stickyhardsphere.html.
15. Vrugt, J. A. *et al.* Accelerating Markov chain Monte Carlo simulation by differential evolution with self-adaptive randomized subspace sampling. *International Journal of Nonlinear Sciences and Numerical Simulation* **10**, 273–290 (2009).
16. broad_peak — SasView 5.0.5 documentation. https://www.sasview.org/docs/user/models/broad_peak.html.
17. Liu, Y., Li, M., Bansil, R. & Steinhart, M. Kinetics of phase transition from lamellar to hexagonally packed cylinders for a triblock copolymer in a selective solvent.
18. Hammouda, B. & IUCr. A new Guinier–Porod model. *urn: issn:0021-8898* **43**, 716–719 (2010).
19. Pedersen, J. S. & Schurtenberger, P. Scattering functions of semiflexible polymers with and without excluded volume effects. *Macromolecules* **29**, 7602–7612 (1996).
20. flexible_cylinder — SasView 5.0.6 documentation. https://www.sasview.org/docs/user/models/flexible_cylinder.html.
21. Skov Pedersen, J. Form factors of block copolymer micelles with spherical, ellipsoidal and cylindrical cores. *J. Appl. Cryst* **33**, 637–640 (2000).
22. Choi, S.-H., Lee, W. B., Lodge, T. P. & Bates, F. S. Structure of Poly(styrene-b-ethylene-alt-propylene) Diblock Copolymer Micelles in Binary Solvent Mixtures. *J. Polym. Sci., Part B: Polym. Phys* **54**, 22–31 (2015).
23. Lawrence Bragg – Biographical - NobelPrize.org. https://www.nobelprize.org/prizes/physics/1915/wl-bragg/biographical/.

Chapter 3: Solid Blends of Conjugated Polymer and Polystyrene

The work presented in this section is also reported in the following publication:

Wolf, C. M., Guio, L., Scheiwiller, S., O'Hara, R. P., Luscombe, C., Pozzo, L. D. "Blend Morphology in Polythiophene–Polystyrene Composites from Neutron and X-ray Scattering". Manuscript published 2021 in Macromolecules.

The author would like to acknowledge the significant contributions of coauthors for the following work and makes no claim of sole contribution to the data. Sections that the author worked on with significant contributions are included here, and all sections can be found in the above work.

3.1 Introduction

Electronics made from conjugated polymers (CP) blends rely on the performance of the conjugated polymers to create high efficiency and reliable blends, so understanding how CPs work is vital. In pure P3HT films, charge mobility, a metric of electronic performance, is thought to be affected by interactions between ordered and disordered regions[1,2]. Movement within the bulk polymer requires a charge to pass easily through ordered regions, and then cross less favorable disordered regions. Within the ordered regions, charge can move through intra-chain charge transport along the conjugated backbone, or through the weaker inter-chain charge transport through the π-orbital overlap with neighboring chains. In disordered regions, charge can move intra-chain through tie-chains or inter-chain through chain cross over points. By refining the creation of tie-chains, the entire system mobility can be improved, and a host of research has been done on pure CP systems working to quantify and refine tie chain assembly[3–6]. While the pure CP system has understood electronic properties, the physical drawbacks of pure CP's encourage the use of blended systems. In blended systems, the complex polymer-polymer and polymer-solvent interactions can modify the expected morphology and change the electronic performance of the blend. Research on blends has found many refinements for CP aggregation, such as including block co-polymers which allow for small scale aggregation while blends encourage large scale aggegations[7], using semi-crystalline matrix polymers to encourage CP crystallization[8], and utilizing solvents of various qualities to modify thermodynamic pressures[9,10]. With this in mind, we look to fully characterize the polymer assembly process and the resulting blend morphologies

through the use of contrast-variation small angle neutron scattering (CV-SANS), with relation to the measured electronic properties of the final blends.

We look to explore a set of semi-crystalline polythiophene conjugated polymers that differ in side-chain length and side chain density along the backbone, as well as a regiorandom (RRa-P3HT) conjugated polymer in order to investigate the effect of CP crystallinity on aggregation. We also looked to investigate the morphology of castings from various solvents of different qualities. We used toluene, a poor solvent, chloroform, a moderate solvent, and bromobenzene, a good solvent, to process compositionally identical samples, then evaporated the samples until completely dry[11]. All of the dried blends were measured with CV-SANS to determine the shape and size of CP aggregations, while wide angle x-ray scattering (WAXS) was used to measure extent and direction of crystallinity. Conductivity measurements were made to relate the observed morphologies to electrical properties. This work was led by a motivation to probe the morphology of solid conjugated polymer blend films, further understand the mechanisms of the formation of nanofibers, and connect the structure to material properties.

3.2 Materials and Methods

3.2.1 Materials

Poly(3-dodecylthiophene) (P3DDT) (MW = 39 kg mol^{-1}, Đ = 1.8, Product 4005-E), regio-random poly(3-hexylthiophene) (RRa-P3HT) (MW = 63 kg mol^{-1}, Đ = 2.4, Product 4007), and regio- regular poly(3-hexylthiophene) (RRe-P3HT-2) (MW = 55 kg mol^{-1}, Đ = 2.4, Product 4002-EE) were purchased from Rieke Metals (Lincoln, NE USA). Poly(3,3‴-didodecyl [2,2′:5′,2″:5″,2‴- quaterthio-phene]-5,5‴-diyl) (PQT-12) (MW = 40 kg mol^{-1}, Đ = 1.7, Product SOL4150) was purchased from Solaris Chem (Vaudreuil-Dorion, Quebec Canada). Hydrogenated polystyrene (PS-H8) (MW = 278 kg mol^{-1}, Đ = 1.07, Product P8610-S) and fully deuterated polystyrene (PS-d8)(MW = 305 kg mol^{-1}, Đ = 1.08, Product P19833-dPS) were purchased from Polymer Source (Dorval, Montreal, Quebec Canada). All polymers were used as received. Finally, an additional regio-regular poly(3-hexylthiophene) (RRe-P3HT, MW = 22.7 kg mol^{-1}, Đ = 1.2) was synthesized according to the literature procedure[12] with minor modifications and characterized by size exclusion chromatography and nuclear magnetic resonance. All solvents in this work were used as received. Bromobenzene was purchased from Aldrich Chemistry (St. Louis, MO USA), and chloroform, toluene, and chlorobenzene were purchased from Fisher Chemical (Waltham, MA USA).

3.2.2 Film Preparation

A schematic diagram of the preparation process for solid blend films is shown in **Figure 3.1**. A conjugated polymer (RRe-P3HT, RRa-P3HT, P3DDT, or PQT-12) was co-dissolved in solution with PS-d8 at a specified target ratio and a total polymer concentration of 50 mg/mL. A fully deuterated matrix polymer (PS-d8) was chosen to create sufficient contrast for SANS measurements. The relative concentration of the CP in the solid blends ranged from 0 to 50 wt %. The solvents used for co-dissolving the polymer blends were bromobenzene (good solvent for P3HT), chloroform (moderate solvent for P3HT), or toluene (poor solvent for P3HT). All solutions were heated to 50°C until fully dissolved then drop-cast from solution onto a watch glass and placed on a hot plate set at 50°C to allow for solvent evaporation. Samples were left to dry on the watch glass then placed in a vacuum oven at 50°C for 24 h to remove any residual solvent. The solid samples were then pressed at 150°C using steel precision spacers with inner diameters of either 0.625 or 1 in. and a thickness of 0.01 in. (254 μm) to create a smooth and uniform film. This temperature was above the glass transition of both PS-d8 and PS-H8, which was at 106 and 107°C, respectively, and well below the melting temperature of RRe-P3HT, which was determined to be 240°C. The samples were folded and repeatedly pressed 3 times to ensure a consistent, homogeneous sample that completely filled the mold. Each press cycle was sustained for 5 or 2 min for the initial and final presses, respectively.

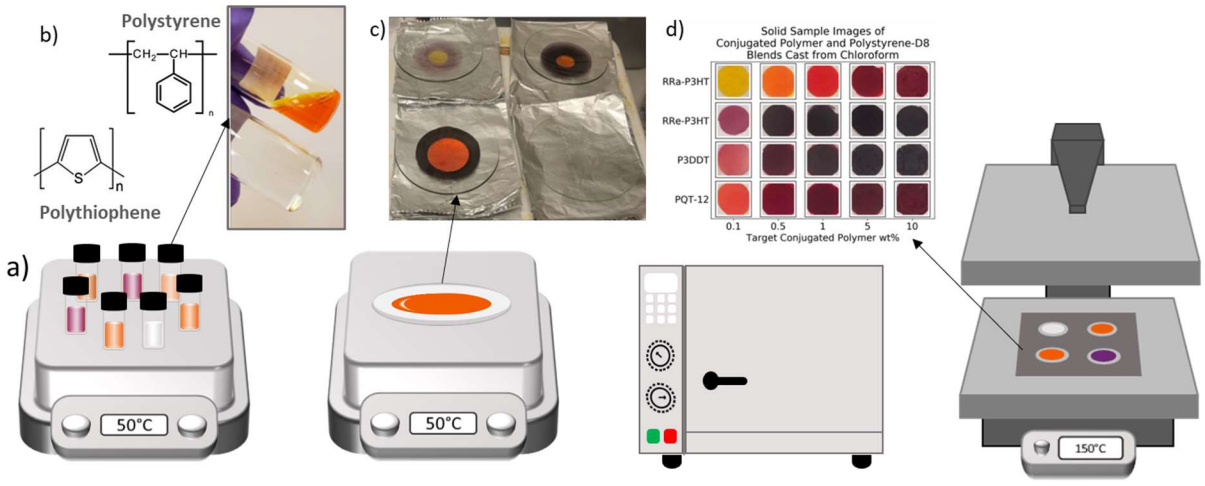

Figure 3.1: a) Schematic of blend processing method, with b) specific polymers used and examples of co-dissolved polymers, c) polymer solutions in the process of drying, and d) an array of all polymer blends cast from chloroform, emphasizing the color range observed.

3.2.3 SANS

SANS and ultra-high resolution small-angle neutron scattering (USANS) measurements were used to investigate the conformation of the CP phase within the PS-d8 matrix of our solid polymer blend samples. We utilized contrast variation to increase the SLD and therefore increase the scattering between the matrix polymer and fully hydrogenated CP. All SANS and USANS experiments were performed at the National Institute of Standards and Technology (NIST) Center for Neutron Research (NCNR) in Gaithersburg, MD. SANS data was collected using the NG-3 45 m very small-angle neutron scattering (VSANS) and the NG-7 30 m SANS instruments, both configured for a Q-range of 0.002− 0.1 Å−1. USANS data were collected using the BT-5 USANS instrument configured for a Q-range of 0.00004−0.003 Å−1. NCNR SANS and USANS reduction macros[13] for Igor Pro were used to reduce the data, integrating 2D scattering images to 1D profiles, correcting for the instrument background, and to determine absolute scaling of scattering intensity. Further SANS/USANS analysis and modeling were performed using the SasView/sasmodels[14–16] packages for Python. Solid samples were measured using titanium and cadmium sample frames that enabled the beam to pass through the sample only. Liquid samples were measured in standard titanium demountable cells with quartz windows and a 2 mm path length. Smearing of the USANS data for the solid samples was accounted for using the SasView/sasmodels[15,16] package, and so all USANS data for these samples are presented in the smeared form. However, the USANS data for the solution samples were de-smeared using USANS reduction macros[13] for Igor Pro.

3.2.4 SANS Data Analysis

First, Porod analysis[17] was applied to the scattering profiles of all solid samples. At the high-Q limit, the scattering intensity can be defined as[15]

$$I(Q) = \frac{C}{Q^m} + background \tag{3.1}$$

where I(Q) is the scattering intensity in units cm^{-1}, C is the Porod constant, Q is the scattering vector in units $Å^{-1}$, m is the Porod exponent, and the background encompasses the incoherent scattering. When performing the analysis, the PS-d8 components were found to make significant contributions to the scattering intensity due to density fluctuations in the material. Considerable research has been conducted on the assembly and ordering of amorphous, glassy polymers over wide length scales (10−10,000 Å), which can be dependent on their thermal and mechanical history[18–23]. We anticipate that the density fluctuations we observe were due to the processing

method used in the film creation. To account for this, the Porod equation is separated into CP and PS-d8 components as seen in equation (3.2).

$$I(Q) = \phi_{CP}\frac{C_{CP}}{Q^{m_{CP}}} + (1-\phi_{CP})\frac{C_{PS}}{Q^{m_{PS}}} + background \tag{3.2}$$

where CP and PS refer to the CP and PS-d8 contributions, respectively, and ϕ_{CP} is the volume fraction of the CP. The CP Porod constant, C_{CP}, can then be extracted to quantify the interfacial concentration in our sample[24]

$$C_{CP} = 2\pi\Delta\rho^2\frac{S}{V} \tag{3.3}$$

where $\Delta\rho^2$ is the scattering contrast or the difference in scattering length density for the PS-d8 and CP components squared and $\frac{S}{V}$ is the surface area-to-volume ratio or interfacial concentration.

The total SANS scattering intensity can also be broken down into the following guiding equation 2.1, which is reproduced below:[24]

$$I(Q) = \phi\Delta\rho^2 VP(Q)S(Q) \tag{2.1) (3.4}$$

where ϕ is the scale or volume fraction of scattering domains in the sample, V is the volume of the scattering domain, P(Q) is the form factor, which includes information about the shape of the scattering domain, and S(Q) is the structure factor, which includes information about correlations between domains distributed throughout the sample.

In complex multi-component systems, the scattering intensity can also be defined with respect to the self- and cross-interaction terms between components. In solid polymer blends, there are three sources for scattering contribution expected: (1) PS-d8 density fluctuations, (2) isolated or "free" CP chains, and (3) phase-aggregated or self-assembled CP structures (e.g., globular domains and nanofibers). Each of these sources contribute to the scattering intensity, as they generate contrast with respect to the average PS-d8 SLD. We can simplify this equation by reducing cross-terms as the structures are independent of each other, i.e., the location of assembled CP is not related to the location of the free CP chains. Therefore, by applying a mass balance we generalize the scattering intensity for each sample as

$$I(Q) = \phi_{CP}\sum_{k=1}^{K}\left[x_k I_{CP,k}(Q)\right] + (1-\phi_{CP})I_{PS}(Q) + background \tag{3.5}$$

where x_k is the fraction of CPs present in form 'k' of 'K' total conformations and $\Sigma k=1$, $I_{CP,k}(Q)$ is the scattering intensity due to conformation k (e.g., phase-aggregated CP or free polymer

chains), and $I_{PS}(Q)$ is the scattering intensity from the density fluctuations of the PS-d8 phase. The PS-d8 contribution was fit using a Guinier-Porod model on the PS controls, while the conjugated polymer contributions were represented using spherical or ellipsoidal form factors for the globular domains and a long cylinder form factor for the nanofibers. Model names of "sphere", "ellipsoid", "sphere + cylinder", and "ellipsoid + cylinder" are used to indicate which form factors are included in the CP contribution of equation (3.5) while always maintaining a CP mass balance. While not being explicitly stated in the naming convention, these combined models always include the PS-d8 contribution. However, we note that there is no molecular justification for the specific form factors that were chosen (i.e., sphere vs ellipsoid) to capture the globular domains of the conjugated component. We used the simplest models that would accurately capture the shape and length scales of these globular domains. Therefore, in generalized terms, we will also refer to these fits as "globular domains" or "globular domains + nanofibers". To compare a common size parameter between the sphere and ellipsoid globular domains that are formed in the samples, we use the radius of gyration (R_g).

3.2.5 WAXS

SAXS and WAXS data for the samples containing PS-d8 were collected at the 9ID beamline at the Advanced Photon Source at Argonne National Laboratory[25,26]. The instrument used an X-ray source of 21 keV and a beam size of 0.8 × 0.8 mm with a flux density of approximately 5 × 1012 photons/s/mm2. SAXS and WAXS data were collected with exposure times of 10 s each. Samples were mounted using custom- designed 3D-printed 48-sample frames[27] that enabled execution of remote experiments during COVID-19-constrained access. SAXS and WAXS data were reduced, de-smeared, and corrected to absolute intensity using the Nika package[28] for Igor Pro. This package was also used to combine the data from the SAXS and WAXS detectors to produce datasets that will be referred to as "WAXS data" for the remainder of the work. WAXS data for additional sample batches containing either RRe-P3HT-2 or RRa-P3HT in PS-H8 were measured using an Anton-Paar (Graz, Austria) SAXSess X-ray scattering instrument. The instrument was operated in the line collimation mode with a Cu Kα source (wavelength of 1.54 Å). Solid polymer blends were placed in a custom 3D-printed frame to hold the sample in place and ensure that the X-ray beam passed through the middle of the sample. The sample chamber was held under vacuum at ambient temperature (approx. 20 °C) during all measurements. Data were collected using Fujifilm (Greenwood, SC USA) image plates and read using a PerkinElmer

Cyclone (Covina, CA USA) image plate reader. Anton-Paar SAXSQuant software was used to reduce data from 2D scattering images to 1D plots of scattering intensity (I) versus scattering vector (Q), remove contributions from the background, and de-smear the data. Analysis of WAXS data was performed using the SasView/ sasmodels[14–16] packages for Python. The PS-d8 peaks were first fit using three Gaussian distributions for the polymerization peak, the amorphous peak, and a trailing background peak[17]. For blend samples, peaks relating to the [100] and [010] reflections of the polythiophene crystal were fit in the 0.25−0.35 and 1.6−1.7 $Å^{-1}$ ranges, respectively.

3.2.6 Conductivity Measurements

Conductivity measurements were performed by co-author Lorenzo Guio and further information on conductivity results can be found in the published work. Measurements were taken on an Ametek (Berwyn, PA, USA) Parstat 4000a potentiostat using a RHD Instruments (Darmstadt, Germany) TSC SW closed measuring cell. The samples were first prepared by blade coating square electrodes on each side of the films with silver paste. The square electrodes had a side length of roughly 2 mm. The DC current was measured across the thickness of the samples (254 μm) as a potential was applied ranging from 1 to 10 V. The conductivity was then derived using geometric calculations. For high-resistance samples, the entire measuring cell was enclosed in an aluminum- mesh enclosure to shield from electromagnetic interference.

3.2.7 Python

Analysis and modeling of UV−Vis, WAXS, SANS, and conductivity data were performed using Python 3, which enabled us to maintain reproducible work as we progressed through our analyses of the collected data. Moreover, the SasView/sasmodels and bumps packages for Python 3 allowed us to perform rapid, parallel, and partially automated fitting of the scattering data. To promote open science, all raw data, results, figures, notebooks, and scripts associated with this work are available in a GitHub repository, which can be accessed at https://github.com/pozzo-research-group/c-wolf-blends-morphology[29]. We hope that by providing these files, we can increase transparency of our analysis, encourage reproducibility, and make data accessible to the community for new or improved analysis methods in the future.

3.3 Results and Discussion

We began analysis using Porod modeling at the high-Q limit to investigate the interfacial area between the CP and the PS-d8 phases. The Porod exponent for the PS-d8 was determined to be 3.5 by fitting the control samples and suggests rough interfaces, which is expected due to the

density fluctuations typically observed in glassy PS samples. When the conjugated polymer is added, the fit Porod exponent approaches 4, indicating the formation of smooth interfaces. We then refit the models using a fixed value of 4 for the Porod exponent and extract the interfacial area per volume from these fits. First, we look at the samples consisting of polystyrene and various conjugated polymers cast from chloroform in **Figure 3.2**. We see that the interfacial concentration is inversely related to conjugated polymer concentration, suggesting growing phase-separated regimes for all samples. The RRa-P3HT samples reach lower overall values, suggesting larger globular structures than the P3DDT or the PQT-12 samples. The RRe-P3HT samples show a peak indicating a more complex growth method.

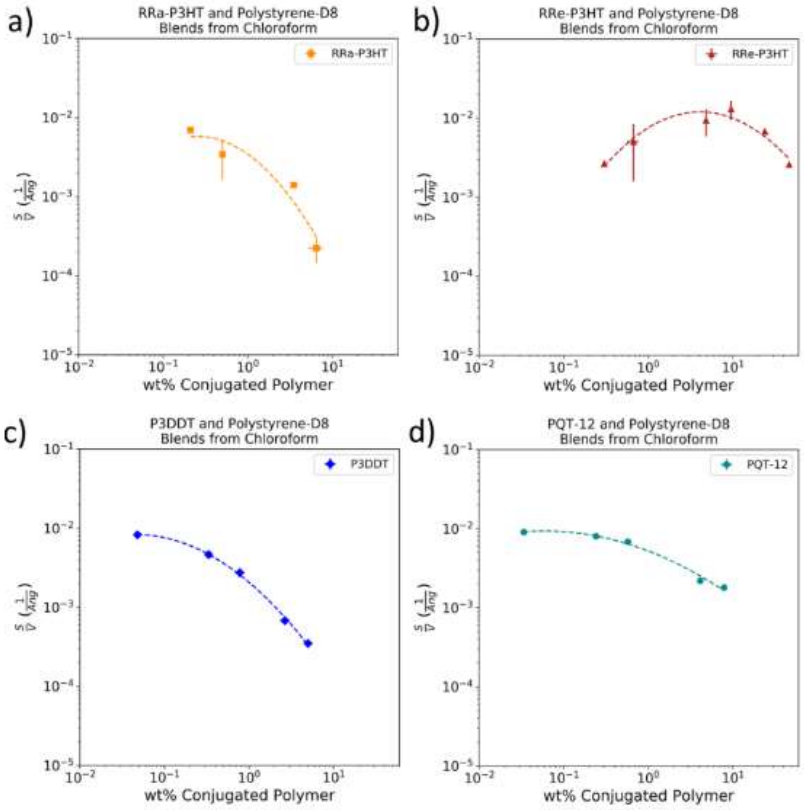

Figure 3.2: Interfacial concentration, S/V, for CP and PS-d8 blends cast from solutions in chloroform. The CP used in each blend is either a) RRa-P3HT, b) RRe-P3HT, c) P3DDT, or d) PQT-12. When present, vertical, and horizontal error bars correspond to the standard deviation of S/V and CP concentration, respectively, as determined by sample replicates ($n \leq 3$). Dashed lines show polynomial fit to guide the eye only.

This investigation was continued with RRe-P3HT and P3DDT cast from two solvents with different solvent qualities. We see that the P3DDT samples cast from bromobenzene and toluene

show similar activity as the sample cast from chloroform above, but RRe-P3HT performs differently **(Figure 3.3)**. Previously, the RRe-P3HT sample showed a concentration dependence on interfacial area, but the values for interfacial area for bromobenzene and toluene are relatively constant. This indicates that the growth pattern observed for RRe-P3HT may be dependent on solvent properties.

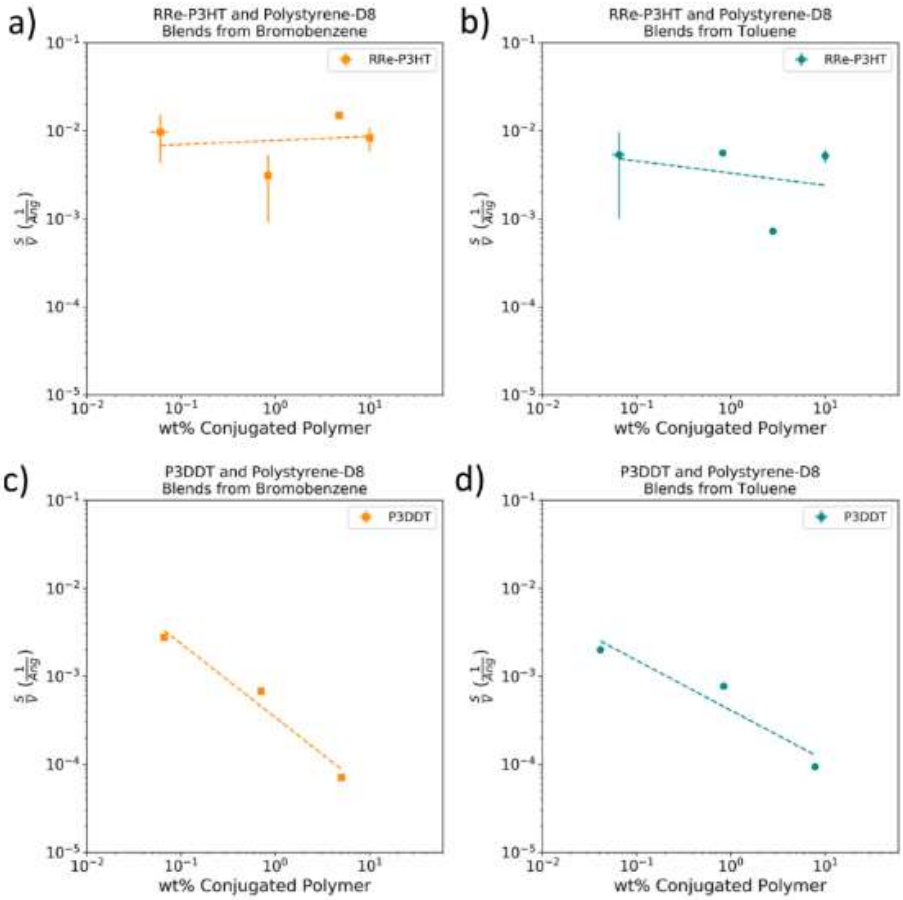

Figure 3.3: Interfacial concentration, S/V, for CP and PS-d8 blends cast from solutions of bromobenzene (a, c) or Toluene (b, d). The CP used in each blend is (a, b) RRe-P3HT, (c, d) P3DDT. When present, vertical, and horizontal error bars correspond to the standard deviation of S/V and CP concentration, respectively, as determined by sample replicates ($n \leq 3$). Dashed lines show polynomial fit to guide the eye only.

We also fit all of the data collected with shape dependent models. These models were combined models of a Guinier-Porod polystyrene fit, and a globular or nanofiber conjugated polymer fit. The globular models included both spherical and ellipsoid shapes, while the nanofiber were represented by cylindrical models. All data points were fit, and the radius of gyration (R_g)

was extracted to determine the size of the domains that were being formed. Shown in **Figure 3.4**, we see a considerable jump in domain size at a critical concentration (C_{crit}), which is different for each conjugated polymer.

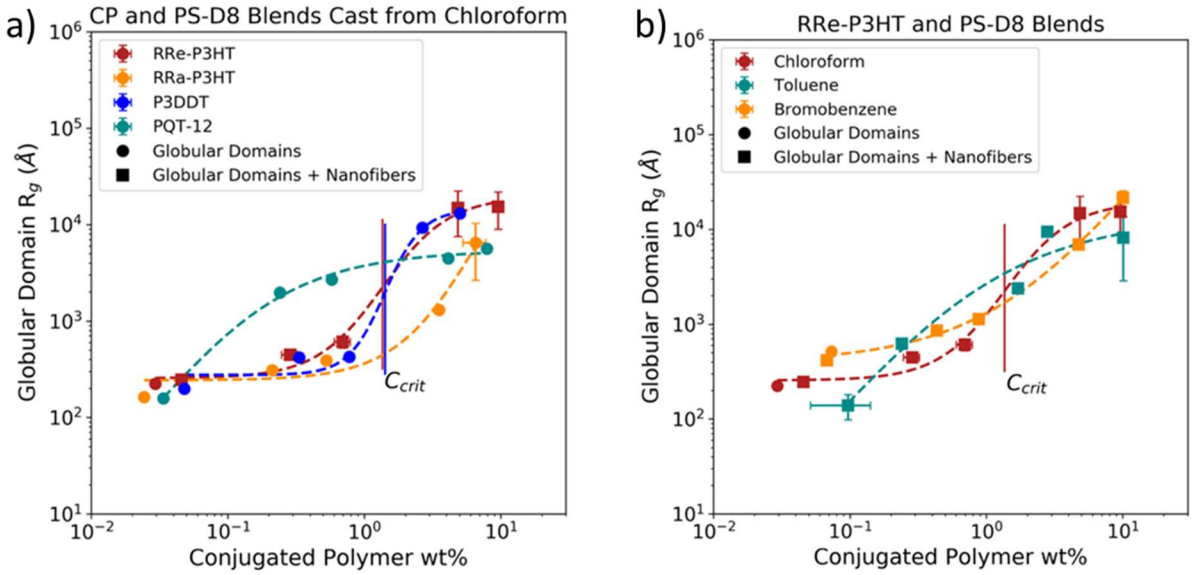

Figure 3.4: Radius of gyration for the globular domain phase (spheres and ellipsoids) in all replicate blends of all CP in PS-D blends cast from Chloroform (a), and RRe-P3HT in PS-D cast from chloroform, toluene, or bromobenzene. A fit of the logistic function is provided as a trendline only to guide the eye and estimate C_{crit}.

We estimate this transition to be 6.5 wt % for RRa-P3HT samples, 1.4 wt % for P3DDT samples, less than 0.034 wt % for PQT-12 samples, and 1.4 wt % for RRe-P3HT samples by fitting the data to a logistic function. The trend for the size of the globular domains correlates to the degree of phase separation observed in the Porod S/V analysis as seen in **Figure 3.2**. For the solvent varied samples, we found that globular domains were often not sufficient to fully model the system and cylindrical models had to be added to model elongated nanostructures. We also observe a C_{crit} for each of RRe-P3HT samples, with 0.097 wt % for RRe-P3HT samples cast from toluene, 1.4 wt % for samples cast from chloroform, and at least 10 wt % for samples cast from bromobenzene.

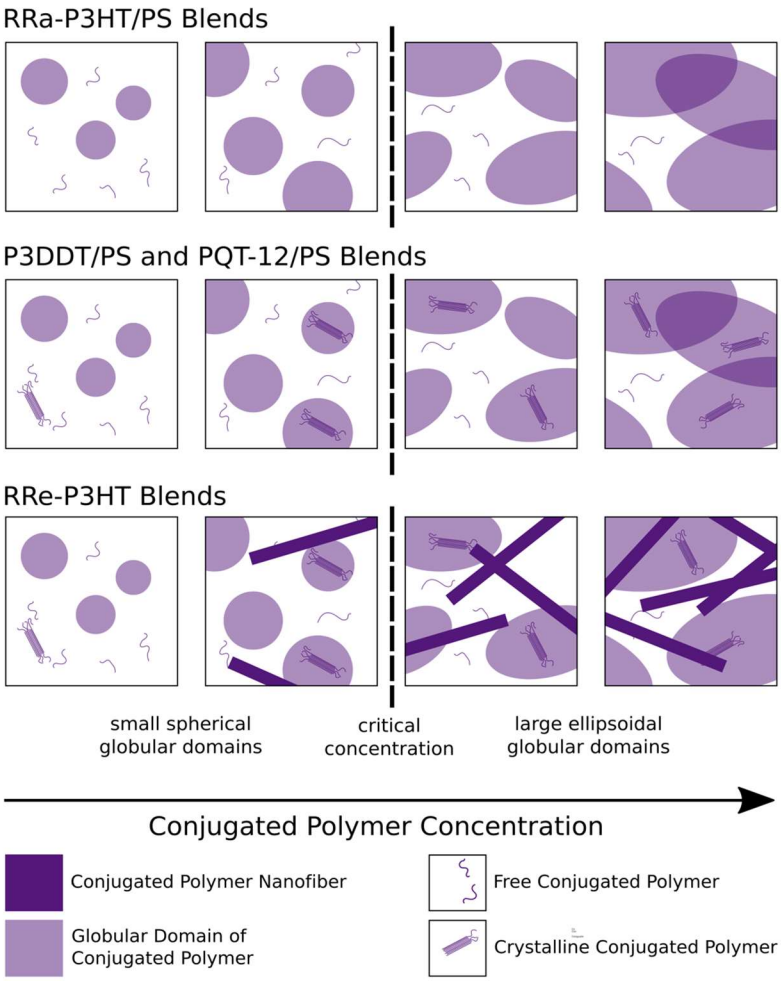

Figure 3.5: Schematic diagram of hypothesis of conjugated polymer blend morphology

With all of our previous analysis in mind, we pulled a few conclusions away from this work. The first focuses on the "critical concentration" we found for each blend. We identified that there are component and processing specific factors that affect the extent, size, and onset of aggregations. We also identified that different conjugated polymers produced several types of aggregations, with amorphous conjugated polymers only producing amorphous aggregations. With semicrystalline conjugated polymers, self-assembled crystalline domains emerged, with only one conjugated polymer producing consistent and large nanofiber structures. Alongside the conjugated polymer differences, we identified different structures and onset location of the structures due to different solvents during process. This is important as compositionally all of the blends were identical, but the different thermodynamics during the solution state affected and changed how the blends dried and aggregated.

3.4 Summary

From this work, we showed that a combined approach of neutron and X-ray scattering allows for exploration and understanding of the bulk morphology in these polymer blend systems at length scale that are not accessible with conventional methods of microscopy. While this was not the main focus of this work, development, and optimization of methods to investigate the structures that we are looking to isolate is always beneficial to the field. We were also able to address some of our original aims as well. From solutions cast from different solvents, we found that in the less stable interactions of the conjugated polymer and toluene, a poor solvent, we found a higher driving force for the formation of nanofibers. Samples cast from this solvent were found to have a higher percentage of the conjugated polymer in a nanofiber form compared to samples cast from better solvents such as chloroform or bromobenzene. These findings echo other studies of 'solution memory,' indicating that the nanofiber formation begins to occur in the solution phase, and that the solution phase will have an impact on the resulting film morphology.

This work set the precedent for the rest of the chapters in a few ways. The first is in the development of the processing method. In Chapters 4 and 5, a version of this heat processing method is used to make all of the samples, and multiple variations on this method are investigated in Chapter 5. We identified in this work that solvent has an impact on these PS/CP blends, and we need to consider how the choices we make in processing affect the blend morphology of compositionally identical samples. The second is the use of sasmodels to fit data, which is used in all subsequent chapters, and the ability to use SasView/sasmodels to refine and modify models to fit complex systems, which is addressed in Chapters 6 and 7.

3.5 References

1. Vakhshouri, K. *et al.* Signatures of intracrystallite and intercrystallite limitations of charge transport in polythiophenes. *Macromolecules* **49**, 7359–7369 (2016).
2. Rivnay, J. *et al.* Large modulation of carrier transport by grain-boundary molecular packing and microstructure in organic thin films. *Nature Materials 2009 8:12* **8**, 952–958 (2009).
3. Gu, K. & Loo, Y. L. The Polymer Physics of Multiscale Charge Transport in Conjugated Systems. *J Polym Sci B Polym Phys* **57**, 1559–1571 (2019).
4. Gu, K. *et al.* Assessing the Huang-Brown Description of Tie Chains for Charge Transport in Conjugated Polymers. *ACS Macro Lett* **7**, 1333–1338 (2018).
5. Newbloom, G. M., Kim, F. S., Jenekhe, S. A. & Pozzo, D. C. Mesoscale Morphology and Charge Transport in Colloidal Networks of Poly(3-hexylthiophene). **44**, 3801–3809 (2011).
6. Xi, Y. & Pozzo, L. D. Electric field directed formation of aligned conjugated polymer fibers. *Soft Matter* **13**, 3894–3908 (2017).
7. Kumar, A., Baklar, M. A., Scott, K., Kreouzis, T. & Stingelin-Stutzmann, N. Efficient, Stable Bulk Charge Transport in Crystalline/ Crystalline Semiconductor-Insulator Blends. doi:10.1002/adma.200900717.

8. Goffri, S. *et al.* Multicomponent semiconducting polymer systems with low crystallization- induced percolation threshold. *Nat Mater* **5**, 950–956 (2006).
9. Qiu, L. *et al.* Organic thin-film transistors based on polythiophene nanowires embedded in insulating polymer. *Advanced Materials* **21**, 1349–1353 (2009).
10. Park, Y. D. *et al.* Solubility-Induced Ordered Polythiophene Precursors for High-Performance Organic Thin-Film Transistors. doi:10.1002/adfm.200801763.
11. Newbloom, G. M. *et al.* Solvatochromism and conformational changes in fully dissolved poly(3-alkylthiophene)s. *Langmuir* **31**, 458–468 (2015).
12. Bronstein, H. A. & Luscombe, C. K. Externally initiated regioregular P3HT with controlled molecular weight and narrow polydispersity. *J Am Chem Soc* **131**, 12894–12895 (2009).
13. Kline, S. R. & IUCr. Reduction and analysis of SANS and USANS data using IGOR Pro. *urn:issn:0021-8898* **39**, 895–900 (2006).
14. Kienzle, P. A. (University of M. C. P., Krycka, J., Patel, N. & Sahin, I. Bumps. Preprint at (2011).
15. Doucet, M. *et al.* SasView. Preprint at (2022).
16. Doucet, M. *et al.* Sasmodels. Preprint at (2020).
17. Wolf, C. M. *et al.* Blend Morphology in Polythiophene−Polystyrene Composites from Neutron and X-ray Scattering. doi: 10.1021/acs.macromol.0c02512.
18. Geil, P. H. Morphology of Amorphous Polymers. *Industrial and Engineering Chemistry Product Research and Development* **14**, 59–71 (1975).
19. Renninger, A. L. & Uhlmann, D. R. Structure of glassy polymers. V. Small-angle x-ray scattering from polystyrene. *Journal of Polymer Science: Polymer Physics Edition* **16**, 2237–2244 (1978).
20. Wendorff, J. H. The structure of amorphous polymers.
21. Roe, R. J. & Curro, J. J. Small-Angle X-ray Scattering Study of Density Fluctuation in Polystyrene Annealed below the Glass Transition Temperature. *Macromolecules* **16**, 428–434 (1983).
22. Furuya, H. *et al.* Molecular Dynamics Simulation of Atactic Polystyrene. 2. Comparison with Neutron Scattering Data. *Macromolecules* **27**, 5674–5680 (1994).
23. Song, H. H. & Roe, R. J. Structural Change Accompanying Volume Change in Amorphous Polystyrene As Studied by Small and Intermediate Angle X-ray Scattering. *Macromolecules* **20**, 2723–2732 (1987).
24. Hammouda, B. PROBING NANOSCALE STRUCTURES-THE SANS TOOLBOX.
25. Ilavsky, J. *et al.* Development of combined microstructure and structure characterization facility for in situ and operando studies at the Advanced Photon Source. *urn: issn:1600-5767* **51**, 867–882 (2018).
26. Ilavsky, J. *et al.* Ultra-small-angle X-ray scattering instrument at the advanced photon source: History, recent development, and current status. *Metall Mater Trans A Phys Metall Mater Sci* **44**, 68–76 (2013).
27. Thing files for USAXS 48 Solid Film Holder by dpozzo - Thingiverse. https://www.thingiverse.com/thing:4639006/files.
28. Ilavsky, J. & IUCr. Nika: software for two-dimensional data reduction. *urn: issn:0021-8898* **45**, 324–328 (2012).
29. Wolf, C. M. pozzo-research-group/c-wolf-blends-morphology: Initial Development. Preprint at (2020).

Chapter 4: Blend Morphology of Conjugated Polymers and Elastomers in Solution and Solid States

4.1 Introduction

4.1.1 Elastomeric Polymers

Elastomers are at the forefront of development in the field of flexible electronics, including healthcare sensors[1–3], electronic skin[4–6], stretchable OLED[7] displays[8,9], and flexible solar cells[10–12]. These electronic technologies come in many forms, such as metallic circuits suspended on elastomeric substrates[13,14], resilient electronic fibers embedded within stretchable materials[15,16], or stretchable electrodes that can distort and move with a flexible device[17,18]. The base of all these materials are elastomers in a variety of forms. We focus on commonly used block copolymers, which are complex polymers consisting of two or more sections of homopolymers that are bonded together.

Block copolymers (BCPs) can be designed as diblock, triblock, or multiblock to create complex nanoscale architectures. Our focus is on a triblock thermoplastic elastomer composed of styrene-based ABA copolymer polystyrene-block-polyisoprene-block-polystyrene (PS-PI-PS or SIS) (**Figure 4.1a**). Elastic properties emerge from the restoring force of this polymer, which are a result of physical crosslinks from the glassy polystyrene end-blocks and the rubbery nature of the polyisoprene. These crosslinks involve non-covalent molecular associations that provide strength and structure while facilitating processing due to the possibility of thermally reversing the crosslinking process. Physical crosslinking in a SIS polymer occurs when the hard glassy polystyrene blocks associate with each other during processing and act as physical connections while the rubbery flexible polyisoprene block is able to deform and stretch[19]. These unique physical properties are a result of large difference in glass transition temperature between polystyrene (~100 ºC) and polyisoprene (-57 ºC)[20,21]. The combination of flexible rubbery regions and glassy regions allows for the polymer to be mechanically strong, flexible, and resilient, as shown in **Figure 4.1c**.

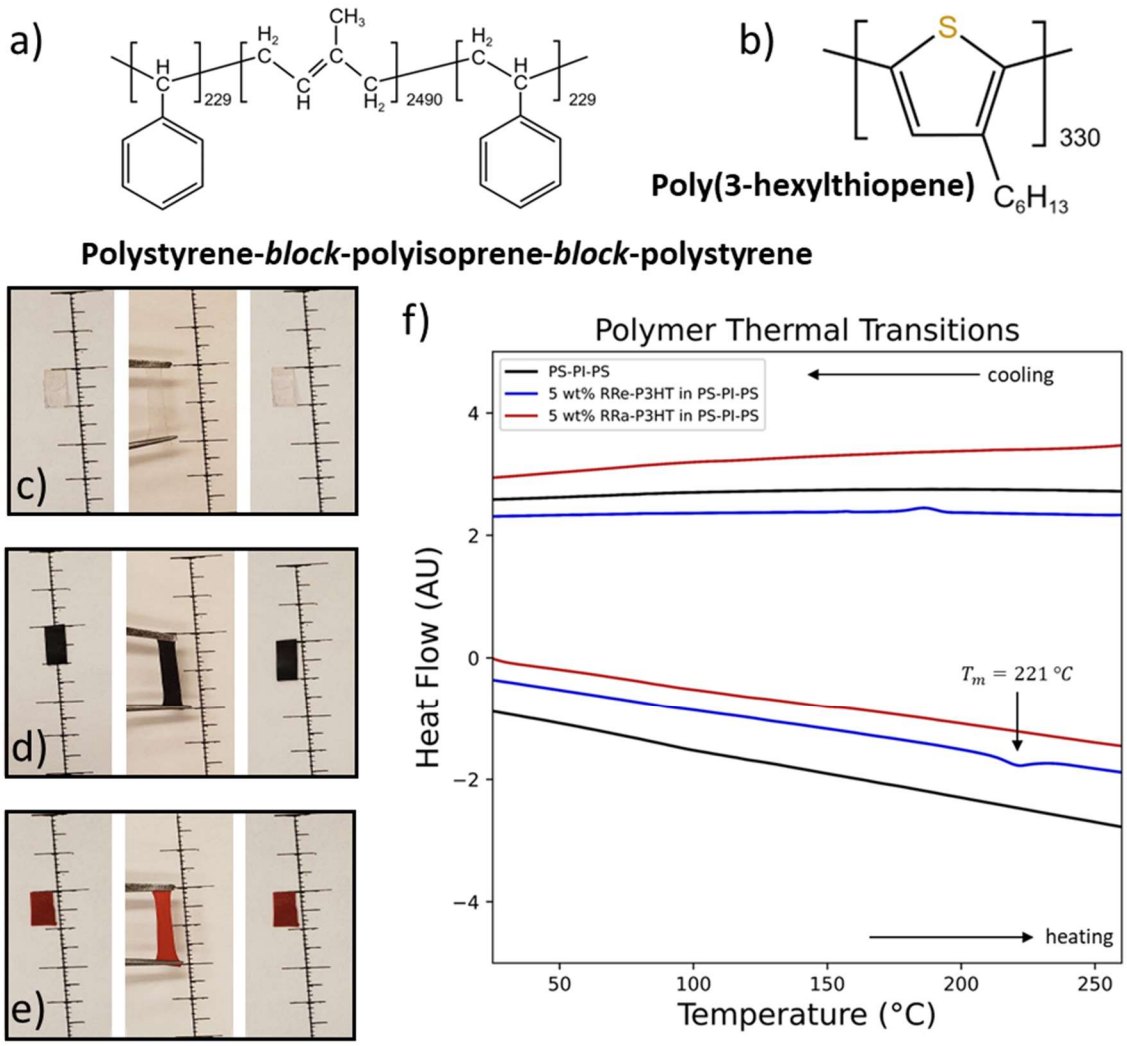

Figure 4.1. Polymer structures of a) PS-PI-PS elastomer block copolymer and b) P3HT conjugated polymer. Images of representative templates and blends at rest before strain, under strain, and at rest after strain for c) PS-PI-PS d) 5 wt % regioregular P3HT in PS-PI-PS blend e) 5 wt % regiorandom P3HT in PS-PI-PS blend. f) Differential Scanning Calorimetry data collected for the representative templates and blends with melting temperature of a 5 wt % RRe-P3HT/PS-PI-PS blend identified.

Polystyrene and polyisoprene chains are known to self-segregate into nanoscale phase-separated morphologies including spherical micelles[22], hexagonal cylinders[23,24], lamellae[25,26], gyrods[27,28], and cubic crystals[29], depending on the polymer architecture [25,30], temperature [31], and processing conditions [32,33]. As established by calculations done by Matsen and Bates, the ratio between the A and B blocks, determined by the degree of polymerization of each block, encourages

specific structures to emerge.[30] In general, when styrene content is low the SIS copolymer forms polystyrene nano-spheres or micelles engulfed in an isoprene matrix. As the styrene content increases, the SIS material transitions to polystyrene cylinders dispersed in an isoprene matrix, then at near equal ratios alternating lamellar structures, and finally at high styrene wt %, creating polyisoprene microdomains within the bulk polystyrene. While the polymer structure has a strong influence on the specific phase that is formed, processing variables also affect the final structure by creating kinetically arrested states and/or altering their macroscopic orientation. Processing and methodology choices established in Chapter 4 are further investigated in Chapter 5 with modifications on the pressing time, solvent, post-processing heat treatment, and shape variation.

4.1.2 Conjugated Polymer Additives

Further complexity in phase and structure emerges with the inclusion of additives to make elastomeric blends. Additives for elastomeric electronics have included carbon nanotubes[34,35], conjugated polymer nanowires[15,36], and bulk conjugated polymer into an elastomeric matrix[37–39].

Conjugated polymers are a unique subset of polymers with alternating saturated and unsaturated bonds along their backbones that allow for electron resonance through the chain and across adjacent chains when found in sufficiently close configurations[40]. The incorporation of conjugated polymers into elastomers has opened a field of new possibilities, by producing elastomeric polymers with electronic capabilities[38,41–44]. Elastic electronic materials are often subjected to long lifespans of continuous deformation and generally need to be thin and compact, requiring both durability and efficiency. The addition of a conjugated polymers allows for the combination of the elastomeric matrix's physical properties and the conjugated polymer's optical and electronic properties even at low loadings (**Figure 4.1c-d**)[43–45]. Experiments by Carpi et al with blends of polydimethylsiloxane and P3HT found that even small amounts of added conjugated polymer (1-6 wt %) showed increases in conductive properties, with a maximum electromechanical response seen at 1 wt % conjugated polymer[38].

Simple blended materials often consist of two homopolymers and more complex systems, such as the replacement of the elastomeric homopolymer with a triblock copolymer, require further insight. With the addition of a conjugated polymer into a triblock copolymer matrix, phase behavior increases in complexity as new interactions between the copolymer blocks and the conjugated polymer emerge. Intermolecular interactions between components ultimately drive these materials to reach a stable thermodynamic equilibrium. However, time scales for achieving

equilibrium can be much longer than practical, and the processing step of solvent evaporation frequently leads to kinetically arrested states. During solvent evaporation, the composition and physical properties of samples changes rapidly and unevenly, resulting in phase separation and solvent-dependent formation of complex structures[32,46,47]. In simulations, Cummings et al depicts the phase segregation of drying solutions through multiple thermodynamic drivers and model how the evaporation of all solvent can lock in kinetically frozen structures[47]. Depending on the kinetics of processing versus the thermodynamic drive, equilibrium may not be achieved for all practical purposes, resulting in materials with a processing-dependent structure. Once dry, temporal fluctuations in amorphous materials are still observed, but often have slow time scales that can only be accelerated through thermal or solvent annealing[48–50]. In solid films, the balance between the kinetics of gradual chain movements and thermodynamics of the material cannot ensure that equilibrium is reached. This competition between kinetics and thermodynamics frequently determines the structural outcome with respect to processing techniques, component architecture, and applied conditions.

4.1.3 Comments on Additional Experiments

During the process of data collection for the elastomer projects, a series of triplicated samples were run at Argonne Photon Source (APS) on the USAXS instrument. The triplicates displayed consistent trends and became the backbone of the elastomer blends work for much of the project. As further experiments were conducted to probe other processing conditions, trends that were observed in the initial triplicate set were not repeated in other samples prepared to study annealing and temperature sensitivity. Further samples were prepared to determine the cause of the trend difference, but no definite cause was found. Samples that were used to discount possible sources of the trend variation are presented in Chapter 4 and 5, highlighting material, temporal, and thermal changes. A selection of these samples is shown in **Figure 4.2**. This includes the triplicate samples discussed in Chapter 9.3 and samples discussed in Chapters 4 and 5, all processed identically, to show the differing trends for the sets. As seen in **Figure 4.2a**, at low wt %s of RRe-P3HT there is not a large difference visually between the scattering profiles of the samples, but above 10 wt % there emerges a large shift and flattening of the peak of interest in the triplicate samples that is not observed in the later sample sets. In the RRa-P3HT (**Figure 4.2b**) samples, the results are more consistent and seem to be within the normal range of observed morphological variations. The PS-PI-PS control samples are also consistent over the replicates.

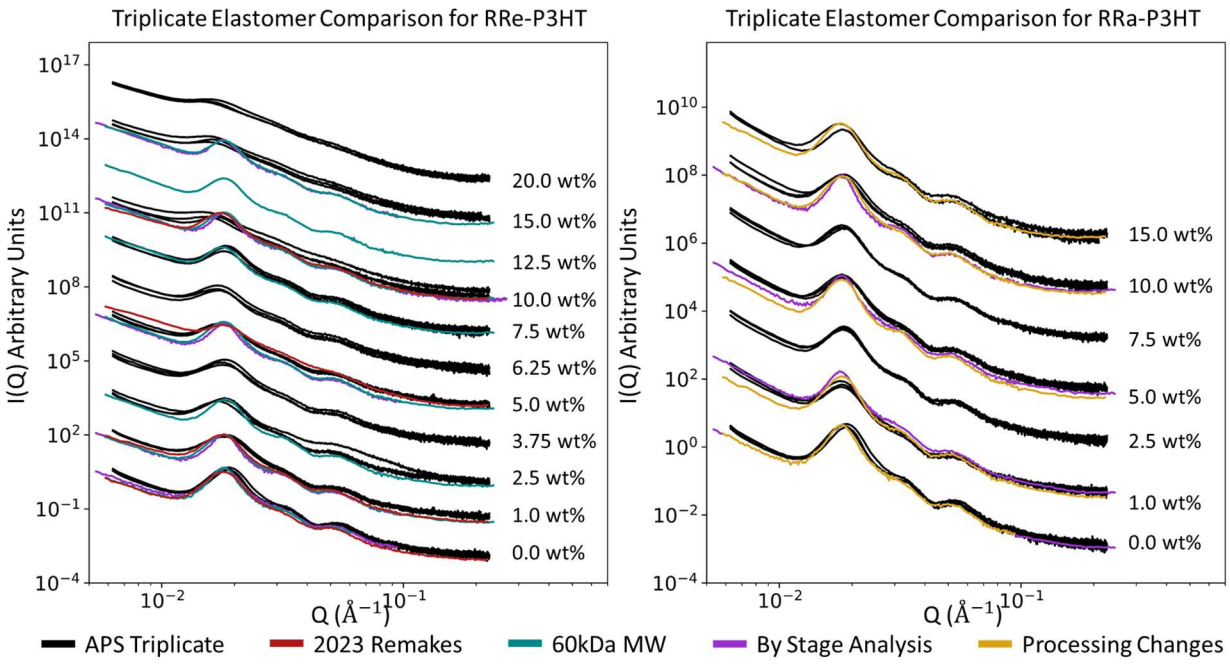

Figure 4.2: Comparisons of data collected in triplicate at the Argonne Photon Source (APS) for a) RRe-P3HT and b) RRa-P3HT alongside a selection of compositionally identical samples described in further detail in Chapter 4 and Chapter 5.

The break from trend appears to be isolated to the RRe-P3HT blends, so specific deviations for that conjugated polymer are addressed here, but the triplicate APS sample set will be addressed in Chapter 9.3. The trends observed in the triplicate data are morphologically interesting and have promise to be conductively impactful, so this data is presented alongside a caveat that while the observations within the set are precise the cause of trend is unknown at this time.

4.2 Materials and Methods

4.2.1 Materials

Regiorandom poly(3-hexylthiophene) (RRa-P3HT) (MW = 63 kg mol^{-1}, Đ = 2.4, Product 4007) and regioregular poly(3-hexylthiophene) (RRe-P3HT) were purchased from Rieke Metals (Lincoln, NE USA). Three different molecular weights of RRe-P3HT were used: Lot BLS26-16 (RRe42) (MW = 42 kg mol^{-1}, Đ = 2.0, RR = 90), Lot PTL43-54 (RRe60) (MW = 60 kg mol^{-1}, Đ = 3.0, RR = 91) and Lot BLS26-96 (RRe77) (MW = 77 kg mol^{-1}, Đ = 2.4, RR = 94). Polystyrene-block-polyisoprene-block-polystyrene (PS-PI-PS) was purchased from Aldrich Chemistry (St. Louis, MO USA). The PS-PI-PS polymer is a 22 % styrene $A_{229}B_{2490}A_{229}$ triblock copolymer (MW 217 kDa) as determined using Gel Permeation Chromatography (GPC). Chloroform was

purchased from Fisher Chemical (Waltham, MA USA). For SANS experiments, fully deuterated chloroform was purchased from Cambridge Isotope Laboratories, Inc. (Tewksbury, MA USA). All chemicals were used as received.

4.2.2 Film Preparation

All solid blend films were prepared in accordance with the schematic diagram shown in **Figure 4.3a**. Carefully weighed portions of conjugated polymer (i.e. RRe-P3HT or RRa-P3HT) were co-dissolved with the elastomeric polymer (PS-PI-PS) until fully homogenous in chloroform, which is a good solvent for all polymers involved, at 50 ºC [51–53]. Each solution was poured over a watch glass on top of a hot plate heated to 50 ºC, covered loosely with aluminum foil to enable a slow evaporation, and allowed to fully dry (~30 minutes). Films were then peeled off the watch glass and left in a fume hood to remove any remaining solvent in the system overnight. The dry polymer blend was then heat pressed using a D16 Digital Combo Swing-Away Press from Geo Knight & Co (Brockton, MA). All samples in this chapter were radially pressed into circular steel precision shims from McMaster Carr (Elmhurst, IL) with a thickness of 254 μm and an inner diameter of 15mm (as shown in **Figure 4.3b)** at the chosen temperature (110 ºC, 150 ºC, 250 ºC). All temperatures were measured by a type-K thermocouple and recorded with an accuracy of ±2 ºC. During pressing, each sample was sandwiched between thermally conductive Kapton and two polished stainless-steel plates to create a smooth and even film. After each pressing, the film was cut, stacked, and pressed again at the same temperature. The total time for each of the three presses was 5 min, 5 min, and 15 min, respectively. Films were then allowed to cool slowly to room temperature over a period of 60 minutes. This repeat pressing process was used to ensure that samples were uniform and to eliminate polymer segregation that could have occurred during drying. Films were then removed from the metal shims and stored at room temperature prior to structural characterization.

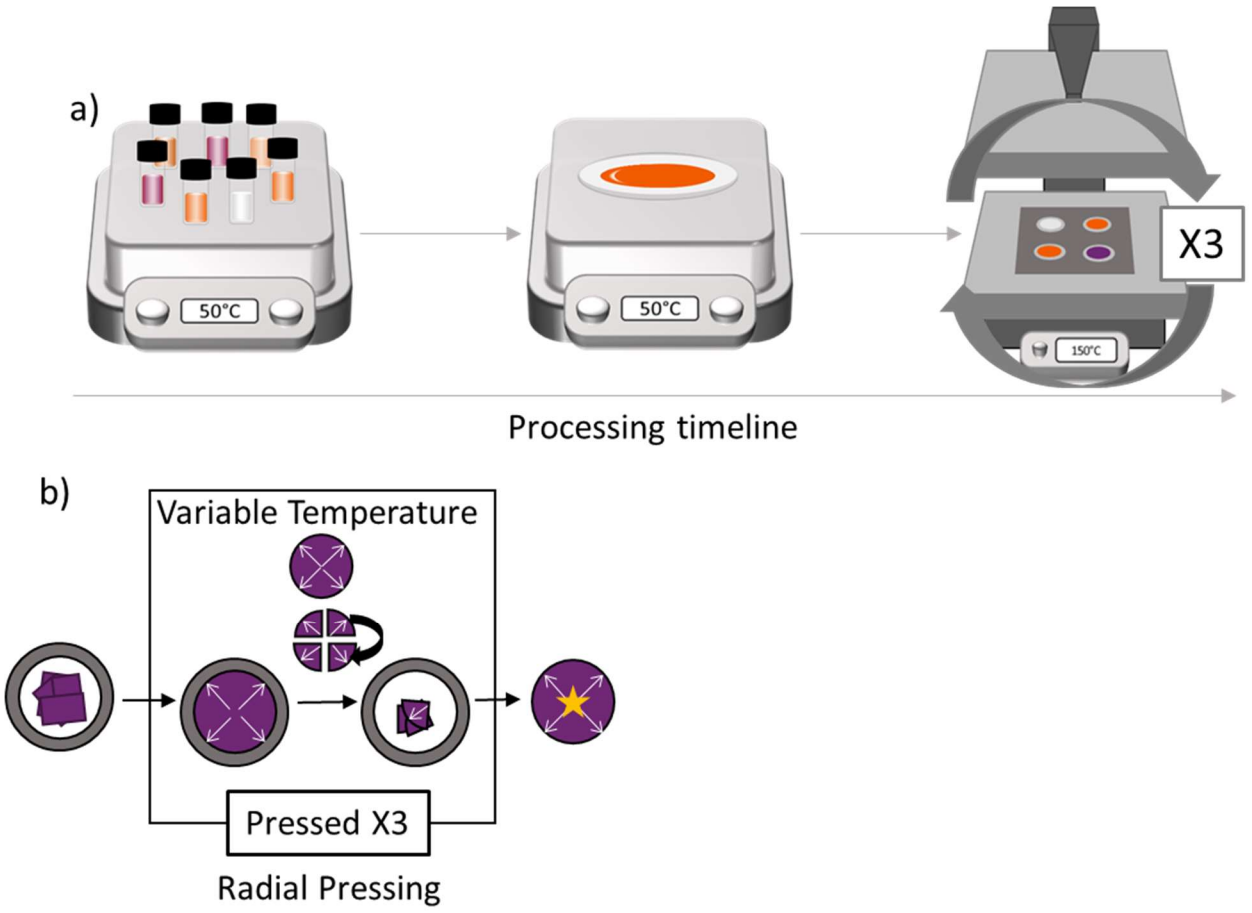

Figure 4.3: Schematics for sample creation for a) the full processing timeline, including co-dissolving of polymers into a solvent on a hotplate set at 50 ºC, samples evaporating in a foil insulated watch glass until fully dry, then being pressed at a set temperature into a shim. Samples were b) radially pressed in circular shims with samples being cut and restacked to be pressed 3 times before being measured at the starred location.

4.2.3 Solution Preparation

Solution samples were prepared at two different concentrations corresponding to either 5 mg/mL (low) or to a higher concentration of 10 mg/mL (high). The solvent for all samples was deuterated chloroform (dCF), which is considered a 'good' solvent for all polymers in the system[51–53]. The lower concentration set included three samples: 5 mg/mL RRe-P3HT in dCF, 5 mg/mL PS-PI-PS in dCF, and a mixed blend of 5mg/mL RRe-P3HT and 5 mg/mL PS-PI-PS in dCF. The higher concentration set was similar with concentrations set to 10 mg/mL. The samples were prepared by carefully weighing portions of the polymers, which were then dissolved in deuterated chloroform at 50 ºC in capped glass containers. For blended solutions, polymers and solvent were

added at the same time and were heated until fully dissolved and homogenous. Each sample was then loaded from the hotplate into 2 mm quartz Hellma cells and stored at 25 ºC before being measured at room temperature.

4.2.4 Differential Scanning Calorimetry (DSC) and Thermogravimetric Analysis (TGA)

Thermophysical analysis was conducted on representative samples including the pure PS-PI-PS matrix, a blend of 5 wt % RRa-P3HT in 95 wt % PS-PI-PS, and a blend of 5 wt % RRe-P3HT in 95 wt % PS-PI-PS. Thermogravimetric Analysis (TGA) was conducted using TA instruments (New Castle, DE) Q50 Thermogravimetric Analyzer between room temperature (23 ºC) and 400 ºC. Differential Scanning Calorimetry (DSC) was conducted using a TA instruments (New Castle, DE) Differential Scanning Calorimeter Q200 between 0 ºC and 280 ºC. Samples were weighed (PS-PI-PS – 7.9 mg, 5wt % RRe-P3HT in PS-PI-PS – 8.0 mg, 5wt % RRa-P3HT in PS-PI-PS – 5.9 mg) and analyzed in sealed aluminum pans. A heat-cool cycle was used with three repetitions of heating and cooling to ensure any thermal history was removed. Analysis was conducted using Python.

4.2.5 USAXS and SAXS

Ultra-small, small, and wide-angle x-ray scattering (USAXS, SAXS, and WAXS) was collected at the University of Washington using a Xenocs (Grenoble, France) Xeuss 3.0 SAXS instrument. This is a pinhole collimated laboratory SAXS instrument equipped with a copper microfocus x-ray source. Samples were collected at three sample-to-detector distances to obtain a wide Q-range. WAXS data (sample to detector distance of 0.07 m) was collected for 60 s, SAXS (sample to detector distance of 0.9 m) for 60 s, and ESAXS (sample to detector distance of 1.8 m) for 360 seconds. Samples were mounted on a 48-sample holder to enable automated processing of multiple samples. The data for each formulation was reduced, averaged (except when analyzed for flow-alignment), and combined to a unified dataset that will be referred to as ‘SAXS data’ through this work. USAXS data was also collected using a Bonse-Hart configuration with two Si crystals, a multi-bounce Bartels Si (111)-crystal monochromator and a 4-bounce Si (111) crystal analyzer. USAXS was collected for two hours for each sample as well as the empty background. The sample chamber was held under vacuum at ambient temperature (approx. 20 °C) for both SAXS and USAXS measurements. Reduction of all data was performed using XSACT, the Xenocs supported software provided with the instrument, with the USAXS data being subtracted and scaled through Xenocs recommended modules.

For the outlier triplicate set of data run at APS, USAXS and SAXS/WAXS data for samples were collected at the 9ID and the 12ID beamline at the Advanced Photon Source at Argonne National Laboratory[57]. USAXS data was collected in the Bonse-Hart configuration using Si [200] crystals in the standard instrument configuration. The instrument used an intense X-ray beam of 21 keV and a beam size of 0.8 × 0.8 mm with a flux density of approximately 5 × 10 photons/s/mm2. Pinhole SAXS and WAXS data were also collected with exposure times of 10 s each, while USAXS was collected with exposure times of 80 s. Samples were mounted using custom-designed 3D-printed 48-sample frames[58] that enabled execution of remote experiments during COVID-19-constrained access. The sample chamber was held under vacuum at ambient temperature (approx. 20°C) during all measurements. USAXS, SAXS and WAXS data were reduced, de-smeared (USAXS), and set to absolute intensity units using the Nika package[59] for Igor Pro[60]. This package was also used to combine the 'pinhole' data from the SAXS and WAXS detectors to produce datasets that will be referred to as 'WAXS data' for the remainder of the work.

SAXS and WAXS data for these outlier triplicate samples were recollected at the University of Washington using a Xenocs (Grenoble, France) Xeuss 3.0 SAXS instrument in the same manner described for the other set of elastomer samples.

4.2.6 Small Angle Neutron Scattering (SANS)

Small angle Neutron Scattering (SANS) measurements were collected at the Quokka beamline at the Open Pool Australian Lightwater (OPAL) source with Australian Nuclear Science and Technology Organisation (ANSTO)[61]. SANS data was collected in three configurations to span the full Q range. All configurations used 5Å ± 0.10Å wavelengths, with low-Q collected at 20m sample to detector distance (600 seconds), mid-Q collected at 12m sample to detector distance (1200 seconds), and high-Q collected with 1.3m sample detector distance (2400 seconds). Samples were loaded into 2mm quartz Hellma cells and mounted into aluminum holders placed into a temperature controlled 20 slot sample environment set to 25ºC. SANS data were reduced, combined, and background subtracted using the Quokka macro in the NIST SANS package for Igor Pro[60].

4.2.7 Scattering Data Analysis

Once fully reduced, data was exported, and further analysis was conducted using SasView[54]/sasmodels[55] and bumps[56] packages for Python. Features in the SAXS data were fit with shape independent models to extract structural parameters when possible.

Peaks in the SAXS region (**Figure 4.3**), which correspond to nanometer scale self-segregation of the block-copolymer matrix, were fit using a generalized broad peak model[62].

$$I(Q) = \frac{A}{q^n} + \frac{C}{1 + (|Q - Q_0|\xi)^m} + B \tag{4.1}$$

Here, A is the Porod scaling factor, n is the Porod exponent, C is a Lorentzian scaling factor, m is the exponent of Q, ξ is the Lorentzian screening length, and B is a flat background. Peak position is determined as Q_0 which is related to d-spacing by $Q_0 = \frac{2\pi}{d_0}$. This model does not assume any given structure (e.g., lamellar, cylindrical, cubic) and is appropriate for samples with variable ranges of order that may also result in changing phases.

In the outlier APS triplicate set a low-Q feature (Figure 4.4.3) in the USAXS regime, associated to polymer phase segregation, was fit using the Guinier-Porod[63] combined model corresponding to the equations below.

$$I(Q) = \frac{G}{Q^s}\exp\left[-\frac{Q^2 R_g^2}{3 - s}\right] when\ Q \leq Q_1 \tag{4.2}$$

$$I(Q) = \frac{D}{Q^m} when\ Q \geq Q_1 \tag{4.3}$$

$$Q_1 = \frac{1}{R_g}\sqrt{\frac{(m - s)(3 - s)}{2}} \tag{4.4}$$

$$D = \frac{G}{R_g^{m-s}}\exp\left[\frac{s - m}{2}\right]\left(\frac{(m - s)(3 - s)}{2}\right)^{\frac{m-s}{2}} \tag{4.5}$$

Where G is a scale factor, R_g is the radius of gyration, m is the Porod Exponent, and s is the dimensionality variable in the range 0 to 2. This variable is related to the dimensionality of the scattering objects, from s = 0 (3D symmetry, such as spheres or globules), s = 1 (2D symmetry, such as rods), and s = 2 (1D symmetry, such as plates).

SANS data were fit using a semi-flexible cylinder model to capture free chains in solution as described by Pedersen et al[64] and which was found to be appropriate for conjugated polymers in prior works[65]. Free chain fits of blends of CP and PS-PI-PS were modeled using sums of the fits for the individual components in solution. This is only appropriate when it is determined that the polymer chains are sufficiently dilute and do not have strong repulsive or associating interactions.

All analysis and modeling of the DSC, USAXS, SAXS, WAXS and SANS data was performed using Python 3 (NumPy[66], pandas[67], Matplotlib[68]), which aids in reproducibility, while the use of SasView[54]/sasmodels[55] and bumps[56] packages for Python, allows for rapid and easily adjustable fitting of the data sets.

4.3 Results and Discussion

Thermogravimetric analysis (TGA) data shows that differences in onset of thermal decay for each sample are minimal, with the PS-PI-PS template being slightly delayed in degradation compared to the blends. A thermal decay onset of 280 ºC was determined as the temperature at which 1 % of material is lost. The peak temperatures for degradation for pure and blended forms of polystyrene (PS) and polyisoprene (PI) have been previously reported around 370 ºC for PI and 420 ºC for PS[69,70]. McNeill and Gupta have also observed a shift in the peak degradation temperature upwards of about 15 ºC when the materials are mixed, due to a stabilization of each component in the blend.[69] Thermal degradation work has also been conducted on P3HT, with no degradation occurring until 440 ºC[71]. Thus, from our experiments and literature, all samples were processed below the degradation temperature of the pure materials and their blends. In longer processing there may be exposure-dependent degradation (e.g., oxidation) that can occur, but for pressing times used in this work, the effect is expected to be minimal[69,71].

Differential Scanning Calorimetry (DSC) (**Figure 4.1f**) provides insight into the phase transitions of crystalline and amorphous regimes in each blend. The semi-crystalline RRe-P3HT blend with PS-PI-PS shows a melting peak at 221 ºC that corresponds well to the melting point of the crystalline regimes of the P3HT. This suggests that the P3HT component is still able to crystallize within these blends. There are no other distinct and obvious transitions in any of the other samples. Literature on PS-PI blends report a glass transition from the PS at a temperature of approximately 85 ºC, which was not observed in our samples[20,72]. It is possible that the DSC instrument used lacked the necessary resolution to accurately measure this subtle transition, or that the PS component of these materials (22 % styrene) was too low. The published glass transition temperature for PS was still considered and set as a minimum for temperatures used in processing.

SANS data collected in the solution state of these samples allows us to identify if polymers interact substantially when co-dissolved in a common solvent prior to drying.

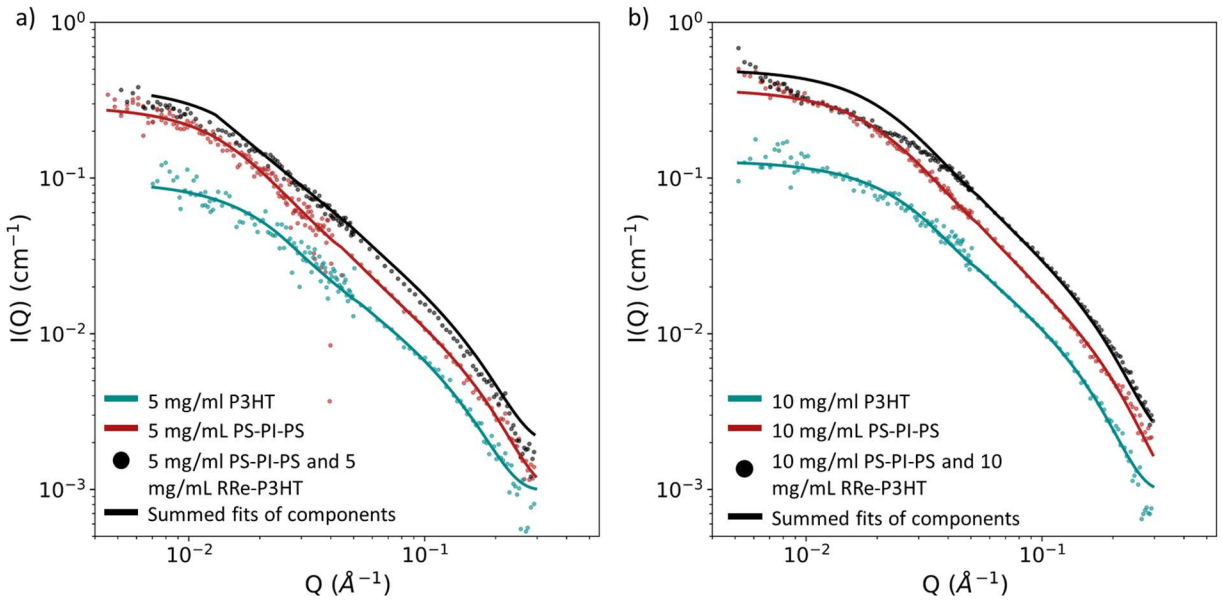

Figure 4.4: SANS plots consisting of models fit to free polymer chains of SIS and RRe-P3HT in chloroform, data from the combined samples, and the sum of the models of the components for the a) low concentration system with 5 mg/ml RRe-P3HT and 5 mg/ml PS-PI-PS and b) high concentration system with 10 mg/ml RRe-P3HT and 10 mg/ml PS-PI-PS.

We observe that all single-polymer samples (i.e. without blending) fit well with the flexible cylinder model, which describes the dimensions of a free chain in solution. Moreover, when polymers were co-dissolved at low concentrations, we find that the scattering intensity is nearly identical to the sum of the individual polymer components (**Figure 4.4a**). We interpret this as the polymers are well dissolved and not interacting substantially at low concentrations. At higher concentrations (**Figure 4.5b**) the sum of the scattering of the individual components does not agree with the data of the experimental blend. This suggests that there is some assembly in solution at higher concentrations due to the interactions of the individual components. During evaporation, the concentration of the cast sample will increase substantially as the solvent is removed from the system. As the concentration increases, we anticipate increased interaction and assembly between the components. With this in mind, we know that structures observed in the solid forms are formed over the course of evaporation and drying and are not solely a result of interactions while in the solution state.

4.3.1 RRe-P3HT and PS-PI-PS blends

X-ray scattering was performed on solid film samples after drying and processing as noted, allowing for structural information at various stages. Through the collection of ultra-small angle X-ray scattering (USAXS), small angle X-ray scattering (SAXS), and wide-angle X-ray scattering (WAXS) data, the full Q range from $3e10^{-4}$ $Å^{-1}$ to 3 $Å^{-1}$ is available, allowing for analysis of features from ~3.2 μm to ~2 Å (**Figure 4.5**). Due to the weight ratio of the polymers, the self-assembled structure of the elastomer component generally dominates the signal over the sparse conjugated polymer. As the loading of conjugated polymer in the blend is changed, the structure of the elastomer matrix is modified, and this is observed in the SAXS and USAXS data. Therefore, the aggregation or segregation of the conjugated polymer within the elastomeric structure is inferred from its impact on the structure of the self-assembled elastomeric matrix.

The data was split into three regions, each covering a different length scale of polymer film morphology and together covering the full scope of the impacts of the conjugated polymer additive on the structure of the elastomeric template. The low-Q USAXS region shows emerging features (i.e., a broad 'hump') with the addition of higher weight percentages of conjugated polymer (either regioregular or regiorandom) which suggest large-scale formations of phase-separated regions. Mid-Q features in the SAXS region are dominated by the emergence of a prominent peak around 0.018 $Å^{-1}$. This peak is present in all samples that are collected, including the pure PS-PI-PS matrix, and is attributed to the characteristic spacing of the ordered structure of the PS and the PI blocks. From previous literature reports for this PS to PI ratio range, as well as peak indexing using known Bragg peak ratios, the phase of the pure block-copolymer matrix is identified to be hexagonally packed cylinders. With the addition of conjugated polymers, we see a characteristic peak shift and a change in shape, suggesting the cylindrical packing structure is affected by the integration of the conjugated polymer into the blend.

At high-Q (i.e., WAXS region) we observe the structure at the smallest molecular and atomic scales. This allows us to determine changes in the crystallinity of the components that make up the composite polymer blend. The PS-PI-PS matrix has peaks characteristic of an amorphous structure and does not display the narrow peaks that are typically attributed to polymer crystallinity. This is consistent with the elastomeric (PI) and glassy (PS) nature of the components that make up the triblock copolymer. When semi-crystalline RRe-P3HT is added, we see the

emergence of two new narrow peaks that correspond to the lamellar and π-stacking peaks that are commonly observed in the literature and that allow us to track the extent of crystallinity[73,74].

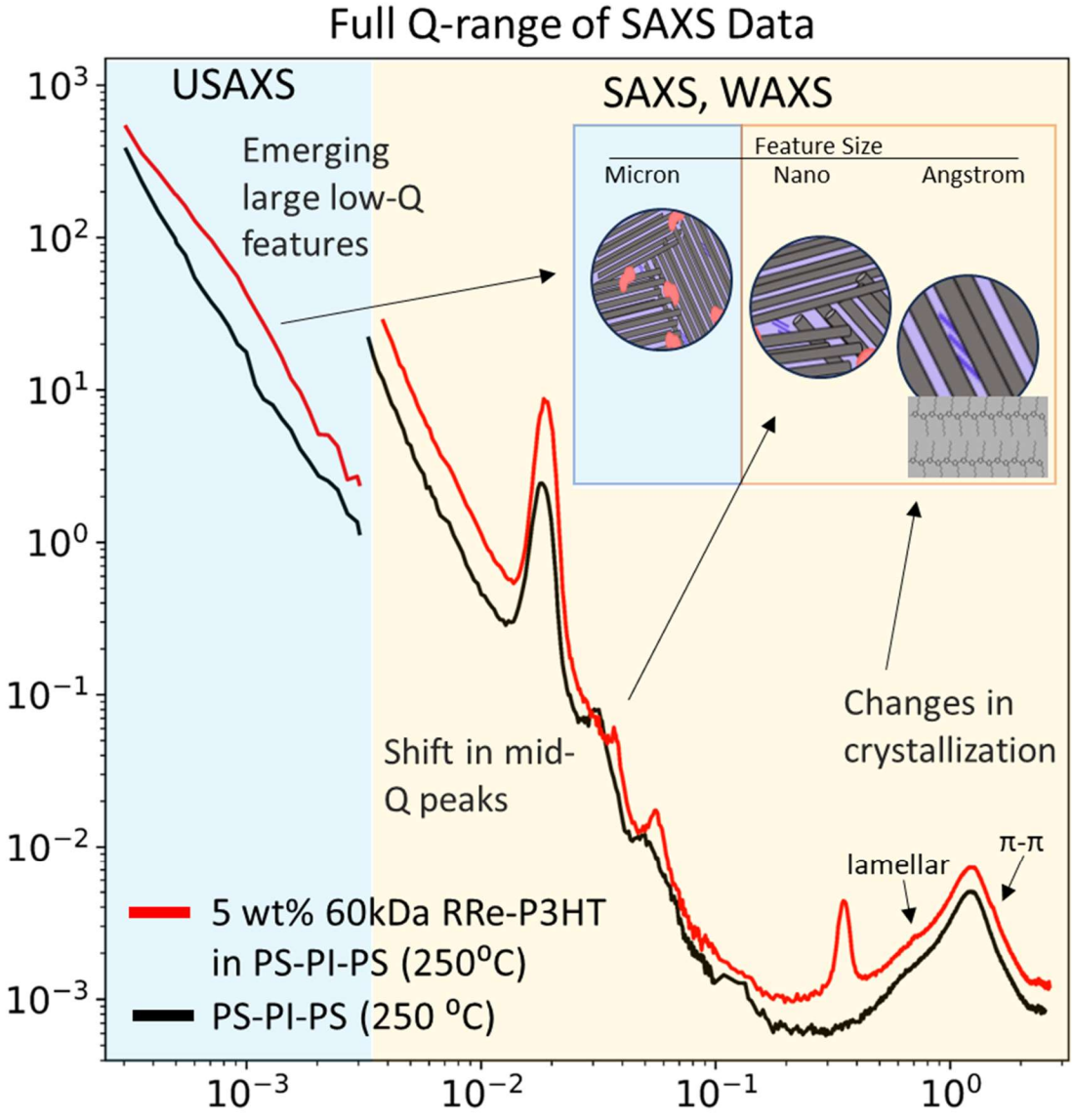

Figure 4.5: Full Q range of USAXS and SAXS data collected on a pure PS-PI-PS matrix sample (black) and a 5 wt % RRe-P3HT composite blend (red) from 3e10^{-4} Å^{-1} to 3 Å^{-1}. Peaks and features of interest have been marked and inset provide scale for each feature observed.

Blends made with the same molecular weight of RRe-P3HT are processed at different temperatures within the range of interest that is established from TGA and DSC. The temperature change is implemented during the pressing stage, with each sample being pressed for the same amount of time, but at a different temperature. Physical differences for each sample are observed,

with the lowest temperature samples (pressed at 110 ºC) not fully melding until the final and longest press cycle. Samples processed at these lowest temperatures visually showed clear physical distinctions where pieces were laid on top of each other. Some initial samples were also tested at 100 ºC and these would not melt and blend even after the final long press cycle. Samples processed at intermediate temperatures (150 ºC and 200 ºC) are physically similar with small inhomogeneities removed in the final and longest press cycle. The highest temperature (250 ºC) is completely homogenous after the first (5-minute) press cycle and is tacky when handled immediately after the press. After the final press and slow cooling, the 250 ºC samples are homogeneous and physically similar to samples processed at intermediate temperatures (150 ºC and 200 ºC). SAXS is also collected on solution cast samples, cut from the film produced by drop casting onto the watch glasses prior to any heat pressing.

SAXS data for these sample was collected with the Xenocs Xeuss III and spans from .01 $Å^{-1}$ to 3 $Å^{-1}$. Starting in the high-Q WAXS region, we can track the emergence of crystalline structures through the development of the π-stacking seen at ~1.7 $Å^{-1}$, and lamellar peaks seen at ~0.4 $Å^{-1}$. As seen in **Figure 4.6a**, these peaks are not visible in the fully amorphous PS-PI-PS matrix but begin to appear starting with the addition of the semi-crystalline RRe-P3HT. The lamellar peak is present in all blended samples, and the height increases as the wt % of RRe-P3HT increases. The π-stacking peak, which is known to be important for electronic performance, emerges as a small feature in the 5 wt % RRe-P3HT sample. As the RRe-P3HT content increases above 5 wt %, the height of the π-stacking peak also increases. The presence and growth of these two peaks above 5 wt % suggest that the semi-crystalline RRe-P3HT does not significantly crystallize before this threshold. Above this concentration, it steadily increases in extent of crystallinity as the weight percent of the conjugated polymer increases. We do not see a significant difference in WAXS peaks due to the processing temperature, suggesting that the assembly seen is set during the solution casting step.

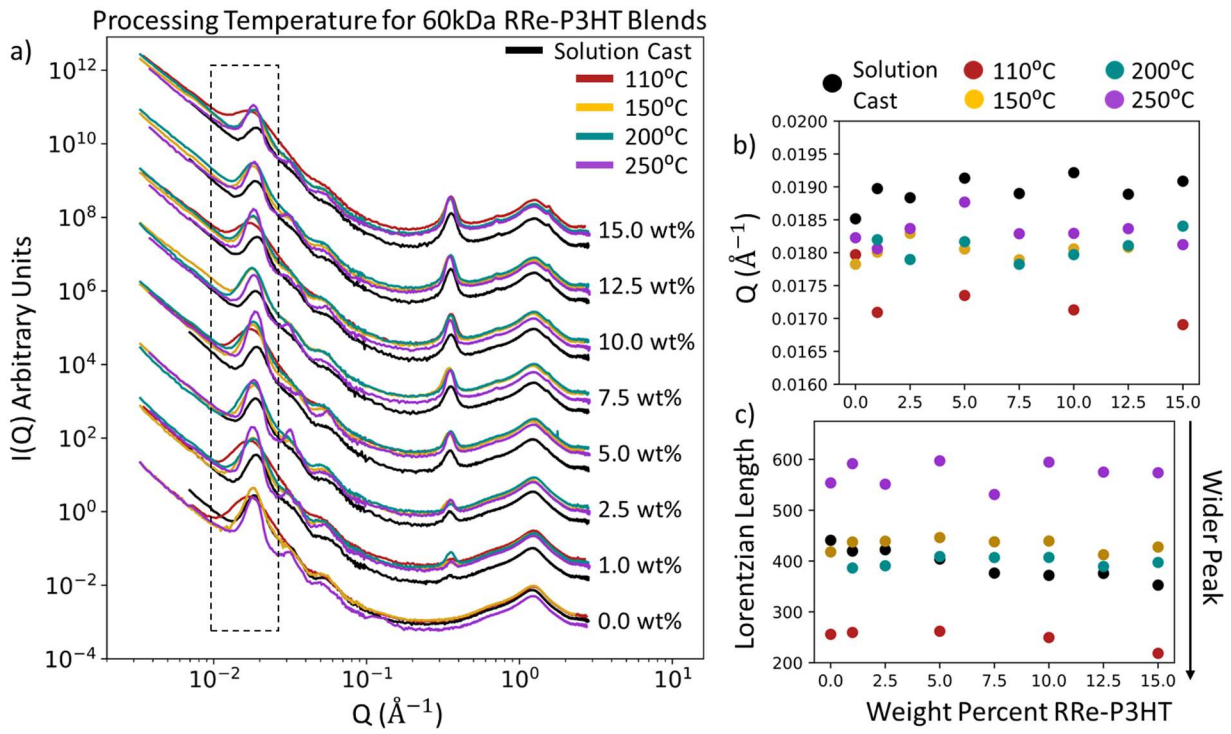

Figure 4.6: a) SAXS data of 60 kDa RRe-P3HT and PS-PI-PS blends, labeled by wt % of RRe-P3HT added to system, and collected as cast from solution and for four different heat pressing temperatures. Data has been arbitrarily shifted to separate samples by wt %. b) peak position parameters from broad peak fits of the .018 $Å^{-1}$ peak with colors dictated by legend above. c) Lorentzian length parameters from broad peak fits of the .018 $Å^{-1}$ peak with colors dictated by legend above.

At mid-Q, we see a large peak around 0.017-0.019 $Å^{-1}$ in all samples. This peak is characteristic to the PS-PI-PS template structure and by tracking changes to peak parameters, such as location and width, we can establish how the addition of RRe-P3HT, sample processing, and temperature affect the template morphology. These peaks have been fit with a broad peak model, allowing us to quantify changes with parameters shown in **Figure 4.6(b-c)**. Starting with the pure PS-PI-PS, we see a large effect of the processing temperature on this peak. At 110 ºC the peak is wide and as the processing temperature increases to 150 ºC the peak sharpens considerably and continues to sharpen at 250 ºC. This trend of increasing processing temperature to decrease peak width is maintained as RRe-P3HT is added and the wt% of the CP in the system increases. As seen in **Figure 4.6c**, the lowest processing temperatures consistently have the widest peaks, and shortest Lorentzian lengths, which is inverse to peak width. The two intermediate processing temperatures,

150 ºC and 200 ºC have similar peak widths, but the highest processing temperature samples display another drastic increase in Lorentzian length. This correlates to the thermodynamic thresholds established by TGA and DSC. The lowest processing temperature, which is only slightly above the T_g of the polystyrene at 95 ºC -105 ºC in the matrix, has the lowest levels of molecular mobility and the highest levels of disorganization in the samples. The disorganization in the 110 ºC is higher than in the drop cast unprocessed samples, which we anticipate is a result of cutting and stacking during pressing without the polystyrene at a temperature to encourage melding. Above ~150 ºC, processing temperatures are well-above the T_g of the polystyrene, allowing for the glassy connections to melt and reorganize to a more stable state. Still, blended samples may be constrained by the T_m of the RRe-P3HT at 221 ºC and these domains may need to reorganize within the blend. The highest processing temperature, which is both well above the T_g of the polystyrene and above the T_m of the RRe-P3HT, allows for full movement and reorganization into a thermodynamically stable structure. With these thermodynamic thresholds in mind, there is also a small shift in the peak location. **Figure 4.6b** shows a shift towards higher Q between processing temperatures of 110 ºC and 150 ºC, with no drastic trends observed with increased processing temperatures past 150 ºC. This implies that once the processing temperature is suitably above the T_g of polystyrene, the spacing of the reorganized structure does not change considerably with processing, only the consistency or organization of the structure.

In this Q region, we also see a less-intense series of peaks emerge at slightly higher Q than the primary peak. Traces of these peaks are present at all temperatures, but they become clear and established at the 250 ºC processing temperature. This again suggests that there is a clear temperature dependent assembly and organization in these materials. With the emergence of secondary peaks, we can now use Bragg diffraction ratios to identify the structural phase formed by these samples and explore how they change with increasing loading of conjugated polymer additives.

Each of the peaks in the series are fitted with the broad peak model to pull the peak position and peak width metrics. These peak positions are then divided by the location of the first peak to determine the $\frac{Q}{Q^*}$ for each secondary peak. The ratios are then compared to known ratios for phase morphologies from literature to identify the sample phase. Some of the peak values do not match exactly with peaks calculated from expected ratios, especially for the peak located at 0.053 $Å^{-1}$. This peak is wide and may encompass multiple peaks that have merged together due to reasons

that may include limited instrumental resolution, co-existence of phases, and the partially disorganized nature of the samples. Best estimates are included for all peaks and ratios, but a level of disorder in all the samples makes exact identification of a few peaks somewhat challenging. A selection of interest is shown in **Figure 4.7a** for the PS-PI-PS template material, a 5 wt % 77 kDa RRe-P3HT in PS-PI-PS blend, and a 15 wt % 77kDa RRe-P3HT in PS-PI-PS, processed at 250 ºC. In **Figure 4.7a**, dotted lines are used to mark where peaks are expected due to the phase ratio but are not able to fit concretely. At all these locations, features emerge but are too spread to be fit absolutely. In the pure PS-PI-PS material, the peak ratios are [1,1.70, 2.08, 2.78] which can be identified as a hexagonally packed cylinder phase. This is consistent with the material architecture and phase-diagrams outlined in the literature[30]. When RRe-P3HT is added into the system at low amounts, 1 w t% and 2.5 wt %, there are no major changes in peak locations or ratios and the hexagonally packed cylinder phase is maintained. At 5 wt % the peak in the .032 $Å^{-1}$ range drops leaving a [1,1.98,2.99] ratio indicative of the formation of a lamellar phase. As more conjugated polymer is added into the system the peak in the 0.032 $Å^{-1}$ range re-emerges and the 7.5 wt %, 10 wt %, and 12.5 wt % samples show a mixture of disordered hexagonally packed cylinder peaks and lamellar peaks. There is a clear peak in the 0.032 $Å^{-1}$ range, which equates to the ~1.7 ratio, but the peak in the 0.053 $Å^{-1}$ range is wide enough that it encompasses the locations for both the 2.64 and 3.0 ratios. At the maximum loading of 15 wt % RRe-P3HT in PS-PI-PS, we see a return to the clearest hexagonally packed cylinder ratios, and a return to similar levels of order as seen in the template.

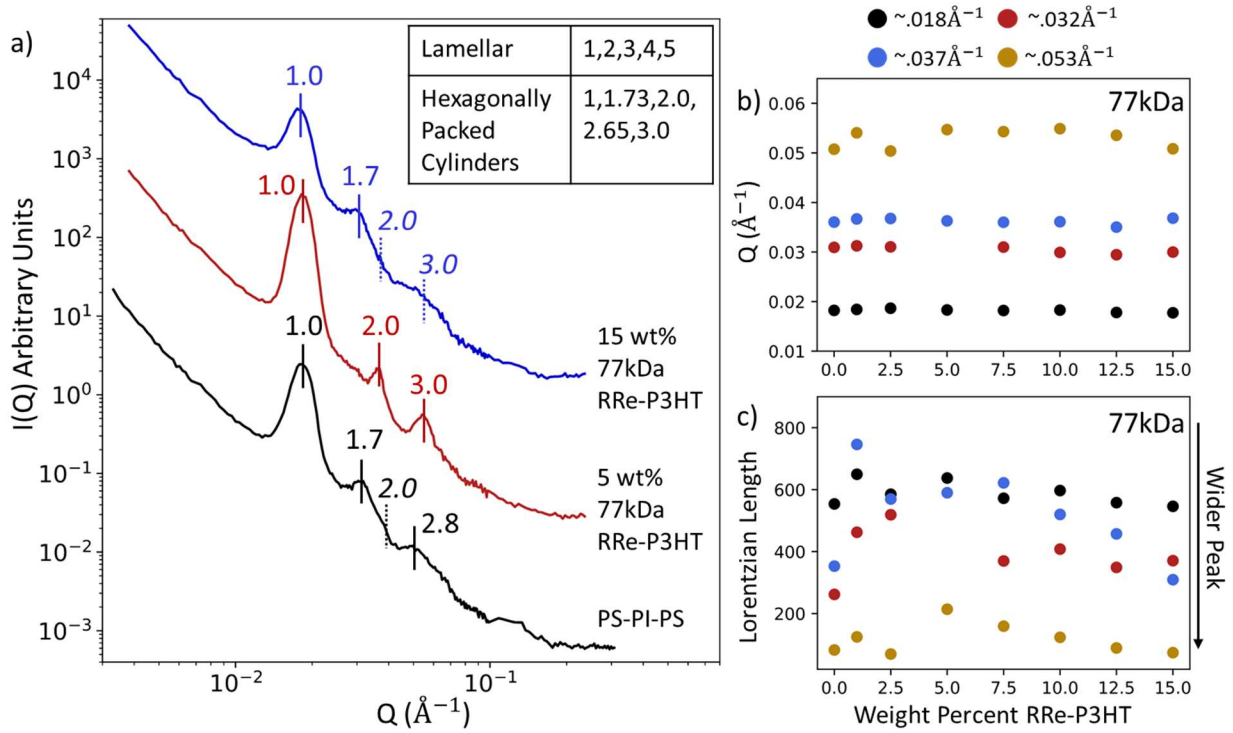

Figure 4.7: a) SAXS data of selected 77 kDa RRe-P3HT and PS-PI-PS blends, labeled by wt % of RRe-P3HT added to system, and collected at 250 ºC. Data is arbitrarily shifted to separate samples into wt %. Dotted lines are used to denote where peaks are expected due to ratios but are not able to be concretely fit. b) peak position parameters from broad peak fits of all peaks with colors dictated by legend above.

Changes are also observed in the low-Q feature that is observed in the USAXS regime for blend samples. Solo samples were measured then rotated 90º then measured again to ensure that any USAXS feature was not dependent on changes in alignment direction of samples. Measured samples shown here were stacked three thick in order to ensure scattering signal was high enough for analysis. Series of 60 kDa RRe-P3HT in PS-PI-PS processed at 250 ºC are shown in **Figure 4.8b** and shows both the region of interest for low-Q analysis as well as the peak at ~ 0.018 Å^{-1} seen in **Figure 4.5a**. As seen in **Figure 4.8a**, the pure PS-PI-PS matrix does not display any noteworthy features in this length scale, beyond the power-law scaling. With the addition of semi-crystalline 60 kDa RRe-P3HT at concentrations of 1 wt % there is no significant change in the shape or intensity of the data. At 5 wt % RRe-P3HT, a feature or 'bump' emerges in the 0.0005 Å^{-1} - 0.001 Å^{-1} region that is indicative of large-scale phase separation. As the conjugated polymer concentration is increased, the intensity increases and the feature shifts further towards lower Q,

indicating that feature is growing. At the highest wt % measured, the feature is absent, and we anticipate that the size of the phase separated regions have grown outside of the length scale of our instrument. The emergence of the feature at 5 wt % conjugated polymer corresponds to phase shift that is observed in the SAXS regime (**Figure 4.7**). We also see the growth of the feature out of our attainable length scales around the 10 wt % sample, earlier than we see in the 250 ºC series.

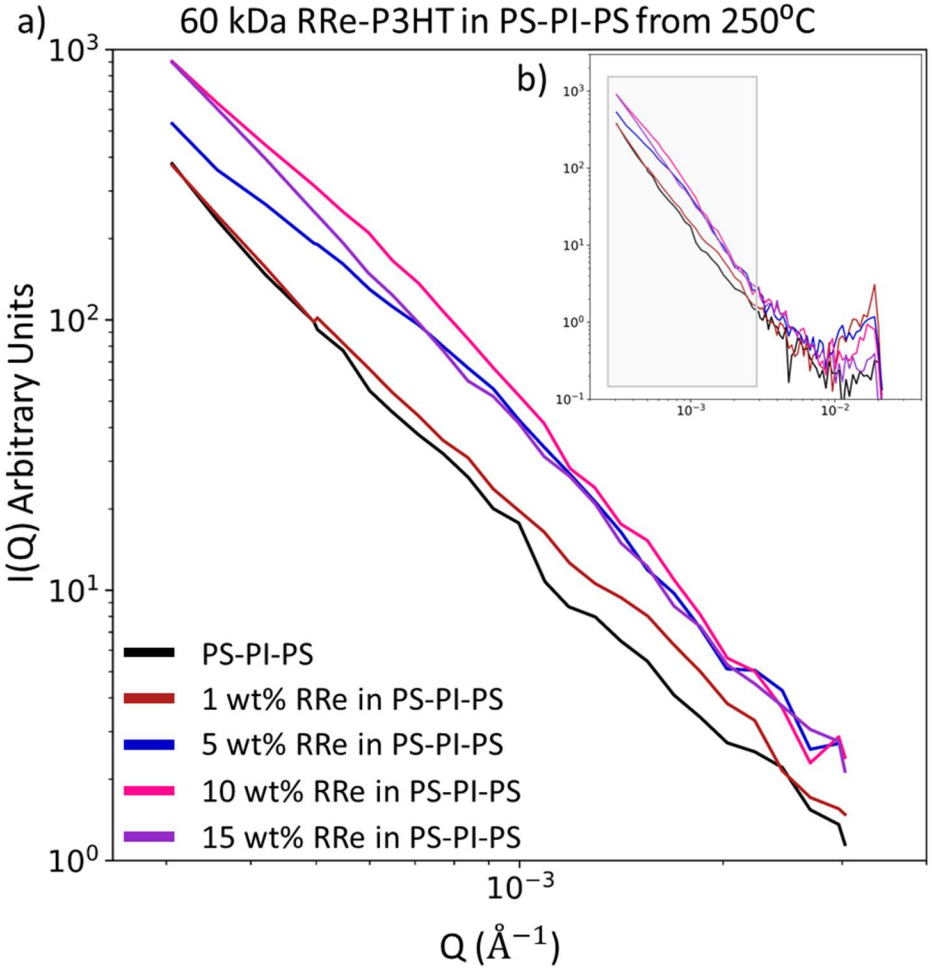

Figure 4.8: a) zoom of region of interest notated in inset b of low-Q region of USAXS data of 60 kDa RRe-P3HT and PS-PI-PS blends processed at 250 ºC. b) full USAXS low-Q data of 60 kDa RRe-P3HT and PS-PI-PS blends processed at 250 ºC with region of interest marked in grey and peak analyzed in SAXS data visible in high-Q indicating data overlap.

4.3.2 Outlier RRe-P3HT and PS-PI-PS Blends

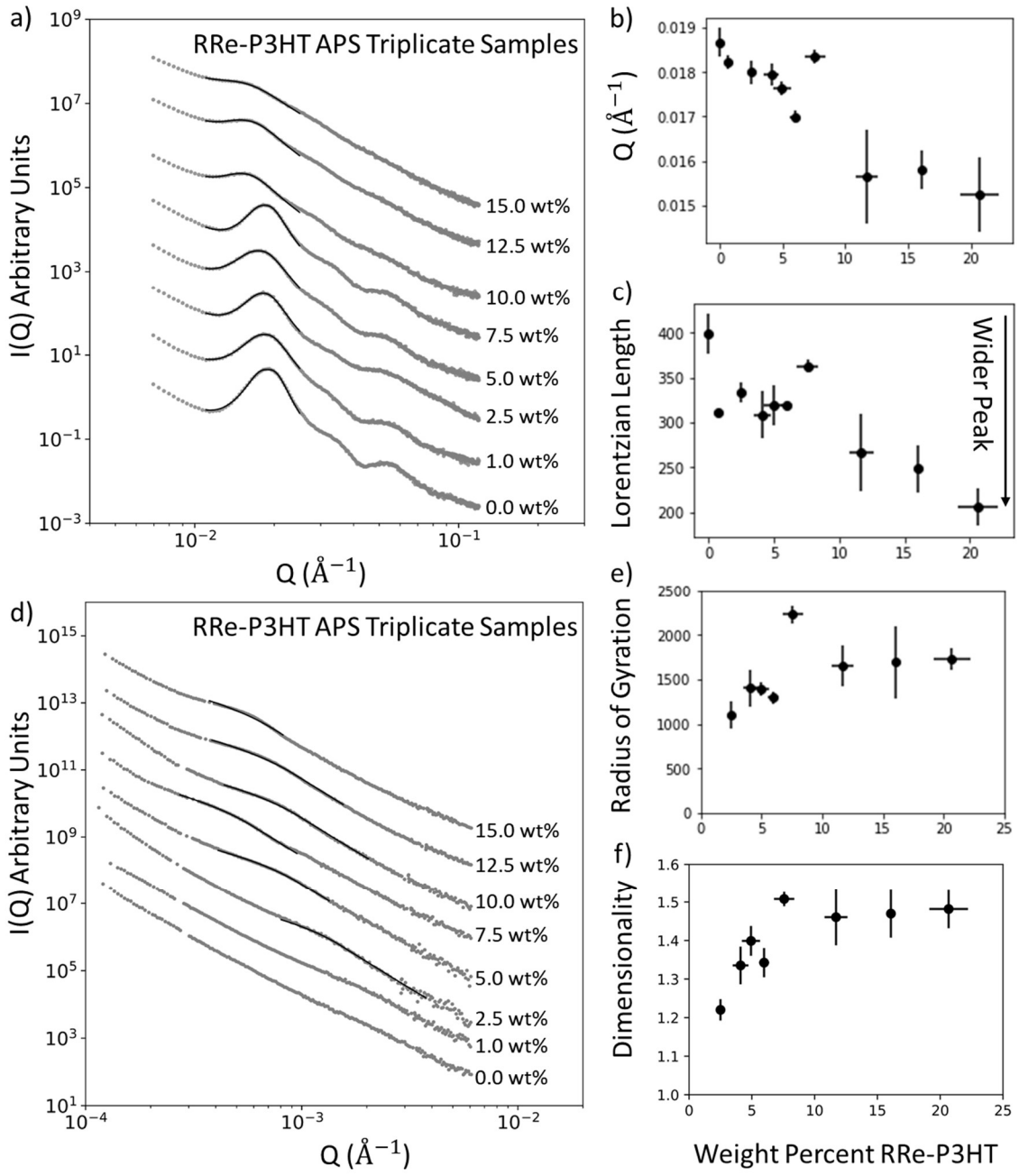

Figure 4.9: SAXS regime plots with broad peak fits of a) regioregular P3HT and PS-PI-PS blends from 0-20 wt % of conjugated polymer. Parameter plots of b) peak location and c) peak width are plotted with both conjugated polymer series. d) USAXS regime plots with Guinier-Porod fits of regioregular P3HT and PS-PI-PS blends from 0-20 weight percent of conjugated polymer. Parameter plots of e) radius of gyration and f) dimensionality coefficient is plotted with both conjugated polymer series.

Turning to the outlying triplicate sample set run at APS, we conduct much of the same analysis as the samples mentioned above. To begin, we fit all the data with a broad peak model, seen in **Figure 4.9a**. The fits for the peak location and Lorentzian length are plotted against weight percent with error bars determined by standard deviation from three or more replicate samples at the same weight percent of additive. Horizontal error bars represent fluctuations between the target CP concentration in preparation, and the actual concentration as determined from UV-Vis measurements. The peak location for the semi-crystalline blends drops in Q rapidly (suggesting a rise in the repeat spacing) before leveling out past 10 weight percent. The extent of the shift observed with these samples at high wt % is larger than any of the subsequent samples created. We see the peak widths for semi-crystalline RRe-P3HT blends fluctuate initially and even seem to sharpen until the 10 wt% RRe-P3HT blend sample before dropping considerably for the highest weight percent samples. Peak indexing was not conducted for these samples as the number and order of the subsequent peaks was not high enough to ensure the locations identified were accurate. These samples were processed at 150 ºC and mirror the extent of secondary peaks observed for this processing temperature as described in Chapter 5.

Changes are also observed in the low-Q feature that is observed in the USAXS regime for blend samples. As seen in **Figure 4.9d**, the control does not display any features in this length scale, but the addition of semi-crystalline RRe-P3HT at concentrations of 2.5 wt % or greater creates a prominent feature that is indicative of large-scale phase separation. As the CP concentration is increased, the feature shifts further towards lower Q, indicating that the characteristic length scale is growing. At and above 12.5 wt % of RRe-P3HT loading, there is a noticeable shift towards high-Q before shifting again towards low-Q with increasing CP loading. Interestingly, this shift corresponds to the loss of order and significant shift in the matrix lamellar spacing that is observed in the SAXS regime (**Figure 4.9a**). This suggests that there is a large-scale phase-separation process that begins with the addition of RRe-P3HT, growing steadily until a shift occurs at ~10 wt %. This phase separation feature has also been observed for CP blends with PS homopolymers[74].

Due to the high power of the instrument used, the USAXS data quality is higher, and the feature is able to be fit confidently with a Guinier-Porod model, allowing for quantitative extraction of parameters of interest. As before, the Porod exponent is fixed to 4, which is typical for sharp interfaces and was also found to be appropriate for the data. The radius of gyration, which

is a general metric of domain size, and the dimensionality coefficient, which is as a metric of shape, are obtained and plotted against the loading of CP in **Figure 4.9**. We see similar trends in both domain size and shape, for both conjugated polymers we worked with. As seen **in Figure 4.9b**, the radius of gyration for the RRe-P3HT features, which is in the range of hundreds of nanometers, grows rapidly before peaking around 7.5 wt %, dropping and leveling out for the highest weight percent samples.

In **Figure 4.9c**, we see similar trends for the shape or dimensionality parameter 's'. The dimensionality variable describes the shape characteristics of the feature and ranges from 1 (rods) to 2 (plates). For both types of CPs, the phase-separated domains tend from more one-dimensional to a more two-dimensional or 'platelike' shape. However, the dimensionality parameter for RRe-P3HT increases more rapidly with increased loading before leveling out at s ~ 1.5 at the highest concentrations.

For further discussion and analysis of these RRe-P3HT samples as well as the RRa-P3HT samples included in this triplicate set, refer to Chapter 9.3.

4.3.3 RRa-P3HT and PS-PI-PS Blends

Additional experiments were conducted using an amorphous regiorandom P3HT (RRa-P3HT) to evaluate the effect regioregularity and P3HT crystallization on the composite structure. Samples were processed, measured, and analyzed in the same way as previously outlined for RRe-P3HT, with samples processed at 110, 150, and 250 ºC. **Figure 4.10a** shows a peak at 0.018 $Å^{-1}$ and similar trends to those observed for RRe-P3HT samples in **Figure 4.6**. We again observe that a wide primary peak that sharpens as the processing temperature increases from 110 ºC to 250 ºC. The Lorentzian length parameters (**Figure 4.10c**) corroborates this observation, with each increase in temperature leading to sharper peaks and more order in the system. There is more variation in peaks parameters, both location and width, for 63 kDa RRa-P3HT than observed with its semi-crystalline counterpart of 60 kDa RRe-P3HT.

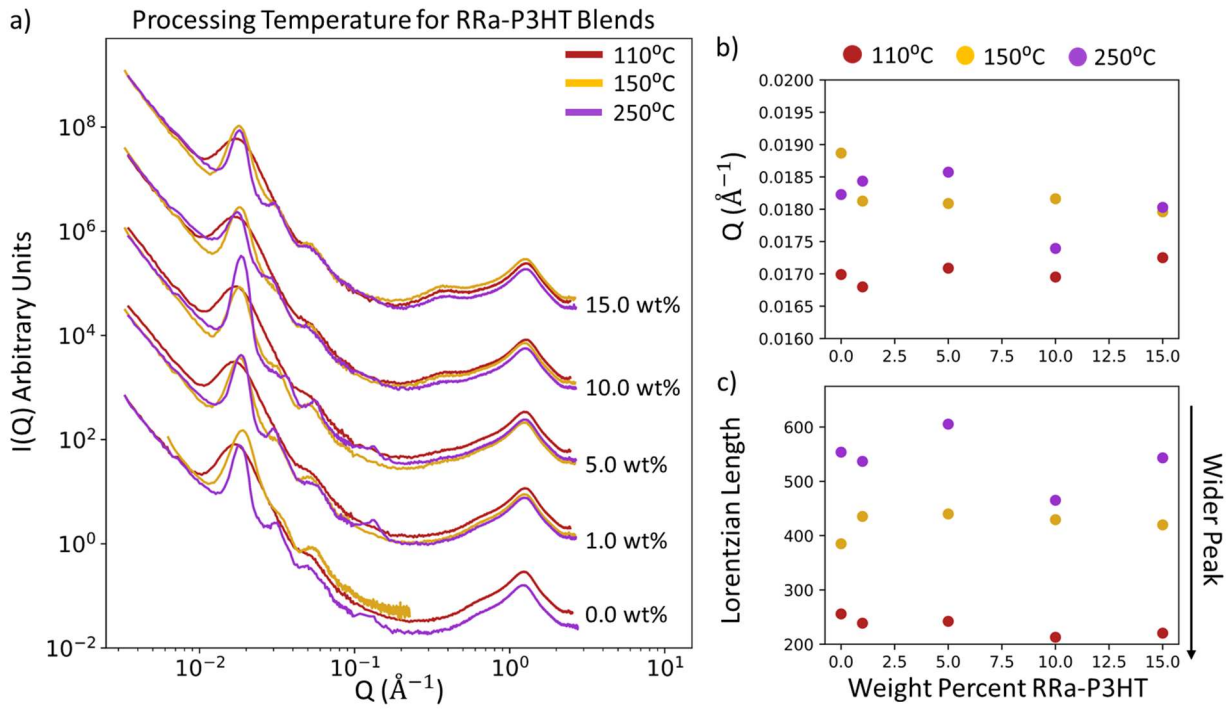

Figure 4.10: a) SAXS data of 63kDa RRa-P3HT and PS-PI-PS blends, labeled by wt % of RRa-P3HT added to system, and collected at three different heat pressing temperatures. Data is arbitrarily shifted to separate samples by wt %. b) Peak position parameters from broad peak fits of the .018 Å^{-1} peak with colors dictated by legend above. c) Lorentzian length parameters from broad peak fits of the .018 Å^{-1} peak with colors dictated by legend above.

When peak indexing and phase identification is performed on the 250 ºC RRa-P3HT samples, we see the same trend observed with the RRe-P3HT samples as seen in **Figure 4.10**. The pure PS-PI-PS is identical to the one used in the RRe-P3HT blends and is identified as hexagonally packed cylinders. As small amounts of RRa-P3HT (1 wt %) are added into the blend, peaks sharpen, and the phase is maintained as hexagonally packed cylinders. At a loading of ~5 wt % RRa-P3HT, the peak at ~0.032 Å^{-1} disappears and a peak at ~0.037 Å^{-1} emerges, consistent with a lamellar. At high loadings of RRa-P3HT, the peaks widen, and the ratios return again towards hexagonally packed cylinder phases.

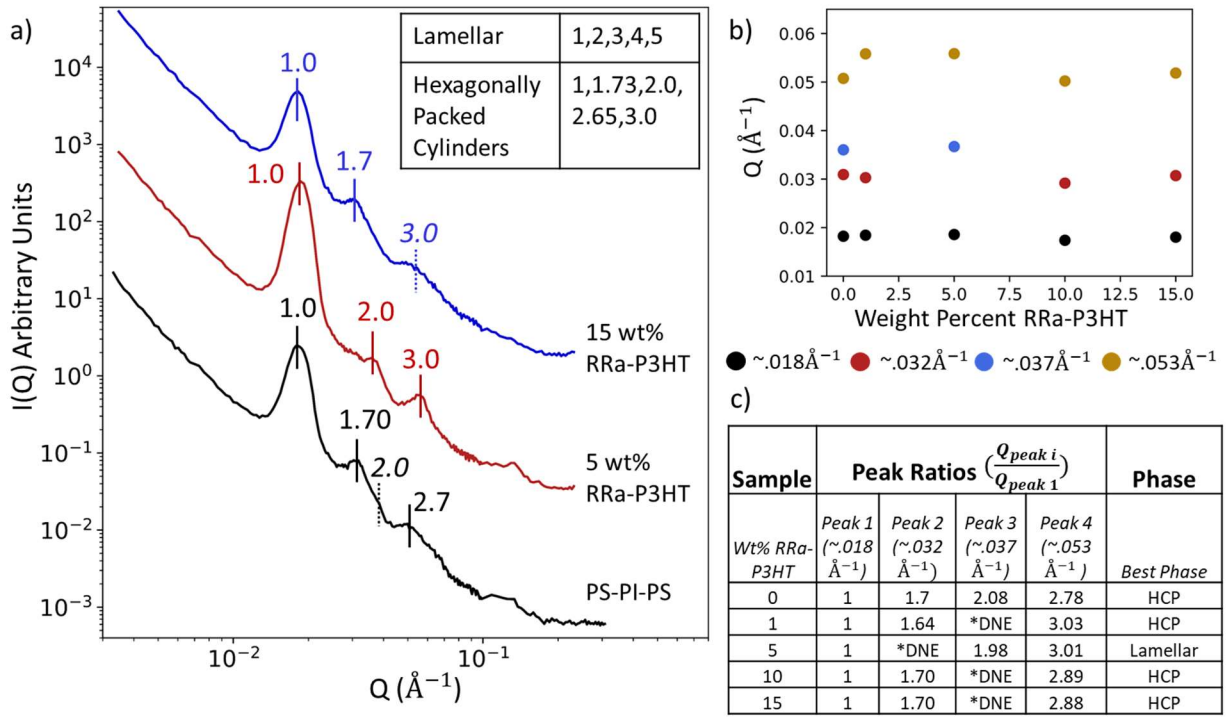

c)

Sample	Peak Ratios ($\frac{Q_{peak\ i}}{Q_{peak\ 1}}$)				Phase
Wt% RRa-P3HT	*Peak 1 (~.018 Å^{-1})*	*Peak 2 (~.032 Å^{-1})*	*Peak 3 (~.037 Å^{-1})*	*Peak 4 (~.053 Å^{-1})*	*Best Phase*
0	1	1.7	2.08	2.78	HCP
1	1	1.64	*DNE	3.03	HCP
5	1	*DNE	1.98	3.01	Lamellar
10	1	1.70	*DNE	2.89	HCP
15	1	1.70	*DNE	2.88	HCP

Figure 4.11: SAXS data of selected a) 63 kDa RRa-P3HT/PS-PI-PS blends labeled by wt % of RRe-P3HT added to system and collected at 250 ºC. Data is arbitrarily shifted to separate samples into wt %. Dotted lines are used where peaks are expected due to ratio but are not able to be concretely fit. b) Peak position parameters from broad peak fits. c) table all calculated peak ratio and determined phase.

4.4 Conclusions

We were able to determine that the processing temperature of a polymeric blend has a significant impact on the morphology, specifically the extent of organization of the elastomer matrix. In the solution state we do not see any assembly in blends, and the structures observed are described well by free chains of the individual components **(Figure 4.4).** Due to this we know that structures observed in the solid forms are formed over the course of evaporation and drying and are not solely a result of interactions while in the solution state. During solution casting, structures are largely determined by kinetic effects of solvent evaporation and the arrest of molecular motions. This is generally insufficient to create clear domain segregation and long-range structural assembly. As seen in **Figure 4.4** and described in **Figure 4.12a**, when processed at low temperatures (110 ºC) the glass transition temperature of the glassy polystyrene (95-105 ºC) is barely surpassed and does not provide the required energy or time that is needed to further

segregate and assemble. This results in a disordered structure that is difficult to identify due to the lack of organized diffraction peaks. Additionally, the cutting and stacking throughout processing without the temperature necessary to allow the PS to be rearranged, leads to more disorder than the solvent cast analog. Higher temperatures facilitate the incorporation of P3HT into the structure of the PS-PI-PS and for the system to assemble and order fully, annealing at higher temperatures is needed. We see improvements in order at the intermediate temperatures (150 and 200 ºC) where the structure becomes more organized and regular. However, when processing at 250 ºC we see the greatest increases in ordering as well as the clarification of phase structures (i.e., close-packed hexagonal cylinders and lamellar phases) due to the formation of higher-order diffraction peaks.

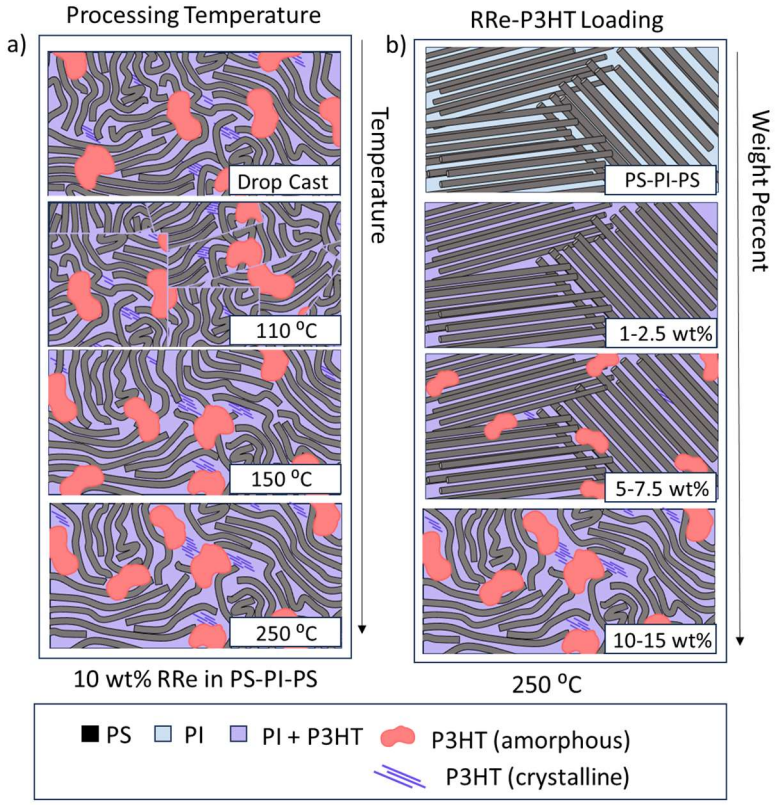

Figure 4.12: Schematic describing the morphology of RRe-P3HT and PS-PI-PS blends as a) RRe-P3HT is added in increasing weight percents to PS-PI-PS, processed at 250 ºC and b) 10 wt % RRe-P3HT is processed at varying temperatures.

We identify the phase of pure PS-PI-PS as hexagonally packed cylinders, consisting of cylinders of polystyrene assembled within a matrix of polyisoprene (**Figure 4.5**). This is consistent with the material architecture and phase-diagrams outlined in the literature[30]. With the addition of RRe-P3HT to the blend, there are evident changes to the morphology of the matrix as a function

of concentration (**Figure 4.6**). We anticipate that P3HT incorporation occurs primarily in the polyisoprene domains due to the more favorable Flory interaction coefficient between P3HT and PI, which is estimated between 0.02 and 0.23[75–77] . The Flory interaction coefficient between PS and P3HT, which is estimated at 0.48, favors phase separation and previous neutron scattering work indeed demonstrated the large-scale phase segregation of P3HT and PS[74,78].

As shown in **Figure 4.12b**, the order and regularity in the system increases at low loadings of conjugated polymer in the blend system. At ~5 wt % loading of RRe-P3HT in PS-PI-PS, a gradual shift occurs from a hexagonally packed cylinder phase to a lamellar-rich phase. Indexing this phase shift over a series of intermediate loadings (2.5 - 10 wt %) is challenging due to these phases coexisting over a broad range. Still, a clear loss of hexagonally packed cylinder peaks for the 5 wt % sample signals a lamellar phase dominated material at this point **(Figure 4.5)**. We anticipate that ~ 5 wt % marks a critical concentration where large-scale segregation emerges, this is confirmed in the appearance of the low-Q feature seen in the USAXS data in **Figure 4.8.**

Increasing concentration past this loading again changes the bulk of the matrix phase from lamellar-rich to hexagonal cylinders. At 7.5 wt% and 10 wt% RRe-P3HT, key peaks for hexagonally packed cylinders reemerge but disorder is increasingly present in the system as noted by the reduced sharpness of the peaks. At the highest loadings (12.5 and 15 wt %) we observe an increase in peak widths indicating an overloading of conjugated polymer in the system leading to increasing disorder in the arrangement of the cylinders and the increase in size of phase-separated RRe-P3HT domains (**Figure 4.8**). This suggests that there is a critical concentration around 5 wt% where there are significant changes in the morphology while incorporating into the PS-PI-PS templated structure.

In this work we utilized SANS, USAXS and SAXS to characterize complex blends of conjugated polymers and elastomeric copolymers while understanding the effect of temperature, composition, and processing. We determined that temperature is a vital consideration in processing blends of CP and thermoplastic elastomers, with increased temperature allowing for system wide changes. Higher temperatures allow for increased consistency of the structures as well as increased incorporation of additives into the established structure. The addition of P3HT additives modifies the phase of the matrix elastomer system with a critical concentration around 5 wt % that marks the maximum amount of P3HT that can be added while preserving high order in blends. A second threshold is reached around 10 wt % where the system increases in disorder, likely due to

overloading and macro phase separation. This work aids in understanding the fundamental structural morphology of complex copolymer blends, and additional work will be necessary to understand how additional processing changes affect the morphology and how these structural modifications can be utilized for property optimization.

4.5 References

1. Sekine, T. *et al.* Fully Printed Wearable Vital Sensor for Human Pulse Rate Monitoring using Ferroelectric Polymer. *Scientific Reports 2018 8:1* **8**, 1–10 (2018).
2. Ha, M., Lim, S. & Ko, H. Wearable and flexible sensors for user-interactive health-monitoring devices. *J Mater Chem B* **6**, 4043–4064 (2018).
3. Amjadi, M. *et al.* Stretchable, Skin-Mountable, and Wearable Strain Sensors and Their Potential Applications: A Review. *Adv Funct Mater* **26**, 1678–1698 (2016).
4. Wang, S., Oh, J. Y., Xu, J., Tran, H. & Bao, Z. Skin-Inspired Electronics: An Emerging Paradigm. *Acc Chem Res* **51**, 1033–1045 (2018).
5. Khalili, N., Naguib, H. E. & Kwon, R. H. A constriction resistance model of conjugated polymer based piezoresistive sensors for electronic skin applications. *Soft Matter* **12**, 4180–4189 (2016).
6. Benight, S. J., Wang, C., Tok, J. B. H. & Bao, Z. Stretchable and self-healing polymers and devices for electronic skin. *Prog Polym Sci* **38**, 1961–1977 (2013).
7. Jeon, K. H. & Park, J. W. Light-Emitting Polymer Blended with Elastomers for Stretchable Polymer Light-Emitting Diodes. *Macromolecules* **55**, 8311–8320 (2022).
8. White, M. S. *et al.* Ultrathin, highly flexible and stretchable PLEDs. *Nature Photonics 2013 7:10* **7**, 811–816 (2013).
9. Koo, J. H., Kim, D. C., Shim, H. J., Kim, T. H. & Kim, D. H. Flexible and Stretchable Smart Display: Materials, Fabrication, Device Design, and System Integration. *Adv Funct Mater* **28**, 1801834 (2018).
10. Tait, J. G. *et al.* Spray coated high-conductivity PEDOT: PSS transparent electrodes for stretchable and mechanically robust organic solar cells. *Solar Energy Materials and Solar Cells* **110**, 98–106 (2013).
11. Lee, C. P. *et al.* A paper-based electrode using a graphene dot/PEDOT: PSS composite for flexible solar cells. *Nano Energy* **36**, 260–267 (2017).
12. Yang, Z. *et al.* Stretchable, Wearable Dye-Sensitized Solar Cells. *Advanced Materials* **26**, 2643–2647 (2014).
13. Kang, D. Y. *et al.* Scalable microfabrication procedures for adhesive-integrated flexible and stretchable electronic sensors. *Sensors (Switzerland)* **15**, 23459–23476 (2015).
14. Wang, L., Zhang, Y., Pan, J. & Peng, H. Stretchable lithium-air batteries for wearable electronics. *J Mater Chem A Mater* **4**, 13419–13424 (2016).
15. Song, E. *et al.* Stretchable and Transparent Organic Semiconducting Thin Film with Conjugated Polymer Nanowires Embedded in an Elastomeric Matrix. *Adv Electron Mater* **2**, 1500250 (2016).
16. Zhu, Y. *et al.* Ag-Doped PEDOT: PSS/CNT composites for thin-film all-solid-state supercapacitors with a stretchability of 480%. *J Mater Chem A Mater* **6**, 941–947 (2018).
17. Song, R. *et al.* Unveiling the Stress−Strain Behavior of Conjugated Polymer Thin Films for Stretchable Device Applications. (2020) doi: 10.1021/acs.macromol.9b02573.
18. Liu, D. *et al.* In Situ Study of Molecular Aggregation in Conjugated Polymer/Elastomer Blends toward Stretchable Electronics. *Macromolecules* **55**, 297–308 (2022).
19. Billiet, S., Hillewaere, X. K. D., Teixeira, R. F. A. & Du Prez, F. E. Chemistry of Crosslinking Processes for Self-Healing Polymers. *Macromol Rapid Commun* **34**, 290–309 (2013).
20. Burfield, D. R. Polymer Glass Transition Temperatures. *Burfield, D. R. Polym. Commun* **61**, 2 (1984).
21. Rieger, J. The glass transition temperature of polystyrene. Results of a round robin test. *Journal of Thermal Analysis* **46**, 965–972 (1996).

22. Inoue, T., Moritani, M., Hashimoto, T. & Kawai, H. Deformation Mechanism of Elastomeric Block Copolymers Having Spherical Domains of Hard Segments under Uniaxial Tensile Stress1. *Macromolecules* **8**, 579 (1970).
23. Eugene Helfand & Z. R. Wasserman. Block Copolymer Theory. 6. Cylindrical Domains. *American Chemical Society* 994–998 (1980).
24. Widin, J. M., Schmitt, A. K., Schmitt, A. L., Im, K. & Mahanthappa, M. K. Unexpected consequences of block polydispersity on the self-assembly of ABA triblock copolymers. *J Am Chem Soc* **134**, 3834–3844 (2012).
25. Hadziioannou, G. & Skoulios, A. Molecular Weight Dependence of Lamellar Structure in Styrene/Isoprene Two-and Three-Block Copolymers. *Separation Methods in Biochemistry* **131**, 533 (1970).
26. Sakurai, S. *et al.* Preferential Orientation of Lamellar Microdomains Induced by Uniaxial Stretching of Cross-Linked Polystyrene-block-polybutadiene-block-polystyrene Triblock Copolymer. (2001) doi:10.1021/ma002123.
27. Vukovic, I., Brinke, G. Ten & Loos, K. Block copolymer template-directed synthesis of well-ordered metallic nanostructures. *Polymer (Guildf)* **54**, 2591–2605 (2013).
28. Laurer, J. H. *et al.* Microstructural analysis of a cubic bicontinuous morphology in a neat SIS triblock copolymer. *Macromolecules* **30**, 3938–3941 (1997).
29. Pedemonte, E., Turturro, A., Bianchi, U. & Devetta, P. The cubic structure of a SIS three block copolymer. *Polymer (Guildf)* **14**, 145–150 (1973).
30. Matsen, M. W. & Bates, F. S. Unifying weak- and strong-segregation block copolymer theories. *Macromolecules* **29**, 1091–1098 (1996).
31. Sakurai, S., Umeda, H., Taie, K. & Nomura, S. Kinetics of morphological transition in Polystyrene-block-polybutadiene-block-polystyrene triblock copolymer melt. *J. Chem. Phys* **105**, 8902–8908 (1996).
32. Qiao, L., Leibig, C., Hahn, S. F. & Winey, K. I. Isolating the effects of morphology and chain architecture on the mechanical properties of triblock copolymers. *Ind Eng Chem Res* **45**, 5598–5602 (2006).
33. Inoue T, Soen T, Hashimoto T & Kawai H. Thermodynamic interpretation of domain structure in solvent-cast films of A–B type block copolymers of styrene and isoprene. *Journal of Polymer Science Part A-2: Polymer Physics* **7**, 1283–1301 (1969).
34. Bokobza, L. Multiwall carbon nanotube elastomeric composites: A review. *Polymer (Guildf)* **48**, 4907–4920 (2007).
35. Perez, L. D., Zuluaga, M. A., Kyu, T., Mark, J. E. & Lopez, B. L. Preparation, characterization, and physical properties of multiwall carbon nanotube/elastomer composites. *Polym Eng Sci* **49**, 866–874 (2009).
36. Xu, J. *et al.* Highly stretchable polymer semiconductor films through the nanoconfinement effect. *Science (1979)* **355**, (2017).
37. Choi, D. *et al.* Elastomer-Polymer Semiconductor Blends for High-Performance Stretchable Charge Transport Networks. *Chemistry of Materials* **28**, 1196–1204 (2016).
38. Carpi, F., Gallone, G., Galantini, F., De Rossi Carpi, D. F. & De Rossi, D. Enhancement of the electromechanical transduction properties of a silicone elastomer by blending with a conjugated polymer. *https://doi.org/10.1117/12.776641* **6927**, 47–57 (2008).
39. Liu, D. *et al.* In Situ Study of Molecular Aggregation in Conjugated Polymer/ Elastomer Blends toward Stretchable Electronics. (2021) doi: 10.1021/acs.macromol.1c01537.
40. Qiu, Z., Hammer, B. A. G. & Müllen, K. Conjugated polymers – Problems and promises. *Progress in Polymer Science* vol. 100 Preprint at https://doi.org/10.1016/j.progpolymsci.2019.101179 (2020).
41. Savagatrup, S., Printz, A. D., Rodriquez, D. & Lipomi, D. J. Best of both worlds: Conjugated polymers exhibiting good photovoltaic behavior and high tensile elasticity. *Macromolecules* **47**, 1981–1992 (2014).
42. Wang, M., Baek, P., Akbarinejad, A., Barker, D. & Travas-Sejdic, J. Conjugated polymers and composites for stretchable organic electronics. *J Mater Chem C Mater* **7**, 5534–5552 (2019).
43. Shim, H. J., Sunwoo, S. H., Kim, Y., Koo, J. H. & Kim, D. H. Functionalized Elastomers for Intrinsically Soft and Biointegrated Electronics. *Adv Healthc Mater* **10**, 2002105 (2021).

44. Shin, M. *et al.* Highly Stretchable Polymer Transistors Consisting Entirely of Stretchable Device Components. *Advanced Materials* **26**, 3706–3711 (2014).
45. Wang, M., Baek, P., Akbarinejad, A., Barker, D. & Travas-Sejdic, J. Conjugated polymers and composites for stretchable organic electronics. *J Mater Chem C Mater* **7**, 5534–5552 (2019).
46. Güldal, N. S. *et al.* Real-time evaluation of thin film drying kinetics using an advanced, multi-probe optical setup. *J Mater Chem C Mater* **4**, 2178–2186 (2016).
47. Cummings, J., Lowengrub, J. S., Sumpter, B. G., Wise, S. M. & Kumar, R. Modeling solvent evaporation during thin film formation in phase separating polymer mixtures. *Soft Matter* **14**, 1833–1846 (2018).
48. Shi, W. *et al.* Morphology re-entry in asymmetric PS-PI-PS' triblock copolymer and PS homopolymer blends. *J Polym Sci B Polym Phys* **54**, 169–179 (2016).
49. Albalak, R. J., Thomas, E. L. & Capel, M. S. Thermal annealing of roll-cast triblock copolymer films. *Polymer (Guildf)* **38**, 3819–3825 (1997).
50. Hadziioannou, G. & Skoulios, A. Melting of Styrene/isoprene Block Copolymers as a Function of Temperature and Time. *Physics of Glassy Polymers* **148**, 3483 (1975).
51. Roesing, M., Howell, J. & Boucher, D. Solubility Characteristics of Poly(3-hexylthiophene). *J. Polym. Sci., Part B: Polym. Phys* **55**, 1075–1087 (2017).
52. Teresa García, M., Gracia, I., Duque, G., de Lucas, A. & Francisco Rodríguez, J. Study of the solubility and stability of polystyrene wastes in a dissolution recycling process. (2009) doi: 10.1016/j.wasman.2009.01.001.
53. Yamazaki, H., Nagasawa, T., Choi, W. & Endo, T. Transformation of vulcanized natural rubber into lower molecular weight polymers and their application to grafted copolymer synthesis with some vinyl monomers. *J Appl Polym Sci* **101**, 4003–4010 (2006).
54. Doucet, M. *et al.* SasView. Preprint at (2022).
55. Doucet, M. *et al.* Sasmodels. Preprint at (2020).
56. Kienzle, P. A. (University of M. C. P., Krycka, J., Patel, N. & Sahin, I. Bumps. Preprint at (2011).
57. Ilavsky, J. *et al.* Development of combined microstructure and structure characterization facility for in situ and operando studies at the Advanced Photon Source. *urn: issn:1600-5767* **51**, 867–882 (2018).
58. Thing files for USAXS 48 Solid Film Holder by dpozzo - Thingiverse. https://www.thingiverse.com/thing:4639006/files.
59. Ilavsky, J. & IUCr. Nika: software for two-dimensional data reduction. *urn: issn:0021-8898* **45**, 324–328 (2012).
60. Kline, S. R. & IUCr. Reduction and analysis of SANS and USANS data using IGOR Pro. *urn: issn:0021-8898* **39**, 895–900 (2006).
61. Wood, K. *et al.* QUOKKA, the pinhole small-angle neutron scattering instrument at the OPAL Research Reactor, Australia: design, performance, operation and scientific highlights. *urn: issn:1600-5767* **51**, 294–314 (2018).
62. broad_peak — SasView 5.0.5 documentation. https://www.sasview.org/docs/user/models/broad_peak.html.
63. Hammouda, B. & IUCr. A new Guinier–Porod model. *urn: issn:0021-8898* **43**, 716–719 (2010).
64. Pedersen, J. S. & Schurtenberger, P. Scattering functions of semiflexible polymers with and without excluded volume effects. *Macromolecules* **29**, 7602–7612 (1996).
65. Xi, Y., Wolf, C. M. & Pozzo, L. D. Self-assembly of donor–acceptor conjugated polymers induced by miscible 'poor' solvents. *Soft Matter* **15**, 1799–1812 (2019).
66. Harris, C. R. *et al.* Array programming with NumPy. *Nature* **585**, 357 (2020).
67. Mckinney, W. Data Structures for Statistical Computing in Python. (2010).
68. Hunter, J. D. Matplotlib: A 2D graphics environment. *Comput Sci Eng* **9**, 90–95 (2007).
69. McNeill, I. C. & Gupta, S. N. Degradation of Blends - Part XI. Blends of Polystyrene with Polyisoprene. *Polym Degrad Stab* (1980).
70. Mcneill, I. C. Thermal degradation of polystyrene in different environments. *Die Angewandte Makromolekulare Chemie* **247**, 179–195 (1997).

71. Rodrigues, A. *et al.* Thermal stability of P3HT and P3HT: PCBM blends in the molten state. *Polym Test* **32**, 1192–1201 (2013).
72. Georgopanos, P. *et al.* Analysis of glass transition and relaxation processes of low molecular weight polystyrene-b-polyisoprene diblock copolymers. *Colloid Polym Sci* **292**, 1877–1891 (2014).
73. Balko, J., Lohwasser, R. H., Sommer, M., Thelakkat, M. & Thurn-Albrecht, T. Determination of the Crystallinity of Semicrystalline Poly(3-hexylthiophene) by Means of Wide-Angle X-ray Scattering. **21**, 38 (2023).
74. Wolf, C. M. *et al.* Blend Morphology in Polythiophene−Polystyrene Composites from Neutron and X-ray Scattering. doi: 10.1021/acs.macromol.0c02512.
75. Olsen, B. D., Shah, M., Ganesan, V. & Segalman, R. A. Universalization of the phase diagram for a model rod-coil diblock copolymer. *Macromolecules* **41**, 6809–6817 (2008).
76. Lim, H., Chao, C.-Y. & Su, W.-F. Modulating Crystallinity of Poly(3-hexylthiophene) via Microphase Separation of Poly(3-hexylthiophene) −Polyisoprene Block Copolymers. (2015) doi:10.1021/ma502417w.
77. Lin, S. H., Wu, S. J., Ho, C. C. & Su, W. F. Rational design of versatile self-assembly morphology of rod-coil block copolymer. *Macromolecules* **46**, 2725–2732 (2013).
78. Emerson, J. A., Toolan, D. T. W., Howse, J. R., Furst, E. M. & Epps, T. H. Determination of Solvent–Polymer and Polymer–Polymer Flory–Huggins Interaction Parameters for Poly(3-hexylthiophene) via Solvent Vapor Swelling. *Macromolecules* **46**, 6533–6540 (2013).

Chapter 5: Processing Effects on Blends of PS-PI-PS/Conjugated Polymers

5.1 Introduction

For all polymers, processing is an important consideration in the utilization and understanding of the final product. There are many processing techniques used in industry, including spin coating, electro spinning, blade coating, drop casting, and heat molding[1–4]. Each method modifies the processing conditions and changes the way the polymer is handled, resulting in a variety of final structures and functionalities. This allows researchers to utilize specific processing methods to enhance desired properties of their final blends, for example, spin coating is often used to encourage nanofiber formation in conjugated polymers in hopes of increasing conductivity[5,6]. Our focus in this work is to understand the interactions between each component of a well-mixed thick film blended system and how those interactions encourage specific microstructures. The blends discussed in Chapter 4 utilized heat pressing as a method of creating fully homogeneous blends, and while we focused mostly on identifying structural changes with the increase of conjugated polymer, we also identified changes when the pressing temperature was modified. This solidifies the need to understand what changes the processing method themselves can induce in a system before we can isolate the extent and impact of compositional changes.

As mentioned in Chapter 4, the competition between the kinetic and thermodynamic timescales may result in non-ideal kinetically arrested states. For instance, during solvent evaporation, the composition and physical properties of samples changes rapidly and unevenly, resulting in phase separation, and solvent-dependent formation of complex structures[7–9]. In simulations, Cummings et al depicts the phase segregation of drying solutions through multiple thermodynamic drivers and model how the evaporation of all solvent can lock in kinetically frozen structures[8]. Altering the solvent properties can change this kinetic and thermodynamic relationship, modifying how the dried polymer is arranged. There have also been investigations into how, with complex multi-component systems, solvent quality can impact on the phase formed by the segregated domains. This has been seen in copolymers similar to the ones discussed in this work, where the polymer block ratios have a strong influence on the specific phase that is formed, but processing variables can affect the final structure by creating kinetically arrested states and/or altering their macroscopic orientation. For styrene weight percentages between 20-40 wt %, solvent choice was found to be exceptionally important in determining phase structure, with samples tending to create continuous polystyrene microdomains when the solvent is more

compatible with polystyrene than with polyisoprene[10,11]. Qiao et al found that changing the solvent while casting SIS or its inverse copolymer (i.e., polyisoprene-b-polystyrene-b-polyisoprene) at fixed molecular weights and compositions, the phase structure could be changed between lamellar, cylindrical and gyroidal[9]. We also observed solvent specific changes in the polystyrene/poly(3-hexylthiophene) blends discussed in Chapter 3, with compositionally identical samples cast from different solvents displaying differences in morphology and conductive properties[12].

These processing changes include post-processing modifications, as methods such as thermal and solvent annealing have been used previously to align and expand ordered packing structures in triblock co-polymers[3], modify output of operating polymer diodes[13], and enhance desired mechanical properties in a common poly(lactic acid) processing technique[14]. A possible side effect of processing that requires heat, or pressure applied in a specific direction can cause structures in the polymer to align. Alignment can occur naturally in some samples, and may be thermodynamically desirable, but may also be artificially added through processing conditions. This is often observed in industrial extrusion processing, in which polymers are heated and then forced through a die mold, often causing extreme stress within the polymer, which is maintained through cooling[15]. This stress can be removed through thermal annealing. This process of heating above transition points, then maintaining the applied heat for enough time for the chains to re-orient into a more thermodynamically stable state allows for a stronger final product[14].

In systems similar to the ones addressed here, Sakurai et.al. studied the effect of annealing on polystyrene-polybutadiene-polystyrene (SBS) elastomer, a closely related thermoplastic elastomer, and found that cast films that initially formed hexagonal cylinders would gradually transition into lamellae upon annealing above the glass transition of polystyrene[16]. Additionally, Hadziioannou et al found that a PS-PI diblock copolymer formed lamellae of ~600 Å wide periods at room temperatures, and these expanded to 710 Å after annealing for 1000 hours at 182 ºC. When exposed to higher temperatures (255 ºC) the lamellar spacing reached values over 1000 Å within just 10 hours[17].

In this work we look to explore various processing techniques using the previously investigated elastomeric polymer blends in order to understand how a complex triblock copolymer/conjugated polymer blends system changes and can be manipulated to encourage or dissuade various configurations. Understanding changes to the structure of polymer blends

throughout processing stages provides valuable insights into how specific steps and integration of conjugated polymer components affect the performance of composite electronic materials.

5.2 Materials and Methods

5.2.1 Materials

Regiorandom poly(3-hexylthiophene) (RRa-P3HT) (MW = 63 kg mol-1, Đ = 2.4, Product 4007) and regioregular poly(3-hexylthiophene) (RRe-P3HT) were purchased from Rieke Metals (Lincoln, NE USA). Three different molecular weights of RRe-P3HT were used: Lot BLS26-16 (RRe42) (MW = 42 kg mol-1, Đ = 2.0, RR = 90), Lot PTL43-54 (RRe60) (MW = 60 kg mol-1, Đ = 3.0, RR = 91) and Lot BLS26-96 (RRe77) (MW = 77 kg mol-1, Đ = 2.4, RR = 94). Polystyrene-block-polyisoprene-block-polystyrene (PS-PI-PS) was purchased from Aldrich Chemistry (St. Louis, MO USA). The PS-PI-PS polymer is a 22% styrene $A_{229}B_{2490}A_{229}$ tri-block-copolymer with a molecular weight of 217 kDa as determined using Gel Permeation Chromatography (GPC). Chloroform and toluene were purchased from Fisher Chemical (Waltham, MA USA). For SANS experiments, fully deuterated chloroform was purchased from Cambridge Isotope Laboratories, Inc. (Tewksbury, MA USA). All chemicals were used as received.

5.2.2 Baseline Heat-Pressed Film Preparation

All solid blend films were prepared in accordance with the schematic diagram shown in **Figure 5.1a**. Carefully weighed portions of conjugated polymer (i.e. RRe-P3HT or RRa-P3HT) were co-dissolved until fully homogenous with the elastomeric polymer (PS-PI-PS) in chloroform, which is a good solvent for all polymers involved at 50 ºC [18–20]. Each solution was poured over a watch glass on top of a hot plate heated to 50 ºC, covered loosely with aluminum foil to enable a slow evaporation, and allowed to fully dry (~30 minutes). Films were then peeled off the watch glass and left in a fume hood to remove any remaining solvent in the system overnight. The dry polymer blend was then heat pressed using a D16 Digital Combo Swing-Away Press from Geo Knight & Co (Brockton, MA). For the radially pressed samples, shown in **Figure 5.1b**, the polymers were pressed into circular steel precision shims from McMaster Carr (Elmhurst, IL) with a thickness of 254 μm and an inner diameter of 15 mm at the chosen temperature. All temperatures were measured by a type-K thermocouple and recorded with an accuracy of ±2 ºC. During pressing, each sample was sandwiched between thermally conductive Kapton and two polished stainless-steel plates to create a smooth and even film. After each pressing, the film was cut, stacked, and pressed again at the same temperature. The total time for each of the three presses

was 5 min, 5 min, 15 min, respectively. Films were then allowed to cool slowly to room temperature over a period of 60 minutes. This repeat pressing process was used to ensure that samples were uniform and to eliminate segregation that could have occurred during drying. Films were then removed from the metal shims and stored at room temperature prior to structural measurements.

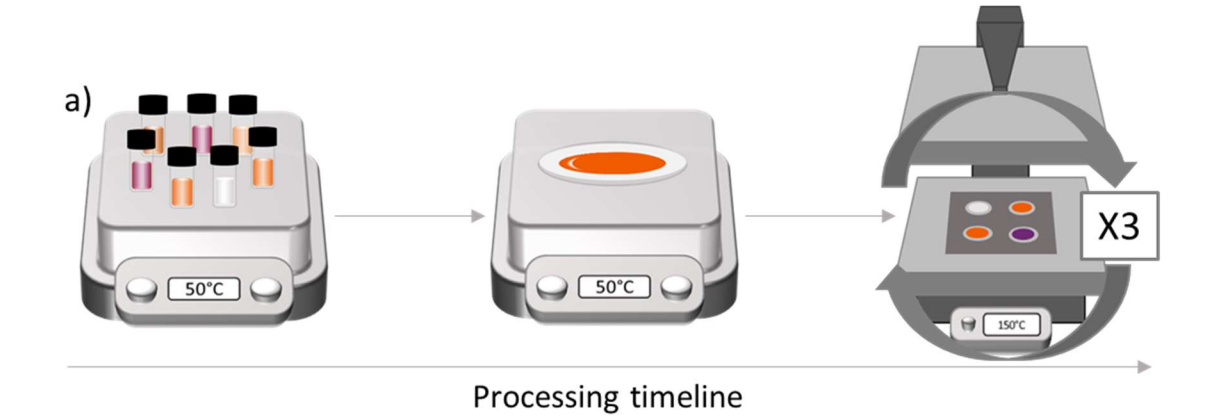

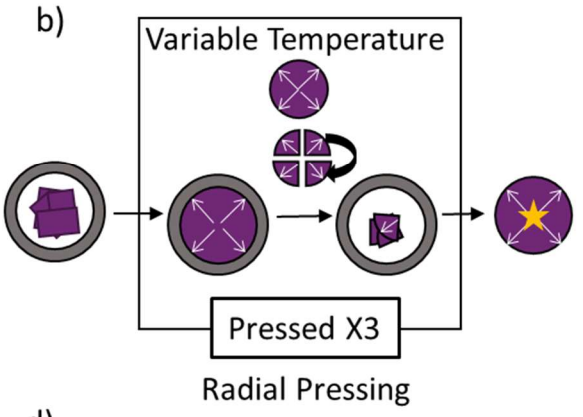

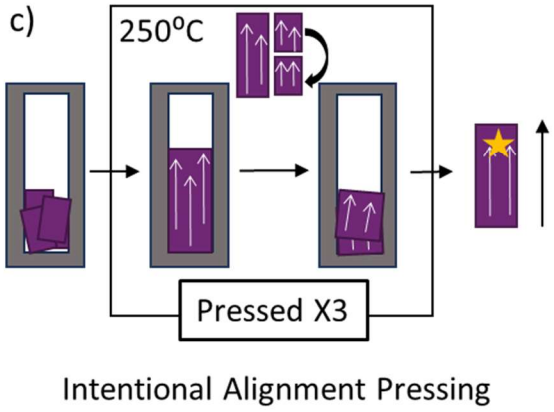

d)

(min)	1st Press	2nd Press	3rd Press	Rest Time
Short	1	1	5	30
Baseline	5	5	15	30
Long	15	15	45	30

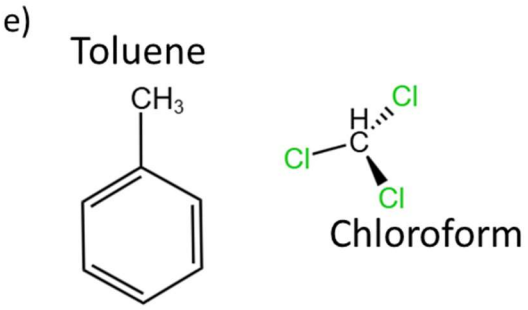

Figure 5.1: Schematics for sample creation for a) the full processing timeline, including co-dissolving of polymers into a solvent on a hotplate set at 50 ºC, solvent evaporating in a foil insulated watch glass until fully dry, and being pressed at a set temperature into a shim. Samples are b) radially pressed in circular shims with samples being cut and restacked to be pressed 3 times

before being measured at the starred location or c) intentionally aligned in a rectangular shim with the samples being cut and restacked with the flow direction preserved to be pressed 3 times before being analyzed at the starred location. d) table of pressing times for three separate time ranges, and e) molecular structures of toluene and chloroform, the solvents used in the solvent variation experiments.

5.2.3 Processing Modifications

Samples Taken from Each Stage of Processing

A series of samples were made with cuttings taken from the bulk at each critical stage of the processing method. Aliquots were taken after solution cast, the first press, the second press, and the final press. This allows the tracking of morphological changes over the course of the processing method.

Pressing Time Variation

Pressing time was modified for a series of samples, with times longer and shorter than the baseline processing time of 5 min, 5 min, 15 min. This variation in time was performed at 150 ºC but comparisons can also be made to the structures formed at 110 ºC and 250 ºC with the baseline pressing time. A breakdown of the times and terms are provided in **Figure 5.1d.**

Casting Solvent Quality

A set of samples were co-dissolved in toluene, a 'poor' solvent for all components, instead of the chloroform used in the baseline samples. The toluene solutions evaporated slower than the chloroform solutions, requiring an hour to fully dry as opposed to 30 minutes. Structures of chloroform and toluene are provided in **Figure 5.1e.**

Drying with Vacuum

A set of samples were processed with the use of a vacuum oven. These samples were co-dissolved, solution cast, and evaporated in the same way as the baseline samples. Once the solution cast samples were removed from the watch glass, they were placed under vacuum at 25 ºC for 15 hours. This ensured that all remnants of solvent were removed from the samples before being heat-pressed using the same methods as the baseline samples.

Flow Aligned Processed Samples

Processing for flow-aligned samples is shown in **Figure 5.1c**. These samples were arranged at one side of a rectangular shim (20.00mm long x 2.75mm wide x 0.45 mm high) while sandwiched between thermally conductive Kapton sheets and two polished stainless-steel plates.

All intentionally aligned samples were pressed at 250 ºC. The films were also cut and stacked, ensuring the flow direction was maintained, and pressed three total times for 5 min, 5 min, 15 min, before being allowed to cool slowly to room temperature over 60 minutes. The films were then gently removed from the rectangular metal shims and stored at room temperature for measurements. The intentionally aligned films were measured at the edge of the flow front, where the sample was forced to flow upon pressing.

5.2.4 Post-Processing Annealing

Two types of annealed samples were prepared. The first set of samples were prepared and pressed in the same way as the baseline samples. The cuts of the fully processed samples were then heated in a vacuum oven at 120-130 °C for a set length of time (4hr, 24hr). A separate cutting was reserved as an unprocessed film control (RT).

The second set of annealed samples were prepared and solution cast using the same process as the baseline samples. Once cast, cuttings underwent various heat treatments without any pressing involved. Samples of all drops-cast films were set aside as references for the material without applied processing. The films were then laid over Kapton sheets and heated in a preheated oven (100ºC, 150ºC, 250ºC) for various lengths of time (10 min, 25 min, 50 min).

5.2.5 USAXS and SAXS

Ultra-small, small, and wide-angle x-ray scattering (USAXS, SAXS, and WAXS) were collected at the University of Washington using a Xenocs (Grenoble, France) Xeuss 3.0 SAXS instrument. This is a pinhole collimated laboratory SAXS instrument equipped with a copper microfocus x-ray source. Samples were collected at three sample-to-detector distances to obtain a wide Q-range. WAXS data (sample to detector distance of 0.07 m) was collected for 60 s, SAXS (sample to detector distance of 0.9 m) for 60 s, and ESAXS (sample to detector distance of 1.8 m) for 360 seconds. Samples were mounted on a 48-sample holder to enable automated processing of multiple samples. The data was reduced, averaged (except when analyzed for flow-alignment), and combined to a unified dataset that will be referred to as 'SAXS data' through this work. Fits and analyses were then conducted using SasView[21]/sasmodels[22] and bumps[23] packages for Python.

2.5.6. Scattering Data Analysis

Once fully reduced, data was exported, and further analyzed using SasView[21]/sasmodels[22] and bumps[23] packages for Python. Features in the SAXS data were fit with shape independent models to extract structural parameters when possible.

Peaks in the SAXS region, which correspond to nanometer scale self-segregation of the block-copolymer matrix, were fit using a generalized broad peak model[24].

$$I(Q) = \frac{A}{q^n} + \frac{C}{1 + (|Q - Q_0|\xi)^m} + B \tag{5.1}$$

Here, A is the Porod scaling factor, n is the Porod exponent, C is a Lorentzian scaling factor, m is the exponent of Q, ξ is the Lorentzian screening length, and B is a flat background. This model does not assume any given structure (e.g., lamellar, cylindrical, cubic) and is appropriate for samples with variable ranges of order that may also result in changing phases.

Alignment factor is a metric to describe the extent of alignment of scattering structures within a sample from 0 (isotropic) to 100 (perfectly aligned). Calculations for the alignment factor were done in XSACT software which extracts alignment parameters from a tensor approach, for which equations and tensors are provided below.

$$\Delta S = \lambda_1 - \lambda_2 = \sqrt{(S_{11} - S_{22})^2 + 4{S_{12}}^2} \tag{5.2}$$

For an isotropic sample then $\lambda_1 = \lambda_2$, i.e., the similarity transforms lead to the identity matrix. This definition holds true for two-fold symmetry but would need to be updated for higher fold symmetries. This can produce an anisotropy tensor in equation 5.3.

$$S = \begin{pmatrix} S_{11} & S_{12} \\ S_{21} & S_{22} \end{pmatrix} \tag{5.3}$$

Where the tensor elements are as follows

$$S_{11} = \langle \cos^2 \Psi \rangle = \frac{\int_0^{2\pi} d\Psi I(\Psi) \cdot \cos^2 \Psi}{\int_0^{2\pi} d\Psi I(\Psi)} \tag{5.4}$$

$$S_{22} = \langle \sin^2 \Psi \rangle = \frac{\int_0^{2\pi} d\Psi I(\Psi) \cdot \sin^2 \Psi}{\int_0^{2\pi} d\Psi I(\Psi)} \tag{5.5}$$

$$S_{12} = S_{21} = \langle \sin \Psi \cos \Psi \rangle = \frac{\int_0^{2\pi} d\Psi I(\Psi) \cdot \sin \Psi \cos \Psi}{\int_0^{2\pi} d\Psi I(\Psi)} \tag{5.6}$$

Where Ψ is the azimuthal angle in the imagery convention (values increase counterclockwise with zero is the X axis at 3 o'clock).

All analysis and modeling of the SAXS, and WAXS data was performed using Python 3 (NumPy[25], pandas[26], Matplotlib[27]), which aids in reproducibility, while the use of

SasView[21]/sasmodels[22] and bumps[23] packages for Python, allows for rapid and easily adjustable fitting of the data sets.

5.3 Results and Discussion

In Chapter 4, we discussed the impact of heat pressing temperature on sample morphology and established a baseline morphology for the sample set. Here, we build upon that foundation with further processing changes in an effort to isolate and identify which processing modifications induce significant changes in these PS-PI-PS/P3HT blends. A set of triplicated samples were processed and characterized at Argonne Photon Source (APS) on the USAXS instrument. Although the replicates within this set were self-consistent, later samples did not corroborate these trends, and information presented in this chapter has helped to discount many possible processing modifications that may have created the new morphology. Further information on the APS triplicate sample set can be found in Chapter 9.3.

5.3.1 Processing Effects at Each Stage

From the analysis of the drop cast and pressed samples in Chapter 4, we know there are morphological changes due to the pressing method, and identifying the extent of these changes is an important first step. New samples were prepared as described in Section 5.3.2**,** with cuttings of each sample characterized at each stage in the pressing methods. The samples were pressed multiple times to ensure homogeneity, and cuttings were taken after each heat press. These cuttings were labeled as first press, second press, and third press, with the third press samples identical to the fully processed samples as discussed in the previous sections. These measurements were conducted with the Xenocs Xeuss 3.0 point-collimated instrument, so both 2D and 1D (radially averaged) data are available. Representative 2D plots are shown in **Figure 5.2**. Investigation of 2D plots allows for analysis of alignment of the cylindrical structures in the solid structure. When structures are oriented in the same direction, the intensity of the scattering signal is stronger in the 2D pattern orthogonal to the aligned direction. This will appear as a 'hot spot,' or regions of the image that are much brighter, signaling locations with higher intensity. Alongside visual analysis of these images, we have calculated the alignment factor, as described in Section 5.3.6**,** which is a representation of the extent of alignment from 0 (isotropic or entirely unaligned) to 100 (perfectly aligned). Analysis of the plots in **Figure 5.2** confirms that drop-cast and annealed samples for both the control and the representative blends show no signs of orientation in the 2D plot. We also see the alignment factor is very low, confirming the lack of alignment. Signs of alignment only emerge

after the first press. After the first press there are clear high intensity points in both samples shown, and with each subsequent press the alignment increases. All P3HT blends and control samples exhibit this increase, with no clear trend between the increase of alignment factor and composition.

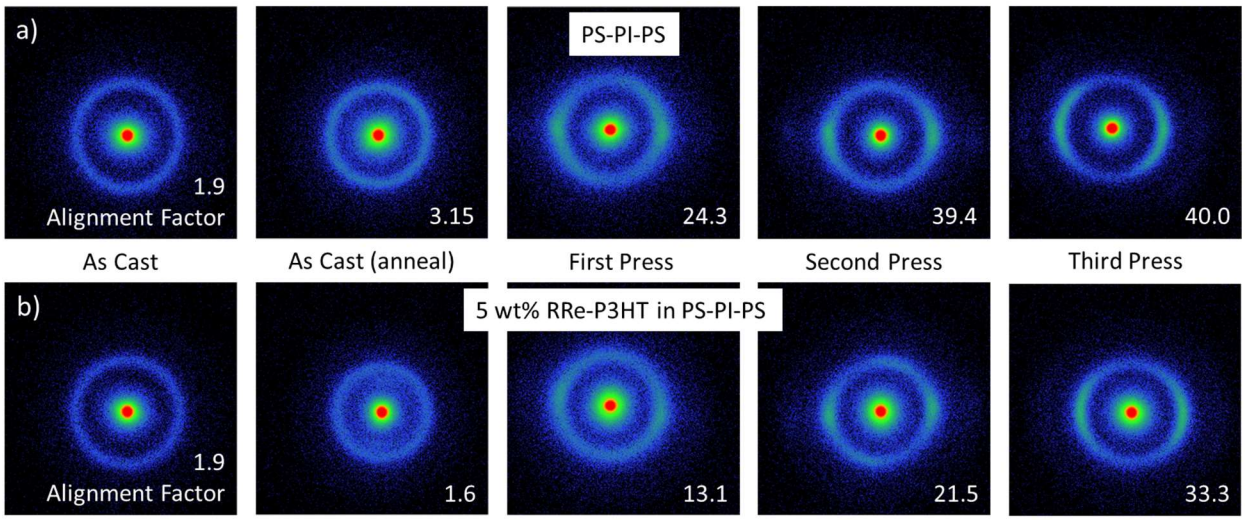

Figure 5.2: 2D SAXS scattering patterns of (a) PS-PI-PS template, (b) representative 5 wt % RRe-P3HT in PS-PI-PS blend from each stage of the processing method. Alignment factors were calculated from each scattering pattern and are plotted against wt %.

We utilize the broad peak fit for the 1D averaged data for these samples through all stages of the processing. As seen in **Figure 5.3a**, the peak of interest is present and the ratio of the peaks remains the same, suggesting that the phase structure is not dependent on processing. There are variations in the location of this characteristic peak, with a unique shift occurring between the drop cast sample and the heat-annealed sample. In **Figure 5.3a**, with the 5 wt% RRe-P3HT blend, we see a similar shift in the drop cast and annealed samples. We also see a slight shift when the samples are pressed, which was not clearly observed in the PS-PI-PS control. These trends become clearer in fit parameters (**Figure 5.3d** and **Figure 5.3e**) with a slight decrease in the peak location as the samples are pressed, and a large decrease in the peak location with annealing but no pressing for both RRe-P3HT and RRa-P3HT. These shifts are slight and are not indicative of a large growth or shrinking of the phase structure. **Figure 5.3b** and **Figure 5.3c** show the Lorentzian length parameter, which is used as a proxy for peak width, changing over the pressing process. The RRe-P3HT chloroform cast samples, both annealed and not, show minor change in the peak width at most loadings. The highest loaded sample, 10 wt %, shows a widening of the peak indicating disorder, but when annealed, all of the samples exhibit no significant difference in peak width.

Once pressed, the peaks widen significantly, indicating disorder, with each subsequent press gradually narrowing the peak until select samples are more ordered than their solution cast counterparts. The RRa-P3HT samples show similar trends but all of the blended samples in the drop cast annealed set show wider peaks and increased disorder. The pressing process shows a similar trend, with a large initial widening of the peaks followed by each subsequent press gradually narrowing and increasing the order of the phase structure.

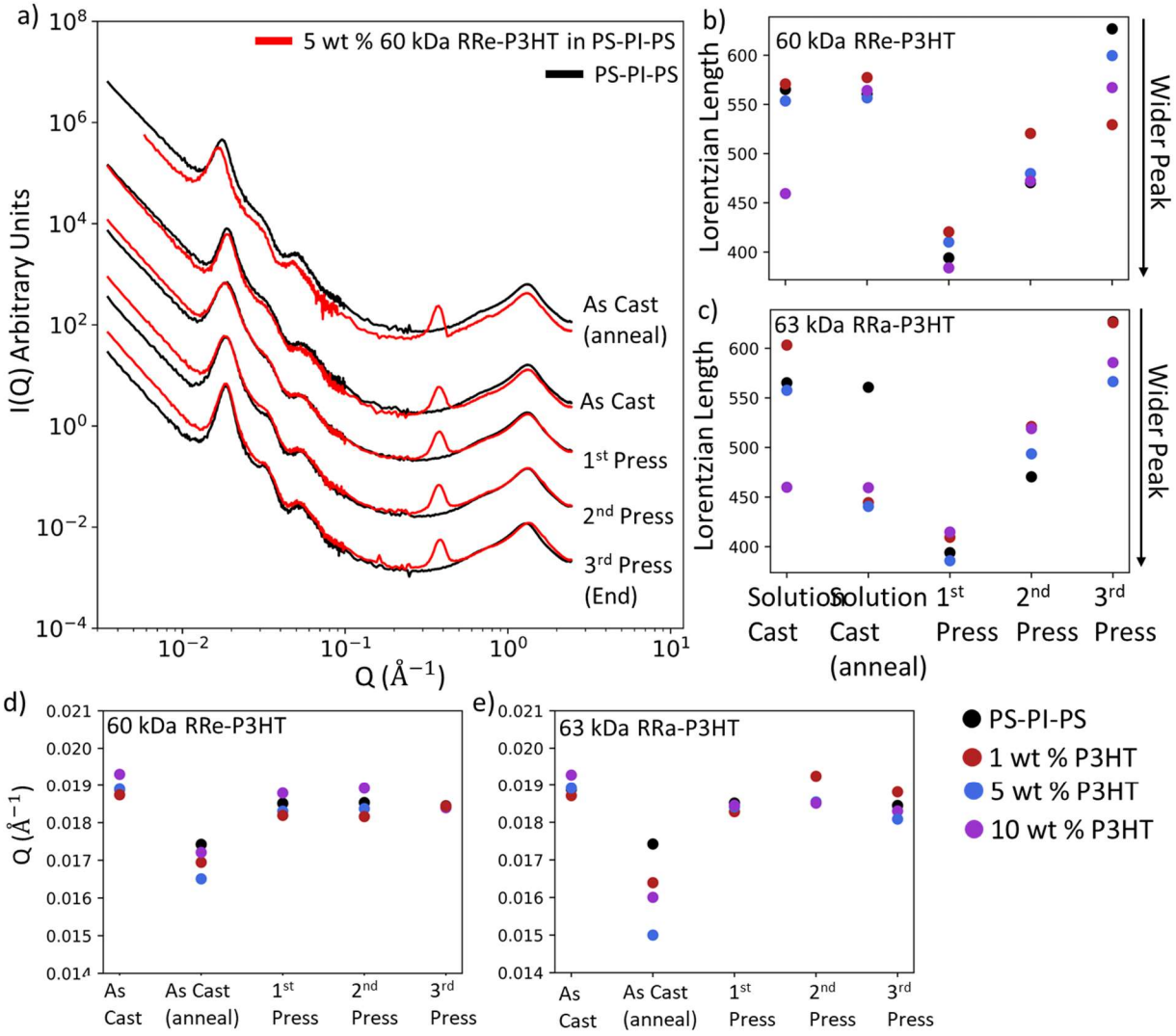

Figure 5.3: Peak characteristics of P3HT/Elastomer blends, with a) SAXS profiles of the PS-PI-PS template and a 5 wt % RRe-P3HT in PS-PI-PS blend co-plotted over samples from each stage of the processing method. Lorentzian length, a proxy for peak width, obtained from broad peak fits of the characteristic peak are plotted for b) RRe-P3HT in PS-PI-PS blends and c) RRa-P3HT

in PS-PI-PS blends. Peak location parameters pulled from broad peak fits of the characteristic peak are plotted for d) RRe-P3HT in PS-PI-PS blends and e) RRa-P3HT in PS-PI-PS blends.

5.3.2 Press Time Variation

We have observed clear changes over the course of the pressing process, and in order to understand these effects better, we modified the pressing schedule as described in section 5.2.3. This experiment investigated the PS-PI-PS template only and did not include blended samples. Further experimentation with blended samples may be insightful here, but with trends observed in Chapter 4 and in the investigation of each stage of processing, we can hypothesize on the effect of P3HT loading.

In **Figure 5.4a**, we can see there is a noticeable difference in the peak location and structural ordering of the samples between the three temperatures. This trend and more discussion on the effect of processing temperature on morphology can be found in Chapter 4. We also identify a slight shift in the peak location and width in the three pressing times at 150 ºC. As the pressing time increases the peak narrows and shifts slightly towards low-Q. We also see the emergence of more defined secondary peaks in the longest 150 ºC press time, but not to the extent seen in the 250 ºC sample. The peaks have been fit with the broad peak model as described before and peak parameters have been extracted. **Figure 5.4b** includes a plot of the peak location, and we can see a general trend that with longer pressing times and high temperatures, the peak location trends from a low-Q shift towards high-Q shift. We see that pressing at a 110 ºC causes a large initial shift peak location, but with additional presses and the time increases on the final press, the peak location shifts towards high-Q. At 150 ºC, the range of the extracted peak locations is small, but as the pressing time increases the peak location shifts towards higher q. At the long press time, the final press (45 minutes at 150 ºC) there is a significant shift towards low-Q. This trend is mirrored in the 250 ºC temperature where the final press (15 minutes) also displays a large shift towards low-Q.

The Lorentzian length parameter is plotted in **Figure 5.4c**. A clear trend emerges with the increase of time and temperature resulting in a narrowing of the peak across all samples. At the lowest temperature there is a large widening of the peak compared to the solution cast sample, which is most likely due to the temperature not being high enough to fully meld the cut PS domains, leaving sizable disorder in the system (see Chapter 4 for more discussion on this). As the temperature increases above the PS glass transition temperature (around 110 ºC) to 150 ºC, the

press time has a significant impact on peak width and structural order. Increasing the pressing time clearly increases the order in the system, allowing sufficient time for the domains to reorganize during pressing. When temperature is increased further, the peak narrows only slightly more than the longest 150 ºC press.

Looking at the trends over a full three press cycle, the order increases over the course of the pressing cycle, with the first press consistently being the most disordered. The third press consistently results in the most ordered sample, and it is important to note that the final press is always the longest press time of a single cycle. Also of note is that all of the presses at 250 ºC are effectively the same peak width, even though the peak location shifts considerably This width is also extremely similar to the final press on the 150 ºC long press series.

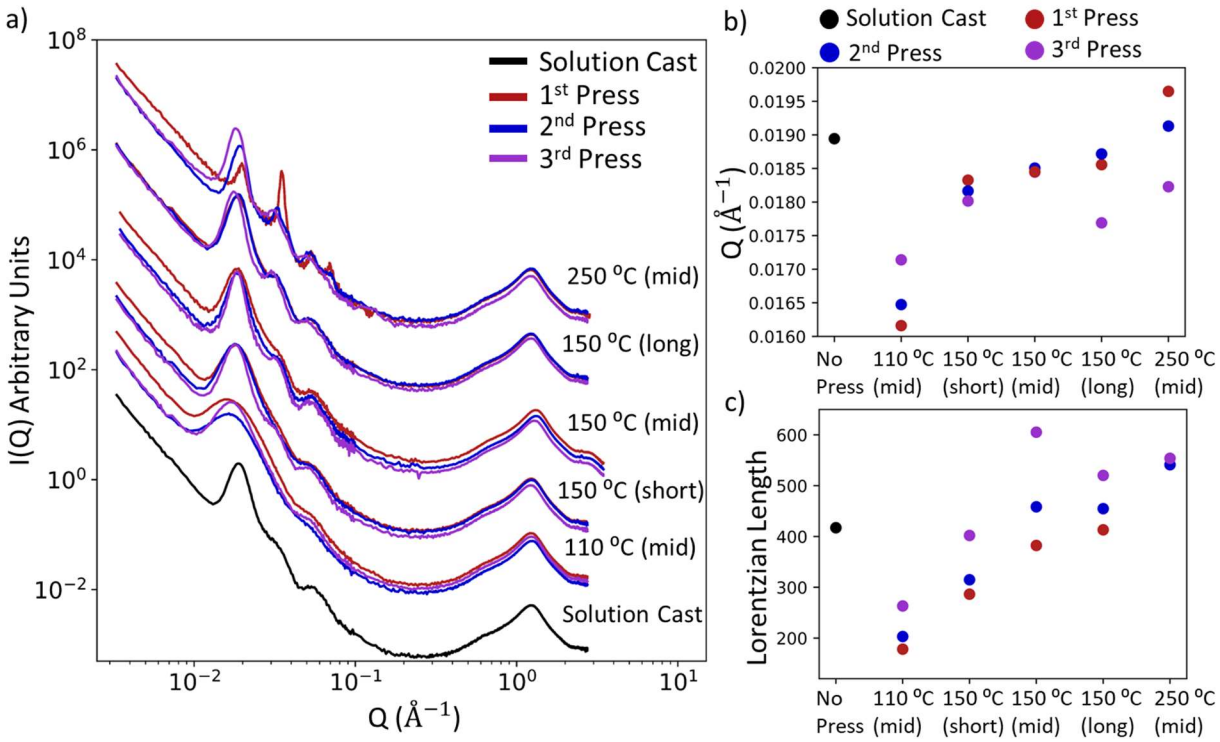

Figure 5.4: Peak characteristics of P3HT/PS-PI-PS blends, with a) SAXS profiles of the PS-PI-PS template co-plotted over each stage of the processing method, at 6 different pressing treatments. b) Peak location and c) Lorentzian length, a proxy for peak width, obtained from broad peak fits of the characteristic peak

5.3.3 Molecular Weight Variation

Alongside processing temperature changes, we studied a series of samples with changed RRe-P3HT lots with low (42 kDa), medium (60 kDa), and high (77 kDa) molecular weights. These

samples were all processed identically, with the only change being the RRe-P3HT molecular weight. When heat pressed at a processing temperature of 150 ºC, as seen in **Figure 5.5**, we see no significant difference between the samples. Slight differences in low-Q can be observed at RRe-P3HT concentrations of 7.5 wt % and higher, but the peaks do not change. Parameters of these ~0.018 $Å^{-1}$ broad peak fits can be seen in **Figure 5.5b** and **Figure 5.5c**. Small fluctuations are also seen in the Lorentzian length, but again, none of these changes are indicative of impact.

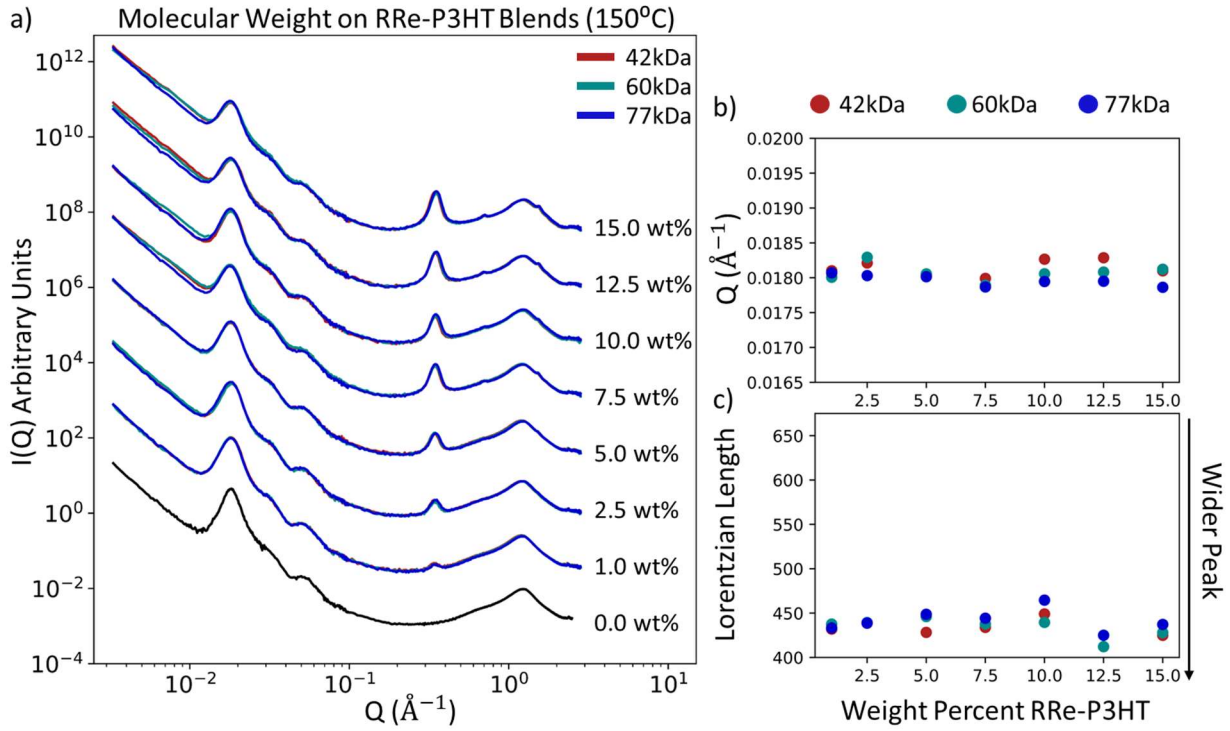

Figure 5.5: a) SAXS data for blends of RRe-P3HT and PS-PI-PS, corresponding to three different molecular weights and labeled by wt % of RRe-P3HT added to system. All samples were collected at 150 ºC. Data is arbitrarily shifted to separate samples by wt %. b) peak position parameters and c) Lorentzian length parameters from broad peak fits.

Identical samples are also processed at 250 ºC, with more apparent differences between the samples than the 150 ºC. As seen in **Figure 5.6a**, by increasing the temperature of processing more variation occurs in the location, width, and prevalence of secondary peaks in the region of interest. There is a clear variability in the peaks between molecular weights of RRe-P3HT as the loading wt % increases. This variability is maintained even within replicates of the same molecular weight as seen in **Figure 5.7**. We anticipate that the higher processing temperature makes samples more sensitive to processing changes, leading to slight variations in the onset, extent, and trends of phase

and order. This variation is present across molecular weights, and we anticipate that any changes that are caused by the increasing molecular weight of RRe-P3HT are disguised within the sample sensitivity. While these variations prevent any concrete analysis of the effect of molecular weight, we can observe general trends as the wt % increases in each series. At intermediate loadings (2.5 - 10.0 wt%) we see the peak at ~0.032 $Å^{-1}$ disappear for all molecular weights and an increase in the prominence of the peak at ~0.037 $Å^{-1}$. By 10 wt % RRe-P3HT, we see the 0.032 $Å^{-1}$ peak reappear for all samples. At the highest loadings of RRe-P3HT (12.5-15 wt %) the peaks widen significantly, indicating increased disorder, and differences between molecular weights of RRe-P3HT is greatly reduced. This is mirrored in the replicates shown in **Figure 5.7** with all samples showing a peak shift between 2.5 wt % and 10 wt % and the variation between samples reduced for low (1 wt%) and high (12.5+ wt %) loadings of RRe-P3HT.

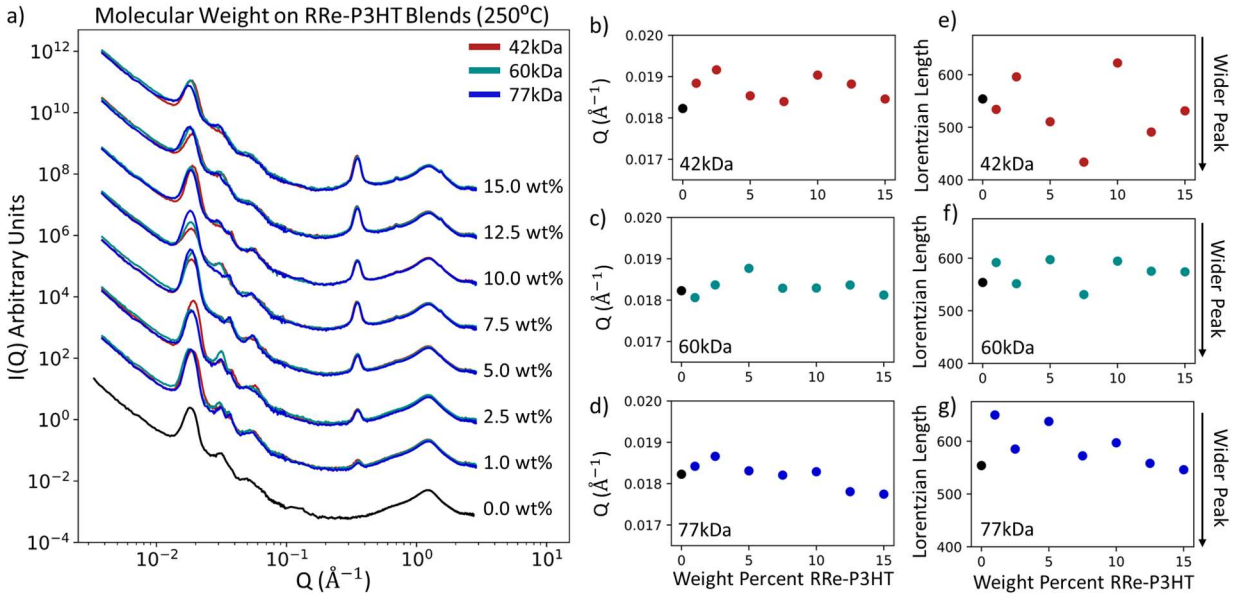

Figure 5.6: a) SAXS data of RRe-P3HT and PS-PI-PS blends corresponding to the three molecular weights of RRE-P3HT and loadings. All samples were heat pressed at a temperature of 250 ºC. Data is arbitrarily shifted to separate samples by P3HT loading. b-d) peak position and e-g) Lorentzian length parameters from broad peak fits of the 0.018 $Å^{-1}$ peak, separated by molecular weight of RRe-P3HT.

The primary peak at 0.018 $Å^{-1}$ is again fit with a broad peak model and select parameters are shown in **Figure 5.6(b-g)**. Due to the processing sensitivity in the mid-wt % range, drawing conclusions about explicit trends is difficult, but a few general observations can be made. Through all the replicates, the 77kDa RRe-P3HT samples trended at a higher Lorentzian length,

corresponding to narrower peaks. This suggests that there is slightly more ordered structure forming in the highest molecular weight series. The 42 kDa RRe-P3HT series consistently exhibited the highest peak locations, suggesting that spacing between the phase units is slightly smaller in the lowest molecular weight.

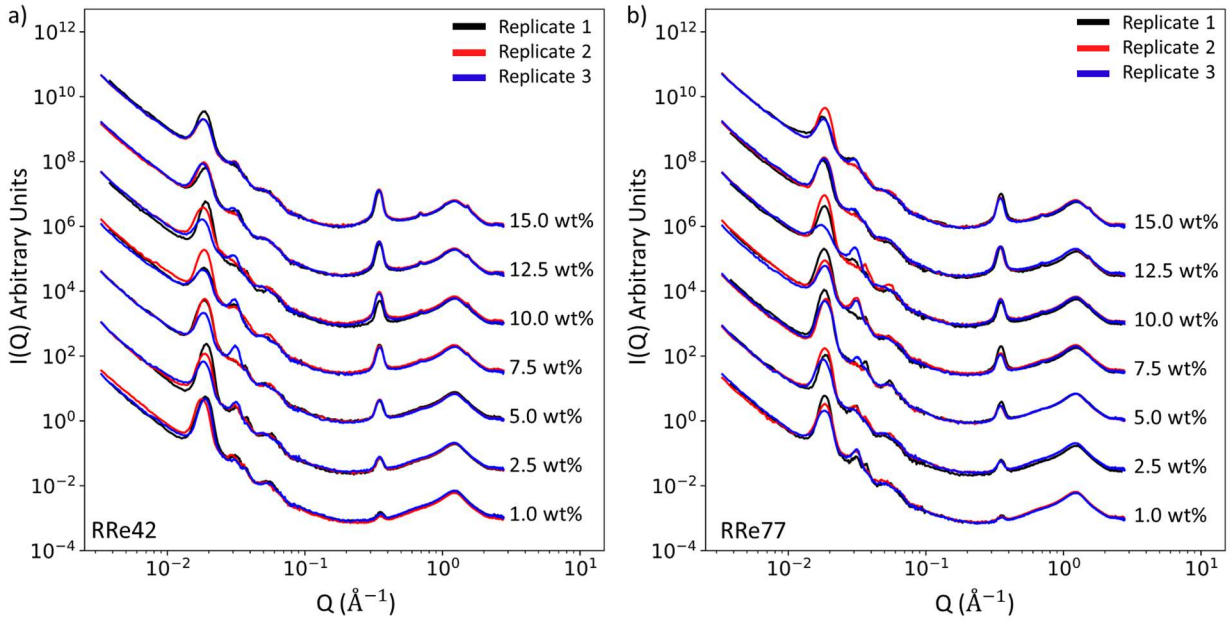

Figure 5.7: a) replicates of blends of 42 kDa RRe-P3HT and PS-PI-PS blends processed at 250ºC b) replicates of blends of 77 kDa RRe-P3HT and PS-PI-PS blends processed at 250ºC. Note the morphological variation in compositionally identical samples in the 2.5 wt % to 10 wt % range.

The impact of RRe-P3HT molecular weight on the phase of the matrix was also examined. As noted in Chapter 4, there is a phase shift from the hexagonally packed cylinders seen in PS-PI-PS to a lamellar phase around 5 wt%, then back to a hexagonally packed cylinder phase with the addition of more P3HT. This trend is maintained regardless of the molecular weight of the P3HT added to the blend. The two molecular weights not addressed in Chapter 4 are shown in **Figure 5.8**, with peak location and ratios determined,

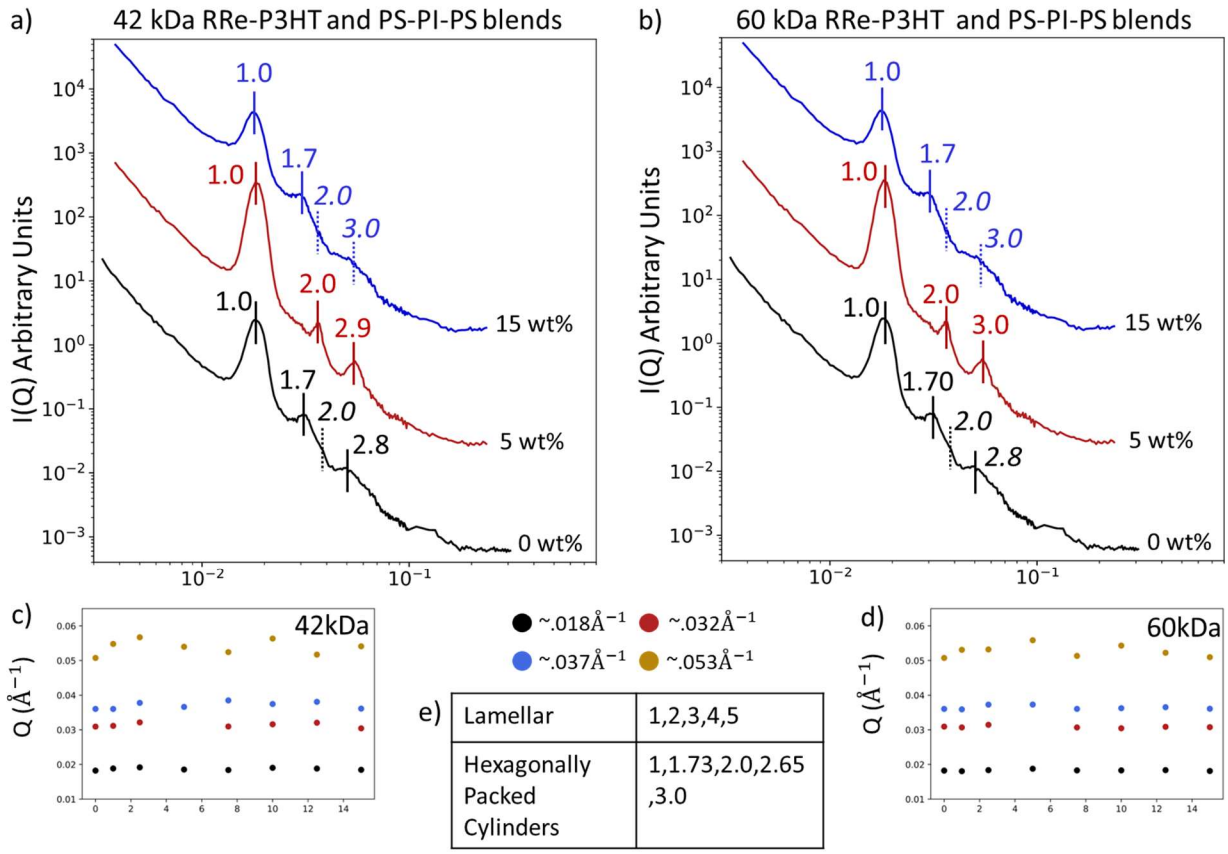

Figure 5.8: SAXS data of selected a) 42 kDa RRe-P3HT/PS-PI-PS and b) 60 kDa RRe-P3HT/PS-PI-PS blends, labeled by wt % of RRe-P3HT added to system, and collected at 250 ºC. Data is arbitrarily shifted to separate samples into wt %. Dotted lines represent expected peaks from ratios, but fitting is not concrete. Peak position parameters from broad peak of c) 42 kDa RRe-P3HT/PS-PI-PS blends and d) 60 kDa RRe-P3HT/PS-PI-PS fits. e) table with known peak ratios for lamellar and hexagonally packed cylinder phases.

5.3.4 Effects of Solvent Variation

From literature and previous experiments[28], we identified an impact of solvent quality on the structure of compositionally identical materials and wished to also investigate the impacts on these blended systems. Sets of samples cast from chloroform and toluene were processed using identical methods and compared to each other to identify structural changes. These samples were processed at four temperatures (solvent cast, 110 ºC, 150 ºC, and 250 ºC) and are shown in **Figure 5.9**. When measured directly after being cast, there is a noticeable change in scattering profiles for samples at and above 5 wt % RRe-P3HT. This appears to be a change in intensity, most likely due to the varying thicknesses of the cast film. The change in solvent shows little effect for the 110 ºC

and 150 ºC samples (**Figure 5.9a-b),** but variations in peak location and width are visible in the 250 ºC samples. Some of this variation is most likely explained by the processing sensitivity at 250 ºC as discussed in Chapter 5.3.3, but we also see variation in the lowest and the highest wt % loadings of RRe-P3HT, which we anticipate is due in some part to the solvent.

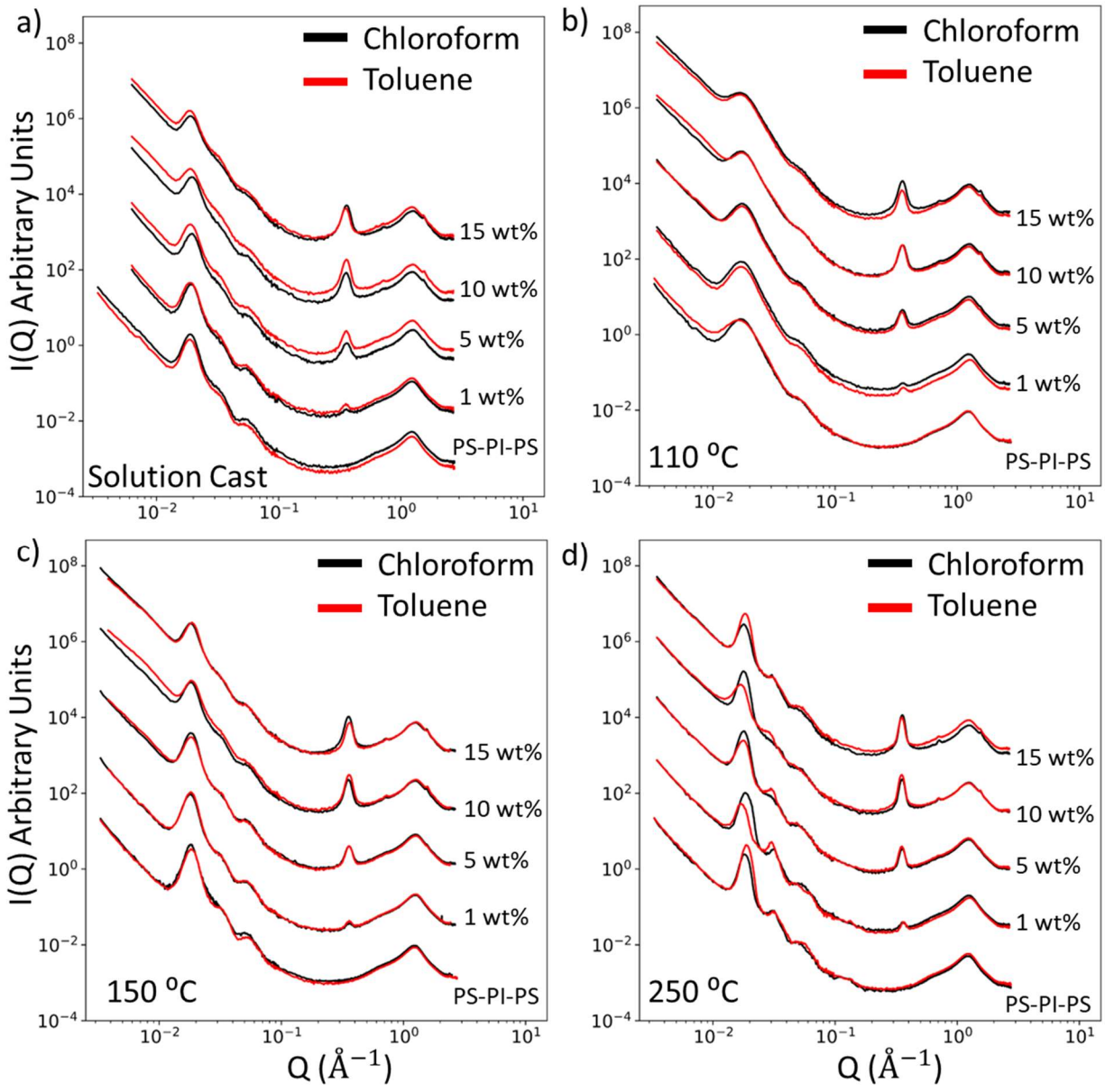

Figure 5.9: SAXS data of 60 kDa RRe-P3HT and PS-PI-PS Blends cast from both chloroform and toluene. a) solution cast samples and samples processed at b)110 ºC, c) 150 ºC, and d) 250 ºC.

This solvent variation experiment was also conducted with amorphous 62 kDa RRa-P3HT and PS-PI-PS blends, with similar results (**Figure 5.10**). We see the 110 ºC and 150 ºC

samples show little variation between the two casting solvents, while the 250 ºC data sets show increased variation, especially for the mid wt % region at 5 wt % RRa-P3HT.

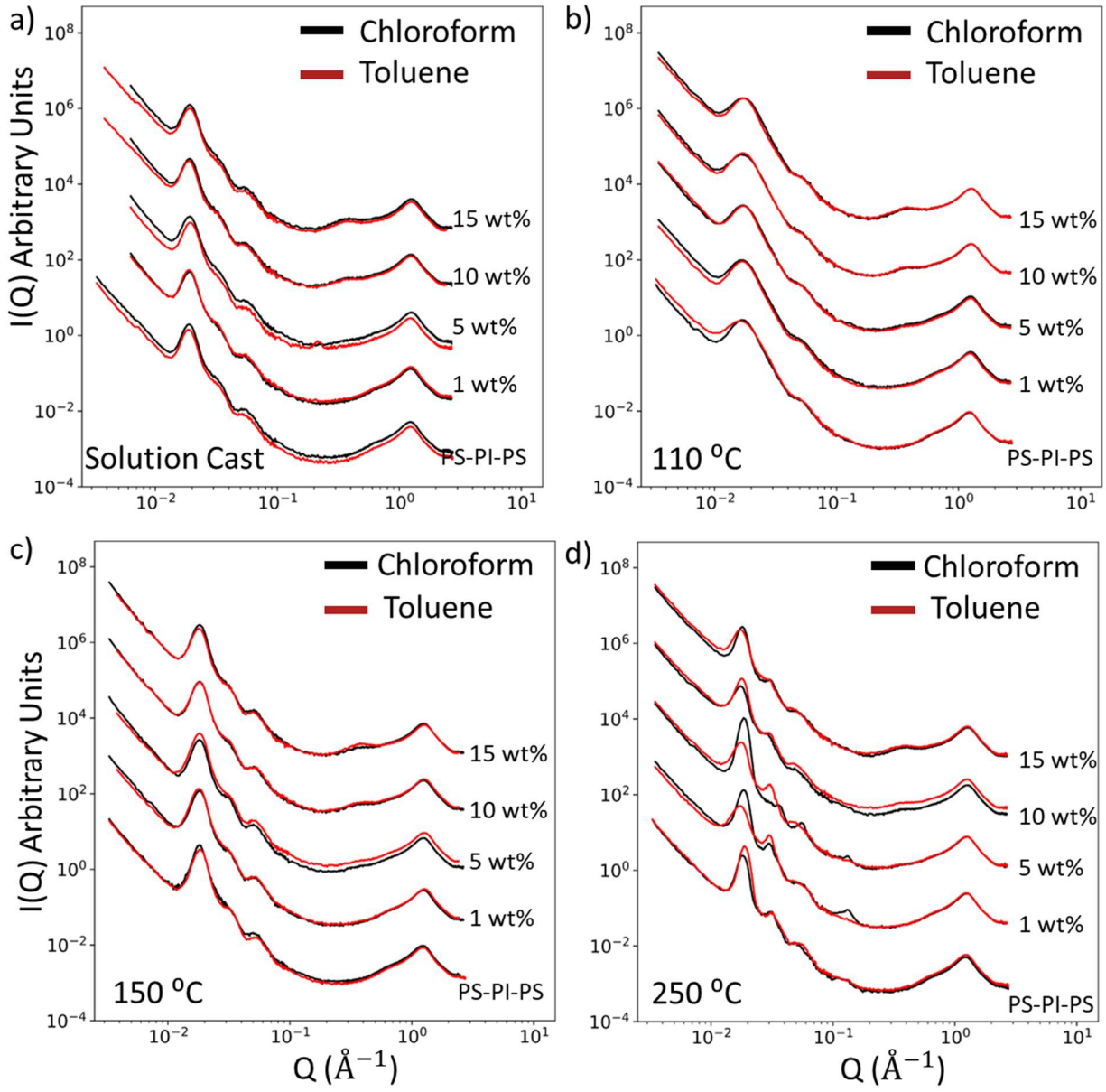

Figure 5.10: SAXS data of 63 kDa RRa-P3HT and PS-PI-PS Blends cast from both chloroform and toluene. a) solution cast samples and samples processed at b) 110 ºC, c) 150 ºC, and d) 250 ºC.

Broad peak fits for the RRe-P3HT samples were conducted for the initial peak at ~0.018 Å, with fit parameters shown in **Figure 5.11a-d**. Observations seen in the 1D datasets also emerge in the fits. For the 110 ºC and 150 ºC samples, we see similar peak locations and widths for both

RRe-P3HT and RRa-P3HT blends. The range of peak locations for the toluene samples is more than the chloroform samples, but the fits for the Lorentzian length parameter, the proxy for peak width, are consistent with similar ranges. The variation in peak location for the toluene samples further increases in the 250 ºC sample set for the RRe-P3HT samples, with a large range and variation for the toluene cast samples. The chloroform cast samples at 250 ºC show variation in the peak width and location, but the range is smaller. The 250 ºC The RRa-P3HT blends do not change in consistency between the chloroform and toluene samples, suggesting that the large increase in the range of peak locations for the RRe-P3HT blends may be an effect of the interaction of the semi-crystalline RRe-P3HT and solvent.

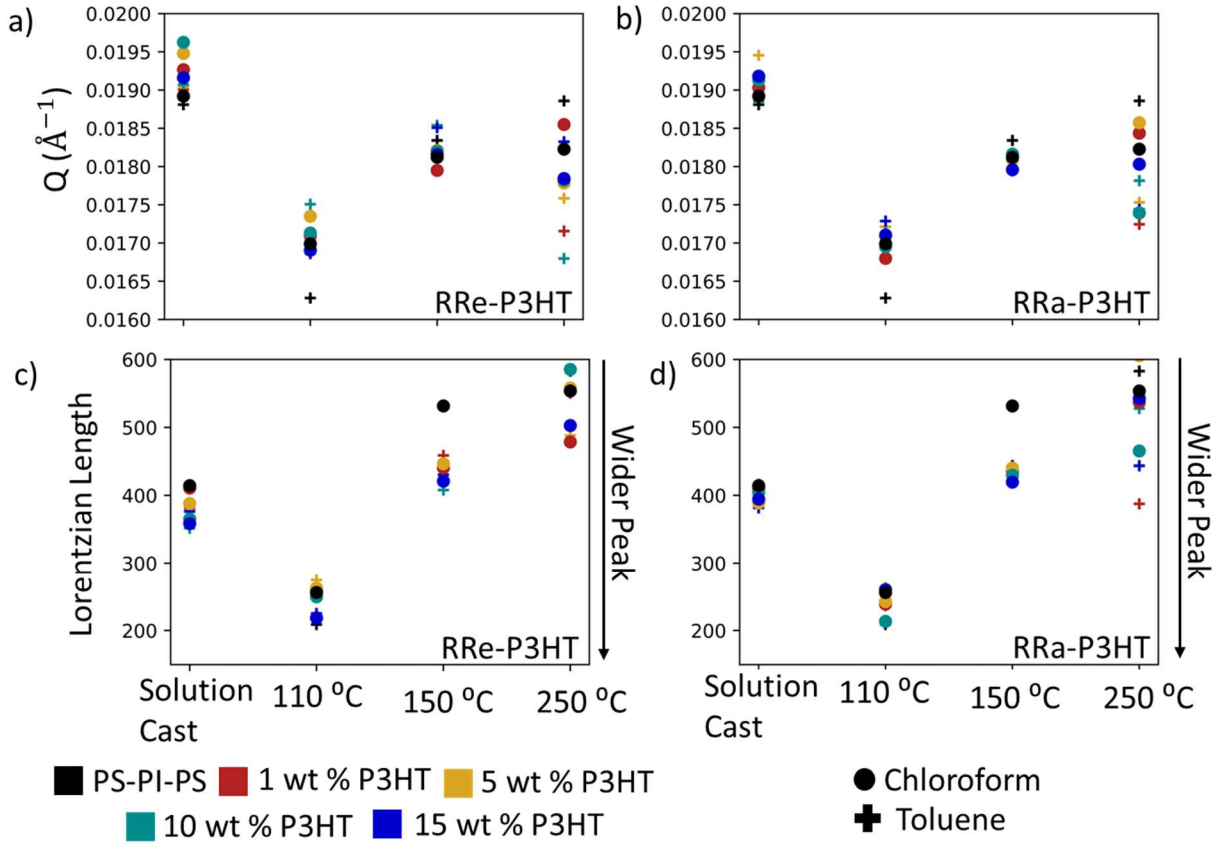

Figure 5.11: Broad peak fits for peak location for a) 60 kDa RRe-P3HT and PS-PI-PS blends and b) 63 kDa RRa-P3HT and PS-PI-PS blends, cast from chloroform or toluene for all heat processing temperatures. Peak fits for Lorentzian length for c) 60 kDa RRe-P3HT and PS-PI-PS blends and d) 63 kDa RRa-P3HT and PS-PI-PS blends cast from chloroform or toluene for all heat processing temperatures.

5.3.5 Application of Vacuum Oven for Evaporation

The control sample set was solution cast at 50 ºC and then left to gently off-gas any remaining solvent overnight in a fume hood. This process allows the sample to dry and removes any remaining traces of solvent, and when heat pressed the next day, there is no observed solvent remaining. In order to test if this overnight fume hood method adequately removes solvent, a set of samples were placed under vacuum overnight. These samples were left under vacuum at room temperature for the same duration as the fume hood samples. Once removed from the vacuum oven, there were no observable differences between the control and test samples. The sample set was then pressed using the same methods as the baseline samples.

When compared, as seen in **Figure 5.12**, there are few differences between the two sets. There is a slight variation in the scattering profiles of the 7.5 wt % and the 10 wt % samples, with the vacuum oven method resulting in samples with slightly sharper peaks, indicative of slightly more order. All other samples in the vacuum oven treated set are functionally identical to the baseline samples, and do not suggest a processing difference between the two. This also suggests that no or negligible trace amounts of solvent remain in the sample after fume hood off-gassing, allowing us to approach the system as fully dry at pressing.

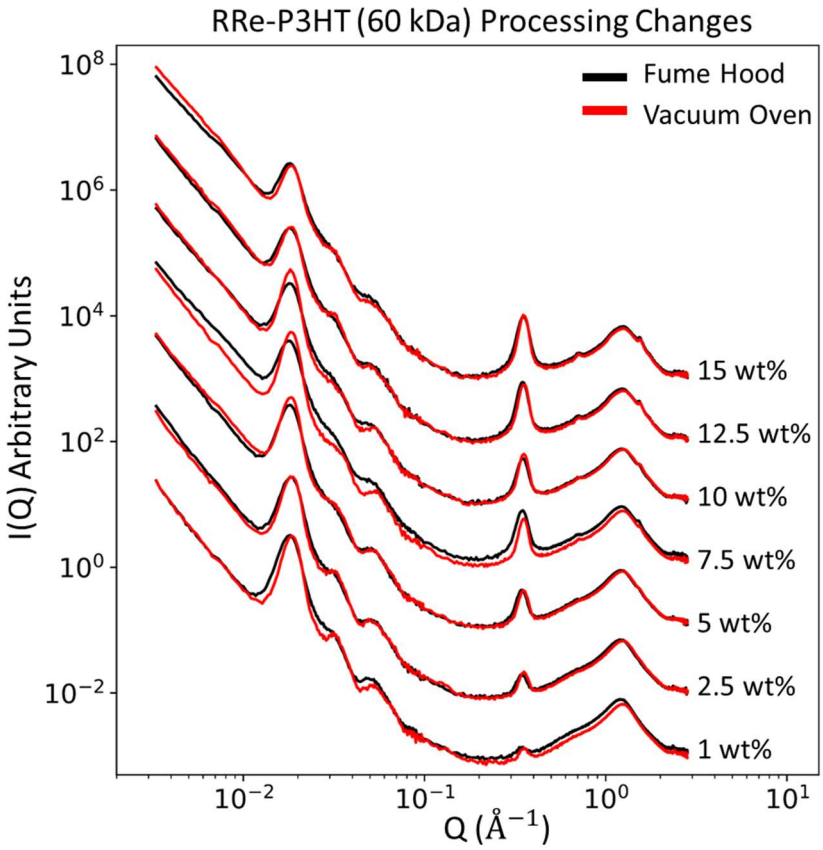

Figure 5.12: SAXS data of 60 kDa RRe-P3HT and PS-PI-PS blends cast from chloroform and left to either off-gas in the fume hood (black) or in a vacuum oven under vacuum at 25 ºC (red), before being pressed in identical ways.

5.3.6 Intentional Alignment Through Sample Flow

The processing methods used in all previously discussed samples utilized a circular mold, with cutting and folding between pressings to minimize any flow-alignment that may occur as samples spread from the center of the shim. Still, flow can vary from sample to sample and press to press without a way to carefully control, repeat, or facilitate the movement. To understand the impact of flow on structure, we prepared a subset of samples in a rectangular shim to intentionally align the structure by forcing the sample to flow in a set direction during processing. The flow pattern was maintained throughout each press, and the sample structures were measured using SAXS at the flow front. For this data set we refer to the direction of flow as "vertical" and the direction orthogonal to flow as "horizontal".

The conversion to 1D data for the intentionally aligned sample was done by sector averaging, with a 30º slice of the image chosen to average Q values. As shown in **Figure 5.13a**, two sections

were chosen for the averaging: a horizontal section to capture the highest intensity regions, and a vertical section to capture the lowest intensity regions. These two regions allow for an analysis and understanding of the 1D peak information in the flow direction and the structures that are not flow aligned. In the 1D plot (**Figure 5.13b)**, we can see that the pure PS-PI-PS and the higher wt % blends (>10 wt % RRe-P3HT) have no scattering features or peaks in the vertical sector, which is a sign of excellent flow-alignment. At intermediate loadings (1 to 7.5 wt % RRe-P3HT), scattering features are observed in the vertical sector with a peak around 0.018 $Å^{-1}$. Still, secondary peaks that are clearly visible in the horizontal sector are not observed in the vertical sector data of samples.

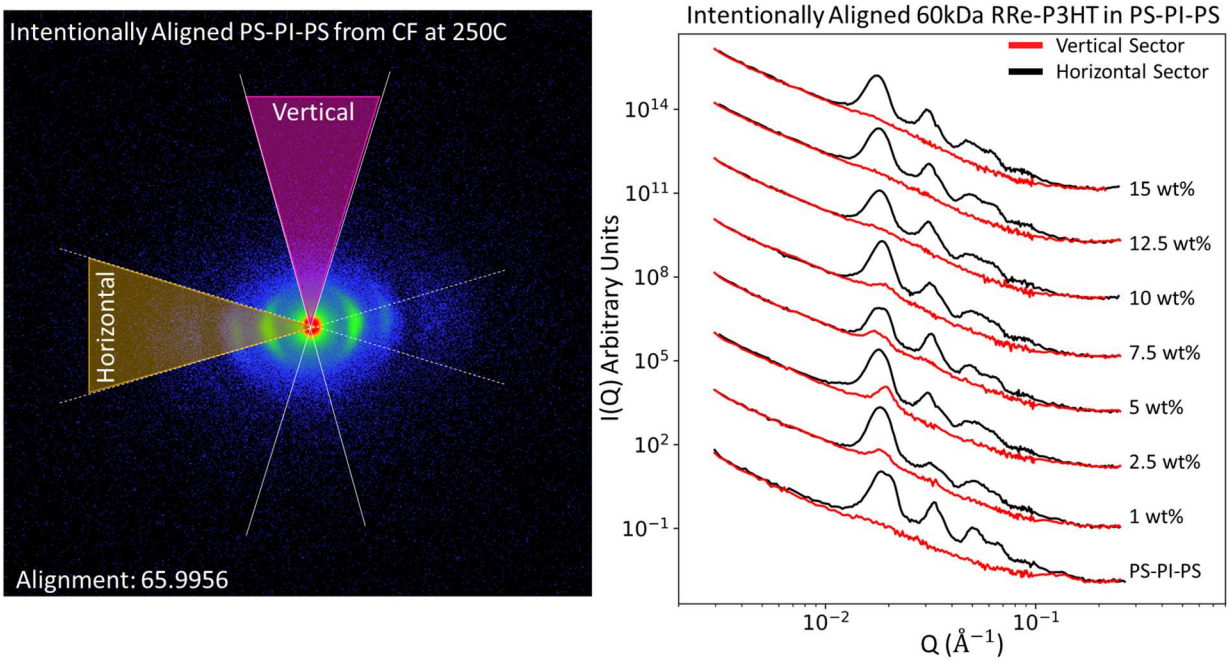

Figure 5.13: a) 2D image from 0.9 m SAXS runs for flow-aligned PS-PI-PS cast from chloroform and processed at 250 ºC with overlays on the sectors radially averaged for the horizontal and vertical directions. b) Vertical and horizontal integrated SAXS data for 60 kDa RRe-P3HT and PS-PI-PS blends, as a function of RRe-P3HT loading. Data have been arbitrarily shifted vertically for clarity.

When indexed, as shown in **Figure 5.14**, all flow-aligned samples were identified as hexagonally packed cylinders at all concentrations. The phase analysis was conducted on the 'horizontal' sector and captures the phase that is aligned in the flow direction. We do not see an

emergence of a lamellae phase around 5 wt% that is seen in radially pressed samples, indicating that the lamellae phase was not oriented in the flow direction in these samples.

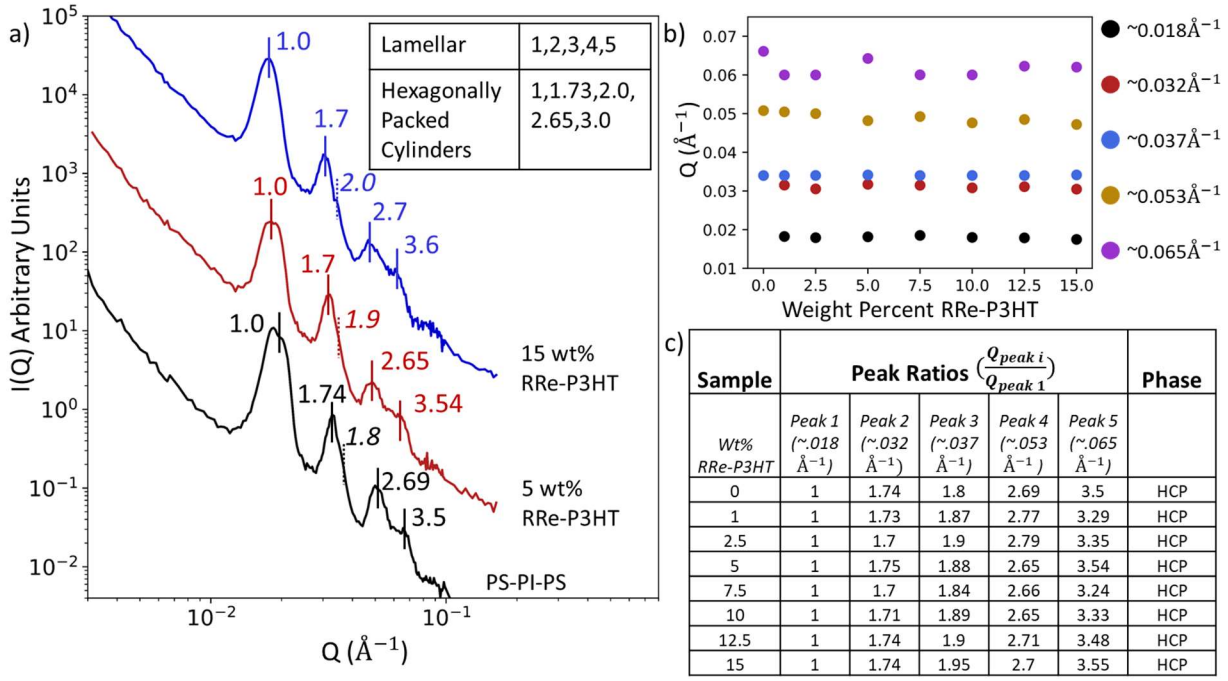

c)

Sample	Peak Ratios ($\frac{Q_{peak\ i}}{Q_{peak\ 1}}$)					Phase
Wt% RRe-P3HT	*Peak 1 (~.018 Å^{-1})*	*Peak 2 (~.032 Å^{-1})*	*Peak 3 (~.037 Å^{-1})*	*Peak 4 (~.053 Å^{-1})*	*Peak 5 (~.065 Å^{-1})*	
0	1	1.74	1.8	2.69	3.5	HCP
1	1	1.73	1.87	2.77	3.29	HCP
2.5	1	1.7	1.9	2.79	3.35	HCP
5	1	1.75	1.88	2.65	3.54	HCP
7.5	1	1.7	1.84	2.66	3.24	HCP
10	1	1.71	1.89	2.65	3.33	HCP
12.5	1	1.74	1.9	2.71	3.48	HCP
15	1	1.74	1.95	2.7	3.55	HCP

Figure 5.14: SAXS data of selected a) 60 kDa RRe-P3HT/PS-PI-PS intentionally aligned blends labeled by wt % of RRe-P3HT added to system and collected at 250 ºC. Data is arbitrarily shifted to separate samples into wt %. Dotted lines represent expected peaks from ratios where fitting is not concrete) Peak position parameters from broad peak fits. e) table all calculated peak ratio and determined phase.

In 2D detector images, samples showed clear signs of alignment that were not as evident in radially pressed samples. In **Figure 5.15**, we see that radially processed samples show low alignment factors and more isotropic scattering patterns, with one highly visible ring correlating to the characteristic peak seen in the 1D data. In contrast, for the intentionally aligned samples, the ring develops into spots of high horizontal intensity that correlates well with the vertical flow direction. We also observe a sizable increase in the alignment factor from 0 (isotropic) to 100 (perfectly aligned), between the radially pressed and intentionally aligned samples. Alignment factors were calculated using XSACT software, which extracts alignment parameters from a tensor approach (equations and tensors are provided in Section 2.5.6. We especially see this increase in alignment in pure PS-PI-PS blends with low loading of P3HT (1 wt %) and in blends with higher loadings of RRe-P3HT (10-15 wt %) blends. The 2D scattering patterns in **Figure 5.15** help to

demonstrate that shear alignment is possible but also strongly dependent on the composition and loading of the blends.

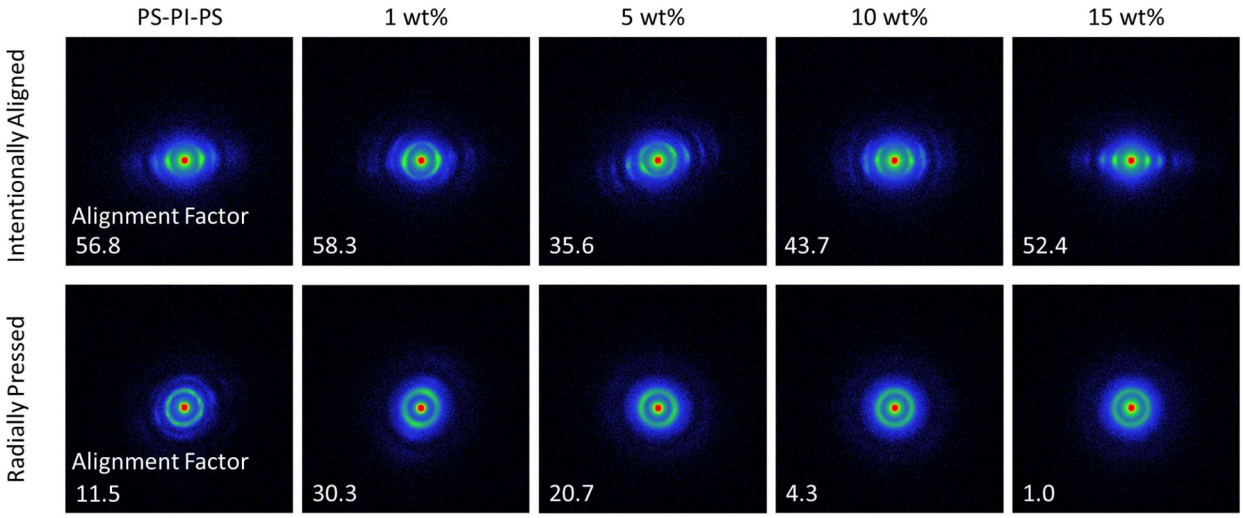

Figure 5.15: 2D images from 0.9 m SAXS runs for a) intentionally aligned samples and b) radially pressed samples of pure and 60 kDa RRe-P3HT and PS-PI-PS blended systems, processed at 250 ºC, denoted by the wt % of RRe-P3HT additive in the mixture. Alignment factors are included for all samples and characterize the extent of alignment, with 0 indicating isotropic and 100 being maximally aligned.

5.3.7 Annealing Solvent Cast Samples

Additional experiments were conducted on solvent cast samples with post-processing annealing. Details of this method can be found in Section 5.2.4. A set of post-processed annealing treatments were performed on solution cast samples. All samples of the same wt % loading were cut from the same solution cast sample, so all differences between these samples are the result solely of the heat-treating process. The temperatures and times chosen to mirror the modified pressing times seen in **Figure 5.1e**, with a mid-length annealing time (25 min) at 100 ºC and 250 ºC. The samples treated at 150 ºC were processed at three lengths of annealing time: short (10 min), medium (25 min), and long (50 min).

The 2D SAXS plots, a selection of which is shown in **Figure 5.16**, exhibit no alignment in any of the post-processed samples. This mirrors the lack of alignment present in the solution cast samples and confirms that treating samples with heat alone does not induce alignment. With increasing time and temperature there is a widening of the ring of intensity, which equates to the

characteristic peak shown in 1D data. At the highest temperature treatment, the ring, while still visible, is less clear than when compared to the non-heat-treated solution cast sample.

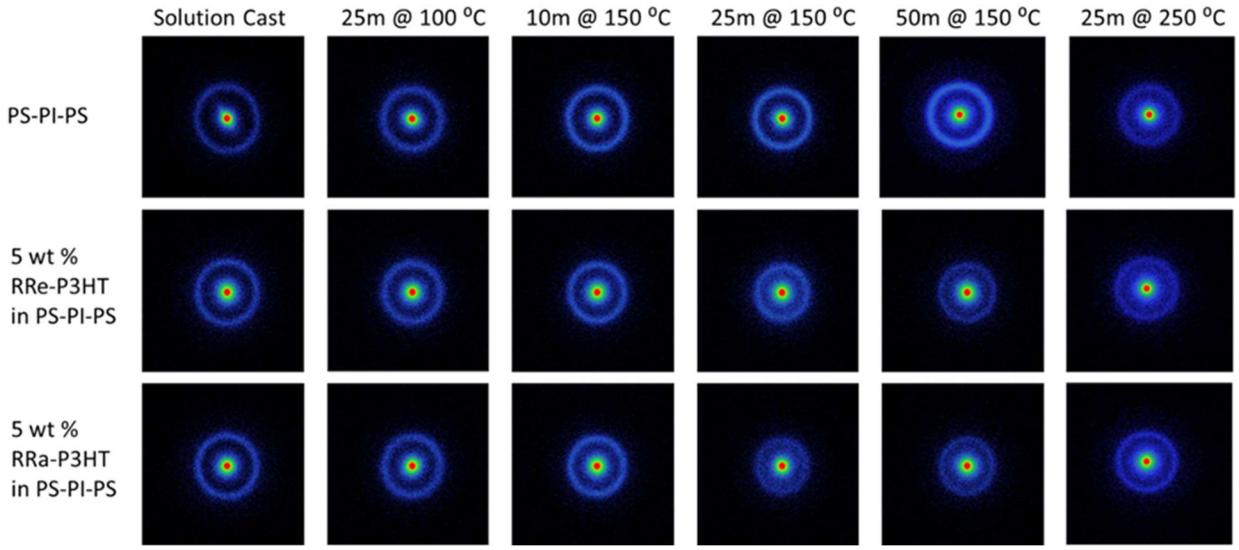

Figure 5.16: 2D SAXS images of a selection of post-processing heat-annealed samples.

The 1D SAXS data for these plots is shown in **Figure 5.17** and displays the changes between the PS-PI-PS control and a representative 5 wt % RRe-P3HT blend. There are visible shifts between the elastomeric control and the blend in all annealing modes, except for the highest temperature (250 ºC). At 250 ºC, both polymers are significantly shifted from the rest of the samples, but do not display a large peak difference between the control and the blend. There are only slight changes in peak shape and location observed at low temperature, where the temperature is just above the PS glass transition temperature, but for higher temperatures and longer durations of annealing the structure changes considerably. We see large increases in peak location and peak width for all the samples annealed at 150 ºC, with increasing times resulting in more significant changes. The changes in the 150 ºC annealing time series are much more noticeable for the RRe-P3HT blended sample than the pure PS-PI-PS template. For the high temperature samples, there was no change from between the PS-PI-PS template and the blends, and all samples show large changes in structure. We also see the intensity of the characteristic peak drop as the length of annealing time and temperature increase, with the shortest time and lowest temperature only causing a slight reduction. In **Figure 5.17b-e**, the parameters from sample fits are plotted. There is a clear decrease in peak location as time and temperature increases, with the elastomer control showing the least amount of shift until the most extreme temperatures. This trend occurs for both the RRa-P3HT and the RRe-P3HT blends, suggesting that the addition of any conjugated polymer

will have an effect on PS-PI-PS morphology, with RRa-P3HT displaying a larger change in layer spacing. It is important to note that for all but the highest annealing temperature, the PS-PI-PS template had the smallest shift in peak position from the untreated sample and typically the least change in peak width. In the lowest temperature samples, the change in peak width for all samples was similar.

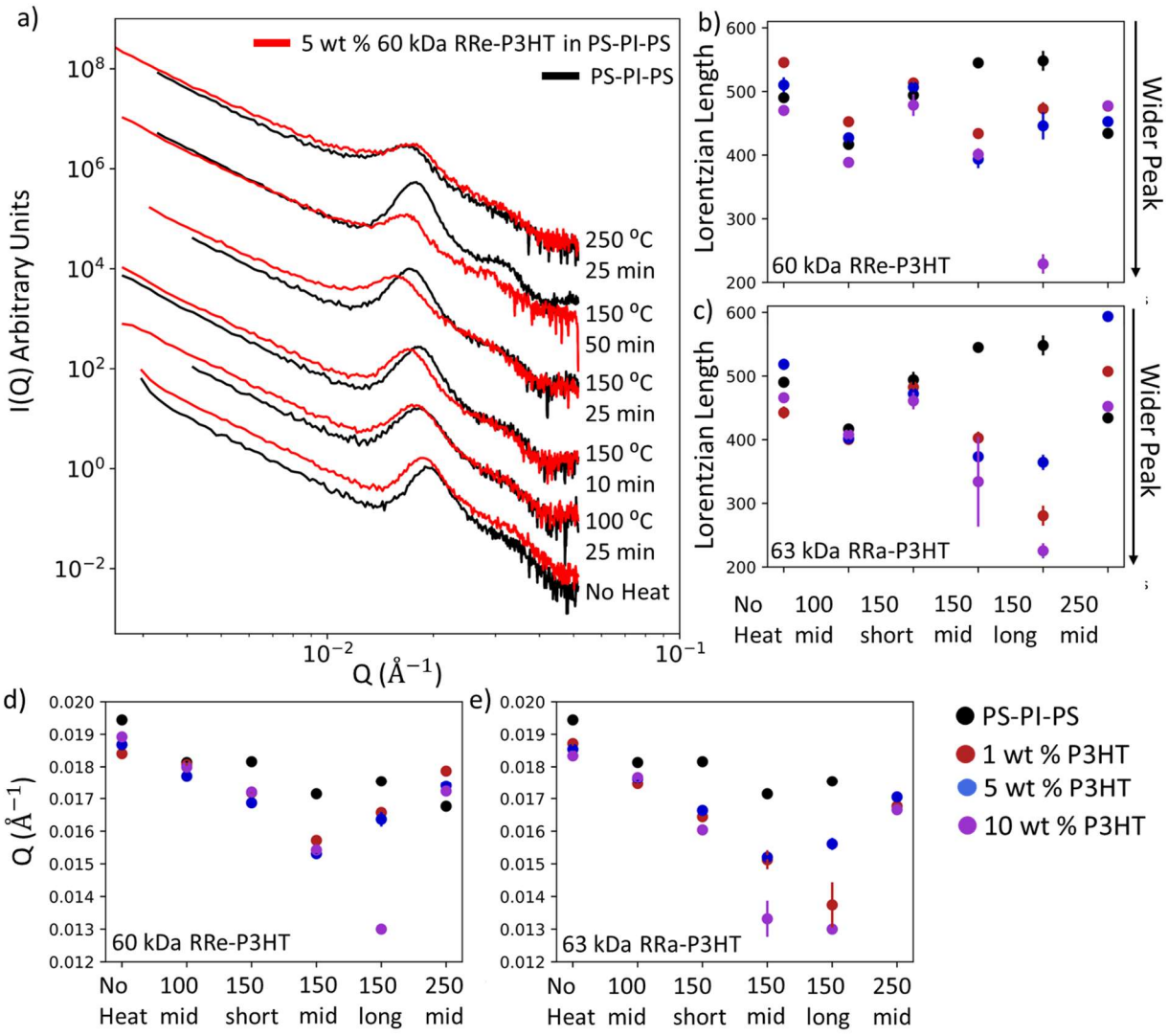

Figure 5.17: Peak characteristics of P3HT/Elastomer blends after annealing at different conditions, with a) SAXS profiles of the PS-PI-PS template and a 5 wt % RRe-P3HT in PS-PI-PS blend co-plotted over all the annealing conditions tested. Peak width parameters pulled from broad peak fits of the characteristic peak are plotted for b) RRe-P3HT in PS-PI-PS blends and c) RRa-P3HT in PS-PI-PS blends. Peak location parameters pulled from broad peak fits of the

characteristic peak are plotted for d) RRe-P3HT in PS-PI-PS blends and e) RRa-P3HT in PS-PI-PS blends.

5.3.8 Annealing Pressed Samples with Time Variation

An additional annealing experiment was conducted on fully processed samples. These samples were prepared using the baseline methods: solvent cast from chloroform, pressed for 5 min, 5 min, and 25 min over three presses at 150 ºC, before being cut to be annealed. A single cutting for each sample was reserved as a non-annealed control, and the other two cuttings were heated in a vacuum oven at 120 ºC -130 ºC for either 4 hours or 24 hours. **Figure 5.18a** shows the 1D SAXS plots of 60 kDa RRe-P3HT in PS-PI-PS samples separated by wt %, plotted with the control sample and both annealing times. A clear peak shift in all the wt % is observed from the control and 4-hour annealed samples to the 24-hour annealed samples. For the 10 wt % sample there is also a clear peak shift between the control sample and the 4-hour annealed sample. The pure PS-PI-PS samples have increased sharpness in the peak, which is a sign of increased consistency of orientation or increased division of the layers. The RRe-P3HT blends show a slight widening from the PS-PI-PS peaks but are mostly unchanged by annealing until the 10 wt % sample as well. At this loading, along with a large peak shift at 24 hours annealing, there is also a significant widening of the peak. This indicates a large disordering of the structure when annealed for long periods of time at high RRe-P3HT loadings.

The RRa-P3HT sample series shows similar trends, but the onset of major peak shifts occurs at a lower loading, beginning with the 5 wt % samples. For the 1 wt % RRa-P3HT samples, there are shifts with the increase of annealing time. These shifts are more significant with the 5 and 10 wt % samples, with the peak widening to the point of distortion, and a large shift towards low-Q. While both the RRe-P3HT and RRa-P3HT samples showed changes in phase spacing and loss of order, the RRa-P3HT samples exhibit an earlier onset of disorder as well as a greater extent of modification due to heating.

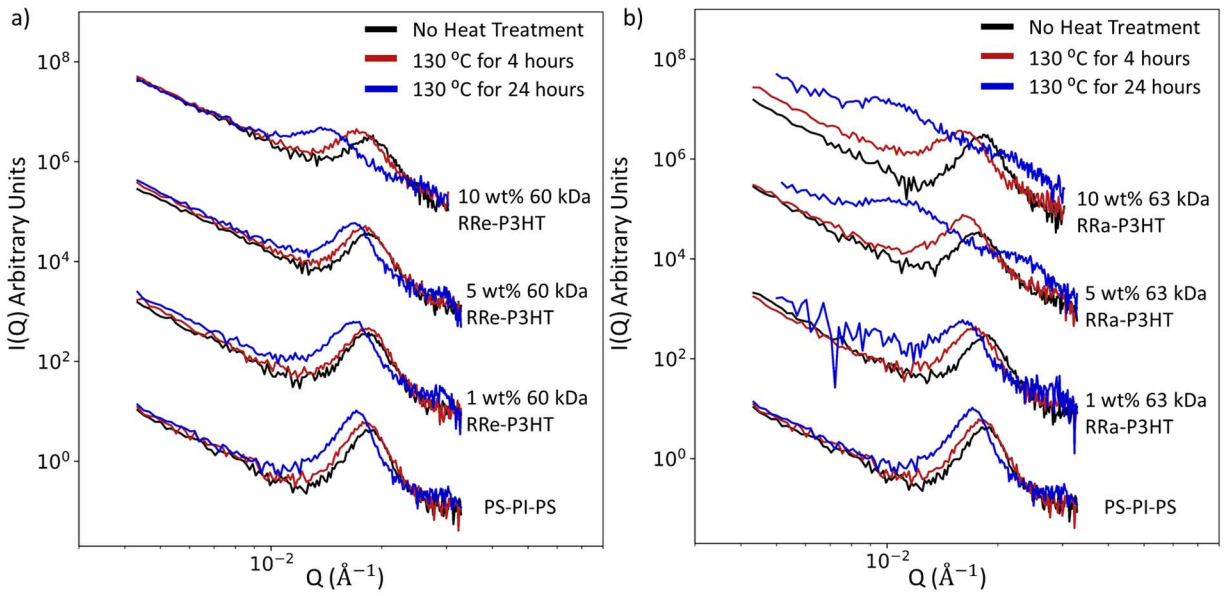

Figure 5.18: SAXS data for the fully processed and post-process annealed samples of a) 60 kDa RRe-P3HT and PS-PI-PS blends and b) 63 kDa RRa-P3HT and PS-PI-PS blends.

5.4 Discussion

Throughout the pressing process we have determined there are factors that can cause major changes to the phase structure and ordering of elastomeric blends. These factors are related to the structural changes caused by processing temperature, as discussed in Chapter 4. As seen in **Figure 5.2,** the process of heat pressing induces alignment and affects the order in the system. We anticipate this is due to the radial pressing method, where the flow is hard to control but applies pressure outward from a central location. This flow creates alignment in the sample, and if given enough time then the disorder created in the system from the cutting and pressing steps can be removed, given that the sample is heated above the glass transition temperature of polystyrene. We see this to a greater extent in **Figure 5.3**, with variable press times. We also see how increased exposure, either through raising the temperature of the press or lengthening the time of the pressing step, can increase the order in the system. This sample set also solidifies the importance of multiple presses, as each press results in a more ordered sample in all samples but the hottest treatments. We also may be reaching a threshold for the ordering of the PS-PI-PS in this experiment and the order does not increase for either the longest press at 150 ºC or the 250 ºC set.

Even when not directly addressing temperature, the importance of temperature is still prevalent. Increased processing temperature also allows us to identify the effects of molecular weight of the RRe-P3HT additive on the structure of the blends. When processed at 150 ºC, there

is no significant change in structure between the sample series, suggesting that the molecular weight does not have an impact on the blend structure (**Figure 5.5**).

When processed at 250 ºC, there are minor differences between sample series, and the effect of molecular weight of RRe-P3HT on blend morphology can be identified (**Figure 5.6**). These differences are minimized due to the increase in processing sensitivity of these samples at higher temperatures, which have been identified in replicates of the same molecular weight (**Figure 5.7**). This sensitivity is highest for samples in the 2.5 -10 wt % range, where phase transitions are identified for all P3HT blends of all molecular weights (**Figure 5.8**). Regardless of the crystallinity or length of P3HT, we can determine that the addition of about ~5 wt % P3HT will induce a change in the structure of the elastomer template. Moreover, order is also lost in all P3HT blend samples when there is an overloading of the system. At the highest temperatures, weight percentages, and molecular weights (10-15 wt% 77 kDa RRe-P3HT processed at 250 ºC) the structure is affected drastically, leading to a collapse of structure and decreased order.

Additional procedural modifications, such as casting solvent (**Figure 9,10,11**) and the use of a vacuum oven (**Figure 12**) for full drying do not have significant impact on structure. The variation in solvent choice when drop cast and pressed at low temperatures is minimal. At 250 ºC pressing temperature the semi-crystalline RRe-P3HT cast from toluene shows increases in range and modifications from the chloroform cast samples. The fully amorphous RRa-P3HT sample does not show this variation in toluene. When processed at a temperature above the melting point of the crystalline regions of the RRe-P3HT, then the structure changes considerably. The fully amorphous RRa-P3HT blends do not have these crystalline domains, and subsequently do not display this variation at 250 ºC. We believe this is due to the lower solvent quality of the toluene encouraging self-segregation of semi-crystalline RRe-P3HT in solution that modifies the cast structure slightly. The use of the vacuum oven for additional drying did not produce significant modifications in morphology (**Figure 12**). This suggests that our samples are fully dry from overnight atmospheric off-gassing, or if any solvent remains in the baseline processing method, then it is negligible.

Using this processing method, composite blend samples can also be flow-aligned at the higher temperatures, leading to an ordered and oriented structure. By using a rectangular shim and creating a constrained flow route during the heat pressing stage, the material is forced to flow in an intended direction. During this process, the domains orient in the direction of flow. This is observed in 2D SAXS images (**Figure 5.15**), with a clear increase in orientation between radially

pressed and intentionally aligned samples. All flow-aligned samples were indexed to be hexagonally packed cylinders (**Figure 5.14**), but with the changed processing method, we believe the mixed phases align at different rates. We anticipate the hexagonally packed cylinder domains are easier to align with than the lamellar domains, leading to disproportionate alignment during flow (**Figure 5.13**). The region of intermediate P3HT loadings that were identified as mixed and lamellar-rich phases in unaligned samples showed significantly less alignment which we anticipate could be due to differences in alignment of cylindrical vs lamellar domains.

Within the flow-aligned series we also see variation in the extent of alignment as the wt % of RRe-P3HT increases. For pure PS-PI-PS, which forms consistent hexagonally packed cylinders, the material aligns well and there are no signs of orientation at orthogonal directions (**Figure 5.13**). When more conjugated polymer is added and the phase shifts towards mixed phases, domains begin to orient in inconsistent directions. At P3HT loadings of 2.5 - 7.5 wt % there are evident features in the flow direction, which is indicative of poor macroscopic orientation. This may be a result of the relative ease of alignment within mixed phase domains, as the flow aligned the more the leaving the lamellar domains unaligned. At higher loadings, 12.5 and 15 wt % of RRe-P3HT, the matrix structure is more disordered but identified as primarily consisting of hexagonally packed cylinders. In this region, the system again shows improved alignment and orientation. There appears to be a relationship between the ability to align a flowed polymer blend and its phase make-up, with more consistent blends producing higher orientation.

Post processing treatments can modify the structure of the polymer substantially. By processing solution cast samples at equivalent temperature exposure but without the addition of pressure from the heat press (**Figure 16** and **Figure 17**), we can identify how the combination of pressure and temperature modifies the morphology of the blends. We are able to establish that processing induced alignment requires pressure, as none of the annealed solution cast samples showed any alignment (**Figure 16**). In temperature processed only blends, the addition of conjugated polymers seems to change the resilience of the template to processing and annealing techniques. The 'bare' PS-PI-PS elastomer shows changes in alignment, layer spacing, and domain homogeneity, but to a lesser extent than the blends (**Figure 17**). This suggests the addition of additives affects the extent of these structural changes. At the low (100 ºC) temperature, there is not considerable changes observed as the glass transition temperature is barely surpassed, not allowing the material to anneal properly. At the medium (150 ºC) temperatures the blends

consistently show increased shifts in peak location and peak width where the PS-PI-PS template shows minimal changes. As the samples are annealed for longer time periods, this trend is maintained. At the highest temperature (250 ºC), both the blends and the PS-PI-PS template are shifted considerably. Blends still display an increased tendency to flow and to disorder, but all materials had changes in spacing and order due to annealing. Due to this increased tendency to deform, we anticipate that the addition of P3HT in temperature only processing reduces the resilience of the PS-PI-PS to processing. We also see similar trends when samples have been fully processed and are then annealed (**Figure 5.18**). For pure PS-PI-PS there are slight shifts in both peak width and location as the time spent annealing is increased, but for blended systems the shifts become drastic as more P3HT is added into the system. We anticipate the incorporation of additives into the PS-PI-PS elastomer changes the properties of the resulting blend, which will change how heating and processing affects the resilience of a blend to processing methods.

5.5 Conclusions

We determined that processing modifications can change the morphology of P3HT and thermoplastic elastomer blends in a variety of ways. The addition of pressure and temperature can induce alignment, either random or intentional, and the time and temperature at pressing will affect the structure. Higher temperatures or longer pressing times allow for increased consistency of the structures as well as increased incorporation of additives, such as conjugated polymer, into the established structure. At higher temperatures, the solvent used in dissolving and casting also begins to affect the structure of the final blends. During pressing, these systems will macroscopically align under pressure and increased temperature and can be intentionally aligned using directed flow during processing. The extent of orientation of the phases in the system are dependent on the type and concentration of additives in the composite sample. With annealed samples, we found that the addition of conjugated polymer resulted in blends with altered thermal properties. These property changes resulted in blends with less resistance to annealing than the pure PS-PI-PS, increasing structural disorder.

This work has shown the importance of understanding the interplay between a matrix polymer and conjugated polymer additives, with large changes observed in the micro and macro structure of such composite blends. For polymers that are commercially utilized and industrially processed, known processing changes may be augmented with the addition of additives, and understanding these changes is vital to controlling structure and performance.

5.6 References

1. Subbiah, T., Bhat, G. S., Tock, R. W., Parameswaran, S. & Ramkumar, S. S. Electrospinning of nanofibers. *Journal of Applied Polymer Science* **96**, 557–569 (2005).
2. Knoll, M., Offenzeller, C., Jakoby, B. & Hilber, W. Screen printed sensors fabricated on non-planar surfaces by water transfer print. *Microelectronic Engineering* **209**, 49–52 (2019).
3. Albalak, R. J., Thomas, E. L. & Capel, M. S. Thermal annealing of roll-cast triblock copolymer films. *Polymer (Guildf)* **38**, 3819–3825 (1997).
4. Obara, S. & McGinity, J. W. Influence of processing variables on the properties of free films prepared from aqueous polymeric dispersions by a spray technique. *International Journal of Pharmaceutics* **126**, 1–10 (1995).
5. Chang, J. F. *et al.* Enhanced Mobility of poly(3-hexylthiophene) transistors by spin-coating from high-boiling-point solvents. *Chemistry of Materials* **16**, 4772–4776 (2004).
6. Medeiros, E. S., Glenn, G. M., Klamczynski, A. P., Orts, W. J. & Mattoso, L. H. C. Solution blow spinning: A new method to produce micro- and nanofibers from polymer solutions. *J Appl Polym Sci* **113**, 2322–2330 (2009).
7. Güldal, N. S. *et al.* Real-time evaluation of thin film drying kinetics using an advanced, multi-probe optical setup. *J Mater Chem C Mater* **4**, 2178–2186 (2016).
8. Cummings, J., Lowengrub, J. S., Sumpter, B. G., Wise, S. M. & Kumar, R. Modeling solvent evaporation during thin film formation in phase separating polymer mixtures. *Soft Matter* **14**, 1833–1846 (2018).
9. Qiao, L., Leibig, C., Hahn, S. F. & Winey, K. I. Isolating the effects of morphology and chain architecture on the mechanical properties of triblock copolymers. *Ind Eng Chem Res* **45**, 5598–5602 (2006).
10. Séguéla, R. & Prud'homme, J. Deformation Mechanism of Thermoplastic Two-Phase Elastomers of Lamellar Morphology Having a High-Volume Fraction of Rubbery Microphase. *Macromolecules* **14**, 197–202 (1981).
11. Inoue, T. *et al.* Deformation Mechanism of Elastomeric Block Copolymers Having Spherical Domains of Hard Segments under Uniaxial Tensile Stress. *Macromolecules* **8**, 579 (1970).
12. Wolf, C. M. *et al.* Blend Morphology in Polythiophene–Polystyrene Composites from Neutron and X-ray Scattering. *Macromolecules* (2021) doi: 10.1021/acs.macromol.0c02512.
13. Guo, T. F. & Yang, Y. In situ study on the reorientation of polymer chains in operating polymer diodes. *Appl Phys Lett* **80**, 148–150 (2002).
14. Wach, R. A. *et al.* Enhancement of Mechanical Properties of FDM-PLA Parts via Thermal Annealing. *Macromol Mater Eng* **303**, 1800169 (2018).
15. So, P. & Broutman, L. J. Residual stresses in polymers and their effect on mechanical behavior. *Polym Eng Sci* **16**, 785–791 (1976).
16. Sakurai, S., Umeda, H., Taie, K. & Nomura, S. Kinetics of morphological transition in Polystyrene-block-polybutadiene-block-polystyrene triblock copolymer melt. *J. Chem. Phys* **105**, 8902–8908 (1996).
17. Hadziioannou, G. & Skoulios, A. Melting of Styrene/isoprene Block Copolymers as a Function of Temperature and Time. *Physics of Glassy Polymers* **148**, 3483 (1975).
18. Roesing, M., Howell, J. & Boucher, D. Solubility Characteristics of Poly(3-hexylthiophene). *J. Polym. Sci., Part B: Polym. Phys* **55**, 1075–1087 (2017).
19. Teresa García, M., Gracia, I., Duque, G., de Lucas, A. & Francisco Rodríguez, J. Study of the solubility and stability of polystyrene wastes in a dissolution recycling process. (2009) doi: 10.1016/j.wasman.2009.01.001.
20. Yamazaki, H., Nagasawa, T., Choi, W. & Endo, T. Transformation of vulcanized natural rubber into lower molecular weight polymers and their application to grafted copolymer synthesis with some vinyl monomers. *J Appl Polym Sci* **101**, 4003–4010 (2006).
21. Doucet, M. *et al.* SasView. Preprint at (2022).
22. Doucet, M. *et al.* Sasmodels. Preprint at (2020).
23. Kienzle, P. A. (University of M. C. P., Krycka, J., Patel, N. & Sahin, I. Bumps. Preprint at (2011).
24. broad_peak — SasView 5.0.5 documentation. https://www.sasview.org/docs/user/models/broad_peak.html.

25. Harris, C. R. *et al.* Array programming with NumPy. *Nature* **585**, 357 (2020).
26. Mckinney, W. Data Structures for Statistical Computing in Python. (2010).
27. Hunter, J. D. Matplotlib: A 2D graphics environment. *Comput Sci Eng* **9**, 90–95 (2007).
28. Wolf, C. M. *et al.* Strategies for the Development of Conjugated Polymer Molecular Dynamics Force Fields Validated with Neutron and X-ray Scattering. *ACS Polymers Au* **1**, 134–152 (2021).

Chapter 6: High-χ Parameter Polymers

The work presented in this section is conducted in collaboration with members from Dr Lilo Pozzo's group (Dr. Kiran Vaddi and Karen Li) as well as from Dr. Matthew Golder's group (Sarah Zeitler).

The author would like to acknowledge the contributions of coauthors for the following work and makes no claim of sole contribution to the data.

6.1 Introduction

High-χ parameter polymers are a subsection of copolymers where the components are thermodynamically incompatible with each other. The χ parameter refers to the Flory Huggins interaction parameter that describes the energy required to mix polymers or a polymer and solution. A high interaction parameter means that the energy threshold to mix is high, and the two components will not mix easily, if at all. When bonded together as in a copolymer, each block is heavily encouraged to self-assemble, creating micro-phase separated domains. While this is achievable with other systems, high-χ copolymers can be made with low molecular mass allowing for very small feature sizes, some less than 10 nanometers[1]. These materials are used in wide range of fields including semiconductors[2], nanolithography[3–5], coatings[6], and encpasulations[7,8]. With nano scale resolution and printing technologies, the applications of a well understood high-χ parameter polymer can vary considerably.

We look to utilize the predisposition of these immiscible materials to self-assemble and form encapsulated stable structures in as ionic-conducting components formulated Organic Mixed Ionic Electronic Conductors (OMIEC's). OMIEC materials display both ionic and electronic properties, and the balance between these two methods of transport is vital for producing useful materials[9]. The subsection of OMIECs that we are specifically focusing on utilizes a conductive conjugated polymer for electronic transport and a polymer electrolyte, with added salt, for ionic transport. To promote the formation of long-range ordered charge carrying structures we aim to encapsulate and stabilize the conductive polymer within self-assembled structures of high-χ copolymers that are preserved after casting and processing. The combination and structure of the blends will be addressed in more detail in Chapter 7. In this chapter we focus primarily on the analysis of the matrix polymer, which must be able to form stable, self-assembled structures, ideally in a cylinder or elongated form. High-χ parameter block copolymers are good candidates for this possibility because they are prone to self-assemble in the right environment to produce

structures with hydrophobic cores where a hydrophobic conjugated polymer can be included. These self-assembled structures would also expose hydrophilic ionic-conducting polyether side chains that have been shown to increase OMIEC performance[10,11].

In order to use these materials purposefully in OMIEC blends, the self-assembly of high-χ parameter copolymers must first be understood in isolation. This chapter focuses on the experiments associated with the investigation of the high-χ polymer of interest and serves as the basis for work discussed in Chapter 7.

6.2 Materials and Methods

6.2.1 Materials

The polymers used in this work are high-χ parameter copolymers synthesized and compositionally analyzed by Sarah Zeitler. Information on the synthesis method is provided in section 6.2.2, and information on composition is reproduced here as given. Additional calculations made for fitting and material parameters are made using the values determined in **Table 6.1.**

The copolymers used are made from a hydrophilic di (ethylene glycol) ethyl ether acrylate (DEGEEA) and a hydrophobic heptafluorobutyl acrylate (HFBA) block, shown in **Figure 6.1a**. In this work the DEGEEA block is referred to as the Ethylene Glycol (EG) block and comes in two forms. The first is a di (ethylene glycol) (DEG) with two repetitions of the ethylene glycol monomer unit, and the second is a poly (ethylene glycol) (PEG) with more repetitions of the ethylene glycol monomer unit. The HFBA block is referred to as the fluorinated (F) block and there are no variations made in the monomer used. The PDEEGA-block-PHFBA (EGF) copolymer is made in 6 different forms, with variation in block length to modify the ratio between the EG block and the F block, with two EGFs based on PEG and four based on DEG, in order to investigate the effect of modifying the length of side chain (PEG v DEG) in the copolymer. All polymers are listed in **Table 6.1**.

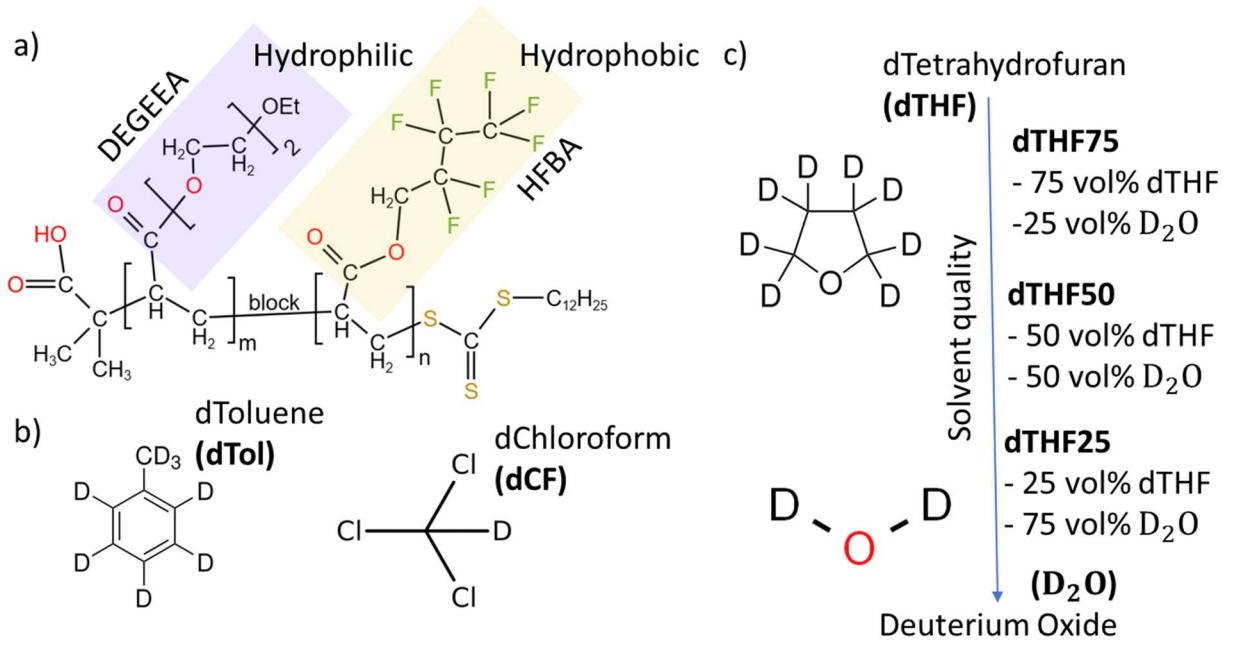

Figure 6.1: a) molecular structure of the high-χ parameter copolymer used in this work b) solvents dTol and dCF as well as SLDs of solvents, each polymer component, and an estimate for full polymer SLD. c) dTHF to D_2O volume series as well as SLD of each ratio.

A variety of solvents were used in this work. The deuterated chloroform (dCF) and toluene D-8 (dTol) were supplied by the Australian Nuclear Science & Technology Organisation (ANSTO), and purchased from Sigma Aldrich (St. Louis, MO). The deuterated tetrahydrofuran (dTHF) was purchased through Novachem, an Australian supplier for Cambridge Isotopes (Tewksbury, MA). Deuterium oxide (D_2O) was supplied by ANSTO through their deuteration facility. The dCF, dTol, and a portion of dTHF were used as received. Additional solutions were made at set volume ratios of dTHF and D_2O to adjust the solvent quality while maintaining a constant scattering length density (SLD). Specified mix ratios and SLDs are shown in **Table 6.2**.

Material	**Calculated SLD ($\frac{10^{-6}}{Å^2}$)**	**Density ($\frac{g}{cm^3}$)**	**Source**
Chloroform-D (**dCF**)	3.16	1.5	VWR[13]
Toluene-D8 (**dTol**)	5.66	.943	VWR[14]
Tetrahydrofuran-D8 (**dTHF**)	6.35	.985	VWR[15]
75 vol % dTHF 25 vol % D_2O (**dTHF75**)	6.35	Using vol % on NIST SLD calculator	
50 vol % dTHF 50 vol % D_2O (**dTHF50**)	6.36	Using vol % on NIST SLD calculator	

25 vol % dTHF 75 vol % D_2O (**dTHF25**)	6.36	Using vol % on NIST SLD calculator	
Deuterium Oxide (**D_2O**)	6.36	1.11	PubChem[16]
EGF (**Full high-χ copolymer**)	1.3	SLD extracted from free chain fit	
PDEGEEA block (**EG**)	0.82	1.10*	Estimated[17,18]
PHFBA block (**F**)	2.65	1.4*	Estimated[19]

Table 6.1: SLDs for all materials calculated from the NIST Neutron activation and scattering calculator[20] using provided densities. *Densities were estimated for each block of the EGF from monomer densities and the estimated densities shown were used in calculations.

All block lengths, molecular weights and dispersity are presented in **Table 6.1**. The block percentages for each polymer were calculated using proton Nuclear Magnetic Resonance (NMR). All of the DEG-based polymers block percentages were calculated using deuterated chloroform NMR's, while the PEG-based polymers block percentages were calculated using acetone D-6. The block length and molecular weight for the EG block was measured using Gel Permeation Chromatography (GPC) in chloroform. Using the block percentages and information collected with GPC, the block length and molecular weight for the F block as well as the molecular weight for the total polymer were calculated.

Code	Short Form	Block % (EG)	Block % (F)	Block Length (EG)	Block Length (F)	M_n (g/mol)	Dispersity
DEG50F25	D50F25	60	40	42	28	15060	1.16
DEG50F50	D50F50	48	52	43	46	19805	1.06
DEG50F75	D50F75	37	63	44	74	27077	1.35
PEG50F25*	P50F25	55	45	40	33	27647	1.7
PEG50F50*	P50F50	50	50	57	57	41487	1.36

Table 6.2: All polymer information for each of the polymers used in this work, along with reference names for each polymer.

6.2.2 Polymer Synthesis

The synthesis method is described in detail in *Mechanoredox Catalysis Enables a sustainable and Versatile Reversible Addition-Fragmentation Chain Transfer Polymerization Process*[21], published by collaborators. These polymers were synthesized and compositionally analyzed by Sarah Zeitler and the composition has been reproduced in **Table 6.2** as given.

This method utilizes the reversible addition fragmentation chain transfer (RAFT) polymerization method, which is a commonly used living synthesis method with a wide range of functional groups that can be utlized[22]. This method is combined with mechanical energy through the use of a ball mill with specially chosen additives to encourage polymer growth. The use of a ball mill device greatly reduces the solvents required to trivial amounts and allows for immiscible materials to be processed in batches[23]. Traditional techniques require a co-solvent, and for high-χ parameter polymers that have very few, if any, shared good solvents, polymerization becomes difficult. Synthesis of the polymers used in this work start with batch polymerization of the hydrophilic DEGEEA block, and once confirmed to the proper length, the monomer for the second HFBA block is added directly with additional catalyst. The combination of the two are processed for additional time, and the resulting product is a combined diblock copolymer with a hydrophilic PDEGEEA block and a hydrophobic PHFBA block. These block lengths are refinable for length and can be modified through changes in the monomers provided. Additional information for the synthesis can be found in the paper above[21].

6.2.3 Solution Preparation

Carefully weighed portions of the EGF copolymer is first dissolved in the solvent of choice and heated on a hot plate at 60 ºC in a sealed vial. These samples are then further diluted with additional solvent to reach the desired concentration, still remaining on the hot plate to ensure adequate dissolution and mixing. Each sample was then loaded from the hotplate into 2 mm quartz Hellma cells and was stored at 26ºC for an extended period of time (15-18 hours) before being measured in the small angle neutron scattering (SANS) instrument. Initial samples run immediately after preparation were shown to continue to assemble while being measured (**Figure 6.2a**). Each sample is composed of three measured configurations stitched together, and as some samples continued to assemble between configurations, the features did not agree at the overlapping points. When the samples were allowed sufficient time to achieve a steady state of assembly (15-18 hours), there is no observed structural evolution while being measured (**Figure 6.2b**).

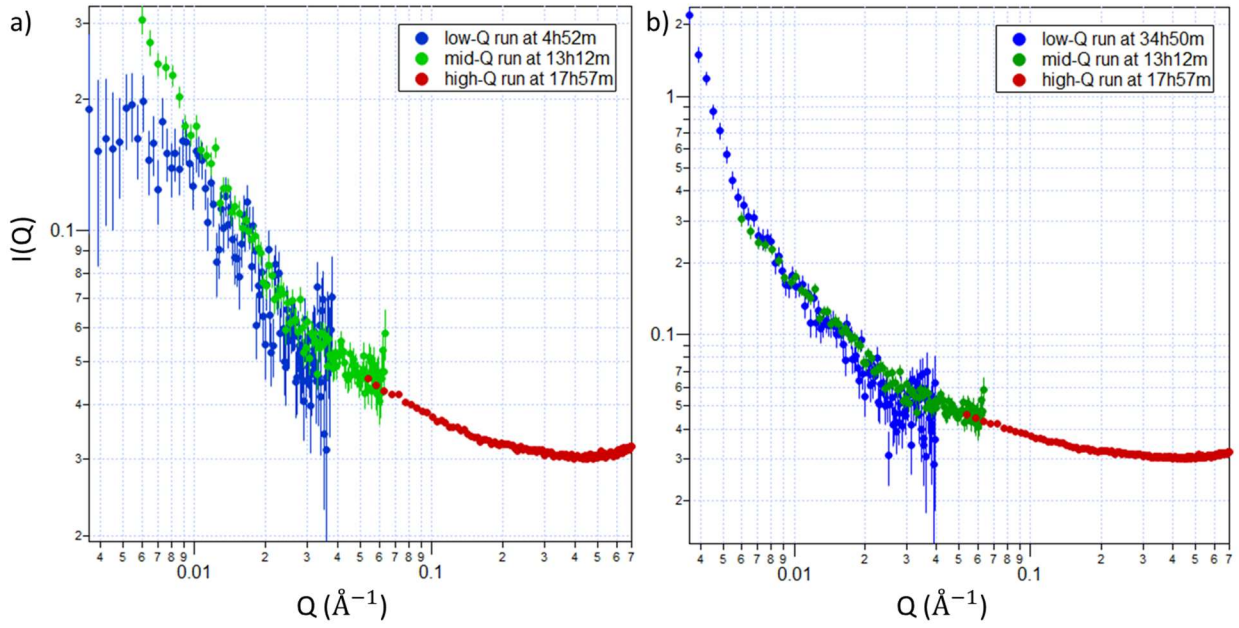

Figure 6.2: SANS data of DEG50F75 in dCF split into individual configurations labeled with time since creation for a) unrested 20 m low-Q measurement and b) rested 20 m low-Q measurement.

Solutions made of the dTHF/D_2O blended system were prepared and dissolved fully in dTHF before the D_2O was added immediately before loading to Hellma cells. Any assembly in solution was allowed to occur within the Hellma cells during the allotted 15-18 hour resting window.

6.2.4 SANS

Small Angle Neutron Scattering (SANS) measurements were collected at the Quokka beamline at the Open Pool Australian Lightwater (OPAL) source within the Australian Nuclear Science and Technology Organisation (ANSTO)[24]. SANS data was collected in three configurations to span the full Q range. All non-lenses configurations used 6Å ± 0.10Å wavelengths, the low-Q lens configuration used 8.1Å ± 0.10Å. Samples were measured for differing times and configurations due to their differing scattering intensity. Low scatterers (e.g., samples in dCF) were measured with low-Q collected at 20 m sample to detector distance (2400 seconds), mid-Q collected at 12 m sample to detector distance (1200 seconds), and high-Q collected with 1.3 m sample detector distance (600 seconds). Samples with mid ranged scattering (e.g. samples in dTHF and dTol) were measured with low-Q collected at 20 m sample to detector distance with lenses (1600 seconds), mid-Q collected at 12 m sample to detector distance (800 seconds), and high-Q collected with 1.3 m sample detector distance (400 seconds). Samples with

high scattering (e.g. dTHF/ D_2O mixed samples) were measured with low-Q collected at 20 m sample to detector distance with lenses (900 seconds), mid-Q collected at 12 m sample to detector distance (500 seconds), and high-Q collected with 1.3 m sample detector distance (300 seconds).Samples were loaded into 2 mm quartz Hellma cells and mounted into aluminum holders placed into a temperature controlled 20 slot sample environment set to 26 ºC. SANS data were reduced, combined, and background subtracted using the Quokka macro in the NIST SANS package for Igor Pro[25]. Further analysis of SANS data was performed using the SasView[26]/sasmodels[27] and bumps[28] packages for Python.

6.2.5 SANS Data Analysis

6.2.5.1: Free Chains in solution

Samples that are well dissolved in the solvent are modeled with the flexible cylinder model, which describes the scattering of semi-flexible polymers with excluded volume[29]. For model simplicity, the two blocks are treated as a single uniform system and a combined SLD of 1.3 is used to fit the data. All fit parameters are assumed to be constant over the length chain, even though each block may have slight variations in radius or Kuhn length.

6.2.5.2: Spherical Micelles with Gaussian Chain Corona

The full equation describing scattering for a sphere with a self-associating core and a corona of gaussian chains surrounding the core is described by equation 6.1 and a schematic is shown in **Figure 6.3b**[30]**.**

$$F_{mic}(q) = N^2{\beta_s}^2F_s(q) + N{\beta_c}^2F_c(q) + 2N^2\beta_s\beta_cS_{sc}(q) + N(N-1){\beta_c}^2S_{cc}(q) \quad (6.1)$$

where N^2 is the number of chines in the micelle, $\beta_s$is the scattering length density of the sphere core, β_c is the scattering length density of the chains in the corona and all other factors are as follows.

The form factor for a sphere is described by $F_s(q)$ as a function of q and sphere radius (R).

$$F_s(q) = \Phi^2(qR) \quad (6.2)$$

$$\Phi^2(qR) = \frac{3[\sin(qR) - qR\cos(qR)]}{(qR)^3} \quad (6.3)$$

The form factor for the flexible chains in the corona are described as follows:

$$F_c(q) = \frac{2[e^{-x} - 1 + x]}{x^2} \quad (6.4)$$

where $x = {R_g}^2q^2$

The structure factor for the interactions between the sphere and each of the chains in the corona is shown in equation 6.5.

$$S_{sc}(q) = \Phi(qR)\psi(qR_g)\frac{\sin(q[R + dR_g])}{q[R + dR_g]} \tag{6.5}$$

where R is the radius of the core, R_g is the radius of gyration of the chains, and $\psi(qR_g)$ is shown in equation 6.6.

$$\psi(qR_g) = \frac{[1 - e^{-(qR_g)}]}{qR_g} \tag{6.6}$$

The structure factor for the interactions between each chain surrounding the core is given in equation 6.7.

$$S_{cc}(q) = \psi^2(qR_g)\left[\frac{\sin(q[R + dR_g])}{q[R + dR_g]}\right]^2 \tag{6.7}$$

This equation assumes that the core is 'dry' with the only volume and SLD contributions emerging from the polymer in the core, which in our case is assumed to be the hydrophobic fluorinated polymer. However, we do not anticipate the cores to be fully 'dry' and believe that the core is often partially solvated and has a volume fraction (ϕ_{sol}) of solvent that is expanding the volume of the core. Similar systems have been addressed with similar solvated spheres, and fitting was approached by allowing both the radius of the core R_c and the number of chains in the micelle N_{agg} to be fit. The solvent volume fraction is then calculated using the volume of the polymer block in the core (V_{core}) and equation 6.8. [31]

$$(1 - \phi_{sol})\frac{4}{3}\pi {R_c}^3 = N_{agg}V_{core} \tag{6.8}$$

The volume of the polymer block in the core (V_{core}) and the volume of the poylmer block in the corona (V_{corona}) are fixed parameters calculated from polymer architecture and composition in **Table 6.2**.

$$V_{core} = DOP_F * Conversion * \frac{\rho_F * Mw_F}{NA} \tag{6.9}$$

$$V_{corona} = DOP_{EG} * Conversion * \frac{\rho_{EG} * Mw_{EG}}{NA} \tag{6.10}$$

Where NA is Avogadro's number, ρ_i is the density of the monomer, Mw_i is the molecular weight of the monomer, conversion is 1e24 to convert from cm^3 to scattering relevant $Å^3$, and

DOP_i is the degree of polymerization for the block of interest. These were set for each polymer and unchanged throughout fitting and calculations.

6.2.5.3: Cylindrical Micelles with Chain Corona

The full equation describing scattering for a cylinder with a self-associating core and a corona of gaussian chains surrounding the core is described by equation 6.11 and a schematic is shown in **Figure 6.3c**[30]**.**

$$F_{mic}(q) = N^2{\beta_s}^2 F_{cs}(q,R)F_L(q,L) + N{\beta_c}^2 F_c(q) + 2N^2\beta_s\beta_c S_{sc}(q) + N(N-1){\beta_c}^2 S_{cc}(q) \quad (6.11)$$

where N^2 is the number of chines in the micelle, $\beta_s$is the scattering length density of the sphere core, β_c is the scattering length density of the chains in the corona and all other factors are as follows.

The form factor for the cross-section of the cylinder is described by $F_{sc}(q,R)$ as a function of q and sphere radius (R).

$$F_{cs}(q,R) = \left[\frac{2B_1(qR)}{qR}\right]^2 \quad (6.12)$$

where B_1 is the first order Bessel function of the first kind. The longitudinal form factor for a long cylinder is described by $F_L(q,L)$, a form factor of an infinitely thin rod.

$$F_L(q,L) = \frac{2Si(qL)}{qL} - \frac{4\sin^2(\frac{qL}{2})}{q^2L^2} \quad (6.13)$$

where

$$Si(x) = \int_0^x t^{-1}\sin t\, dt \quad (6.14)$$

The form factor for the flexible chains in the corona are described as follows:

$$F_c(q) = \frac{2[e^{-x} - 1 + x]}{x^2} \quad (6.15)$$

where $x = {R_g}^2 q^2$

The structure factor for the interactions between the cylinder and each of the chains in the corona is shown in equation 6.16.

$$S_{sc}(q) = \psi(qR_g)\frac{2B_1(qR)}{qR}B_0\left[q\left(R + dR_g\right)\right]F_L(q,L) \quad (6.16)$$

where R is the radius of the core, R_g is the radius of gyration of the chains, B_0 is a zeroth order Bessel function of the first kind, and $\psi(qR_g)$ is shown in equation 6.6.

The structure factor for the interactions between each chain surrounding the core is given in equation 6.17.

$$S_{cc}(q) = \psi^2(qR_g)^2 B_0\left[q\left(R + dR_g\right)\right]^2 F_L(q, L) \tag{6.17}$$

These structures are also presumed to not have 'dry' cores and are fit with a ϕ_{sol} parameter which is used to calculate the number of chains in a single micelle.

6.2.5.4: Macroscopic Phase Separation

A portion of the samples investigated were identified as macroscopically phase separated. These samples are not fit with a shape dependent model. Select samples were fit with a shape independent Guinier fit to estimate the size of the visible feature, which is anticipated to correlate with the size of the phase-separated domains.

$$I(q) = scale * e^{\left[\frac{-Q^2 {R_g}^2}{3}\right]} + background \tag{6.18}$$

where R_g is the radius of gyration of the feature and a metric of size.

6.3 Results

To cover the full range of solvent quality, interaction potentials, and concentration effects, we ran all polymers in multiple solvents, with a few selected samples run at multiple concentrations. This large collection of samples displayed multiple structures as the solvent quality, polymer architecture, and concentration were all changed. These structures fall into four categories described in **Figure 6.3**. The first subsection of structure is free chains in solution, and an example dataset and a schematic for free chains is given in **Figure 6.3a**. These are polymer chains fully dissolved in solution without aggregation. The 1D data of these structures show a smooth featureless curve that levels out to a Guinier plateau within the Q range observed[32]. The second structure category is spherical micelles, shown in **Figure 6.3b**. These are collections of chains that assemble with the hydrophobic fluorinated blocks forming a spherical core, surrounded by a corona of their attached hydrophilic EG blocks. These 1D plots are characterized by a high-Q hump, a sharp increase in intensity in mid-Q, and a flattening at low-Q (Guinier region). The feature at high-Q is related to the size of the chains in the corona, while the feature in mid-Q is dependent on the number of chains aggregating in the micelle as well as the radius of the core. A few of these spherical samples show a sharp increase at low-Q, which is indicative of macro scale

aggregation or a collection of these spherical micelles coming together to form aggregates of discrete micelles. Shown in **Figure 6.3c** is a 1D plot and schematic for cylindrical micelles, which are a collection of EGF chains aggregated with a cylindrical core of fluorinated blocks surrounded by a corona of the attached hydrophilic EG blocks. These 1D datasets are characterized with the spherical features for radius of gyration of the EG chains, the radius of the core, and the aggregation number, but also by an upturn at low-Q with a power-law 'slope' of -1. This power law dependence is characteristic of long cylinders and indicates a total cylinder length, or Guinier turnover, which is outside of our measurable Q range. The final categorization of samples is shown in **Figure 6.3d**, corresponding to phase separation. These samples are disordered large aggregations of EGF chains that are characterized by the lack of features at all Q ranges except for a high-Q change in power-law 'slope'. There is only one phase separated sample that shows a turnover within our measured Q range, and it is fit with a Guinier fit to extract a measure of the size of the aggregations. However, for most of these phase-separated structures, the size of the domains is much larger than we can measure in the available instrument range.

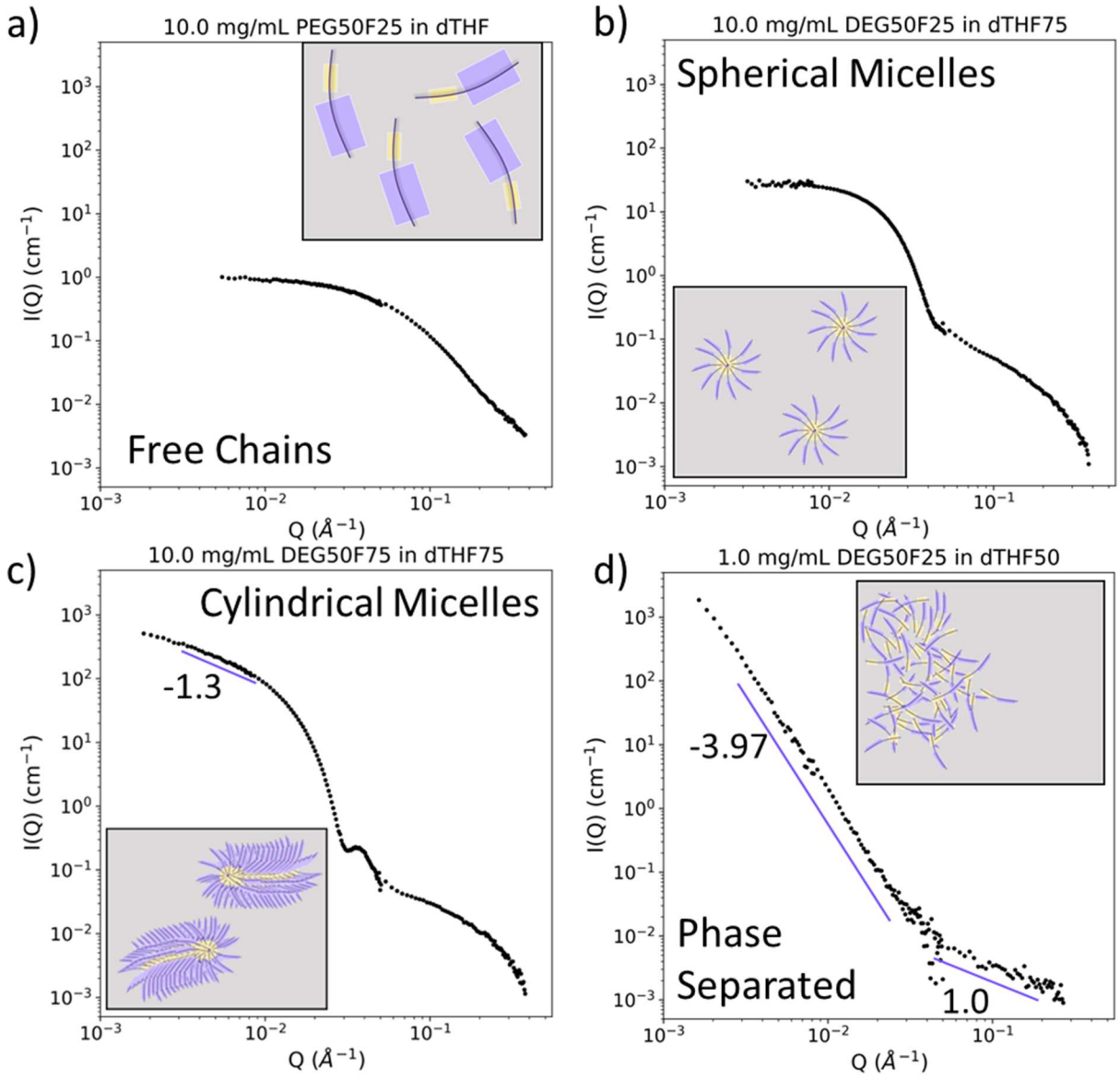

Figure 6.3: Representative plots and schematics of the four identified structures in the sample set, including regions of interest for relevant parameters. The four structures are a) free chains in solution b) spherical micelles with gaussian chain corona c) cylindrical micelles with gaussian chain corona d) phase separated and aggregated chains.

With all samples organized into characteristic structures, we can pull trends and identify the effect of polymer architecture and solvent quality on the structures that are formed. The identified phases for a selection of samples are shown in **Table 6.3**. These samples were all run at a polymer concentration of 10 mg/ml and vary in architecture across the columns and solvent across the rows. All samples identified as "crashed – DNR" in red were made as described in

section 6.2.3 but during the allotted waiting time sedimented and were not run (DNR – Did Not Run).

10 mg/mL	DEG50F25	DEG50F50	DEG50F75	PEG50F25	PEG50F50
dTOL	Free Chain	**Spherical** Micelle	**Spherical** Micelle	**Spherical** Micelle (aggregated)	**Spherical** Micelle (aggregated)
dCF	Free Chain	Free Chain	Free Chain*	Free Chain	Free Chain
dTHF100	Free Chain	Free Chain	Free Chain	Free Chain	Free Chain
dTHF75	**Spherical** Micelle	**Spherical** Micelle	**Cylindrical** Micelle	**Spherical** Micelle	**Spherical** Micelle
dTHF50	Phase Separated	**Cylindrical** Micelle	**Cylindrical** Micelle	**Spherical** Micelle	**Spherical** Micelle
dTHF25	Crashed - DNR	Crashed - DNR	Crashed - DNR	**Spherical** Micelle	**Spherical** Micelle

Table 6.3: All samples run at 10 mg/mL with variations in solvent and polymer architecture. Data has been assigned one of the four structure categories (free chain, spherical micelle, cylindrical micelle, phase separated). Samples that were prepared but sedimented before running are labeled as "Crashed – DNR". *DEG50F75 in dCF appears to be a free chain with a feature in mid-Q. Is not well fit by either free chain or spherical micelle.

From **Table 6.3** we can see some clear trends within a single solvent, which we can fit and analyze. For instance, shown in **Figure 6.4** are all of the EGFs in the two best solvents, dCF in **Figure 6.4a** and dTHF in **Figure 6.4b**. Most of the polymers are freely dissolved chains in both solvents, indicating these solvents are good solvents for the EGF as a whole. We can see that in **Figure 6.4a** the intensity is reduced, and the noise is increased due to a lower contrast between the EGF (SLD ~ 1.3e6 $Å^{-2}$) and dCF (SLD = 3.15e6 $Å^{-2}$). The lowered contrast reduces the confidence in the data (i.e., high background and noise relative to signal), but all efforts to ensure quality fits are taken. All free chain samples are fit with the flexible cylinder model used to describe freely dissolved semi-flexible polymer chains as described in 6.2.5.1.

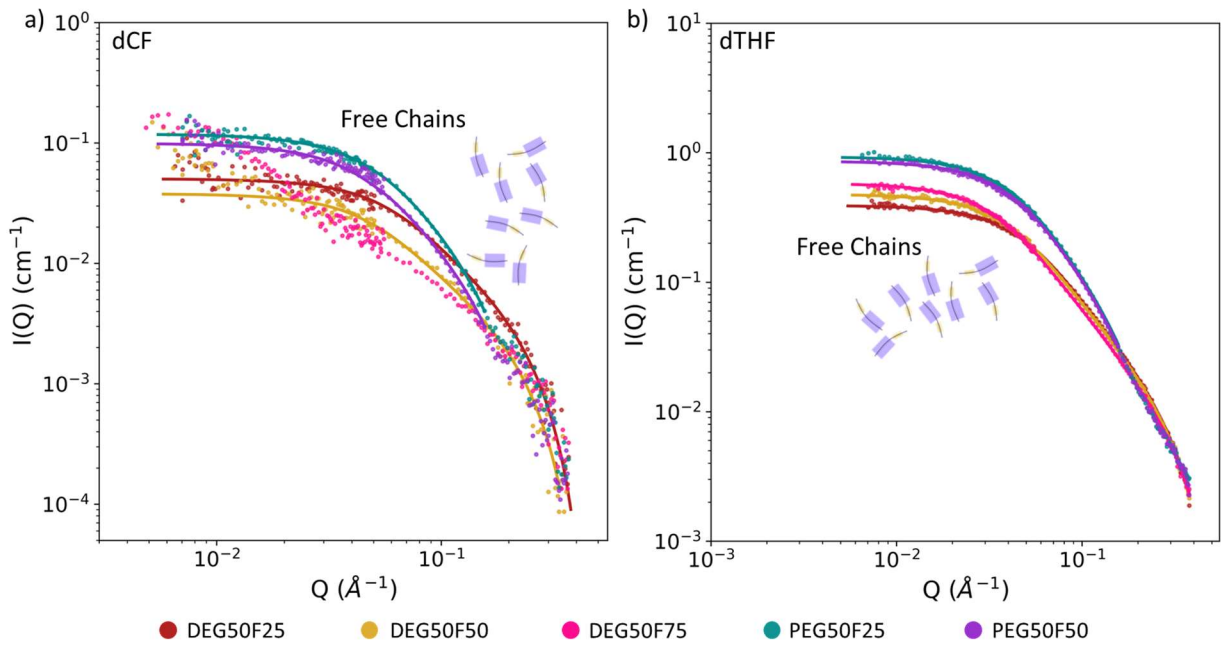

Figure 6.4: SANS data for all EGFs at 10 mg/mL in a) dCF and b) dTHF.

Fits for both the dCF samples (**Figure 6.5 a-c**) and dTHF (**Figure 6.5 d-e**) are shown. A single sample in the dCF fits (marked on **Table 6.3** as a Free Chain*) is not fit well by a free chain and is not included in these fits. This sample shows features similar to some spherical micelles but also is not fit well with a spherical micelle model. From the free chain fits, we have extracted parameters that describe the length (contour length), the Kuhn length (a measure of flexibility) and the radius of the cylinder or chain. The length-based parameter (contour length) is plotted across the total calculated backbone length, while the Kuhn length and radius of the chain is plotted across the architecture changes.

We can see in **Figure 6.5a** and **Figure 6.5d** that for the DEG samples, the contour length of the polymer in solution increases as the backbone length increases. For the PEG samples we do not see an increase in the contour length as the backbone length increases. We also see a large jump in length in the dTHF as the length of the F-block increases in the DEG-based polymers, indicating a large expansion with an increase in the ratio of the length of F to EG-block. The length of the blocks in dTHF are also significantly larger than in dCF. In dCF, the contour length is approximately the calculated backbone length, suggesting that the structures that are fit are most likely a single chain of the EGF in solution. For the dTHF, the contour length is greater than the calculated backbone length, between 1.2 and 2.5 times the calculated length. This suggests that the structure being fit is actually more than one chain of the EGF in assembly. This is still being

investigated, and further work will need to be done in order to determine the specifics of the 'flexible cylinder' being fit.

In **Figure 6.5b** and **6.5e**, we have plots of the Kuhn length over architecture. Kuhn length is a metric of flexibility, and a lower Kuhn length is indicative of a more flexible polymer. We see that there are no large changes in the Kuhn length due to ratio changes of F to EG-block, but we do see a change in the Kuhn length between dCF and dTHF. This is a sign of the solvent quality of dTHF being higher than dCF. We also see in both solvents an increase in flexibility (decrease in Kuhn length) between the DEG-based polymers and the PEG-based polymers. This change is slight, but consistent between the solvents. We predict that the long PEG sidechains sterically inhibit movement and prevent the EGF to be as flexible as their shorter sidechain counterparts in solution.

The chain radius is plotted over architecture in **Figure 6.5c** and **6.5f**. The radius is constant over F-block length changes in each solvent and increases substantially between the DEG-based and PEG-based EGFs. Also of note is the dCF chains have a larger radius than their dTHF counterparts, as well as a larger increase between analogous DEG and PEG samples. This suggests that dCF is a better solvent specifically for the EG-block, as the increase in EG sidechain length creates a larger increase in radius than in dTHF. While the specifics of which solvent is better is not the primary focus of this work, it is important to note that solvent quality will vary between the blocks for a single solvent. We expect this when using a high-χ parameter co-polymer, and it is important to understand how those effects are seen in the data.

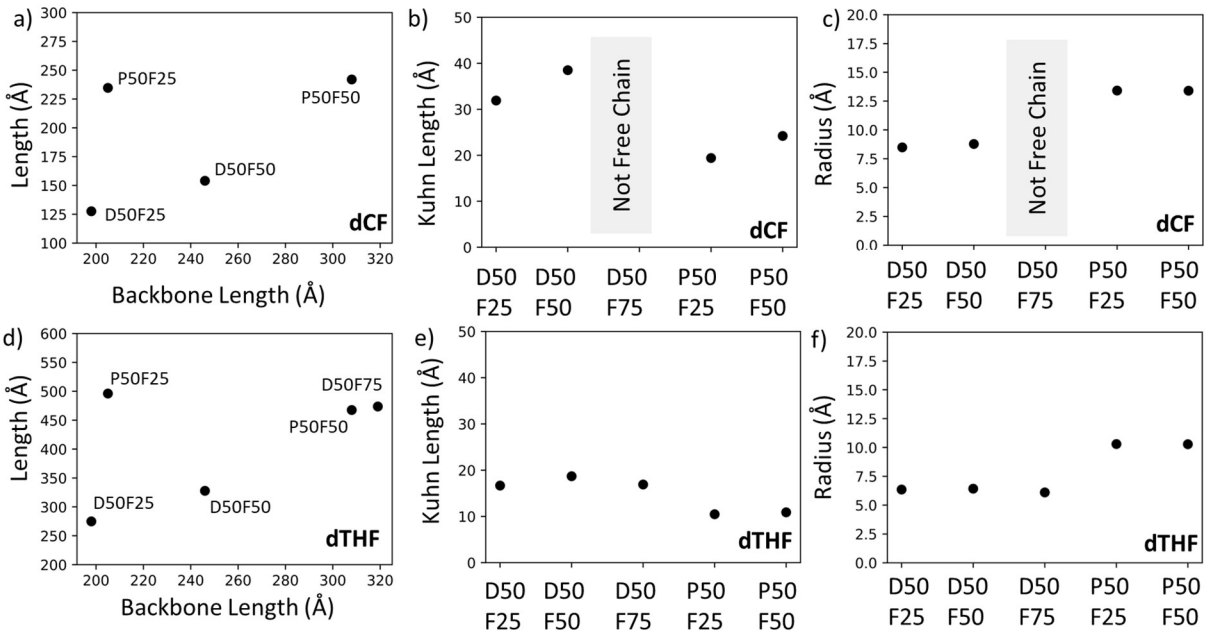

Figure 6.5: Parameters from fitting flexible cylinder models to free chains in both dCF and dTHF. Contor length is plotted against backbone length in a) dCF and d)dTHF. Kuhn length is plotted against backbone length in b) dCF and e) dTHF. Chain radius is plotted against polymer architecture in c) dCF and f) dTHF.

These free chain fits can aid in understanding how the changing architecture and length of the F-block can affect the structure of an EGF in a good solvent. Experiments were also conducted in poor solvents, as shown in **Figure 6.6**, of all EGFs measured in dTol, a worse solvents for all polymers in the system. In dTol, a single EGF is freely dissolved in solution, DEG50F25, which is labled in **Figure 6.6** and removed from the spherical micelle fits in **Figure 6.7**. All other polymers in the solvent are spherical micelles, with sizable structural differences between each EGF. In **Figure 6.6**, we can see a few standout features, such as the decrease in intensity in high-Q feature, as well as the Q-shift in the turnover indicating variation in size. We also see an uptick at low-Q for the PEG-based poylmers asociated with aggregation of spherical micelles.

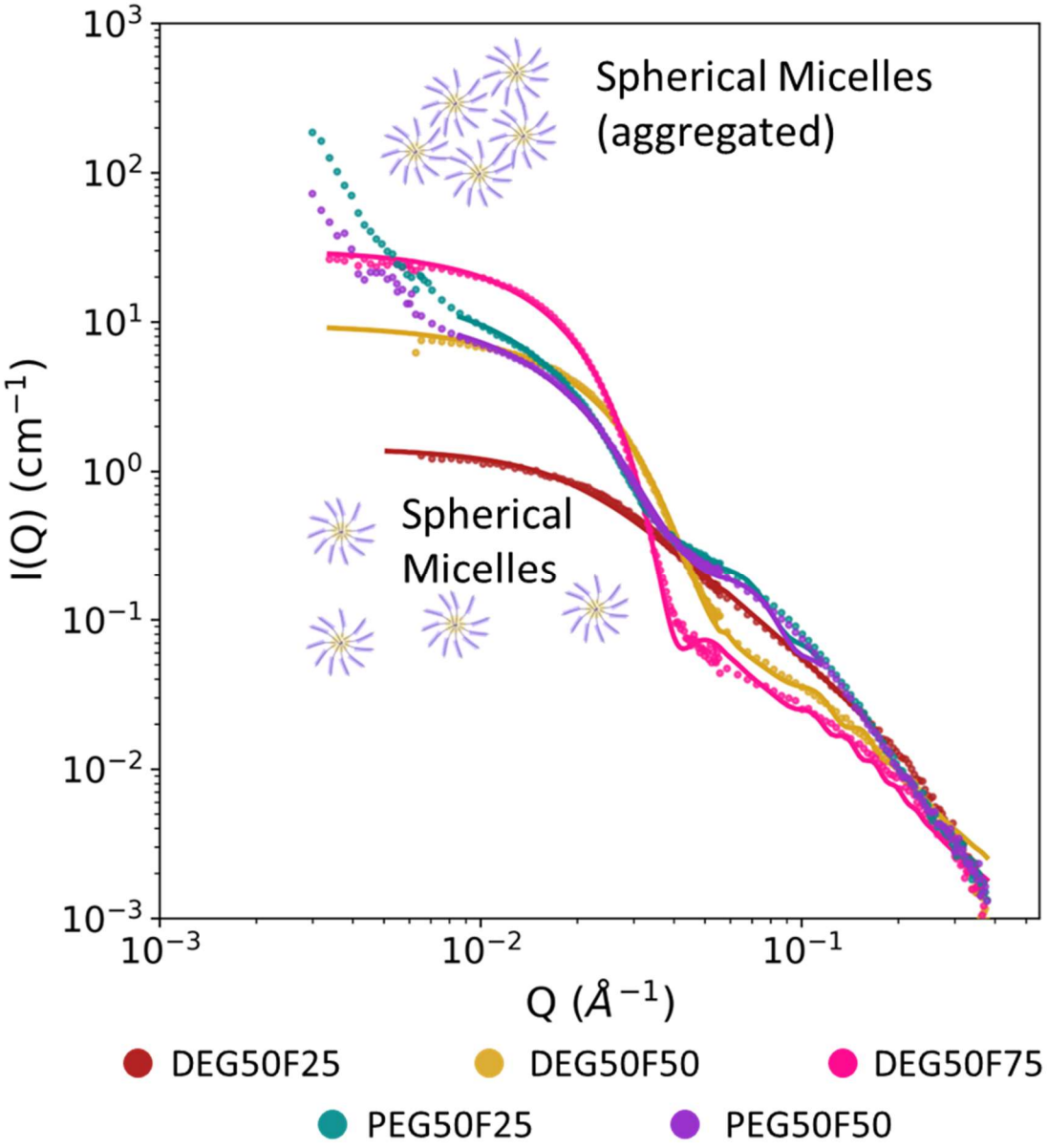

Figure 6.6: SANS data for all EGFs at 10 mg/mL in dTol. The fit for DEG50F25 is a free chain, and all other structures are spherical micelles, with PEG-based polymers producing aggregated spherical micelles.

These polymers were all fit with models of their respective structures, and the spherical micelle parameters are shown in **Figure 5.7**. All parameters are plotted against architecture, allowing for trends due to increasing F-block lengths as well as PEG/DEG modifications. In **Figure 5.7a**, we can see a decrease in the core radius as the length of the F-block of the DEG polymers increases, with a sharp spike upwards in the D50F75 polymer. This spike can be observed

in **Figure 6.6**, as the turnover for the D50F75 data is shifted considerably towards lower Q than the D50F50 polymers. The radius of the PEG series is constant regardless of F-block length and slightly smaller than any of the DEG polymers. This suggests that the length of the fluorinated block increases, larger spherical micelles form, as longer sections of hydrophobic polymer are now encased in the core. For the PEG-based polymers the increased side chain length prevents this growth, instead encouraging a smaller sphere to form.

The radius of gyration of the corona chains is plotted in **Figure 6.7b**. For the DEG-based polymers, as the F-block length increases, the spread of the EG chains in solution decreases with the two highest F-block length polymers having similar sized chains. The PEG corona chains are much larger than any DEG chain, which is expected due to the increased side chain length of the monomer itself. There is a slight decrease in the radius of gyration due to increasing F-block length but is still much larger than its DEG counterpart.

Aggregation numbers measure the number of chains involved in the spherical micelle and are plotted over architecture in **Figure 6.7c**. As the F-block length increases for the DEG polymers there is a significant increase in the number of chains in the micelle. This agrees with observations seen in the core radius, as the sphere is now larger and contains more chains. This is not seen in the PEG polymers as both polymers have similar aggregation numbers that are not affected by the increase in F-block length.

The solvent fraction in the core is calculated from equation 6.8, and relies on the core radius, the aggregation number, and calculated volumes of the fluorinated block for each polymer. Lower solvent volume fractions correlate to a ‘drier’ core or a core that is more resistant to the solvent. These are plotted against architecture in **Figure 6.7d**. For the DEG blocks as the length of the F-block increases, the solvent fraction in the core decreases, suggesting the core is a higher percentage polymer. The PEG base samples also show a decrease in core solvation as the F-block length increases, but both have a slightly higher volume fraction than their DEG counterparts.

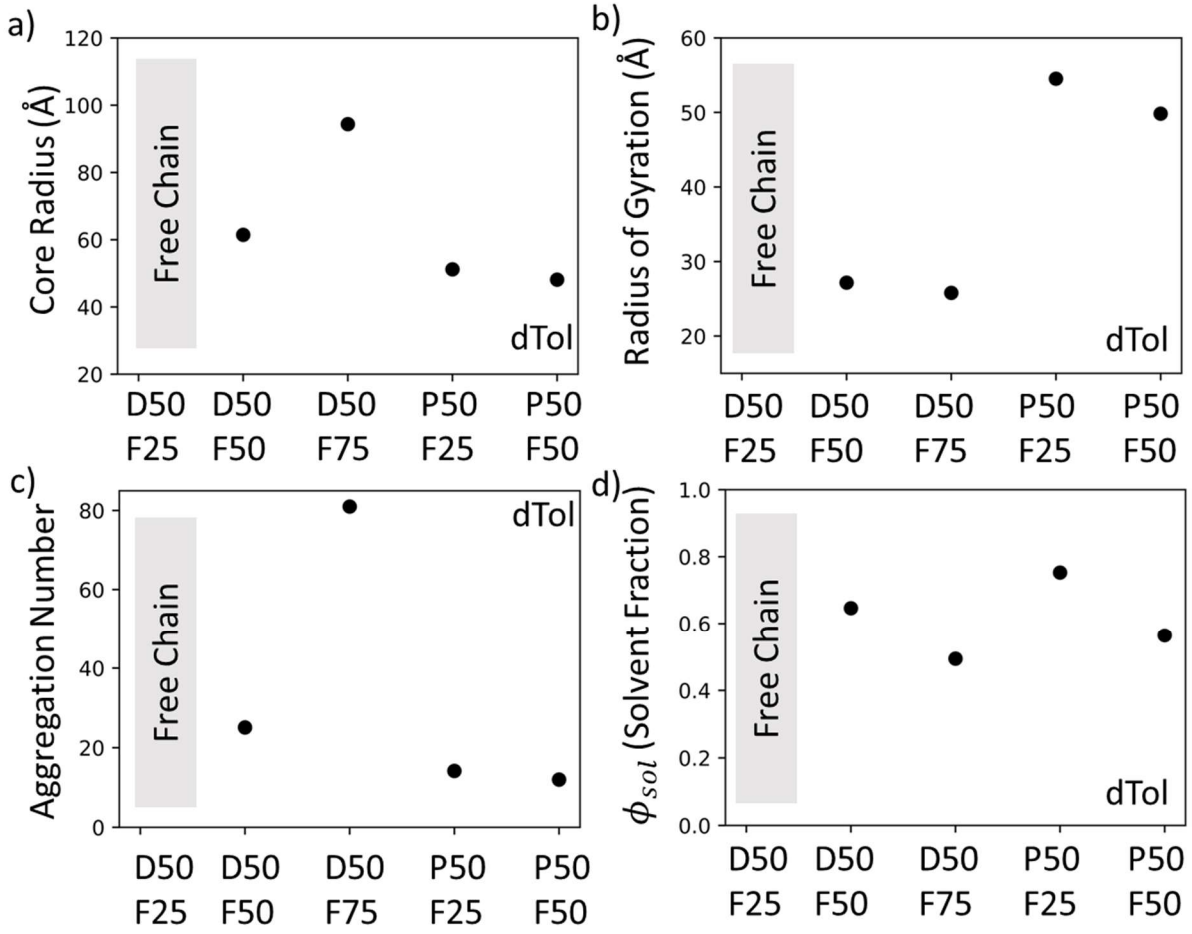

Figure 6.7: Parameters from fitting spherical micelle models to free chains in dTol. The D50F25 sample is removed from the fitting due to being a free chain. All parameters are plotted against poylmer architecture and include a) core radius, b) radius of gyration of the EG chains in the corona c) aggregation number d) volume fraction of solvent in the core.

Another interesting solvent series to pull from **Table 6.3**, is the dTHF to D_2O series. This series is special as the SLD of the dTHF and the D_2O have negligible differences (dTHF = 6.35, D_2O = 6.36). The contrast between the two being zero allows us to use a miscible set of solvents to adjust the solvent quality of a system without adding scattering between molecular domains that can be created in non-ideal mixtures the solvent. We have already addressed the structures found in dTHF in **Figure 6.4** and **Figure 6.5**, but with a decrease in solvent quality we see significant changes in structure as seen in **Figure 6.8b.** All DEG-based polymers form a micelle, with the lower F-block length polymers forming spherical micelles, and the longest F-block length (DEG50F75) polymer forming a cylindrical micelle. This cylindrical micelle is considered to be a

long cylinder with a radius of 100 Å and a length of ~1110Å. The radius of gyration of the EG chains in solution is in trend to all of the observed DEG values of approximately 25 Å and the solvent fraction is approaching zero, suggesting the core is very 'dry'. In the high-Q region associated with EG chains size, we see a decrease in intensity and shift in that feature. Further towards mid-Q we see a shift towards a low-Q of the turnover of the feature, indicating an increase in the radius of the sphere. At low-Q we see the characteristic ~ -1 power law slope associated with cylindrical micelles for the DEG50F75 polymer only.

a)

10 mg/mL	dTHF75
DEG50F25	**Spherical** Micelle
DEG50F50	**Spherical** Micelle
DEG50F75	**Cylindrical** Micelle

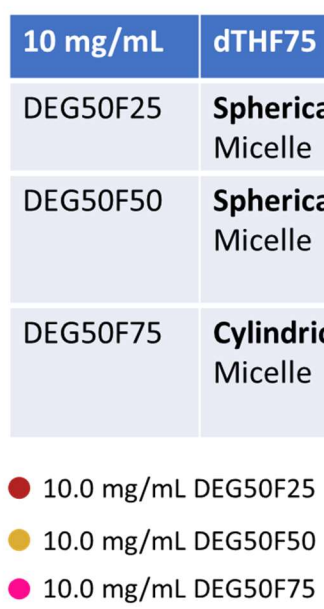

b)

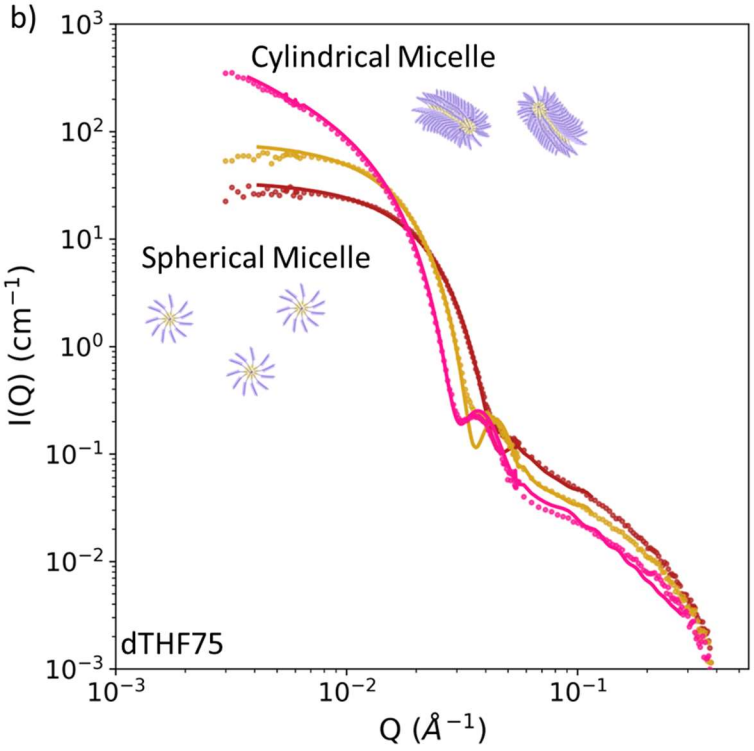

Figure 6.8: a) relevant section of **Table 6.3** b) SANS data for all DEG-based EGFs at 10 mg/mL in dTHF75 series. The fit for DEG50F75 is a cylindrical micelle, and all other structures are spherical micelles.

Observations in **Figure 6.8** are confirmed in the spherical fits shown in **Figure 6.9**. Fits for the PEG counterparts are also included, although not shown in **Figure 6.8**. As the F-block length increases, the core radius increases, growing from 70 Å for DEG50F25 to 100 Å for D50F50. The PEG samples do not show a marked increase, with only a slight change between the two samples (70 Å to 66 Å). The trend observed with the radius of gyration of the corona side chains is also seen in the fits in **Figure 6.9b,** with increasing the length of the F-block causing a slight decrease

in the radius of gyration. As seen in the dTol (**Figure 6.7**) fits, the PEG blocks have a much higher radius of gyration than the corresponding DEG blocks, which is expected due to the vastly increased side chain length of the monomer. The increased length of the side chain also increases the steric repulsion between neighboring chains, causing them to be more 'stretched' out away from the core. The aggregation number also increases drastically between the D50F25 and the D50F50 samples, with no significant difference observed between the PEG-based polymers. The extent of solvation of the micelle core is also changing with the polymer architecture. In general, higher degrees of polymerization of the F-block causes a 'dryer' micelle core.

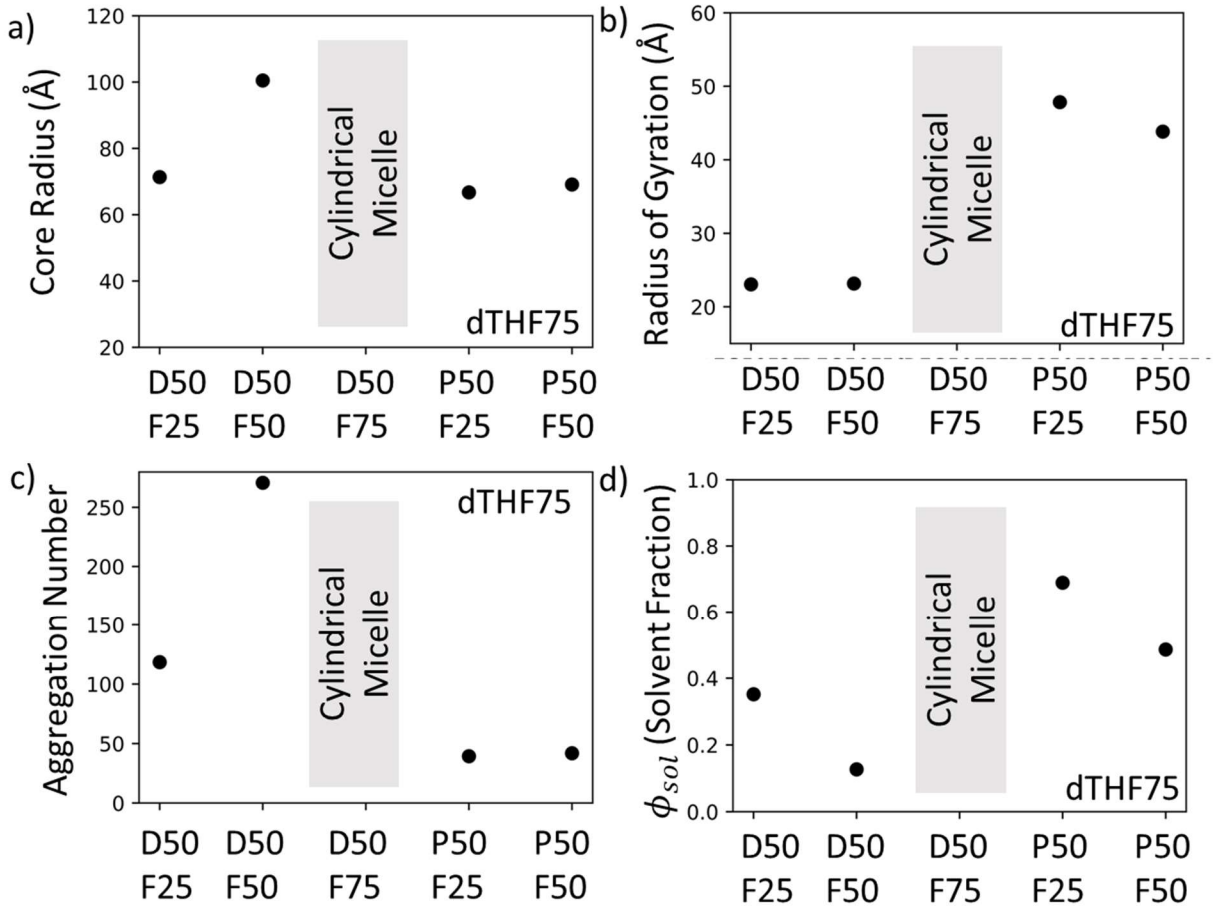

Figure 6.9: Parameters from fitting spherical micelle models to free chains in dTHF75. The D50F75 sample is removed from the fitting due to being a cylindrical micelle. All parameters are plotted against poylmer architecture and include a) core radius, b) radius of gryration of the EG chains in the corona c) aggregation number) volume fraction of solvent in the core.

These previous sample sets focused on how the architecture affects the way the polymer interacts in the solvent, but we can also isolate the effect of solvent quality. We can analyze a single

polymer architecture as a function of solvent quality by taking advantage of the miscibility of dTHF and D_2O. A series of interest is shown in **Figure 6.10**, with the relevant portion of **Table 6.3** reproduced in **Figure 6.10a**. This is a portion of the dTHF to D_2O solvent quality modification series for the EGF DEG50F50. By decreasing the ratio of the volume of dTHF to D_2O we can worsen the quality of the solvent for the fluorinated block and create higher driving forces for the self-assembly of the EGF in solution. This EGF has short side chains in the EG block and a balanced ratio of hydrophobic and hydrophilic blocks. We can see from **Figure 6.10a**, that there is a structure modification at every new dTHF[X] sample and for the highest volume of D_2O the sample that was made sedimented and it was impossible to run. The 1D data is shown in **Figure 6.10b**, and we can see clear changes between solvents. With pure dTHF, the chain is dissolved freely and does not show signs associated with self-assembly. Once the poor solvent (D_2O) is introduced self-assembly emerges and is evident in the evolution of the SANS profile. With no D_2O added into the system, the chains are dissolved freely, but with 25 vol % D_2O added, the EGF forms spherical micelles. With further increases in the amount of D_2O added into the mixture, cylindrical micelles form. These cylindrical micelles are stubby, with a radius of 97 Å and a length of 215 Å. Future modifications to this fit may show this sample is fit better with an ellipsoidal micelle model, but a stubby cylindrical model can still provide adequate insight into this structure.

a)

10 mg/mL	DEG50F50
dTHF100	Free Chain
dTHF75	**Spherical** Micelle
dTHF50	**Cylindrical** Micelle
dTHF25	Crashed - DNR

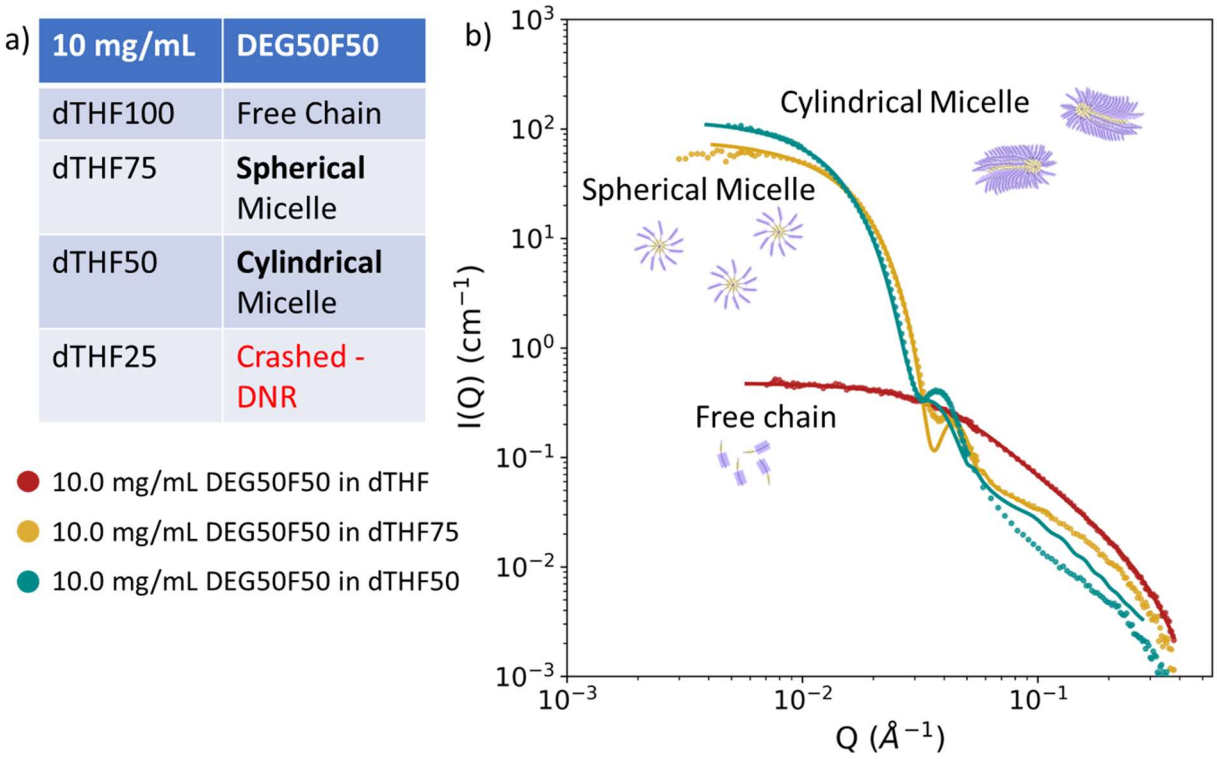

Figure 6.10: a) relevant section of **Table 6.3** b) SANS data for DEG50F50 at 10 mg/mL in dTHF100 through dTHF50. The fit for DEG50F75 is a cylindrical micelle, and all other structures are spherical micelles.

The DEG50F50 polymer showed large changes over the solvent quality decrease, but not all polymers reacted in this way. The PEG series (PEG50F25 and PEG50F50) are shown in **Figure 6.11**, and the changes between solvents are apparent, but less drastic. The relevant portion of **Table 6.3** has been reproduced in **Figure 6.11a**, and the associated 1D plot in **Figure 6.11b**. For all mixed solvents, the increase in the ratio between the EG and the F block does not modify the structure displayed in each solvent. This is especially visible in **Figure 6.11b**, with very little variation shown between each curve at each solvent. There are structural changes in both PEG-based samples as the solvent quality decreases. In the two good solvents, dTHF and dCF, both PEG-based EGFs are freely dissolved without assembly. In the dTHF to D_2O series, once the D_2O is added, the solvent quality drops both of the PEG-based EGFs form spherical micelles without aggregation of those micelles. When dissolved in dTol, both EGFs form spherical micelles that do aggregate into much larger structures.

a)

10 mg/mL	PEG50F25	PEG50F50
dTOL	**Spherical** Micelle	**Spherical** Micelle
dCF	Free Chain	Free Chain
dTHF100	Free Chain	Free Chain
dTHF75	**Spherical** Micelle	**Spherical** Micelle
dTHF50	**Spherical** Micelle	**Spherical** Micelle
dTHF25	**Spherical** Micelle	**Spherical** Micelle

b)

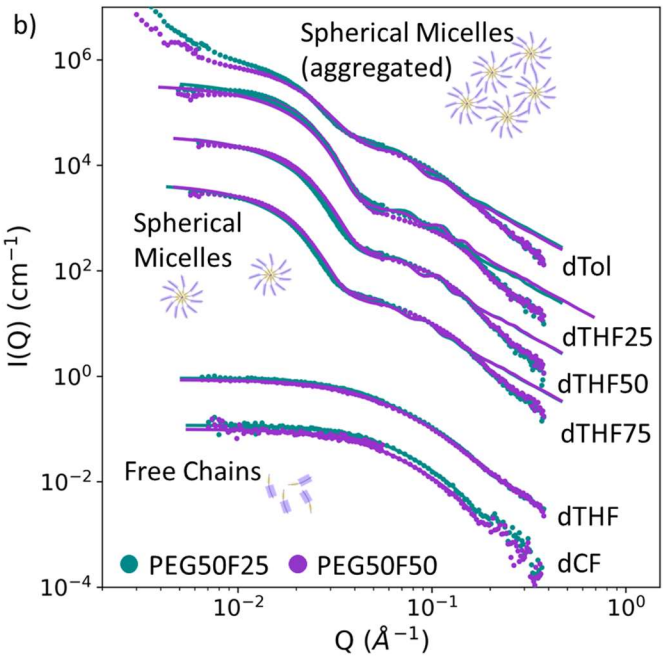

Figure 6.11: a) relevant section of **Table 6.3** b) SANS data for PEG-based polymers at 10 mg/mL in all solvents. Structures are labeled on the plot.

We also ran a series of samples with modified concentrations in solution. For all the previously discussed samples, we prepared the solutions at 10 mg of EGF per 1 mL of solvent. Here, we expanded this analysis to 5 mg EGF/mL and 1 mg EGF/mL. Full series were made for 5 mg/mL and 1 mg/mL for the dTHF50 solvent, which have been all categorized in **Table 6.4**. The red labeled "crashed-DNR" continues to describe samples that were made, and when observed after a waiting period, was sedimented and unable to run.

		DEG50F25	DEG50F50	DEG50F75	PEG50F25	PEG50F50
dTHF50	10 mg/mL	Phase Separated	**Cylindrical** Micelle	**Cylindrical** Micelle	**Spherical** Micelle	**Spherical** Micelle
	5 mg/mL	Phase Separated	Phase Separated	Phase Separated	**Spherical** Micelle	**Spherical** Micelle
	1 mg/mL	Phase Separated	Phase Separated	Phase Separated	**Spherical** Micelle	**Spherical** Micelle

Table 6.4: All samples run at with variations in concentration, in dTHF50 with variations in solvent and polymer architecture. Data has been assigned one of the four structure categories (free chain, spherical micelle, cylindrical micelle, phase separated). Samples that were prepared but sedimented before running are labeled as "crashed – DNR".

We also see that for all DEG samples in dTHF50, reducing the concentration causes samples to phase separate. This occurs for both the 5 mg/mL and the 1 mg/mL samples. At low F-block lengths (DEG50F25) even the highest concentration of EGF phase separates. A selection of DEG samples is plotted in **Figure 6.12b**, and relevant portions of **Table 6.4** are reproduced in **Figure 6.12a**. We can see that the majority of the samples show a characteristic high power-law slope of -4 (Porod) at low-Q that is indicative of large domain formation. We can also note that the DEG50F75 samples at 1 mg/mL show a turnover which is able to be fit with the Guinier plot as discussed in section 6.2.5.4. When fit, the extracted radius of gyration is ~500 Å, which is much larger than any of the ordered micellar structures discussed so far. For the 5 mg/mL samples none of the plots show a turnover, but there is a feature in the DEG50F75 that is not seen in either of the other EGFs at 5 mg/mL. At the 10 mg/mL concentration that seen in the previous series, the two samples with the highest F to EG ratio show a cylindrical micelle structure. Again, these two dTHF50 cylindrical micelles are stubby, both with a radius: length ratio of ~0.4.

a)

mg/mL	DEG50F25	DEG50F50	DEG50F75
10	Phase Separated	**Cylindrical** Micelle	**Cylindrical** Micelle
5	Phase Separated	Phase Separated	Phase Separated
1	Phase Separated	Phase Separated	Phase Separated

● DEG50F25 ● DEG50F50 ● DEG50F75

b)

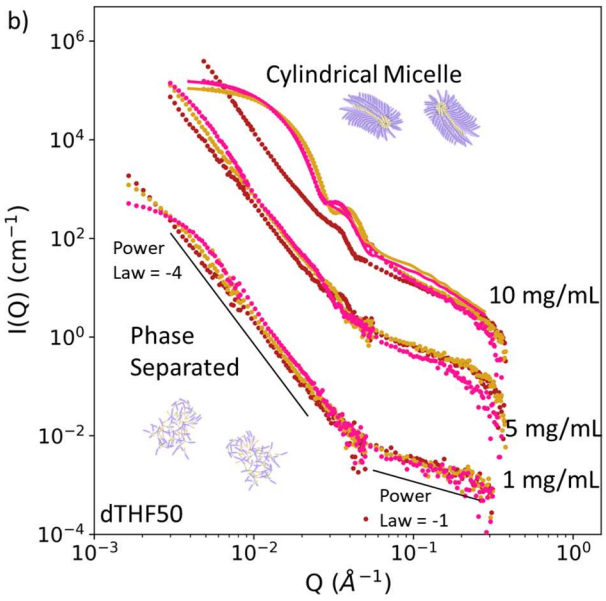

Figure 6.12: a) relevant section of **Table 6.4** b) SANS data for a selection of DEG-based polymers at various concentrations (1, 5 and 10 mg/mL) in all dTHF50. Structures are labeled on the plot.

For the PEG samples, reducing the concentration maintains the spherical micelle structure, with variation in the parameters extracted when fit. **Figure 6.13** shows the relevant samples from **Table 6.4** as well as the 1D plots of all the figures, where, again, we observe little difference between the two PEG architectures.

a)

mg/mL	PEG50F25	PEG50F50
10	**Spherical** Micelle	**Spherical** Micelle
5	**Spherical** Micelle	**Spherical** Micelle
1	**Spherical** Micelle	**Spherical** Micelle

● PEG50F25 ● PEG50F50

b)

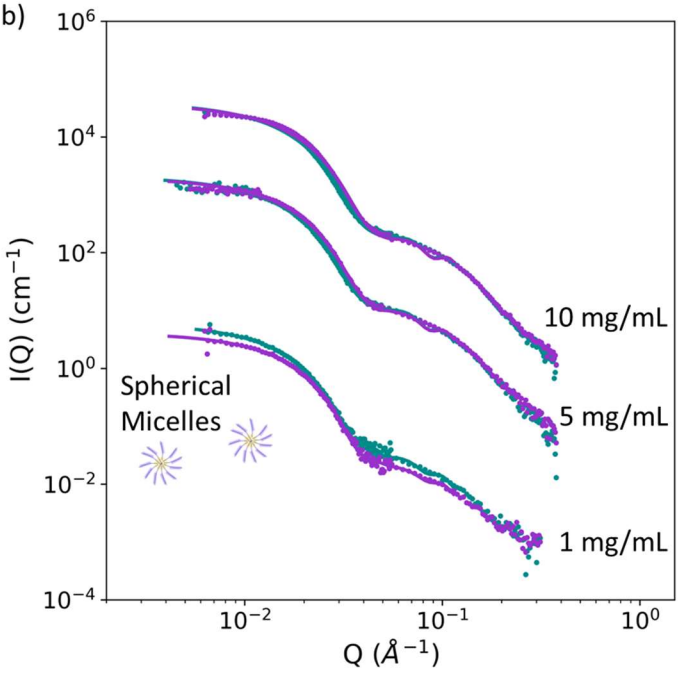

Figure 6.13: a) relevant section of **Table 6.4** b) SANS data for a selection of PEG-based polymers at various concentrations (1, 5 and 10 mg/mL) in all dTHF50. Structures are labeled on the plot.

Observations made in **Figure 6.13b** agree with fits from the spherical micelle modeling. Both PEG50F25 and PEG50F50 display the same trend with slight differences in the values. We can see that as the concentration of the EGF increases in solution, the core radius decreases. The radius of gyration and the aggregation number are relatively constant, without a clear increase or decrease in either following the concentration increase. In contrast, the aggregation number is observed to increase as the concentration of polymer in solution increases. The solvent fraction also displays a clear trend with increasing concentration decreasing the fraction of the solvent in the core. At the highest concentration of PEG50F50, the solvent fraction is zero, suggesting a fully 'dry' core. These effects are also more pronounced as the degree of polymerization of the F-block increases.

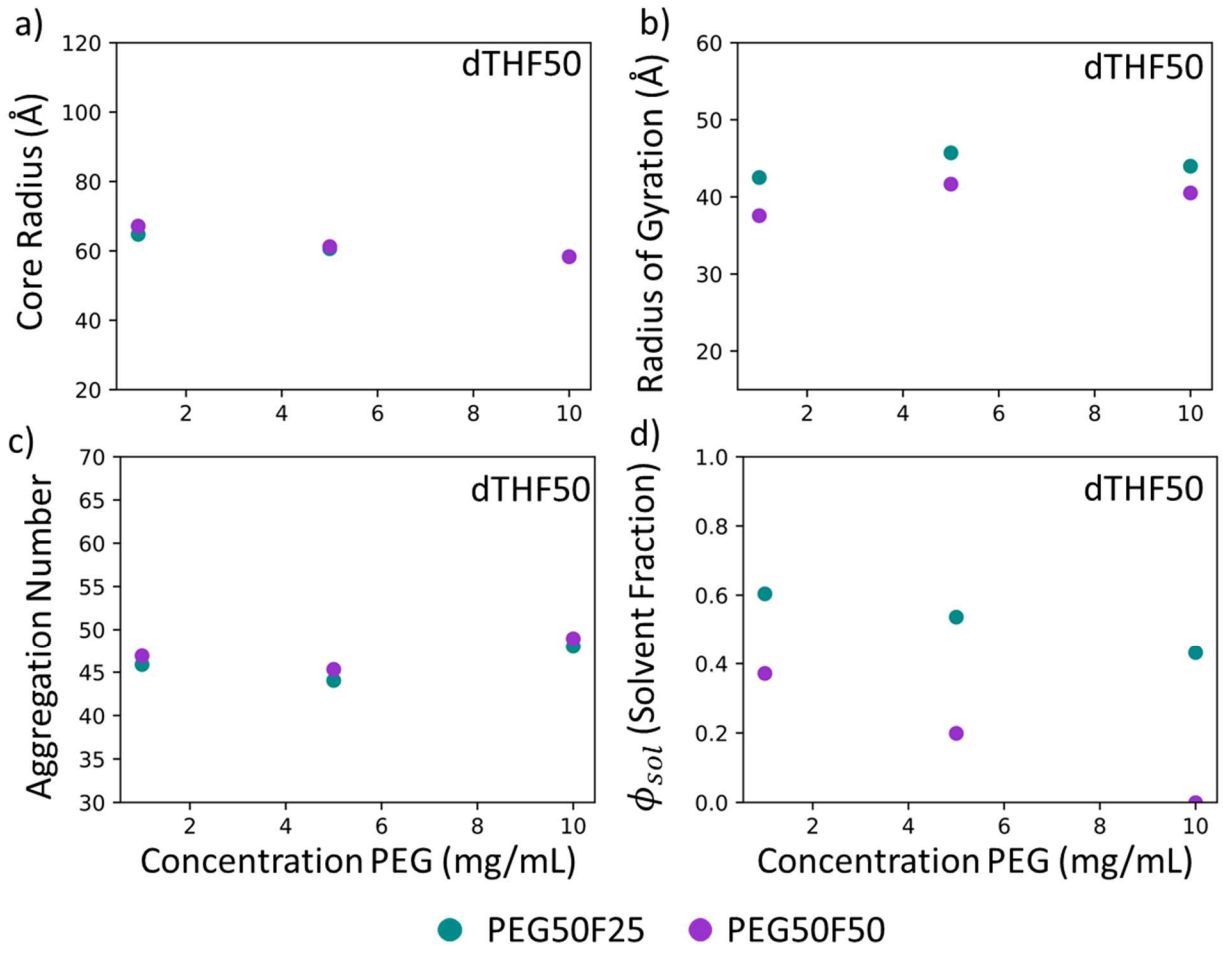

Figure 6.14: Parameters from fitting spherical micelle models to structures at varying concetrations in dTHF50. All DEG samples are either cylindrical micelles at 10 mg/mL or phase separated at lower concetrations and fits are not shown here. All parameters are plotted against polymer architecture and include a) core radius, b) radius of gyration of the EG chains in the corona c) aggregation number and d) volume fraction of solvent in the core.

6.4 Discussion

There are clear variations in self-assembly by changing the architecture of the polymer, the solvent in the system, or the concentration of the EGF in solution. It seems the DEG-based polymers display clearer trends as the ratio between the F and EG block changes, as there is little variation in the PEG-based polymers between the two F block lengths (**Figure 6.11**). There also seems to be a tendency for the DEG polymers with higher ratios of the fluorinated block to form spherical micelles, and in worse solvents, cylindrical micelles. For spherical micelles that were formed in polymers with high degree of polymerization of the fluorinated block, the volume

fraction of the core that is solvent decreases, but still remains 'wet' (**Figure 6.7**). When DEG-based polymers form spherical micelles, it seems that the increasing fluorination of the EGF encourages the aggregation of more chains into the micelle (**Figure 6.7**). This increased aggregation number, coupled with the slight decrease in radius, is also consistent with a reduction of solvent in the core. This tendency to form cylindrical micelles in poor solvents is not observed in polymers with PEG-based hydrophilic blocks. No PEG-based sample formed a cylindrical micelle, and even in the worst solvents (dTHF25), spherical micelles were formed, but with were fully dry micelle cores.

Solvent quality creates large changes in the structures that are formed, and even in two 'good' solvents the structural parameters of the fully dissolved chains are observed to vary (**Figure 6.5**). This is likely related to how each block (hydrophilic and hydrophobic) of each chain interacts with the solvent. We anticipate that dTHF is the best solvent for the EGF as a whole, but dCF is a better solvent for the EG block specifically. DTHF as the overall best solvent can be seen in the increased flexibility of the polymer as a whole and with all architectures forming free chains in solution as observed in **Figure 6.5d** and **6.5e.** This is contrasted by the increased radius of the polymer in dCF, which suggests that the hydrophilic chains are in a more extended configuration (**Figure 6.5c**). The lack of variation in the calculated radius of the chain as the fluorination increases suggests, as expected, that the modeled radius is dominated by the radius of the EG block. If the EG block is responsible for the modeled chain radius, and the EG block is more spread in the dCF, then it follows that dCF is a better solvent for the EG block specifically.

We also see large changes in structure in a single polymer architecture over modified solvent quality, as shown in **Figure 6.10**. Depending on the polymer architecture, materials are found to form free chains, spherical micelles, or cylindrical micelles. The dTHF to D_2O solvent series also suggests that polymers with higher degree of polymerization in the F block are more resilient to solvent quality changes, with an ability to form ordered structures in solvents of decreasing 'quality' (**Figure 6.8**). PEG-based and DEG-based polymers also show very different behavior as a function of solvent quality. For PEG-based polymers, as the solvent worsens, there is a decrease of solvent present in the core of the micelle. This is expected as the addition of D_2O is less likely to coexist with the fluorinated block in the core.

Trends in **Table 6.4** show phase separation as a function of decreasing polymer concentration[33–35]. This conflicts with typically observed results for other block-copolymers in

solution. We would anticipate that at low concentrations, the chains would be dissolved freely until a critical micelle concentration (CMC) is reached and micellization[35]. If the formation of the spherical or cylindrical micelle is reliant on a high concentration of material in solution, then it would be expected that decreasing the concentration can induce less of the formed structure or unassociated chains in solution. What we see here is the reduction of concentration of EGF in solution induces large scale unordered aggregation of the chains not the solubilization of free chains in solution. This is a portion of this work we are still investigating and the driving forces behind these observations are not yet understood.

6.5 Conclusions

Polymer structure, solvent quality, and concentration all produce large changes in the ability to assemble in solution and affect the structure of the assembly. Understanding the effect of these changes on the structure can help researchers refine and optimize these systems for use in applied materials. This co-polymer was chosen to be used in OMIEC systems, and we have shown that, with an eye on system variables, EGFs in isolation can form self-assembled micellar structures. Some of these structures match our anticipated goal of a hydrophobic core that, with a conjugated polymer added, may ensure electronic conductivity, and is supported by hydrophilic chains that should allow for ionic transport. While these systems can form structures that are useful for our end goal needs, understanding these trends and observations is vital in order to build a foundation to understand more complex blended systems. While we understand these materials in isolation, we also need to establish the changes we observe with the addition of a conjugated polymer into the system, as investigated in Chapter 7.

6.6 References

1. Menno A. van Dijk & Andre Wakker. *Concepts of Polymer Thermodynamics*. (1997).
2. Ouhib, F. *et al.* Transparent superhydrophobic coatings from amphiphilic-fluorinated block copolymers synthesized by aqueous polymerization-induced self-assembly. *Polym. Chem* **7**, 3998 (2016).
3. Ko, J. H., Bhattacharya, A., Terashima, T., Sawamoto, M. & Maynard, H. D. Amphiphilic Fluorous Random Copolymer Self-Assembly for Encapsulation of a Fluorinated Agrochemical. *J. Polym. Sci., Part A: Polym. Chem* **57**, 352–359 (2019).
4. Sinturel, C., Bates, F. S. & Hillmyer, M. A. High-χ−Low N Block Polymers: How Far Can We Go? **18**, 9 (2024).
5. Morris, M. A. Directed self-assembly of block copolymers for nanocircuitry fabrication. *Microelectron Eng* **132**, 207–217 (2015).
6. Nunns, A., Gwyther, J. & Manners, I. Inorganic block copolymer lithography. *Polymer (Guildf)* **54**, 1269–1284 (2013).
7. Jeong, S. J., Kim, J. Y., Kim, B. H., Moon, H. S. & Kim, S. O. Directed self-assembly of block copolymers for next generation nanolithography. *Materials Today* **16**, 468–476 (2013).

8. Bates, C. M., Maher, M. J., Janes, D. W., Ellison, C. J. & Willson, C. G. Block copolymer lithography. *Macromolecules* **47**, 2–12 (2014).
9. Bhambere, D. Effect of Polymer and Formulation Variables on Properties of Self-Assembled Polymeric Micellar Nanoparticles Nanomedicine & Biotherapeutic Discovery. *Article in Journal of Nanomedicine & Biotherapeutic Discovery* **4**, 3 (2014).
10. Paulsen, B. D., Tybrandt, K., Stavrinidou, E. & Rivnay, J. Organic mixed ionic–electronic conductors. *Nature Materials* vol. 19 13–26 Preprint at https://doi.org/10.1038/s41563-019-0435-z (2020).
11. Christine Luscombe, S. K., He, Y., Kukhta, N. A., Marks, A. & Luscombe, C. K. The effect of side chain engineering on conjugated polymers in organic electrochemical transistors for bioelectronic applications. *Royal Society of Chemistry* **10**, 2314 (2022).
12. Khot, A. & Savoie, B. M. How side-chain hydrophilicity modulates morphology and charge transport in mixed conducting polymers. (2021) doi:10.1002/pol.20210773.
13. Chloroform-[D_1] (99.8% D) (Isotopic) for NMR spectroscopy | VWR. https://pr.vwr.com/store/product/7488784/chloroform-d1-99-8-d-isotopic-for-nmr-spectroscopy.
14. Toluene-[D_8] 99+ atom % D for NMR spectroscopy | VWR. https://us.vwr.com/store/product/7516136/toluene-d8.
15. Tetrahydrofuran-[D_8] (99.5% D) for NMR spectroscopy | VWR. https://in.vwr.com/store/product/4690875/tetrahydrofuran-d8-99-5-d-for-nmr-spectroscopy.
16. Deuterium Oxide | H2O | CID 24602 - PubChem. https://pubchem.ncbi.nlm.nih.gov/compound/Deuterium-Oxide.
17. Di(ethylene glycol) methyl ether methacrylate 95 45103-58-0. https://www.sigmaaldrich.com/US/en/product/aldrich/447927.
18. Poly(ethylene glycol) methyl ether acrylate average Mn 480, MEHQ 100ppm inhibitor, BHT 100ppm inhibitor 32171-39-4. https://www.sigmaaldrich.com/US/en/product/aldrich/454990.
19. 2,2,3,3,4,4,4-Heptafluorobutyl acrylate 97 424-64-6. https://www.sigmaaldrich.com/US/en/product/aldrich/443751.
20. Neutron Activation and Scattering Calculator. https://www.ncnr.nist.gov/resources/activation/.
21. Chakma, P. *et al.* Mechanoredox Catalysis Enables a Sustainable and Versatile Reversible Addition-Fragmentation Chain Transfer Polymerization Process. (2022) doi:10.1002/anie.202215733.
22. Hill, M. R., Carmean, R. N. & Sumerlin, B. S. Expanding the Scope of RAFT Polymerization: Recent Advances and New Horizons. *Macromolecules* **48**, 5459–5469 (2015).
23. Egorov, I. N. *et al.* Ball milling: an efficient and green approach for asymmetric organic syntheses. *Green Chemistry* **22**, 302–315 (2020).
24. Wood, K. *et al.* QUOKKA, the pinhole small-angle neutron scattering instrument at the OPAL Research Reactor, Australia: design, performance, operation and scientific highlights. *urn: issn:1600-5767* **51**, 294–314 (2018).
25. Kline, S. R. & IUCr. Reduction and analysis of SANS and USANS data using IGOR Pro. *urn: issn:0021-8898* **39**, 895–900 (2006).
26. Doucet, M. *et al.* SasView. Preprint at (2022).
27. Doucet, M. *et al.* Sasmodels. Preprint at (2020).
28. Kienzle, P. A. (University of M. C. P., Krycka, J., Patel, N. & Sahin, I. Bumps. Preprint at (2011).
29. Pedersen, J. S. & Schurtenberger, P. Scattering functions of semiflexible polymers with and without excluded volume effects. *Macromolecules* **29**, 7602–7612 (1996).
30. Skov Pedersen, J. Form factors of block copolymer micelles with spherical, ellipsoidal and cylindrical cores. *J. Appl. Cryst* **33**, 637–640 (2000).
31. Choi, S.-H., Lee, W. B., Lodge, T. P. & Bates, F. S. Structure of Poly(styrene-b-ethylene-alt-propylene) Diblock Copolymer Micelles in Binary Solvent Mixtures. *J. Polym. Sci., Part B: Polym. Phys* **54**, 22–31 (2015).

32. Linder, P. & Zemb, Th. *Neutrons, X-Rays and Light: Scattering Methods Applied to Soft Condensed Matter*. (Elsevier Science, 2002).
33. Malmeten, M. & Lindman, B. Self-Assembly in Aqueous Block Copolymer Solutions. *Macromolecules* **25**, 5440–5445 (1992).
34. Choucair, A. & Eisenberg, A. Control of amphiphilic block copolymer morphologies using solution conditions. *Eur. Phys. J. E* **10**, 37–44 (2003).
35. Gao7, Z. & Eisenberg, A. A Model of Micellization for Block Copolymers in Solutions. *Macromolecules* **26**, 7353 (1993).

Chapter 7: OMIEC Blends with Conjugated Polymers

The work presented in this section is conducted in collaboration with members from Dr Lilo Pozzo's group (Dr. Kiran Vaddi and Karen Li) as well as from Dr. Matthew Golder's group (Sarah Zeitler).

The author would like to acknowledge the contributions of coauthors for the following work and makes no claim of sole contribution to the data. Additional work on property characterization will be conducted and identification of ionic and electronic potential and motivators will be identified in future work by collaborators.

7.1 Introduction

Organic Mixed Ionic Electric Conductive (OMEIC) materials are soft materials, typically polymers which can display conduction from both electronic and ionic methods[1–3]. Current interest in OMIEC materials covers many fields including actuators[4], electronic devices [5,6], chemical sensors[7], ion pumps[8], and organic sensors for haptics and feedback[6,9–11]. OMIEC materials utilize three physical processes to balance their unique properties: ionic-electronic coupling, ionic transport, and electronic transport[1]. Ionic transport involves the movement of ions, while electronic transport relies on the movement of electrons or holes. Ionic-electronic coupling describes the mechanism for conversion between ionic and electronic conductivity and the resulting feedback cycle that leads to improved material conductivity[12–14]. Each of these processes provides a form of conductivity and can be managed and utilized for specific device purposes. While the only requirement for OMIECs is to have both ionic and electronic conductivity, there are a multitude of materials that could accomplish these requirements. A common trait, and the origin for the mixed ionic and electronic conductive properties, is the existence of a conjugated polymer component (electronic) and a polymeric electrolyte component (ionic). Our OMEICs of interest consist of blending or formulating a conjugated polymer, such as poly 3-hexylthiophene (P3HT), and a high-χ-parameter copolymer as the electrolyte. Chapter 6 addresses the self-assembly of high-χ parameter polymers in greater detail.

OMIECS require a balance between ionic and electronic pathways, which can be difficult to maintain as the requirements for each pathway are in direct conflict. Ionic transport is encouraged through water solvated, amorphous, and loose structures where ions can easily diffuse through the structure[1,15,16]. Electronic transport is generally facilitated by organized and crystalline structures, where electrons or holes can move through resonant backbones or through assembled

organized structures. The final piece of OMIEC conductance, ionic-electronic coupling, requires close proximity between ionic and electronic transport and a careful balance between the two. In our system, the conjugated polymer P3HT provides electronic transport and self-assembly of conductive nanowires must be encouraged in the final blend to maximize electronic mobility. The high-χ parameter polymer matrix, which is composed of a block copolymer (EGF) with a hydrophilic ethylene glycol (EG) oligomer block and a hydrophobic fluorinated block (F), provides ionic transport through hydrophilic regions as well as self-assembly. Hydrophilic ethylene-glycol sidechains promote ionic transport in similar systems, and it is anticipated that these will serve the same purpose when assembled[15,16]. As discussed in Chapter 6, the EGF on its own will assemble into spherical or cylindrical micelles, with a hydrophobic core and hydrophilic corona. In solution, the P3HT can provide a cylindrical seed to form micelles and it is hypothesized to be stabilized by the EGF 'shell', creating an electronic channel that is surrounded by a hydrophilic and conductive motivated corona.

7.2 Materials and Methods

7.2.1 Materials

The polymers used in this work are high-χ parameter copolymers synthesized and compositionally analyzed by Sarah Zeitler. Information on the synthesis method is provided in **section 6.2.2**, and information on composition is reproduced here as given. Additional calculations made for fitting and material parameters are made using the values determined in **Table 7.1.**

The copolymers used are prepared from a hydrophilic di (ethylene glycol) ethyl ether acrylate (DEGEEA) and a hydrophobic heptafluorobutyl acrylate (HFBA) block, shown in **Figure 7.1a**. In this work the DEGEEA block is referred to as the Ethylene glycol (EG) block and comes in two forms. The first is a di (ethylene glycol) (DEG) with two repetitions of the ethylene glycol segment, the second is a poly (ethylene glycol) (PEG) with twelve repetitions of the ethylene glycol segment. The HFBA block is referred to as the fluorinated (F) block and there are no variations made in the monomer used. The PDEEGA-block-PHFBA (EGF) copolymer is made in 6 different forms, with variation in block length to modify the ratio between the EG block and the F block, as well as to investigate the effect of modifying the length of side chain (PEG v DEG) in the copolymer.

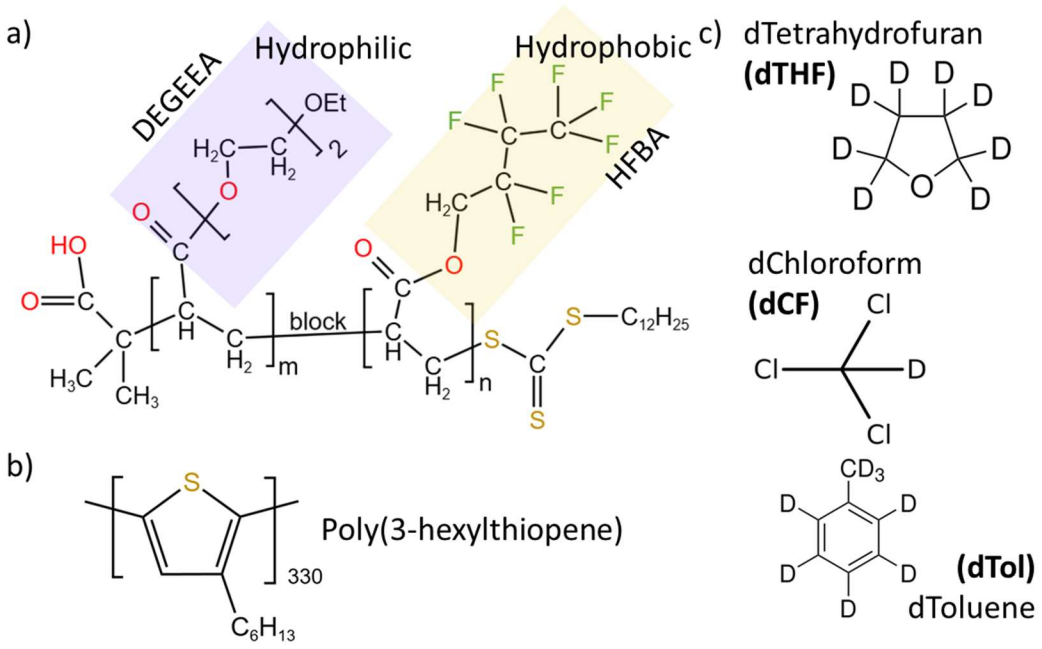

Figure 7.1: Molecular structure of the a) high-χ parameter copolymer b) conjugated polymer P3HT, and c) solvents used in this work.

Regio-random poly(3-hexylthiophene) (RRa-P3HT) (MW = 63 kg mol-1, Đ = 2.4, Product 4007) and regio-regular poly(3-hexylthiophene) (RRe-P3HT) (MW = 77 kg mol-1, Đ = 2.4, RR = 94) were purchased from Rieke Metals (Lincoln, NE USA). Both were used as purchased.

A variety of solvents were used in this work. The deuterated chloroform (dCF) and toluene D-8 (dTol) were supplied by the Australian Nuclear Science & Technology Organisation (ANSTO), and purchased from Sigma Aldrich (St. Louis, MO). Molecular structures are shown in **Figure 7.1c**. The deuterated tetrahydrofuran (dTHF) was purchased through Novachem, an Australian supplier for Cambridge Isotopes (Tewksbury, MA). The dCF, dTol, and a portion of dTHF were used as received. Scattering length densities (SLD) of all materials were calculated using NIST activation calculator and shown densities.

Material	Calculated SLD ($\frac{10^{-6}}{Å^2}$)	Density ($\frac{g}{cm^3}$)	Source
Chloroform-D (**dCF**)	3.16	1.5	VWR[17]
Toluene-D8 (**dTol**)	5.66	.943	VWR[18]
Tetrahydrofuran-D8 (**dTHF**)	6.35	.985	VWR[19]

EGF (Full high-χ copolymer)	1.3	SLD extracted from fit	
PDEGEEA block (**EG**)	0.82	1.10*	Estimated[20,21]
PHFBA block (**F**)	1.85	1*	Estimated[22]
Poly(3-hexylthiopene) (**P3HT**)	0.676	1.1	[Literature][23]

Table 7.1: SLDs for all materials calculated from the NIST Neutron activation and scattering calculator[24] using provided densities. *Densities were estimated for each block of the EGF from monomer densities and the estimated densities shown were used in calculations.

All block lengths, molecular weights and dispersity are presented in **Table 7.2**. The block percentages for each polymer were calculated using proton Nuclear Magnetic Resonance (NMR). All DEG-based polymers block percentages were calculated using deuterated chloroform NMR's, while the PEG-based polymers block percentages were calculated using acetone D-6. The block length and molecular weight for the EG block was measured using Gel Permeation Chromatography (GPC) in chloroform. Using the block percentages and information collected with GPC, the block length and molecular weight for the F block as well as the molecular weight for the total polymer were calculated.

Code	Short Form	Block % (EG)	Block % (F)	Block Length (EG)	Block Length (F)	M_n (g/mol)	Dispersity
DEG50F25	D50F25	60	40	42	28	15060	1.16
DEG50F50	D50F50	48	52	43	46	19805	1.06
DEG50F75	D50F75	37	63	44	74	27077	1.35
PEG50F25*	P50F25	55	45	40	33	27647	1.7
PEG50F50*	P50F50	50	50	57	57	41487	1.36

Table 7.2: All polymer information for each of the polymers used in this work, along with reference names for each polymer.

7.2.2 Solution Preparation

Carefully weighed portions of the EGF or conjugated polymer are dissolved in the solvent of choice and heated on a hot plate at 60 ºC. These stock solutions are then mixed to form blended solution state samples while remaining on the hot plate to ensure adequate dissolution and mixing.

Each sample was then loaded directly from the hotplate into 2mm quartz Hellma cells and stored at 26ºC for an extended period of time (15-18 hours) before being measured.

7.2.3 SANS

Small Angle Neutron Scattering (SANS) measurements were collected at the Quokka beamline at the Open Pool Australian Lightwater (OPAL) source with Australian Nuclear Science and Technology Organisation (ANSTO)[17]. SANS data was collected in three configurations to span the full Q range. All non-lenses configurations used 6Å ± 0.10Å wavelengths, the low-Q lens configuration used 8.1Å ± 0.10Å. Samples were measured for differing times and configurations due to scattering ability. Low scatterers (dCF) were measured with low-Q collected at 20m sample to detector distance (2400 seconds), mid-Q collected at 12m sample to detector distance (1200 seconds), and high-Q collected with 1.3m sample detector distance (600 seconds). Samples with mid ranged scattering (dTHF and dTol) were measured with low-Q collected at 20m sample to detector distance with lenses (1600 seconds), mid-Q collected at 12m sample to detector distance (800 seconds), and high-Q collected with 1.3m sample detector distance (400 seconds). Samples were loaded into 2mm quartz Hellma cells and mounted into aluminum holders placed into a temperature controlled 20 slot sample environment set to 26ºC. SANS data were reduced, combined, and background subtracted using the Quokka macro in the NIST SANS package for Igor Pro[18]. Further analysis of SANS data was performed using the SasView[19]/sasmodels[20] and bumps[21] packages for Python.

7.2.4 SANS Data Analysis

Current data analysis consists of arithmetic modifications of the components of each blend in comparison to the blended sample. A similar technique was used in Chapter 4 with the elastomer blend solution samples.

The fits and structure identification for the EGF matrix polymers in pure form were established in Chapter 6, and information on the models and fits is included in that chapter. The pure P3HT in solution is also modeled with the flexible cylinder model which accurately describes free chains in solutions and has been used in previous works[30].

Future analysis will include fitting of the composite blend materials SANS data directly. However, at the time of writing, the model for fitting cylindrical micellar structures was not fully available or implemented in SasView. Still, most of the blended samples would appear to be accurately described by a cylindrical micelle core-shell model.

Shape independent power law fits were performed on low-Q and mid-Q regions to extract the power law exponents in these regions. Equation 7.1 shows the model used. [31]

$$I(q) = scale * q^{-power} + background \quad (7.1)$$

In these fits, background is set to 0 while the power is extracted. Due to the log-log plotting the exponent of the fit is visually observed as the slope of the data.

7.3 Results and Discussion

This work builds upon the structural analysis on the poly di (ethylene glycol) ethyl ether acrylate -block - poly heptafluorobutyl acrylate (PDEEGA-block-PHFBA or EGF) matrix, but only blends will be addressed in depth here. Information on the EGF structure and trends is provided in Chapter 6.

Most samples were prepared at concentrations of 10 mg/mL of the EGF and 10 mg/mL of RRe-P3HT dissolved together and loaded into Hellma cells while fully dissolved. They were allowed to rest overnight to assemble before being measured, and during this waiting period, all the RRe-P3HT solutions darkened and turned a purple color. This is indicative of the RRe-P3HT assembling in solution and has been observed in previous work[32]. Starting with the blends determined in Chapter 6 to be free chains of EGF dissolved in solution, we can identify if the addition of the self-assembling and semicrystalline RRe-P3HT changes the blended structure in solution. The dCF samples, shown in **Figure 7.2**, show the EGF and RRe-P3HT blends, labeled by the EGF used in the solution, as well as a pure solution of the RRe-P3HT in dCF. We can see that the scattering of all the blends shows features that are not present in the pure conjugated polymer. This indicates that there are changes in the structure of the blends due to the architecture of the polymer, but there are no obvious changes in the type of structure formed. A key feature in high-Q, the hump most prominent in the PEG-based sample, is indicative of scattering from the EG portion. This feature was observed in pure EGF samples as the radius of gyration of the EG chains in a micellar structure seen in Chapter 6. This feature is noticeably higher for the PEG-based chains and in the DEG-based chains, there is a slight drop with the increase in the length in the fluorinated block. The second feature is at low-Q, with an upturn or power-law dependence with a ‘slope’ or exponent approximating 1.2 for PEG-based EGFs and 1.3 for DEG-based EGFs. We can see again see a change between the PEG and the DEG-based polymers, with only slight changes in the DEG-based series with changes in the length of the F block.

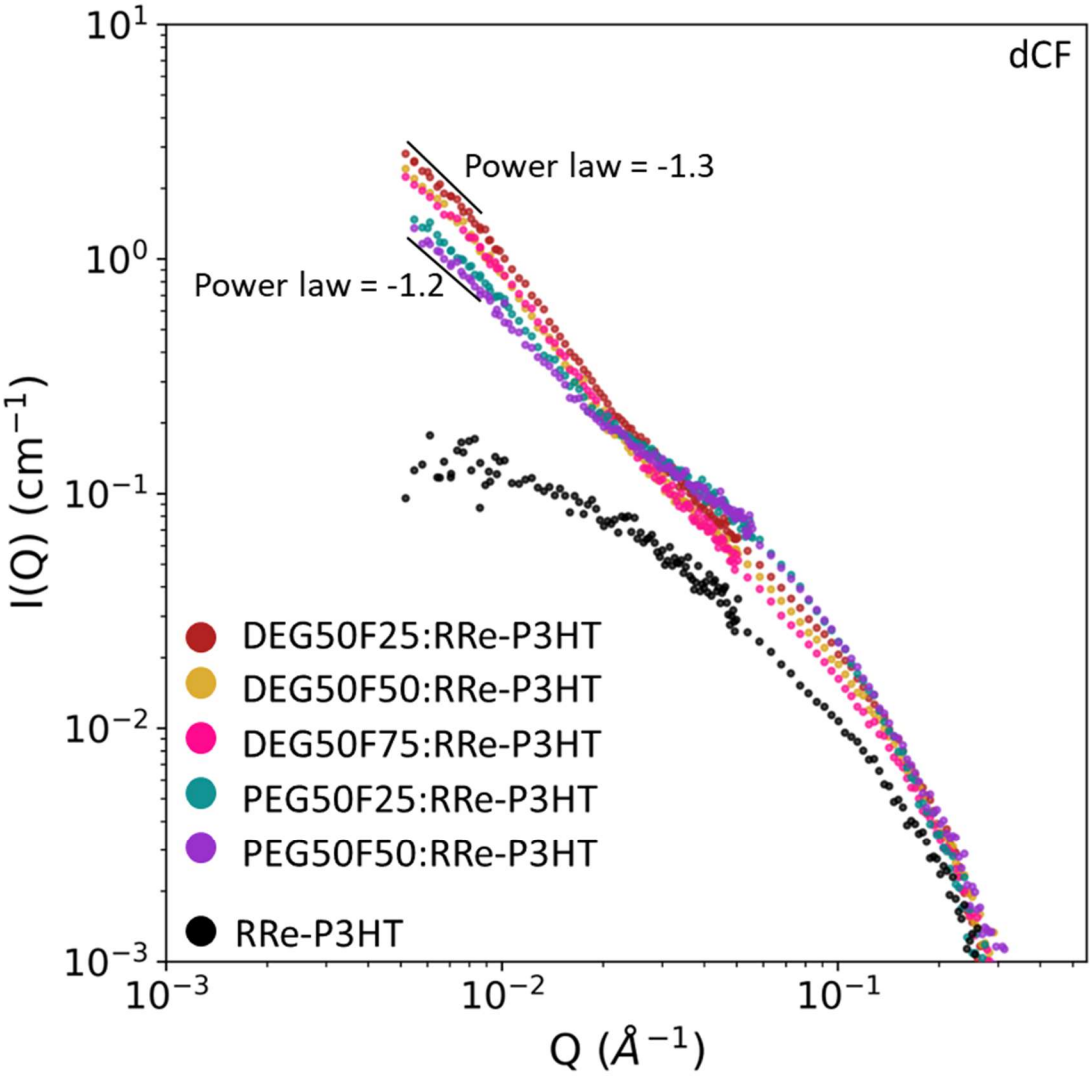

Figure 7.2: SANS data of 10 mg/mL EGF and 10 mg/mL RRe-P3HT blends in dCF

By simple view of the data, it is difficult to determine if there is additional co-assembly in solution that is not simply the contributions of isolated EGF solutions and isolated RRe-P3HT contributions (**Figure 7.2)**. Arithmetical transformations of the data sets can clarify observations. For isolated dilute and non-interacting macromolecules in mixed solutions, the total scattering is expected to be similar to the sum of the scattering contributions of the pure components. Thus, by summing the datasets for the pure RRe-P3HT and the respective pure EGF solution, we can quantativly compare the summed dataset to the experimental data collected for the corresponding blend. This way, we can determine if there is additional excess scattering that would be indicative of complexation or co-assembly. In blended samples, where all the scattering is from independent

assemblies of the EGF and RRe-P3HT components, with no interaction between the two, the sum of the individual pure solutions is expected to be equal to the experimental blend data. If there is additional scattering in the blended solution, then interactions between the two componets in solution is significant. In **Figure 7.3**, the data for each component, the sum of the individual components, and the experimental data of the blended system are all plotted together. All of the DEG series (**Figure 3 a-d**), show the same trends. The summed data and the experimental data overlaps at high and mid-Q until the upturn occurs in the experimental data at very low-Q. This suggests that the features observed in the individual components in this region, including the feature describing the EG chains in solution, are also observed in blended solutions. However, the feature at low-Q is not observed in the summed data, and it is evidence of complexation between the EGF and the RRe-P3HT chains in a combined assembly. The intensity difference becomes less apparent between the summed data and the experimental data as the flourinated block length increases. This is likely due to the increased propesity for assembly of the EGF in the pure solution and a reduced driving force for co-assembly with RRe-P3HT. The PEG-based samples show a similar trend, but the region of overlap between the summed and experimental blends is shifted towards low-Q.

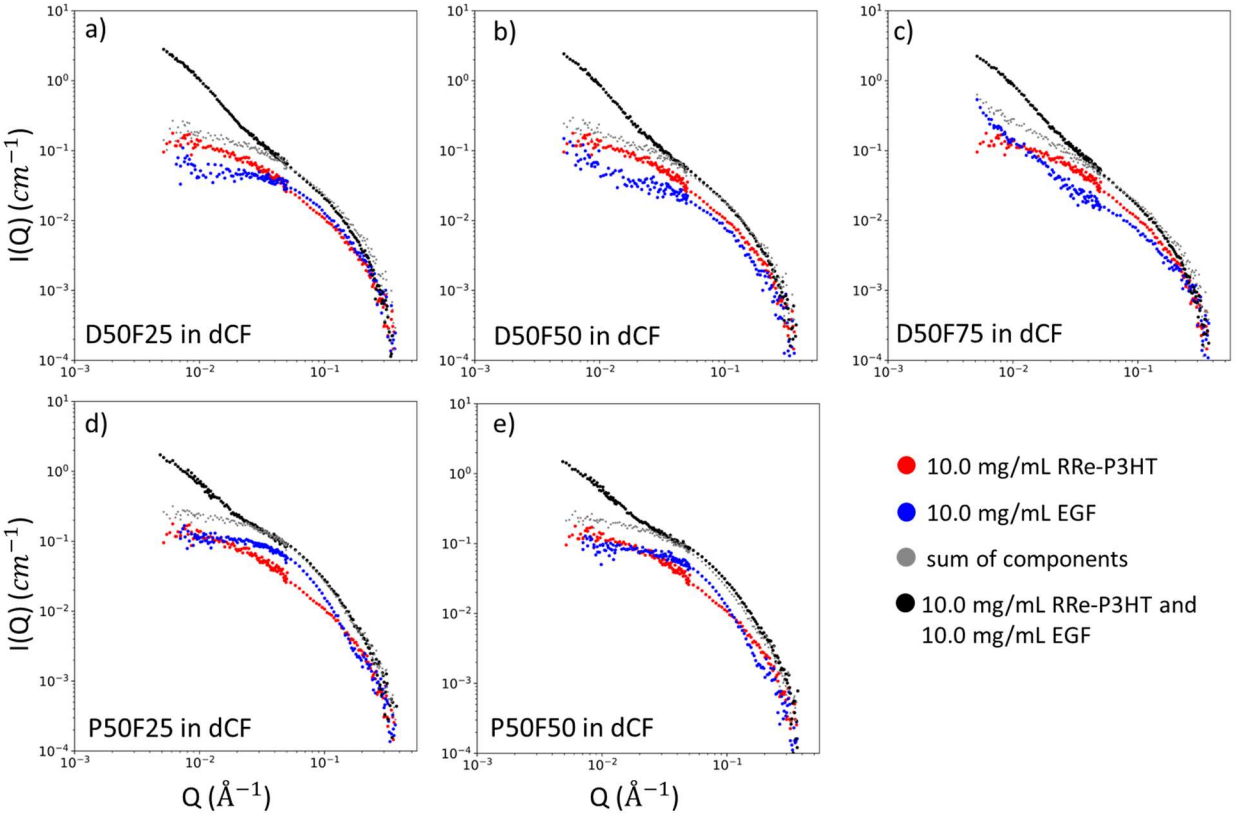

Figure 7.3: Individual plots for a) DEG50F25, b) DEG50F50, c) DEG50F75, d) PEG50F25, e) PEG50F50 with the pure solution of 10 mg/mL RRe-P3HT, the pure solution of 10 mg/mL of the EGF, the sum of the individual componets, and the experimental data for the blended system in dCF

The other solution that produced consistent free chains in solution for the pure EGF is dTHF. The same samples were repeated and **Figure 7.4** shows the series of all EGF polymer architetures blended with RRe-P3HT in dTHF. A similar trend observed in the dCF samples is observed here in terms of the two features. The mid/high-Q feature has a separation of the PEG-based samples and then for the DEG-based samples, a decrease in intensity. The low-Q upturn is more defined for the dTHF samples, with possibly a more defined turnover, which could be indicative of a Guinier region, due to use of lenses to expand the Q range lower. There is also an increased assembly in the pure RRe-P3HT sample, with a much larger structure being formed, indicative of self-assembly of nanowires.

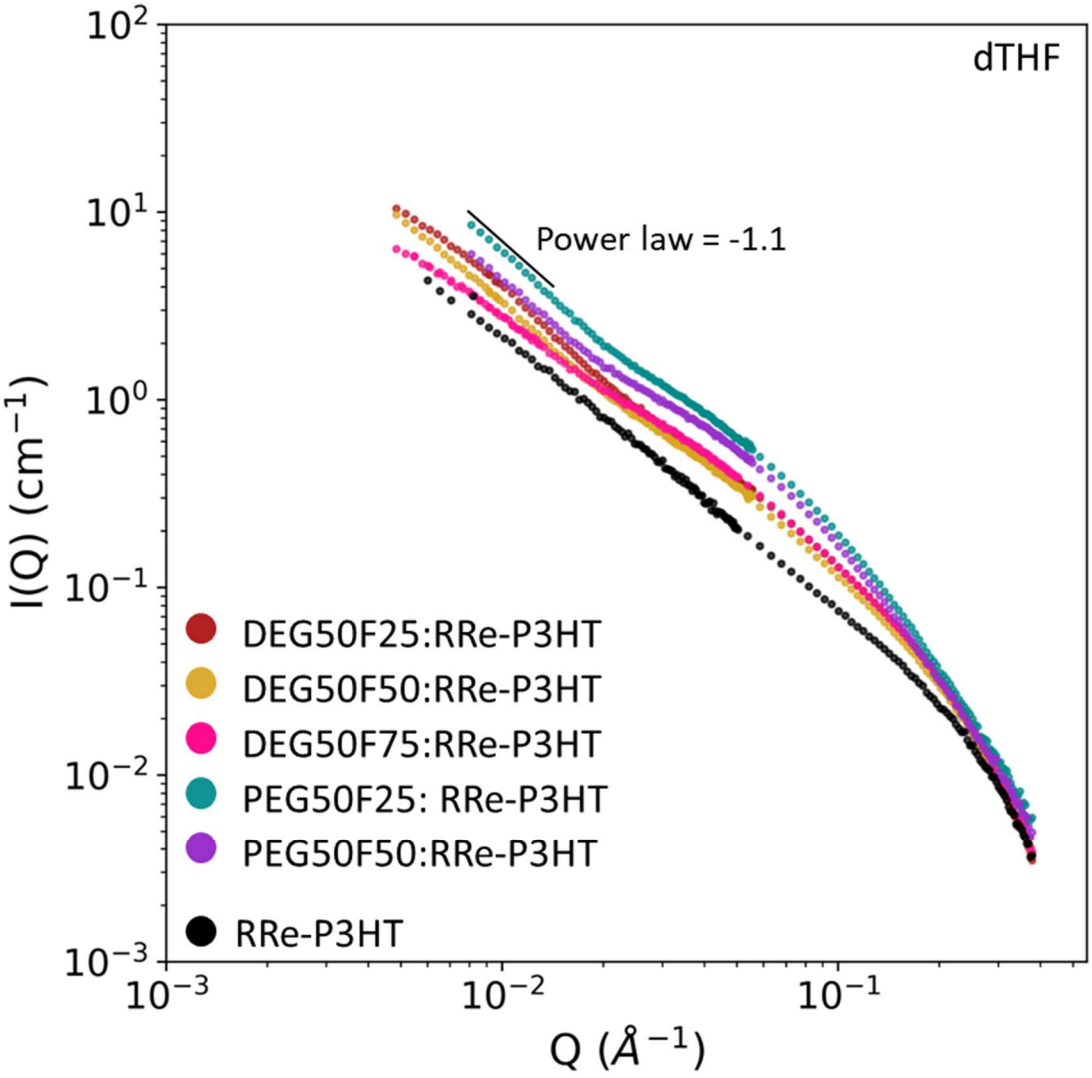

Figure 7.4: SANS data of 10 mg/mL EGF and 10 mg/mL RRe-P3HT blends in dTHF

The data from the pure components of each of these samples were also summed and compared to the blended composite sample, as shown in **Figure 7.5**. For all polymers, the summed data and the experimental data shows a large region of overlap, with only low-Q showing a clear separation. For the DEG samples, as the length of the fluorinated block increases, the gap closes, with the summed DEG50F75 sample being essentially fully overlapped with the experimental data. This indicates that as the flourinated block length of the sample increases, the blended solution acts more like a fully dissolved and dilute system of the individual components. This sample is repeated in the PEG samples, with the similarity between the blend and the summed data increasing as the fluoriniated block length increases.

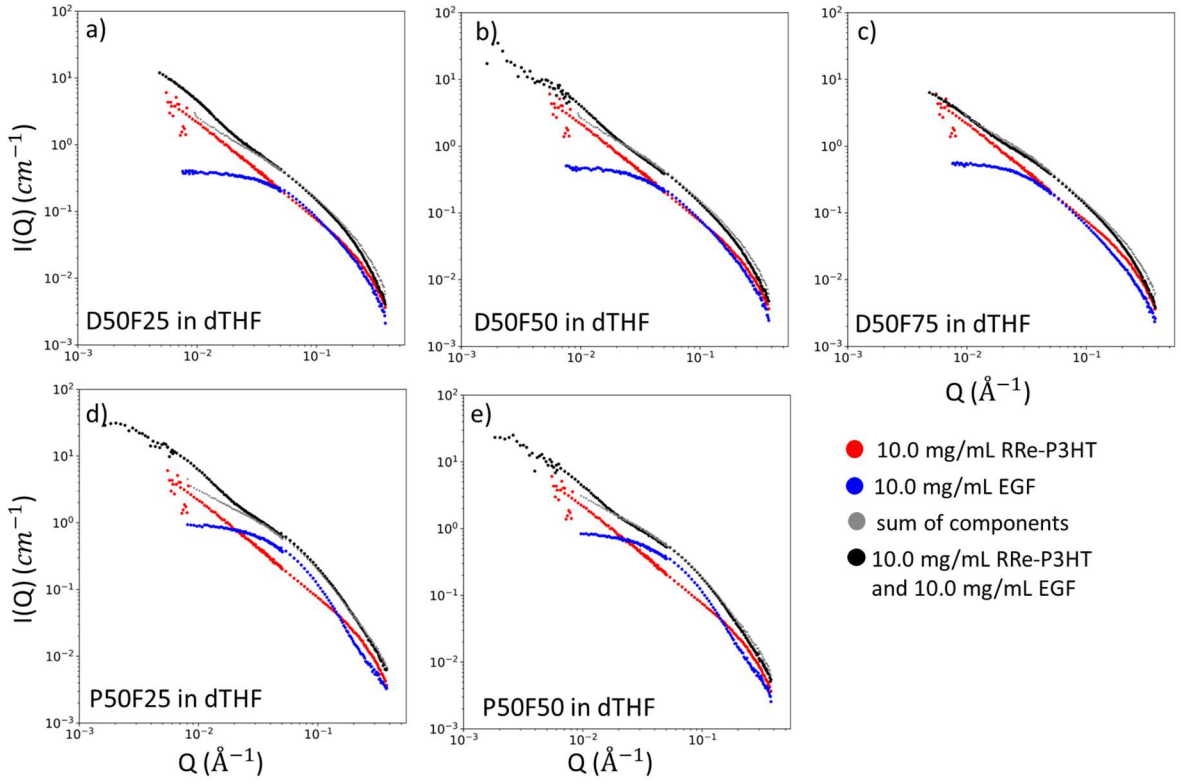

Figure 7.5: Individual plots for a) DEG50F25, b) DEG50F50, c) DEG50F75, d) PEG50F25, e) PEG50F50 with the pure solution of 10 mg/mL RRe-P3HT, the pure solution of 10 mg/mL of the EGF, the sum of the individual componets, and the experimental data for the blended system in dTHF

In both dCF and dTHF, the EGF polymers were fully dissolved free chains, indicating they are good solvents for the polymers. In dTHF, while the EGF is fully dissolved, the RRe-P3HT has an increased tendency to assemble into nanowires, leading to reduced differences in this solvent. Blended samples were also prepared in a solvent of poor quality, dTol, as plotted in **Figure 7.6**. These samples show greater variation in the structure of assembly, with the DEG series showing large variation as the length of the fluorinated block increases. In the DEG50F25 sample, the curve is similar to those in dCF and dTHF. However, for the DEG50F50, sample the curve is similar to the pure spherical micelles observed and discussed in Chapter 6. The DEG50F75 sample shows even further defined spherical micelle features. The PEG samples also show clear spherical traits that are identical between the two architectures. It is possible that a large proportion of the EGF of long fluorinated block-lengths is not forming complexes with P3HT. There are two clear low-Q

regions of power law exponents that emerge. At very low-Q we observe a 'slope' of approximately -1.4 for all samples, then around 0.01 $Å^{-1}$ a region of a 'slope' around -0.9. We also see increased assembly in the RRe-P3HT in dTol over the dCF solution, which is expected due to solvent quality decreases[22,23].

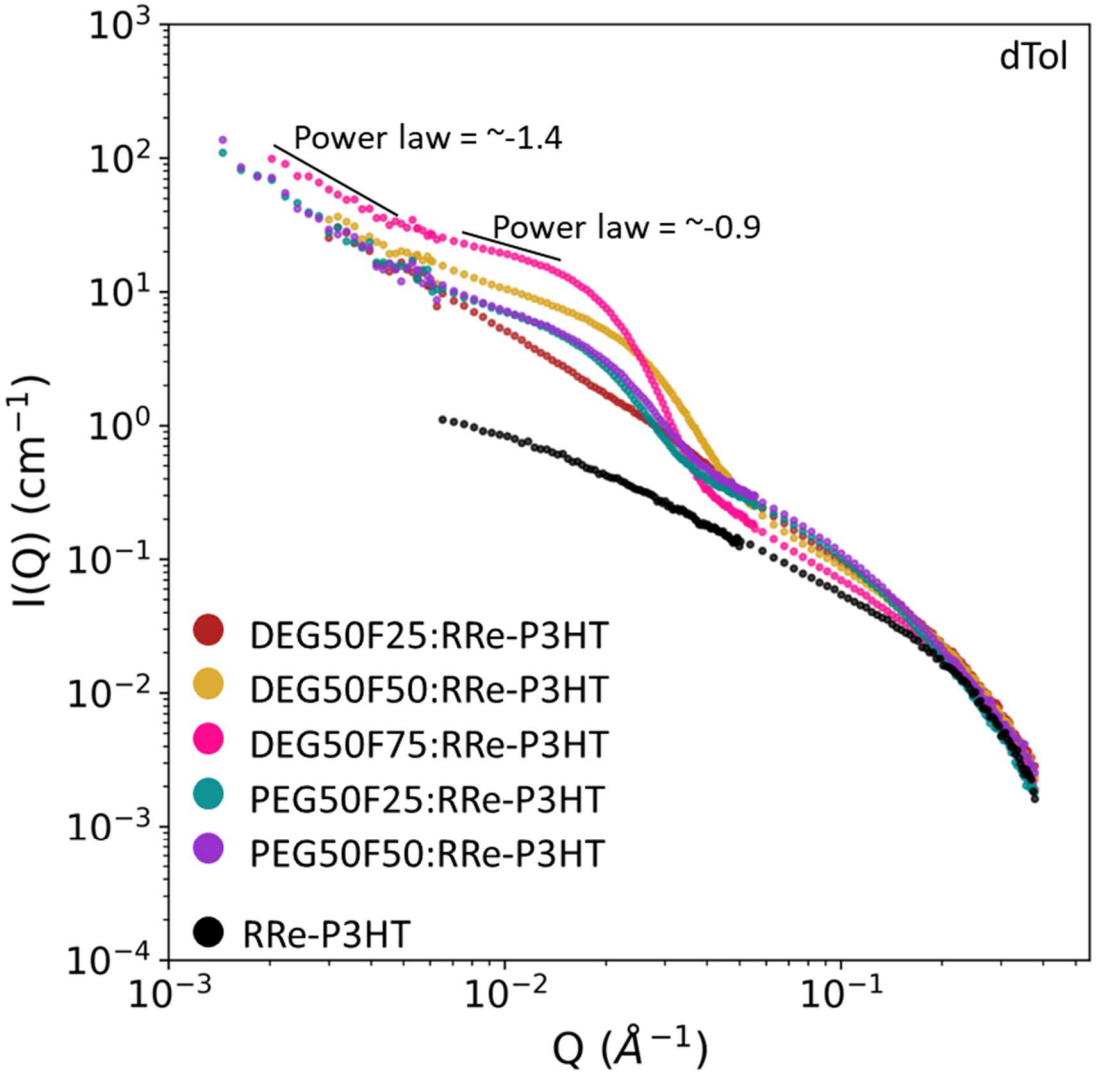

Figure 7.6: SANS data of 10 mg/mL EGF and 10 mg/mL RRe-P3HT blends in dTol

When the individual EGF components and the RRe-P3HT data sets are summed in the same way as before, shown in **Figure 7.7**, we see a trend similar to the dTHF solutions. For the DEG samples, the samples (DEG50F25) with shorter fluorinated block lengths show a larger gap, and there is increased evidence of co-assembly in the blended solution (low-Q upturn). As the block length of the fluorinated component increases, excess scattering decreases, until the

DEG50F75 sample only shows little increased scattering at very low-Q. Additionally the features of the blend specific assembly appear to be similar to formations of large-scale aggregation. For the PEG samples, neither of the two EGFs show any difference between the summed data and the experimental blend data. This suggests that in dTol, the PEG-based blends act as well dissolved, dilute, and non-interacting systems between the EGF and the P3HT.

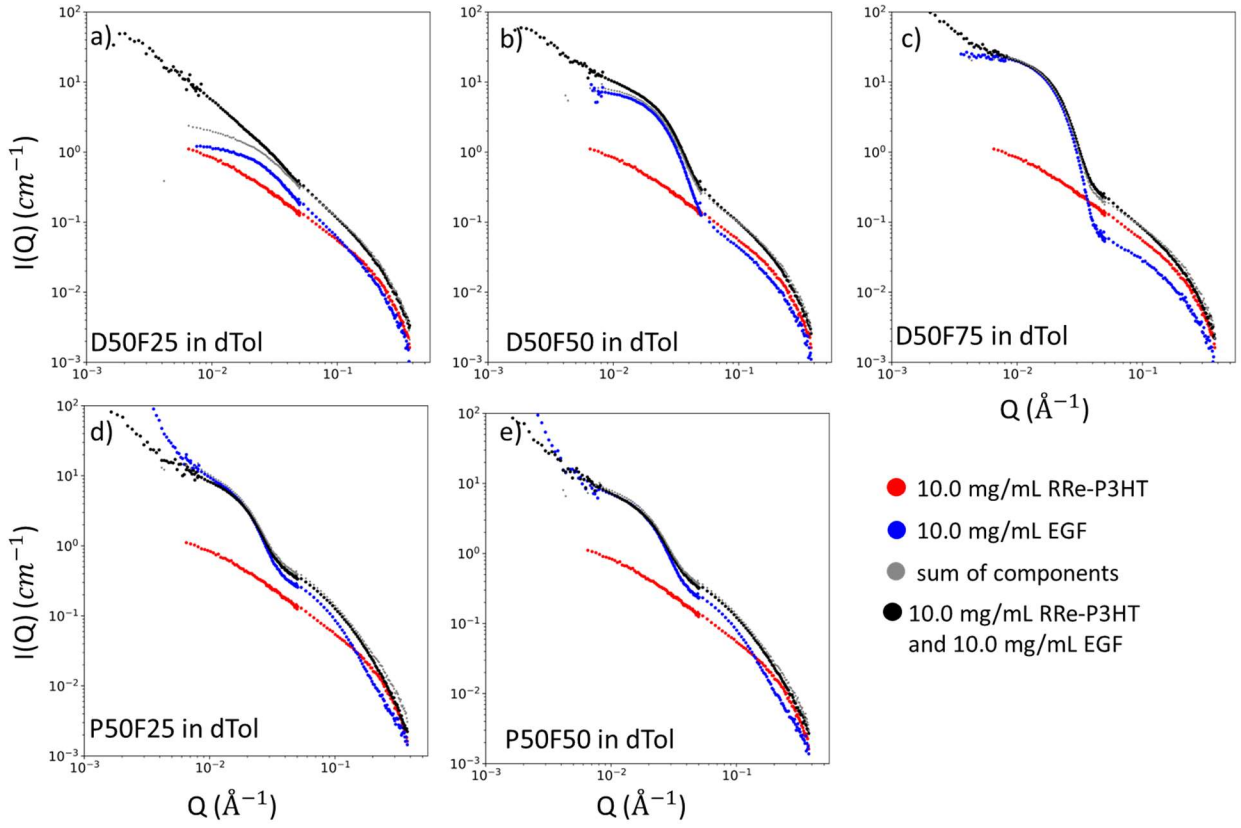

Figure 7.7: Individual plots for a) DEG50F25, b) DEG50F50, c) DEG50F75, d) PEG50F25, e) PEG50F50 with the pure solution of 10 mg/mL RRe-P3HT, the pure solution of 10 mg/mL of the EGF, the sum of the individual componets, and the experimental data for the blended system in dTol

Additionally, we ran a fully amorphous RRa-P3HT blended series in dTHF. RRa-P3HT does not self-assemble into nanowires in solution, and if there is any driving factor for increased assembly due to the self-assembly of the semi-crystalline P3HT, these samples can help isolate that change. In the plot seen in **Figure 7.8**, we can see all samples show similar features to free chains in solution that can be fit well with a free chain model. Both the RRa-P3HT and the EGFs in solution can also be fit with a model describing free chains, which doesn't necessarily mean

there is no interactions between the two components in solution, but complexation is likely minimal.

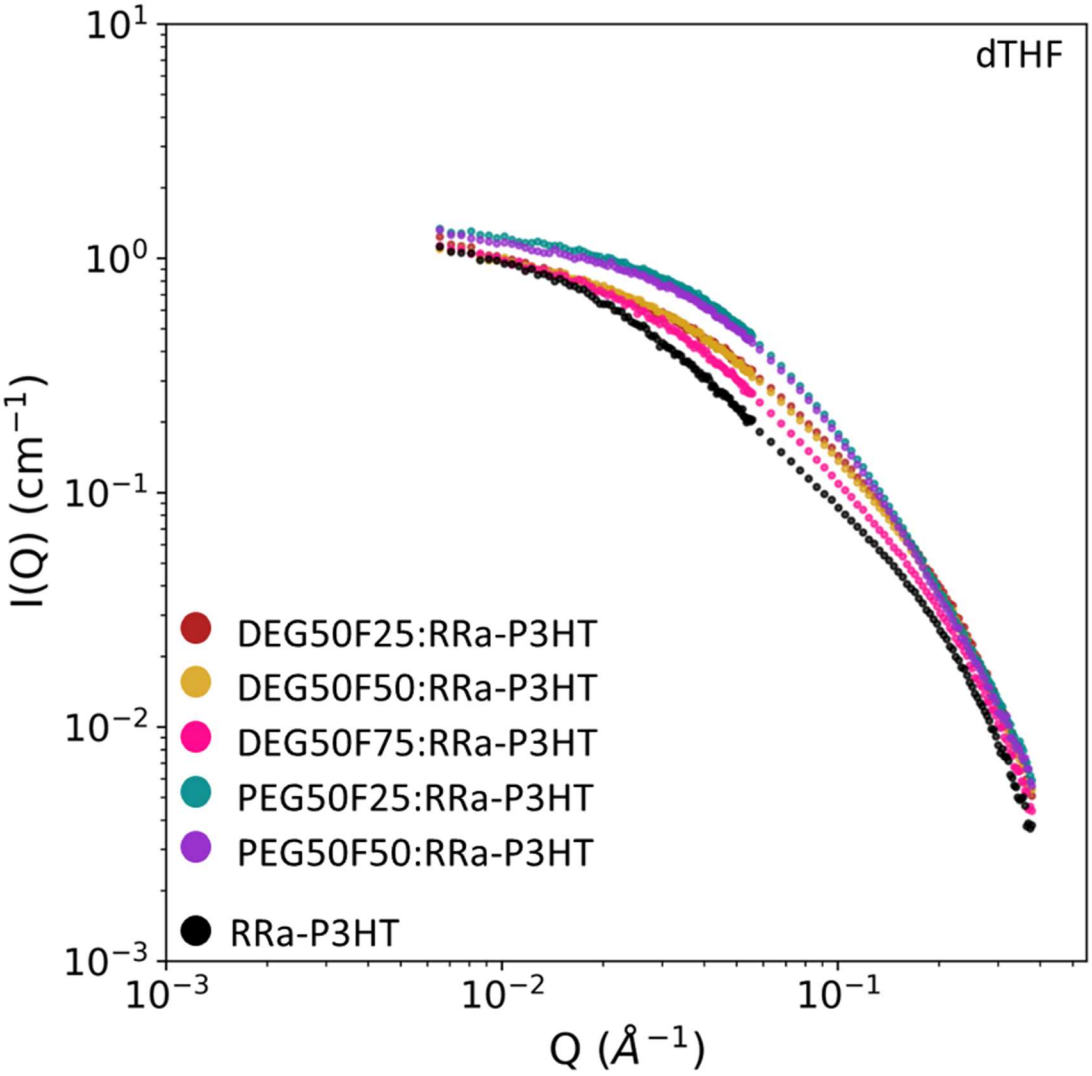

Figure 7.8: SANS data of 10 mg/mL EGF and 10 mg/mL RRa-P3HT blends in dTHF

Summing the individual components, as shown in **Figure 7.9**, we can see that there is no increased assembly in the blended solution above the summed data. Curiously, we see that the summed data 'scatters' above the experimental data for the blends, suggesting that there is increased scattering when the components are separate than if they were blended together. This is highly unusual and warrants further investigation.

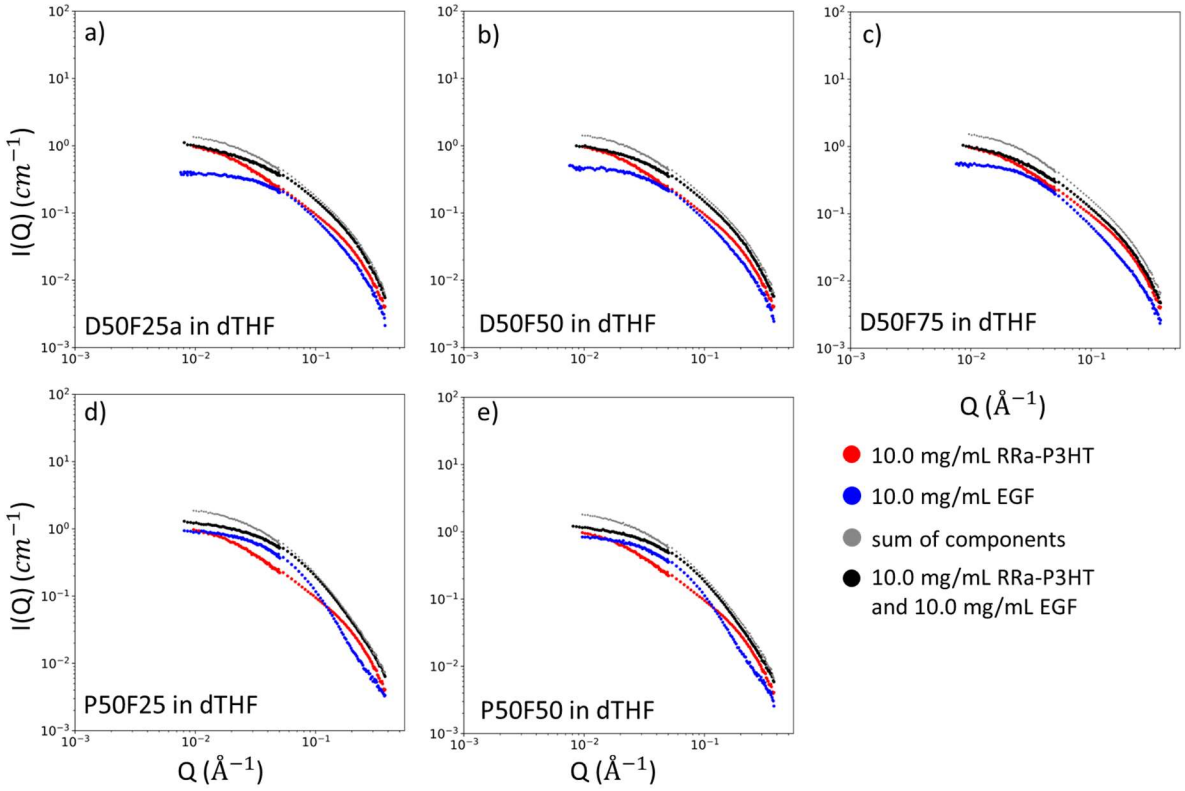

Figure 7.9: Individual plots for a) DEG50F25, b) DEG50F50, c) DEG50F75, d) PEG50F25, e) PEG50F50 with the pure solution of 10 mg/mL RRa-P3HT, the pure solution of 10 mg/mL of the EGF, the sum of the individual componets, and the experimental data for the blended system in dTHF

An additional series of samples was also run with modified concentrations (ratios) of conjugated polymer to EGF. A series of samples were made in dTol with adjusted EGF concentration (**Figure 7.10**). All of the samples contained 10 mg/mL of RRe-P3HT, but the low concentration samples have 1 mg/mL of EGF, the mid concentration has 5 mg/mL of EGF, and the high concentration samples have the same 10 mg/mL of EGF as discussed in **Figure 7.6**. In chapter 6, we observed major changes in the structure of the pure EGF samples with decreasing the concentration in dTHF50 and looked to identify if the addition of P3HT helped to stabilize the lower concentration of EGF in the blends. We see structural changes with each decrease in the concentration of the EGF in the blended solution. For the 5 mg/mL solution, there are traces of the spherical micelle features seen in the PEG-based models as well has the highest measured fluorination ratio of the DEG (DEG50F50). With the 1 mg/mL EGF: 10 mg/mL RRe-P3HT blended samples, we see all samples show trends similar to those in better solvents (dCF, dTHF),

a gradual curve with features in mid-Q and high-Q. At low concentrations of EGF there is no feature difference in the high-Q feature, with only slight variations at low-Q. Measurements for pure EGF in solution at reduced concentrations were not run and therefore identification of the impact of the EGF on the scattering seen in the blended sample is not clear.

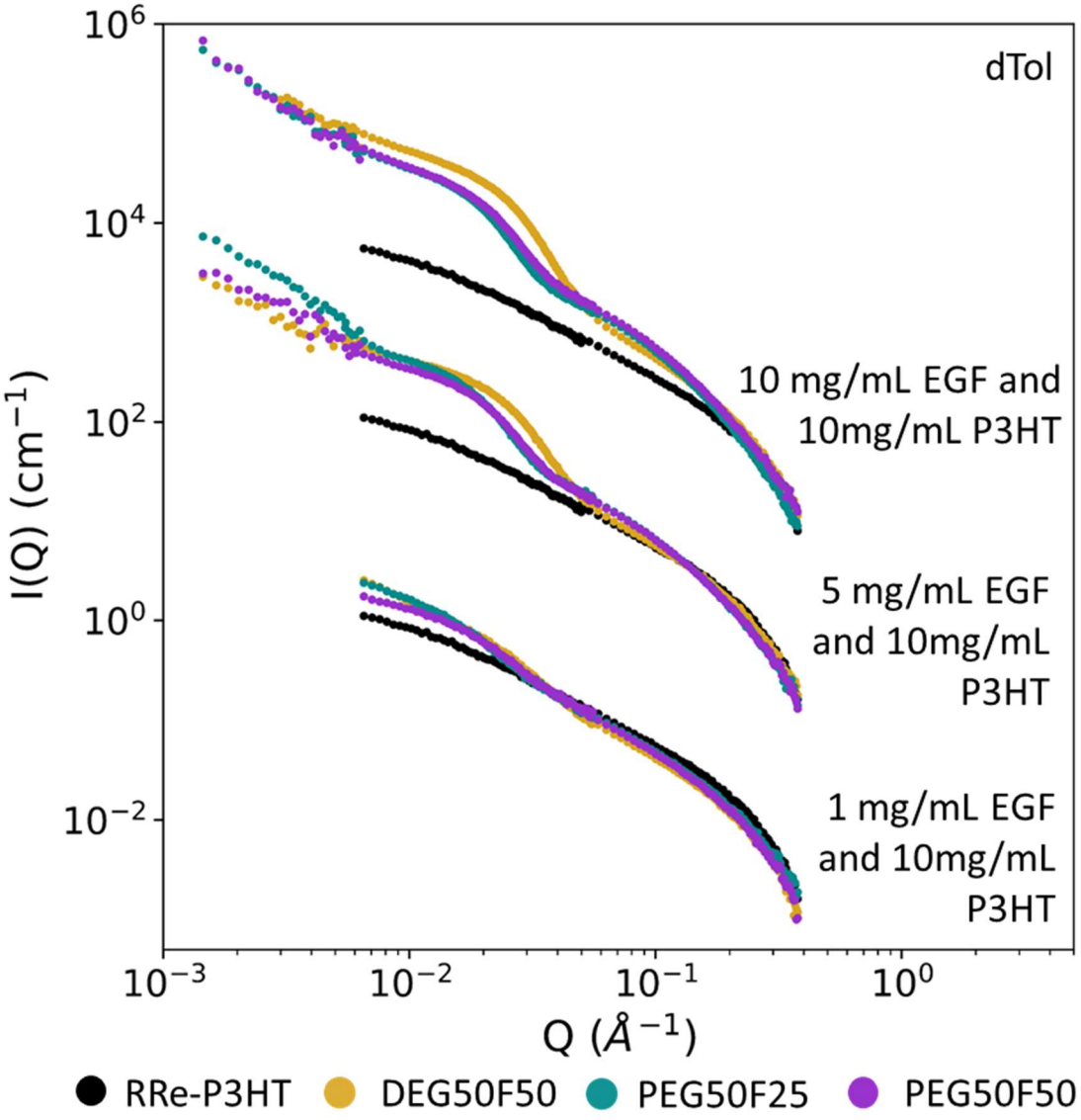

Figure 7.10: SANS data of samples with varying concentrations of EGF (10 mg/mL, 5 mg/mL, and 1 mg/mL) and 10 mg/mL RRe-P3HT blends in dTol.

This sample set was repeated in dTHF, with the same high, medium, and low concentration of EGF and a set concentration of 10 mg/mL of RRe-P3HT in the blend. This series is shown in **Figure 7.11a.** We have previously addressed the highest concentration samples in **Figure 7.4**, and

we can see changes between the high and medium concentration. The variation of the high-Q feature is reduced and the variation between the turnovers at low-Q are also reduced. The features further change with the reduction in concentration again. The DEG samples lose more intensity at low-Q, separating from the PEG-based blends. This separation is extended all the way down through to low-Q, with the DEG-based sample dropping below the PEG-based samples. We anticipate that the PEG-based blends display more assembly in solution at low concentrations than the DEG-based sample. For all reductions in concentration, there is a considerable drop in intensity, which can be tracked by the intensity separation between the 10 mg/mL RRe-P3HT and the blended samples. This reduction in intensity suggests there is less assembly of the EGF or co-assembly of the EGF and the RRe-P3HT at low concentration. The 10 mg/mL RRe-P3HT is present in all of the samples, so any scattering above the conjugated polymer is due to either contributions from the pure EGF or the interactions between the EGF and the P3HT. As seen in **Figure 7.11b**, pure DEG50F50 was measured at 5 mg/mL and therefore a sum of the components can be created. We observe excess scattering at low-Q of the experimental blend which is not seen in the sum of the components, suggesting there is excess scattering due to co-assembly of the EGF and P3HT at this lower concentration. As seen in **Figure 5b**, there is very little excess scattering seen at the 10 mg/mL P3HT: 10 mg/mL DEG50F50, so the decrease in concentration of the EGF seems to encourage co-assembly between the P3HT and the EGF. The other EGFs measured in lower concentration blends were not measured in isolation, so it is not clear if this trend is seen in other architectures or concentrations.

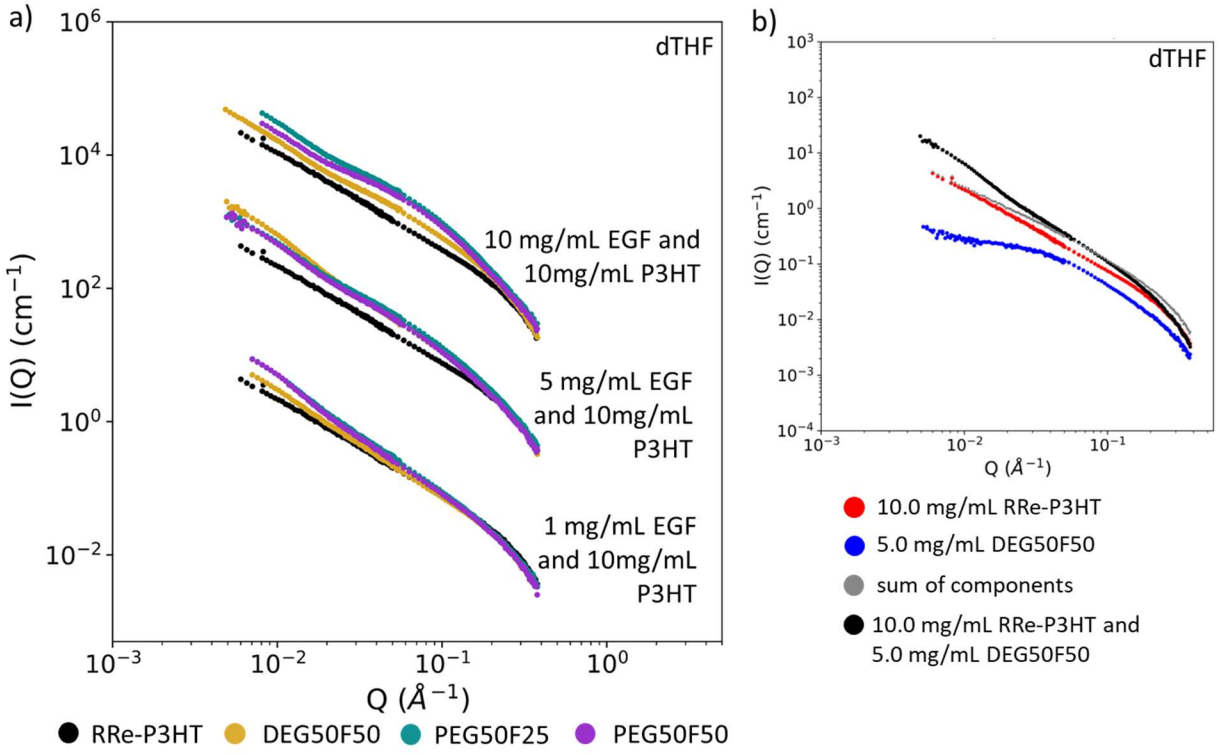

Figure 7.11: a) SANS data of samples with varying concentrations of EGF (10 mg/mL, 5 mg/mL, and 1 mg/mL) and 10 mg/mL RRe-P3HT blends in dTHF b) Individual plot for DEG50F50 with the pure solution of 10 mg/mL RRa-P3HT, the pure solution of 5 mg/mL of the EGF, the sum of the individual componets, and the experimental data for the blended system in dTHF.

7.4 Discussion

Changes in the solvent modifies the extent of interaction between the EGF and the P3HT in solution. In the best solvents, such as shown in **Figure 7.4** plot of dTHF, there is a large overlap between the sum of the individual components and the experimental blend data. This overlap increased with the length of the fluorinated block, suggesting that dTHF is a better solvent for the F block. The large overlap between the summed data of the individual components and the blend suggests that the blend is acting like a dilute solution with limited complexation. The extent and trends for the overlap in the summed individual components and the experimental blend data vary from solvent to solvent. In dCF (**Figure 7.2**), the overlap covers the high-Q region completely, but there is significant excess scattering in the low-Q portion of the experimental blends. This difference decreases as the length of the F-block increases but is maintained over all samples and architectures. In solvents that were determined to be poor in Chapter 6, shown in **Figure 7.6**, the experimental blend scattering in dTol is mostly identical to the sum of the individual components,

except for the low-Q region. The increased scattering is most likely due to large scale aggregation of the structures formed in the similar samples encouraged by the presence of the P3HT. In solutions made from fully amorphous RRa-P3HT, the summed data scatters over the blended solution, which will need to be investigated and analyzed further.

The concentration series showed structural changes in the scattering blends by decreasing the amount of EGF in the solution while maintaining the RRe-P3HT concentration. Large spherical-micelle-appearing structures shifted towards free chains structures as the concentration of the EGFs decreased. The effect on the structure was more prevalent in the DEG-based samples as opposed to the PEG-based ones. This agrees with the observations in Chapter 6 about the stability of the PEG-based polymers through architecture and solvent changes.

7.5 Conclusions

This work is still in the preliminary stages and many of the points raised need further investigation as well as solidified connections to the work done in Chapter 6. As anticipated, the systems became more complex with the addition of the P3HT and careful separation of each components scattering contribution is necessary to identify structure and parameters of the co-assembly. We observe co-assembly that is not present in the isolated component systems which is encouraging for creation of combined EGF and P3HT micelles. Part of the future work will involve fitting models to the data to extract parameters, and while this is not done yet, initial checks seem to agree well with cylindrical micelles, which is also encouraging for our goal OMIEC structures. Alongside structural modeling, additional work into characterizing the ionic and electronic properties is required to determine the effect of architecture, identified structure, and system parameters on the functional properties of an OMIEC.

7.6 References

1. Paulsen, B. D., Tybrandt, K., Stavrinidou, E. & Rivnay, J. Organic mixed ionic–electronic conductors. *Nature Materials* vol. 19 13–26 Preprint at https://doi.org/10.1038/s41563-019-0435-z (2020).
2. Tropp, J., Meli, D. & Rivnay, J. Organic mixed conductors for electrochemical transistors. *Matter* (2023) doi: 10.1016/j.matt.2023.05.001.
3. Tan, S. T. M. *et al.* Mixed Ionic–Electronic Conduction, a Multifunctional Property in Organic Conductors. *Advanced Materials* **34**, (2022).
4. Smela, E. Conjugated polymer actuators for biomedical applications. *Advanced Materials* **15**, 481–494 (2003).
5. Tropp, J., Meli, D. & Rivnay, J. Organic mixed conductors for electrochemical transistors. *Matter* **6**, 3132–3164 (2023).
6. Li, G. PEDOT: PSS-based intrinsically soft and stretchable bioelectronics. *Soft Science* **2**, 7 (2022).
7. Jang, J., Ha, J. & Cho, J. Fabrication of water-dispersible polyaniline-poly(4-styrenesulfonate) nanoparticles for inkjet-printed chemical-sensor applications. *Advanced Materials* **19**, 1772–1775 (2007).

8. Isaksson, J. *et al.* Electronic control of Ca 2+ signaling in neuronal cells using an organic electronic ion pump. (2007) doi:10.1038/nmat1963.
9. Boehler, C., Aqrawe, Z. & Asplund, M. Applications of PEDOT in bioelectronic medicine. doi:10.2217/bem-2019-0014.
10. van de Burgt, Y. *et al.* A non-volatile organic electrochemical device as a low-voltage artificial synapse for neuromorphic computing. (2017) doi:10.1038/NMAT4856.
11. Kim, B. G. *et al.* Chronic neural recordings using silicon microelectrode arrays electrochemically deposited with a poly(3,4-ethylenedioxythiophene) (PEDOT) film. (2006) doi:10.1088/1741-2560/3/1/007.
12. Savva, A., Wustoni, S. & Inal, S. Ionic-to-electronic coupling efficiency in PEDOT: PSS films operated in aqueous electrolytes †. *J. Mater. Chem. C* **6**, 12023 (2018).
13. Keene, S. T., Rao, A. & Malliaras, G. G. The relationship between ionic-electronic coupling and transport in organic mixed conductors. (2023).
14. Panzer, M. J. & Frisbie, C. D. Exploiting ionic coupling in electronic devices: Electrolyte-gated organic field-effect transistors. *Advanced Materials* **20**, 3177–3180 (2008).
15. Christine Luscombe, S. K., He, Y., Kukhta, N. A., Marks, A. & Luscombe, C. K. The effect of side chain engineering on conjugated polymers in organic electrochemical transistors for bioelectronic applications. *Royal Society of Chemistry* **10**, 2314 (2022).
16. Khot, A. & Savoie, B. M. How side-chain hydrophilicity modulates morphology and charge transport in mixed conducting polymers. (2021) doi:10.1002/pol.20210773.
17. Chloroform-[D_1] (99.8% D) (Isotopic) for NMR spectroscopy | VWR. https://pr.vwr.com/store/product/7488784/chloroform-d1-99-8-d-isotopic-for-nmr-spectroscopy.
18. Toluene-[D_8] 99+ atom % D for NMR spectroscopy | VWR. https://us.vwr.com/store/product/7516136/toluene-d8.
19. Tetrahydrofuran-[D_8] (99.5% D) for NMR spectroscopy | VWR. https://in.vwr.com/store/product/4690875/tetrahydrofuran-d8-99-5-d-for-nmr-spectroscopy.
20. Di (ethylene glycol) methyl ether methacrylate 95 45103-58-0. https://www.sigmaaldrich.com/US/en/product/aldrich/447927.
21. Poly (ethylene glycol) methyl ether acrylate average Mn 480, MEHQ 100ppm inhibitor, BHT 100ppm inhibitor 32171-39-4. https://www.sigmaaldrich.com/US/en/product/aldrich/454990.
22. 2,2,3,3,4,4,4-Heptafluorobutyl acrylate 97 424-64-6. https://www.sigmaaldrich.com/US/en/product/aldrich/443751.
23. Hiura, S. *et al.* Thermoelectric Properties of Poly(3-Hexylthiophene) Nanofiber Mat with a Large Void Fraction. *Materials* **10**, (2017).
24. Neutron Activation and Scattering Calculator. https://www.ncnr.nist.gov/resources/activation/.
25. Wood, K. *et al.* QUOKKA, the pinhole small-angle neutron scattering instrument at the OPAL Research Reactor, Australia: design, performance, operation and scientific highlights. *urn: issn:1600-5767* **51**, 294–314 (2018).
26. Kline, S. R. & IUCr. Reduction and analysis of SANS and USANS data using IGOR Pro. *urn: issn:0021-8898* **39**, 895–900 (2006).
27. Doucet, M. *et al.* SasView. Preprint at (2022).
28. Doucet, M. *et al.* Sasmodels. Preprint at (2020).
29. Kienzle, P. A. (Unviversity of M. C. P., Krycka, J., Patel, N. & Sahin, I. Bumps. Preprint at (2011).
30. Newbloom, G. M. *et al.* Solvatochromism and conformational changes in fully dissolved poly(3-alkylthiophene) s. *Langmuir* **31**, 458–468 (2015).
31. power_law — SasView 5.0.6 documentation. https://www.sasview.org/docs/user/models/power_law.html.
32. Wolf, C. M. *et al.* Blend Morphology in Polythiophene–Polystyrene Composites from Neutron and X-ray Scattering. *Macromolecules* (2021) doi: 10.1021/acs.macromol.0c02512.

Chapter 8: Conclusions and Outlook

8.1 Summary

Chapter 3 focuses on the structure-property relationship of a polystyrene/conjugated polymer blend system. The bulk of the work done in this system focused on the modeling of a complex system, which is reliant on the crystallinity of the conjugated polymer additive and the solvent used in processing. Amorphous materials produced different films than their semi-crystalline counterparts, due to the self-assembly and nanowire formations within the solution that carried to the dried blend. We also found that compositionally identical samples cast from different solvents showed different structures, as well as changes in the conductivity of the samples. In the process of fitting, we utilized a complex model that accounted for the scattering within the polystyrene, as well as separate fits for amorphous domains and ordered nanowire domains within the polymer.

In Chapter 4 we addressed an elastomeric conjugated polymer blend system of polystyrene-polyisoprene-polystyrene (PS-PI-PS) and poly(3-hexylthiophene) (P3HT). The focus of this work was to identify and understand the morphology of a complex system relevant to elastomeric organic electronics. A series of polymer blends were developed utilizing heat pressing methods developed during the work of Chapter 3. A set of these samples were pressed at a range of system relevant temperatures, and we determined that increasing the temperature of pressing increased the order in the samples, allowing for in-depth analysis and phase identification. We determined that as conjugated polymer was loaded into the system, amorphous or semi-crystalline, the phase shifted from cylindrical micelles to a lamellar dominate mixed phase system back to a cylindrical phase system. This transition is accompanied by slight shifts in phase spacing as well as changes in the order of the system. We established an understanding of a complex multicomponent system, but also identified points of variation and processing effects.

Chapter 5 continued work done on the PS-PI-PS/P3HT system focusing on the processing of these samples. Polymer systems often have dependency on the processing choices itself, including solvent, temperature, and methodology. In an effort to establish the effect of the processing method itself on the morphology observed in Chapter 4, we isolated a selection of processing parameters. We established that heat pressing introduced alignment in the sample and modified the order and spacing of the phase structure. Variations in pressing time have a large effect on morphology but can also be considered in consort with the pressing temperature trends

observed in Chapter 4. Modifying the conjugated polymers molecular weight has minor effects, but replicates made at the high temperature have a natural variation in phase structure, onset, and order within the critical range of P3HT loading. Investigations into the solvent showed little modification in the structure, except at high processing temperatures in RRe-P3HT, where the 'poor' solvent significantly increased structural irregularity. Post processing heating modifies the structure significantly, but without the pressure and physical constraints of pressing, the systems tend towards disorder rather than order. These samples can also be intentionally aligned, with the cylindrical phase aligning easily with the flow and mixed phase system between 2.5 wt % and 10 wt % being partially aligned. This chapter emphasizes the importance of understanding the processing choices and the effect of each, as many of the choices made during 'baseline' processing have the ability to affect the morphology described in Chapter 4.

Chapter 6 shifts to focus on a solution polymer system consisting of a high-χ parameter PDEEGA-block-PHFBA (EGF) polymer. We anticipate the use of this polymer in a P3HT/EGF blend for an Organic Mixed Ionic Electronic Conductor (OMIEC), but before blending we need to establish an understanding for the matrix. We investigated five different polymers using two variations of the EG block and a change in the ratio of the EG to F block. We also investigated solvent quality using multiple solvents, including a series of carefully worsened solvents. We determined that both polymer architecture and solvent quality changed the structure of the EGF in solution. We found that 'poor' solvents encourage the formation of micelles, both spherical and cylindrical, while the type, extent, and dimensions of the structures are dependent on the EGF architecture. We also found that the PEG-based solvents only formed spherical structures and showed less modifications caused by architecture changes and solvent quality. We also found that the reduction in concentration in DEG-based blends led to disordered and aggregated samples. We identified structures present in pure solutions of EGFs and identified a few ways that the composition and processing may affect the OMEIC blends.

The OMEIC work was continued into Chapter 7, with blends of P3HT and the EGFs investigated in Chapter 6. We found that the inclusion of the conjugated polymer in solution encouraged the growth of cylindrical structures. In solutions where the conjugated polymer was entirely amorphous and there was no self-assembly in solution, the blends were consistent with free chains in solution suggesting the self-assembly of the semi-crystalline conjugate polymer encourage the growth of micelles. For some blends, the two components did not interact at all in

solution, as the sum of the pure EGF and the pure P3HT scattering data was the same as the scattering of the experimental blended samples. We also identified that changes in concentration change the size and shape of the structures formed. With a strong understanding of the behavior of the pure solution we can identify how the blended systems change with the addition of the conjugated polymer. This work lays out preliminary analysis and identifies specific questions for further investigation.

8.2 Future Work

The elastomeric polymer work focused on morphology, phase behavior, and processing variables in the heat pressing method that we developed. This method mimics industrial heat pressing but on a smaller scale and this work produces relevant understandings for similar methods of heated pressing and molding. This system is now fairly well understood in a heat pressed processing method, but this understanding is not applicable to PS-PI-PS/P3HT systems in other processing methods. It would be interesting to see how the morphology and phase behavior would vary with other processing methods. Perhaps there is removal of all traces of aligned cylindrical phases in spin coated sample, or if the rapid speed of evaporation halts all assembly, preventing any of the morphology we observed in our much slower dried samples. It would also be interesting to identify the effect of the relevant processing variables addressed here in different processing methods. This expansion would be niche fundamental work on a specific system, but we anticipate that modified processing would continue to produce modified structures.

The EGF/OMIEC work has much more work to be done. Additional analysis of these samples is required, by expanding the fitting to include cylindrical micelles, specifically in the blended samples. These samples should also be characterized for both ionic and electronic transport, connecting the observations seen in their structure to the properties we are selecting for. With these samples finalized both structure and property-wise, investigation of the samples over the course of drying and device manufacture would be necessary. From previous work, we know that the structure seen in the solution phase is maintained and can affect the solid cast phase, but the thermodynamic forces acting during evaporation are extreme and can cause large changes. Understanding how the solvent quality not only changes the solution phase structure but also the cast phase structure would complete the understanding of this sample set.

Chapter 9: Appendix

9.1 Pallicera: Taste-Masking Pediatric Medications

The author would like to acknowledge the contributions of mentees for the following work and makes no claim of sole contribution to the data. The work was started in collaboration with a senior design class project over two years, with contributions from eight undergraduate students. Students in the 2018-2019 school year (Gary Boon, Zayed Mohideen, Redeen Duran, Emily Rhodes) helped receive a Foster School of Business Prototype Funding Award and participate as a finalist in the Alaska Airlines Environmental Innovation Challenge and Hollomon Health Innovation Challenge. Students in the 2019-2020 school year (Mariam Hussein, David Jiang, Aiden Jackson, Bri Stokes, Emily Rhodes) helped with business planning, and market discovery, receiving a UW NSF Innovation Corps Award. Emily Rhodes participated in the senior design both years and was also the co-founder of Pallicera, helping the startup to participate in the Jones and Foster Accelerator, receiving the award from the accelerator as well as McAleer Early Start funding.

9.2.1 Introduction and Problem Addressed

According to the 2018 World Health Organization's (WHO) yearly malaria report, the reported malaria cases have slowly been decreasing since 2010, but still number over two hundred million separate cases. Diseases like malaria disproportionally affect certain populations, with 80% of malaria cases in only fifteen countries, and with children under the age of 5 years old accounting for 61% of all malaria deaths: 266,000 out of 435,000[1]. Young children are often without the proper immunities to effectively combat such an illness and are often without the proper formulation of medication. Most medications that are developed for serious diseases are designed with adults in mind, the dosage is for an adult, the method of administering the medication is for an adult, and the taste necessary for adherence is designed for an adult as well. This often leaves gaps in the treatment plan for children, as the treatment is not designed with them in mind.

In an exploration of the taste of molecules, researchers discovered that the majority, about 77%, of randomly generated natural and presumed therapeutic molecules were determined to be bitter[2]. This helps explain the unpalatable taste profile of many pharmaceuticals, with the vast majority of possible therapeutic molecules contributing undesirable notes. For example, a large class of medications currently in use for the treatment of malaria is derived from quinine, a notoriously bitter substance. Quinine is a historical treatment for malaria derived from the bark of

a tree in the Cinchona family and has pulled the focus of western medicines treatment of malaria since the 1800s[3]. As quinine-resistant strains of the parasite emerged, multiple synthetic derivatives of quinine were identified as effective treatments and were produced synthetically, each maintaining a bitter taste. As further strains of drug-resistant parasites emerge, new treatment plans are developed, with quinine or its derivatives often included, with many making the 2023 WHO essential medications list[4]. When negotiating treatment for adults, taste isn't an insurmountable barrier, as most adults understand the benefits and are willing to take bitter medication regardless of the taste. Children are often much more difficult to convince, especially when faced with vile tasting treatment. Researchers show that one in three children refuse medication based upon taste, and in large surveys of treatment non-adherence, one of the most common reasons for not finishing a treatment was unpalatable taste[5]. In high-risk diseases, failing to finish a course of medication can be fatal or result in life-long consequences, and this risk is exacerbated in long-term treatment plans. With malaria, treatment occurs over a one to three-week period, and can be extended if the infection is an advanced form, with medication taken twice a day[6]. This means to treat a young child for a low-to-mid-risk malaria infection, the child will have to take 14 to 42 doses of an extremely bitter medication, in order to achieve the best chance of success. For higher risk infections, the number of doses the child will have to take can increase drastically, leading to even higher risks of non-adherence.

Pediatric medications come with a host of considerations that change the way medication is created, formulated, and distributed. Solid state formulations are preferred for safe, stable, and low energy shipment and storage needs, yet children under the age of five often have troubles safely swallowing solid capsules and tablets larger than 10 mm[7]. Solid tablets also are more difficult to modify dose loads for a child, as the required dose changes quite rapidly during the first few years of childhood as the weight rapidly changes. As most solid formulations are designed in adult doses, it is often the responsibility of the caretaker to portion the child's dose. This often creates errors in dosing, by underestimating the dose leading to efficacy issues, overestimating the dose leading to toxicity or increased side effects, or even losing part of the next dose as crumbs during the portioning process. Liquid formulations are usually recommended for children, with over 90 % of pediatric specific formulations in a liquid form, but these often have complications as well[8]. For adult sized solid tablets, there are many known taste masking methods such as spray film coatings and gel capsules, but it is much harder to taste mask a completely liquid solution.

Oftentimes the taste is simply covered with sugars, flavorings, and other excipients, which may have deadly side-effects in children. For example, propylene glycol is often used a solvent in adult medication without side-effects, but when used for young babies can cause seizures or intercranial hemorrhaging[9]. With neither pure solid tablet nor pure liquid formulations being ideal, in 2008 the WHO proposed a flexible solid-oral dosage form as an ideal formulation[7]. The proposed flexible solid-oral dosage form transports as a solid tablet or pill but can be dispersed in water or juice and administered in a liquid form for easy consumption.

While considering transport, stability, safety, and administration, taste masking adds a few more design considerations. Neither of the two pure phase formulations are ideal for taste, but for different reasons. In a solid pill, often sized for adult dosing, the pill must be ground up, portioned out, and mixed into food or drink for consumption. Due to the grinding, any coating to mask taste is now gone, and oftentimes the food or drink is flavored bitter. The child now must consume a larger quantity of a bitter substance, usually not finishing the full recommended dose. In liquid formulations, the taste is usually not completely masked, but flavored. These additives are designed to be safe for adults, but these additives may have unintended side effects for children over the course of long-term treatment plans. Even the WHO proposed flexible solid-oral formulation doesn't mask the taste and requires mixing into more tasteful foods or drinks, leading to the same problems as the solid pill. Taste is often not considered to be a vital component of the formulation creation, often being passed up for cost, efficacy, and stability, but with the need to improve treatment adherence, modifications must be made to account for taste.

Previous attempts to taste mask these medications for pediatric formulations use a variety of techniques and materials. A series of formulations tested and successful in laboratory settings used an ion exchange resin which can buffer the bitter or ill tasting molecules using an insoluble polyelectrolyte[10–12]. Additional experiments have focused on formulations similar to the WHO recommended flexible-solid oral formulations, for instance one which focuses on insoluble derivative quinine pamoate, which can be formulated into tablets that quickly break apart during dosing[13]. Other formulations focus on taste masking solid forms suitable for children, such as small ~500 μm pellets with polymer coatings leading to undatable tastes during consumption[14]. We also see multi-layer emulsions with a medication in the center, surrounded by protective water and oil-based layers to prevent breakdown of the emulsion before the stomach[15]. Although there are many

explored taste-masked formulations, there is a still a lack of taste-masked, pediatric-designed formulations on market and in use[16].

We look to determine a way to take an active pharmaceutical ingredient (API) and optimize formulation to have a high drug loading to reduce dose volume, completely taste masked final state, stability during shipment and storage, and a low cost to encourage on market use. Ideally this formulation would also be modifiable, as the emerging drug resistant parasite strains make new API's necessary. With these criteria in mind, there are a few ways to approach the design of this formulation.

9.2.2 Solution

To address all the constraints of pediatric formulation as well as the constraints of the taste masking, it is necessary to work backwards from an ideal final product - the WHO's recommended flexible solid-oral formulation. The final formulation should be a freeze-dried compressed pellet, which can be redistributed in less than a few milliliters of water. This method is used by local non-profit PATH in a method producing freeze-dried fast-dissolving tablet (FDT) of HIV antiretroviral medication, with much success in creating a stable transportation form, yet a small and liquid consumable form[17]. While these FDT's are transportable and consumable, they are not taste masked, but with some planning for the liquid that is to be freeze dried, the rehydrated solution given to the child can be taste masked. The liquid itself needs to have the bitter API in an encapsulated structure that can survive the freeze-drying process. This can be done through stabilized emulsions, with the drug enclosed within coated droplets. With some testing on different surfactants, a coating can be designed that will prevent the contents of the droplet from leaching out, as well as stabilize the droplets through freeze drying. This coating would also allow for the bitter API-laden solvent to completely bypass the taste receptors as shown in **Figure 9.1** below.

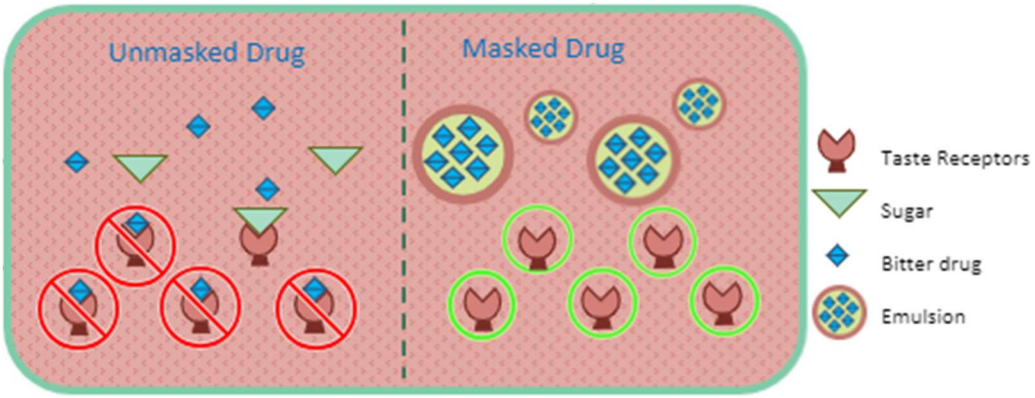

Figure 9.1: Schematic hypothesis of an unmasked bitter drug binding with taste receptors and an emulsified masked drug upon consumption avoiding all of the taste receptors.

To reduce the final dose volume to a minimum, the drug loading capability of the solvent in the interior of the droplet must be maximized. This can be done with a Natural Deep Eutectic Solvent (NaDES), a subset of specially designed materials called Deep Eutectic Solvents (DES). A simple binary DES is composed of two components, which when mixed and melted display different properties than the two components do separately. The most recorded, and property of interest, is the melting temperature of the final DES[18,19]. When the two components are melted, they form complex and strong hydrogen bonds, which modifies the final solvent structure and lowers the melting point of the final solution below the melting point of either component. NaDES rely on components that are naturally derived, and for edible purposes are typically much safer, as most of the individual components are already approved as FDA food safe components[18,20–22]. Other than the natural origin, and some additional bonding pair opportunities, DES and NaDES display very similar properties. With slight modifications, a simple NaDES can be expanded to use quinine (or any other API with hydrogen bonding capability) for a third component, increasing the complexity of the system, but vastly increasing the concentration of drug in the solvent. As opposed to a normal solvent simply dissolving the maximum amount of the API, the solvent can instead be built using the API as a vital component, removing the constraints of solubility. This also allows for the solvent to be created below the melting point of the drug (57 ºC) and, with refinements to the other components, allows for the solvent to be liquid at room temperature. The final NaDES formulation allows for more of the drug to be added into the system - increasing the drug loading, and subsequently lowering the volume of the final solution needed per a tablet dose.

Initial experimentation has been done to determine a few component possibilities and to observe how viscosity (and the correlating melting temperature) varies with component ratio differences. In a system using lactic acid, fructose, and quinine as the three components, various ratios of the three components have created NaDES with high drug loading in some– up to 41 wt % quinine – and low viscosity in others. This investigation into possible solvents only touches the surface of an incredibly diverse component space. For NaDES, possible components include carboxylic acids, sugars, amino acids, urea-based compounds, organic cations, and metal carboxylate salts, with most of these compounds able to bond to each other as well to other compounds within their category[20]. Along with the vast number of combinations of components,

different ratios of each component create DES's with different properties, expanding the large testing space of ternary components to an even larger range. While, through simple sample testing, promising components can be identified, the testing needs to match the scope of the sample space being tested upon. Additional focused research addressing this large sample space is addressed in the next subsection (9.2 - Phase-IR: High Throughput Phase Analysis)

With the optimized proposed solvents, the next step is to envelop the drug loaded solvent with a coating that would prevent leaching of the drug into the mouth. A way to do this is with surfactant stabilized emulsions. Emulsions are a type of colloidal suspension of two liquids, usually with an oil phase liquid and a water phase liquid[23,24]. These emulsions take the form of micron sized droplets of one of the components, suspended in the other component as a continuous phase. In this case, the solvent will be isolated within the droplets, enveloped by a thin shell of surfactant, and surrounded by the other liquid as the continuous phase (**Figure 9.2**)[25–27]. The most economical setup will be with a hydrophobic (oil-phase) solvent, a food-safe polymer or gelling agent, and a water-based continuous phase. Preliminary tests, done in a food safe lab with an edible analog and mechanical emulsification, succeeded in completely covering the taste of the chosen analog, jalapeño oil. Additional preliminary tests have been done with using quinine loaded NaDES and spontaneous emulsification. A NaDES formed from proline, oleic acid, and quinine was dissolved in methanol, which was added to an excess of water, causing turbidity in water, signaling an emulsion is present.

Once a surfactant stabilized emulsion is created, regardless of method of emulsification, the final flexible formulation still needs to be created, and stability confirmed. Similar methods as proposed are used at PATH to create freeze-dried tablets[17]. Their use of a freeze dryer to create small capsules that can easily be rehydrated in a small amount of water, allows for the drug to be easily shipped through inhospitable conditions with no refrigeration. With a strong polymer coating around the solvent, the droplets can be centrifuged from the continuous phase and using a lyophilizer, or freeze dryer, stabilized into an FDT. The dried mixture consists of polymer stabilized solvent droplets, which when re-dispersed in a few milliliters of water, will re-form the taste masked emulsion. Data collected at the national institute for Technology and Standards (NIST) neutron scattering facility is presented in **Figure 9.2**. The freeze-dried formulation was measured at various stages in the processing, including freshly made without stabilization, with stabilization before centrifugation, after centrifugation, and after freeze drying and rehydration.

These stages encompass the identified points where extreme stresses are placed on the system, and emulsion breakage and formulation failure can occur. As we can see from the data, an emulsion is formed both with and without the F88 stabilization polymer. Over the centrifugation step we see a decrease in the feature around 0.003Å^{-1}, indicative of a small breakage of droplets, or the removal of excess material that was not used in the emulsification or stabilization. The emulsions do remain post centrifugation which is key. The next step is to freeze dry the solution, transport it (in this case across the country to NIST), and rehydrate it into a liquid mixture. When comparing the scattering curves of the rehydrated emulsion to the post centrifuged emulsion we see another drop in intensity, indicating that a portion of the droplets did not survive the harsh lyophilization process. While a portion of the droplets broke, there is a still clear emulsion that remains and is stabilized and encapsulated. This data is preliminary and further experimentation would be necessary to determine the specifics of the loss, breakages, and remaining solution, as well as ways to optimize the formulation, but these results show promise.

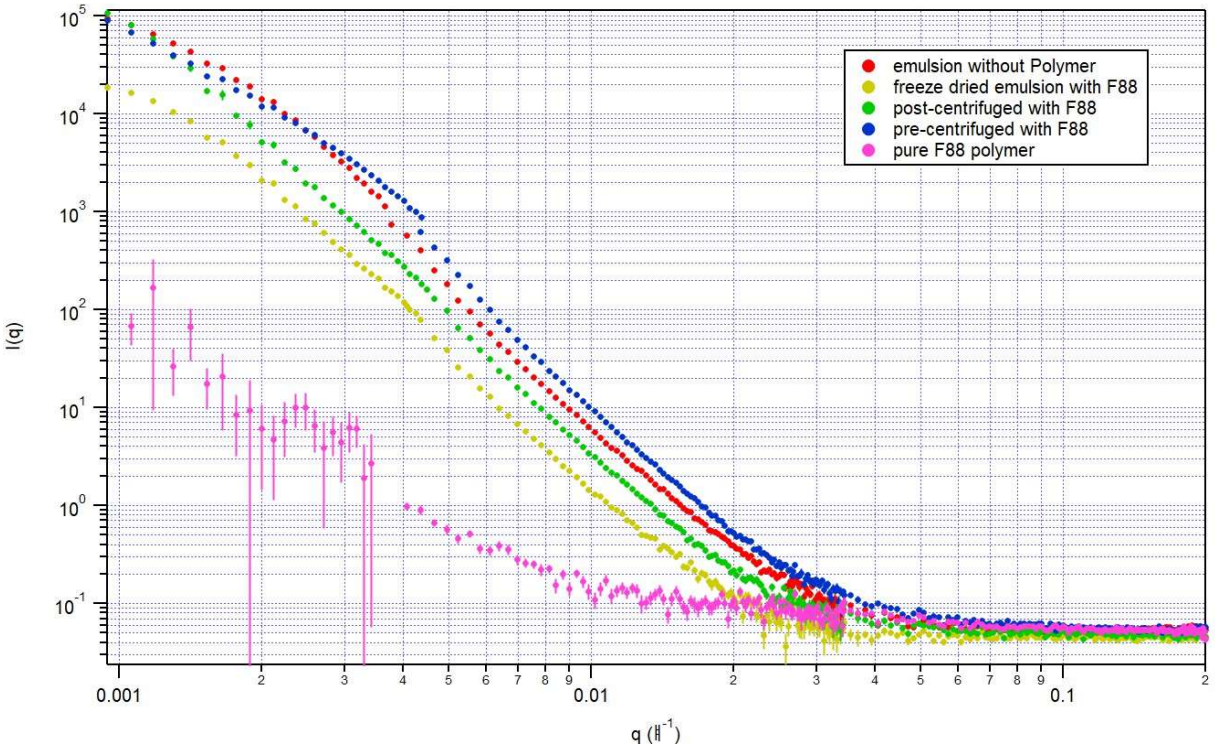

Figure 9.2: Neutron scattering data collected from NIST illustrating the emulsion state at various stages in the processing method, including emulsion creation, stabilization, centrifugation, lyophilization, and rehydration.

Once the final formulation is created, testing of the efficacy of the drug is vital. If the formulation does not work, the taste does not matter in the end. Multiple lab experimentations are possible, as shown in various pharmaceutical research papers[28]. Using a dialysis bag technique with a solution mimicking a pH 7 saliva, the ability of a drug to dissolve in the mouth can be tested. If a formulation dissolves in the mouth, then the drug can be tasted. The formulation should also be tested in a pH 1.5 solution, mimicking a stomach acid environment, where the drug should break down to be distributed into the bloodstream to work. Further tests are recommended in animals, testing the blood plasma levels within set times of drug administration, ensuring that the additions of natural components do not interfere with the API's ability to work. There are measures that can be taken to aid this process, such as ensuring the separate components have no ill effects, and removing excipients that would interfere with the drugs ability to disperse both in stomach acids, and in the blood. None of these steps were tested with the proposed formulation and would need to be in order to ensure viability for application.

Implementing this formulation is complex and requires careful optimization. Each stage of the process is interconnected, as the properties of the solvent affect if spontaneous emulsification is even possible or a different method of taste masking is needed. For example, spontaneous emulsification and freeze drying is currently considered to be the optimal route, so when designing the solvent an emphasis should be placed on water-immiscibility. This whole process consideration should encourage an optimized process, but if a water-miscible solvent is created with remarkably high drug loading and low melting point, auxiliary plans for taste masking and stabilization are in place. This flexibility and optimization potential is a benefit as it also allows for modularity, as through adjustments to the solvent different API's can be implemented into the NaDES but requires more work to ensure an efficient formulation. Measures of success also need to be taken, including pharmacokinetic efficacy, completeness of taste masking, and stability of the freeze-dried tablet through long transport and storage.

9.2 Phase-IR: High Throughput Phase Analysis

The work presented in this section is also reported in the following publication:

Rodriguez, J, Politi, M*, **Scheiwiller, S**, Bonageri, S, Adler, S, Beck, D and Pozzo, LD. 2021. PhasIR: An Instrumentation and Analysis Software for High-throughput Phase Transition Temperature Measurements. Journal of Open Hardware, 5(1): 6, pp. 1–13. DOI: https://doi.org/10.5334/joh.39*[29]

The author would like to acknowledge the significant contributions of coauthors for the following work and makes no claim of sole contribution to the data. All sections included here are for clarity and a comprehensive understanding of the work, and more information can be found in the above publication.

9.2.1 Introduction

Thermal analysis consists of determining melting/boiling points, phase transitions, contamination, and stability. These metrics are integral to material development in many fields, including pharmaceuticals[30,31], electronics[32–34], polymers[35–37], and food science[38–40]. Instruments typically used to for this analysis include differential scanning calorimetry (DSC) and differential thermal analysis (DTA), which compare a sample and reference under identical thermal cycles[41]. The measurements are precise, but are often slow, with a single sample taking upwards of an hour to run, and multi-cycle runs taking many hours. For small batches of samples, the time needed is not a deterrent, but in fields where the sample pool is large, running all the samples with a DSC becomes unreasonable. There are add-ons to these instruments that allow for automated sample measurement, but while this reduces the work of the researcher, the time frame remains lengthy. Therefore, these instruments are not conducive to high-throughput experimentation, inhibiting the use of a powerful materials discovery tool, especially when paired with data science and machine learning algorithms[42–46]. Other researchers have proposed methods of thermal analysis that may be more conducive to high throughput experimentation using infrared (IR) cameras. Kawakami et al introduced this method using an IR camera to observe the melting of common active pharmaceutical agents on a hotplate and was able to determine melting points from a spike in temperature of the sample due to an increase in thermal conductivity upon melting[47]. Other researchers, such as Hou et al. expanded on this method using custom aluminum pans with multiple wells to sample multiple materials at once[48]. These methods have established a proof-of-concept for high-throughput measurement of phase change using IR cameras, but an accessible hardware and software system is not currently available. We set out to develop an effective, low-cost, lab-customizable platform for measurement, detection, and analysis of phase transitions that can be used to measure and quantify large sample sets at one time.

9.2.2 PhaseIR Platform

The PhaseIR platform encompasses both the hardware and software needs for the experiment. The goal of the platform is to provide an instrument capable of performing accurate

high-throughput measurement of the thermal information of a sample set as well as the software necessary to run, collect, process, and quickly analyze the data. All of the resources are provided, and the system is able to be modified by the researcher to account for sample specific or need specific changes.

9.2.2.1 Full Design Overview

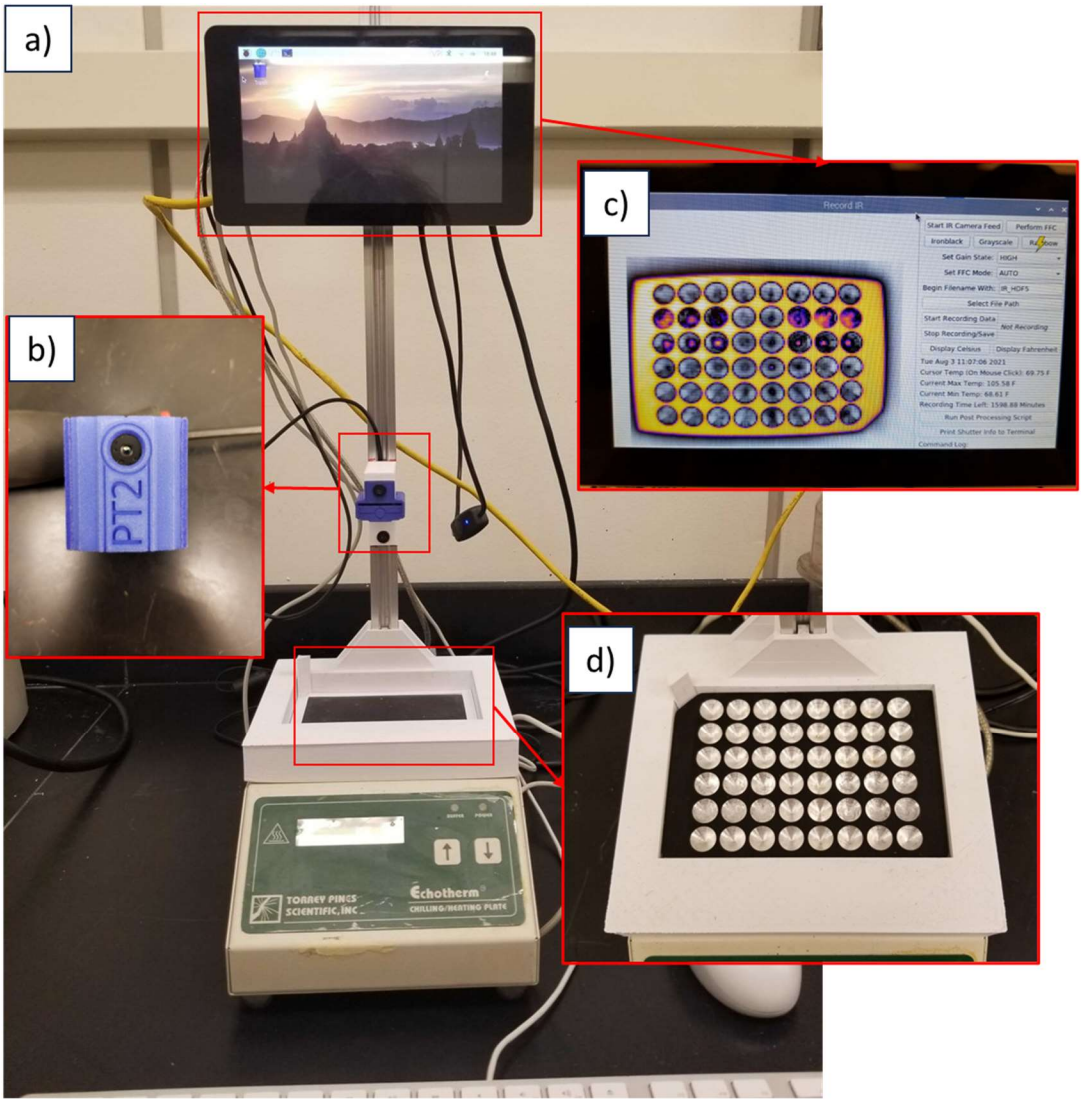

Figure 9.3: Overview of the PhaseIR system. a) show the full system as set up for use, b) is a close up of the FLIR Lepton 3.5 camera which collects the IR data from the samples, c) is a close up of the Raspberry pi powered computer with software GUI for running, d) is a close up of the sample location on top of the hotplate with an alignment grid and aluminum well plate where the samples are melted.

The PhaseIR system was designed to be easily constructable and inexpensive, so all parts are either individually purchased commercially, machined, or 3D-printed. The total cost of the system at the time it was built was $1,800. The system utilizes a FLIR Lepton 3.5 IR camera placed at a fixed position above an Echotherm IC25 Peltier plate with a sample holder. The sample holder consists of a machined aluminum well plate, with options for 96, 48, or 24 conical sample locations, and a 3D-printed Acrylonitrile Butadiene Styrene (ABS) sample enclosure for consistent placement of the well plates below the camera. The conical wells and ABS enclosure aids in sample positioning, ensuring that the location of the sample is known, and the data is streamlined for analysis. During the measurement, the IR camera records the entire plate, and each frame of the recording is saved in a collected HDF5 file. The data file is then processed by the accompanying open-source software package, and, like DTA techniques, the sample temperature is compared to a reference point on the black anodized aluminum plate to determine phase information[30].

9.2.2.2 Hardware Specifics

We utilized a FLIR Lepton 3.5 Radiometric IR camera procured from GroupGets to capture thermal processes occurring because of the simultaneous heating/cooling of samples in parallel. The dynamic range of this camera varies from –10°C to +140°C in high-gain mode and –10°C to +400°C in low-gain mode, with radiometric accuracy of 5% and 10%, respectively. This is adequate for capturing a wide range of phase transitions occurring in organic materials and covers the entire operable range of the chosen heating/cooling plate. The image size obtained from the Lepton 3.5 is 160 × 120 pixels. The Lepton 3.5 camera core was integrated with the PureThermal 2 Smart I/O module procured from GroupGets to interface as a USB webcam, Figure 3c. The Lepton 3.5 and PureThermal 2 board were both enclosed in a case that was also provided by GroupGets. To obtain a collection of thermal images and save them using the IR camera, the open-source software purethermal1-uvc-capture available on Github was used[49]. This software starts the camera, obtains a real-time frame of the system, records and saves the data collected into an .HDF5 file, all from the same window. The well plates were designed from 6061 black anodized aluminum bars procured from McMaster Carr (#7083T47) with length, width, and height dimensions of 12 × 6 × 0.5 inches (30.48 × 15.24 × 1.27 cm). These aluminum bars were anodized with black dye to maximize the emissivity and minimize reflectivity of the system, which is critical for the IR camera to obtain a proper radiometric measurement. A Tormach 1100M CNC mill was used to machine the aluminum bars into the approximate length and width of the ANSI/SLAS standard microplates

that are routinely used in biotech analyses, 5” by 3.4” (12.7 by 8.64 cm). Three well plates can be obtained from each stock piece of aluminum. Plate designs with 96, 48, and 24 conical wells were machined. The wells were machined specifically with a 90-degree countersink end mill. As for the heating element, a Torrey Pines Scientific Inc. Echotherm IC25 Chilling/Heating Peltier plate was used but other heating/cooling plates would also be suitable to use with minor modifications to the camera and plate stabilization hardware design. The operable temperature range for this Echotherm plate is between –10°C to +100°C. The rectangular active heating element on the Echotherm measures approximately 4.3” by 2.8” (10.92 by 7.11 cm) which is very similar to the size of the designed well plates, making it ideal for integration into the PhasIR system. Changes to the heating element may also require changes to the IR camera (increasing measurable range for high temperature samples) and enclosure material (preventing deformation at high temperatures). A 3-D printed enclosure was secured to the Echotherm via screws on the main body. This helps to hold the aluminum well plate in a consistent position during the entire measurement, prevents movements of the IR camera after it is locked in place, and provides thermal insulation on the sides of the aluminum plates to minimize lateral temperature gradients. The enclosure was printed from ABS filament, which is heat resistant to ~100°C with no noticeable deformation. Poly-lactic-acid (PLA) would not be suitable due to its low temperature stability. A 19-inch (48.26 cm) V-slot aluminum extrusion was used and secured vertically to the enclosure via a dedicated 3D-printed slot, which allows the Lepton 3.5 to be mounted facing directly above the aluminum well plate. The mount can be easily adjusted to give the Lepton 3.5 a larger or smaller field of view. At the top of the V-slot rail, a Raspberry Pi 3 B+ and the standard 7” (17.8 cm) touch-screen display is mounted in an additional 3D printed enclosure. This integration allows the entire data collection process to be interfaced and initiated without the need for an additional computer.

STL files for 3D printing and machining, as well as a full list of materials can be found on the GitHub repository: https://github.com/pozzo-research-group/phasIR.

9.2.2.3 Software Specifics

The PhasIR hardware is accompanied by an open-source Python-based package that allows for high-throughput analysis of the output video from the IR camera. The package is designed to streamline the data exploration by allowing the user to extract and analyze the results directly from a Jupyter Notebook. The open-source package can be divided into two main sections: image analysis and thermal analysis. The former module allows for the initial analysis of the frames that

are collected by the IR camera. The image can be cropped and resized to remove any objects in the field of view that are neither samples nor part of the well plate (e.g., insulating plastic enclosures). Next the position of the wells containing the samples can be obtained automatically or selected manually on a sample frame. The average sample temperature is obtained from the average pixel values across a circular region of variable diameter that is positioned around each well's centroid across all frames of the video. For each well identified in the image, the plate temperature is identified as four equidistant points placed diagonally with respect to the well centroid. The latter module allows us to measure the temperature profile for each well and to analyze the curve, plotted relative to the plate temperature, to identify the phase transition temperature of each sample. Finally, the phase transition point is then obtained by identifying the onset of the peak that is formed by the curve that is obtained when subtracting the plate temperature from each sample temperature. This information can then be extracted and saved for further analysis.

Examples and further documentation of the open-source package can be found on the GitHub repository: https://github.com/pozzo-research-group/phasIR.

9.2.3 Experimental Validation

Results from PhaseIR were compared to samples run in the industry standard for thermal analysis, the DSC. A TA Discovery 2500 DSC with auto sampling capabilities was used to identify the melting point of a selection of materials, which were then duplicated in the PhaseIR system. The PhaseIR run was completed in under 15 minutes, compared to the over 5 hours needed for the DSC. For pure substances run in both instruments, the results are within experimental error, with the highest discrepancy being less than 10%, which is below the temperature accuracy limit reported by the IR camera. All measurements were performed in triplicate on 24-well plates. We also tested the precision of the PhaseIR system by performing 24 measurements each of xylitol and candelilla wax on the 48-well plate. The results change minimally across the plate and help to ensure that the location of the sample does not affect the temperature measurement.

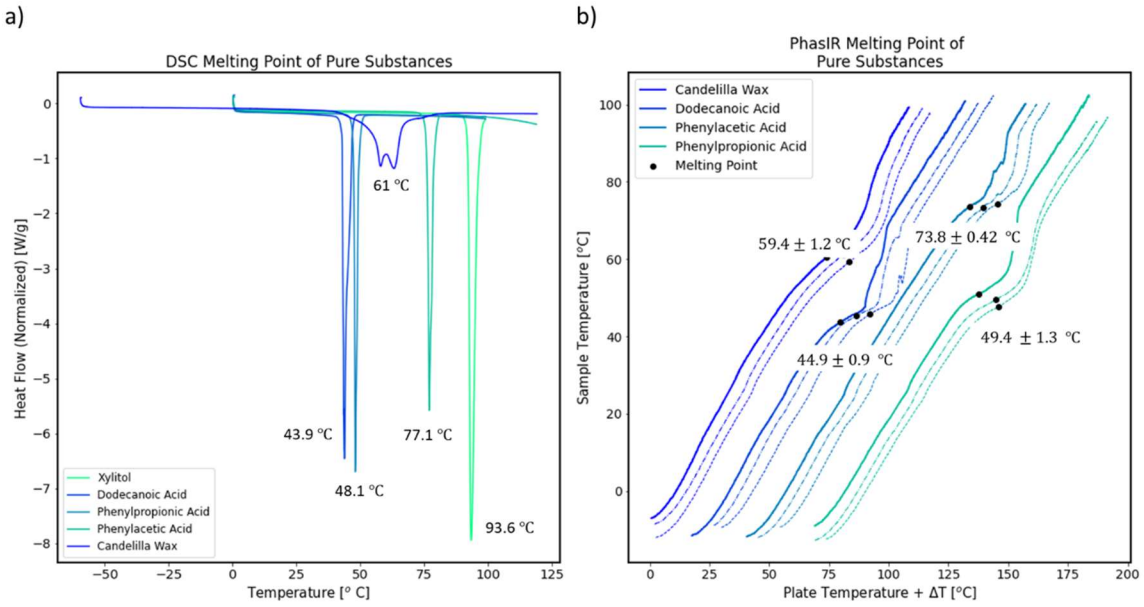

Figure 9.4: a) collected Differential Scanning Calorimetry data for substances of interest, with melting points marked for each material b) PhaseIR data for the substances of interest, with melting points and deviation marked for each material.

Sample	DSC	PhaseIR	Literature	Reference
[-]	[ºC]	[ºC]	[ºC]	[-]
Candella Wax	61	59.4 ± 1.2	68-72	[ref][50]
Dodecanoic Acid	43.9	44.9 ± 0.9	44-46	[ref][51]
Phenylpropinoic Acid	48.1	49.4 ± 1.3	45-48	[ref][52]
Phenylacetic Acid	77.1	73.8 ± 0.42	76-78	[ref][53]

Table 9.1: Table with materials of interest, the DSC value, the phase IR value with deviation, the literature values observed for the material, and reference information for the materials.

9.2.4 Conclusions

We have successfully created an effective, low-cost platform for high-throughput thermal analysis, with agreement to industry standard Differential Scanning Calorimetry (DSC) data. The PhaseIR results agree with a maximum deviation below 10%, while also being capable of collecting up to 96 samples of information in under 15 minutes. This is monumentally faster than a single DSC measurement taking upwards of an hour for a single sample. We have also shown the successful use of an IR camera with aluminum well plates to automatically detect and measure phase transition information for pure organic substances and binary mixture deep eutectic solvents.

This suggests adaptability to further samples and expands the use of the system to samples not considered in this work. With the open-source nature of the PhaseIR system, we hope that other users can modify and refine the package and hardware to their specific needs and improve the space for high-throughput techniques.

9.3 Primary Peak Shifting Observed in PS-PI-PS/P3HT Blends

9.3.1 Data Status

During the process of data collection for the elastomer projects, a series of triplicates were run at Argonne Photon Source (APS) on the USAXS instrument. The triplicates agreed with each other and became the backbone of the elastomer blends work for much of the project. As further experiments were conducted to probe other processing conditions, trends that were observed in the initial triplicate set were not repeated in other samples prepared to probe annealing and temperature sensitivity. Further samples were made to determine the cause of the trend difference, but no definite cause was found. Samples that were used to discount causes are presented in (Chapter 4 and 5) highlighting material, temporal, and thermal changes, and their effect on the system. A selection of samples is shown in **Figure 9.5**. This includes the triplicate samples focused on in this section as well as samples discussed in previous chapters, all processed identically, which shows the difference in trend for the sets. As seen in **Figure 9.5a**, at low weight percents of RRe-P3HT there is not a large difference visually between the samples, but above 10 wt% there emerges a large shift and flattening in the triplicate samples that is not observed in the other sample sets. In the RRa-P3HT (**Figure 9.5b**) samples the samples are more consistent and seem to be within the normal range of morphological differences observed. The PS-PI-PS control samples are also consistent over the replicates.

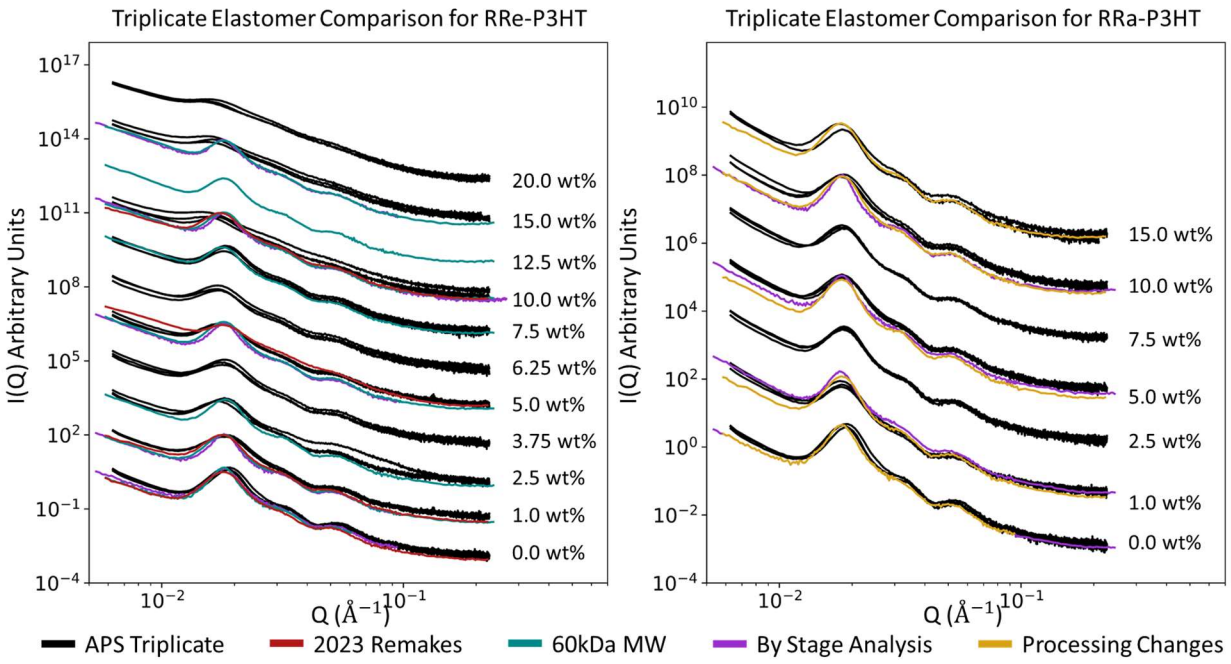

Figure 9.5: Comparisons of data collected in triplicate at the Argonne photon source (APS) for a) RRe-P3HT and b) RRa-P3HT alongside a selection of samples that were processed/treated in the same way.

While it appears the break from trend seems to be isolated to the RRe-P3HT blends, the entire sample set will be addressed here. The trends observed in the triplicate data are morphologically interesting and have promise to be conductively impactful, so this data is presented here alongside a caveat that while the observations within the set are precise the cause of trend is unknown at this time.

9.3.2 Materials and Methods

9.3.2.1 Materials

Regio-random poly(3-hexylthiophene) (RRa-P3HT) (MW = 63 kg mol-1, D = 2.4, Product 4007) and Regio-regular poly(3-hexylthiophene (RRe-P3HT) (MW = 65 kg mol-1, D = 2.4, RR = 95, Product RMI-001EE) were purchased from Rieke Metals (Lincoln, NE USA). Polystyrene-block-Polyisoprene-block-Polystyrene (PS-PI-PS) was purchased from Aldrich Chemistry (St. Louis, MO USA). The PS-PI-PS polymer is a 22% styrene $A_{229}B_{2490}A_{229}$ tri-block-copolymer with a molecular weight of 217,000 as determined using Gel permeation chromatography (GPC). Chloroform was purchased from Fisher Chemical (Waltham, MA USA). For SANS experiments,

fully deuterated Chloroform was purchased from Cambridge Isotope Laboratories, Inc. (Tewksbury, MA USA). All chemicals were used as received.

The same RRa-P3HT and PS-PI-PS were used in the experiments discussed in Chapter 4 and 5, but a different RRe-P3HT was used. Material specifics were explored and determined to not be the cause of trend differences. Replicates were also reproduced using identical RRe-P3HT but still resulted in differences in results from the initial triplicated set.

9.3.2.2 Solid Blend Heat Pressed Film Preparation

All solid blend films were prepared in accordance with the schematic diagram shown in Chapter 4 and 5. Carefully weighed portions of conjugated polymer (RRe-P3HT or RRa-P3HT) are co-dissolved in chloroform (a good solvent for all polymers involved) at 50ºC with the elastomeric commodity polymer (PS-PI-PS) until fully dissolved and homogenous[54–56]. The solutions were then poured out into equally sized, aluminum foil insulated watch glasses on top of a hot plate heated to 50ºC and then covered to achieve a slow solvent evaporation. The samples were left to evaporate for an hour until fully dry, peeled off the watch glass, and left in a fume hood to off gas any remaining solvent in the system overnight. The dry polymer blend was then heat pressed using a D16 Digital Combo Swing-Away Press from Geo Knight & Co (Brockton, MA). The polymers are pressed between steel precision shims from McMaster Carr (Elmhurst, IL) with a thickness of 254 μm and an inner diameter of 15mm at 150ºC. During pressing, each sample was sandwiched between thermally conductive Kapton and two polished stainless-steel plates to create a smooth and even film. The film was cut, stacked, and pressed three additional times for 5 min, 5 min, 10 min respectively, then allowed to cool slowly to room temperature for 30 minutes. This repeat pressing process was used to ensure that samples were uniform. The films were then gently removed from the metal shims and stored at room temperature for measurements.

9.3.2.4 UV-VIS

A Thermo Scientific (Waltham, MA, USA) Evolution 300 UV-Visible spectrophotometer was used to measure and confirm the actual concentration of solid films after preparation. To ensure the models and conclusions drawn are accurate to the actual concentrations of the measured films, weighed portions of the solid samples were re-dissolved into chlorobenzene. The UV-Visible absorption was measured, and the actual concentrations were calculated from a reference calibration curve using the primary absorption peak of P3HT at 450nm.

9.3.2.5 USAXS and SAXS

USAXS and SAXS/WAXS data for samples were collected at the 9ID and the 12ID beamline at the Advanced Photon Source at Argonne National Laboratory[57]. USAXS data was collected in the Bonse-Hart configuration using Si [200] crystals in the standard instrument configuration. The instrument used an intense X-ray beam of 21 keV and a beam size of 0.8 × 0.8 mm with a flux density of approximately 5 × 10 photons/s/mm2. Pinhole SAXS and WAXS data were also collected with exposure times of 10 s each, while USAXS was collected with exposure times of 80 s. Samples were mounted using custom-designed 3D-printed 48-sample frames[58] that enabled execution of remote experiments during COVID-19-constrained access. The sample chamber was held under vacuum at ambient temperature (approx. 20 °C) during all measurements. USAXS, SAXS and WAXS data were reduced, de-smeared (USAXS), and set to absolute intensity units using the Nika package[59] for Igor Pro[60]. This package was also used to combine the 'pinhole' data from the SAXS and WAXS detectors to produce datasets that will be referred to as 'WAXS data' for the remainder of the work. Analysis of WAXS data was performed using the SasView[61]/sasmodels[62] and bumps[63] packages for Python.

SAXS and WAXS data for the same samples were also collected at the University of Washington using a Xenocs (Grenoble, France) Xeuss 3.0 SAXS instrument. This is a pinhole collimated laboratory SAXS instrument with a copper x-ray source. Samples were collected in three modes at various sample-detector distances to collect the full accessible Q range. The 'WAXS' data (sample to detector distance of 0.07m) was collected for 60s, 'SAXS' (sample to detector distance of 0.9m) for 60s, and 'ESAXS' (sample to detector distance of 1.8m) for 300 seconds, while mounted in a 48-sample holder. The data was merged into a combined dataset that will be referred to as 'SAXS data' through this work. The sample chamber was held under vacuum at ambient temperature (approx. 20 °C) for all measurements. Reduction and analysis of all data was performed using XSACT, the Xenocs supported software provided with the instrument. Analysis was then conducted using SasView[61]/sasmodels[62] and bumps[63] packages for Python.

9.3.2.5 Data Analysis

Once fully reduced, data is exported, and further analysis is conducted using SasView[61]/sasmodels[62] and bumps[63] packages for Python. Features in both the USAXS and SAXS data are fit with shape independent models to extract parameters of the features. A low-Q feature

(Figure 3) in the USAXS regime, associated to polymer phase segregation, was fit using the Guinier-Porod[64] combined model as described in chapter 2.

The prominent primary peak in the SAXS data (Figure 3), which corresponds to the nanometer scale self-segregation of the block-copolymer matrix, was fit using a generalized broad peak model[65].

WAXS data are fitted using a combination of Gaussian functions corresponding to each of the peaks observed in the system. First, three broad peaks are fit corresponding to the copolymer matrix peak, the conjugated polymer amorphous peak, and a broad background. Subsequently, the narrower lamellar and π-stacking peaks corresponding to the crystallized fraction of the polythiophene fraction are fit while being constrained to Q-ranges of .25$Å^{-1}$-.35 $Å^{-1}$ and 1.6-$Å^{-1}$1.7 $Å^{-1}$ respectively.

All analysis and modeling of the UV-VIS, DSC, USAXS, SAXS, WAXS and SANS data was performed using Python 3, which aids in reproducibility, while the use of SasView[61]/sasmodels[62] and bumps[63] packages for Python, allows for rapid and easily adjustable fitting of the data sets.

9.3.3 Analysis and Discussion

9.3.3.1 Analysis

We split the data into three regions, each covering a different scale of polymer film morphology and together covering the full scope of the impacts of the conjugated polymer additive on the structure of the elastomeric template. The low-Q USAXS region shows emerging features (i.e., a broad 'hump') with the addition of higher weight percentages of conjugated polymer (either Regio-regular or Regio-random) which suggest large-scale formations of phase-separated regions. Mid-Q features in the SAXS region are dominated by the emergence of a prominent peak around 0.018$Å^{-1}$, which corresponds to a characteristic distance of ~350Å. This peak is present in all samples that are collected, including the pure PS-PI-PS matrix, and it is attributed to the characteristic spacing of the ordered structure of the PS and the PI blocks. From experiments shown in Chapter 4, we have determined the structure of high temperature processed samples to be variable but consist of hexagonally packed cylinder with various levels of mixed phase. For more information, refer to Chapter 4. We anticipate that the structural trend remains the same, with larger events of mixed phases, and will address the structure as so in this section. With the addition of conjugated polymers, we see this characteristic peak shift and change in shape, suggesting the

structure is affected by the integration of the conjugated polymer in the blend. Finally, at high-Q (i.e., WAXS region) we observe the structure at the smallest molecular and atomic scales. This region allows us to determine changes in the crystallinity of the components that make up the composite polymer blend. The PS-PI-PS matrix has peaks characteristic to an amorphous structure but does not display narrow peaks that are typically attributed to crystallinity. When semi-crystalline RRe-P3HT is added, we see the emergence of two new narrow peaks that correspond well to the lamellar and π-stacking peaks that are commonly observed in the literature and that allow us to calculate the extent of crystallinity[66,67].

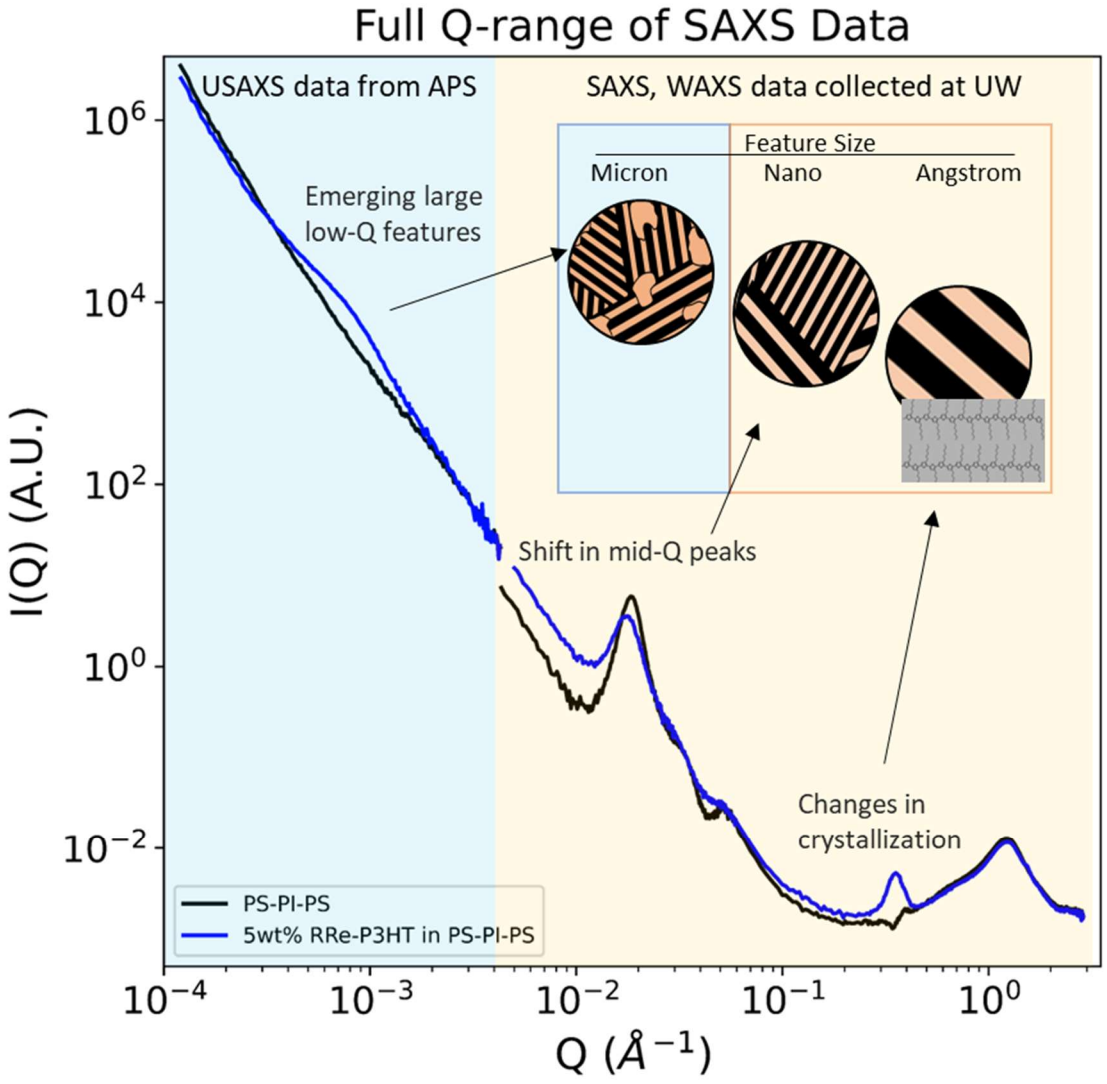

Figure 9.6: Full Q range of SAXS data collected on a pure PS-PI-PS matrix sample (black) and a 5 weight percent RRe-P3HT composite blend (blue) from 10^{-4}Å^{-1} to 3 Å^{-1} . Peaks and features of interest have been marked and inset provide scale for each feature observed.

In the SAXS data range, we observe a characteristic peak corresponding to the PS and PI hexagonally packed cylinder structure. The two polymer blocks in the elastomer do not have thermodynamically favorable interactions, and segregate into self-defined regions as established for SIS block copolymers[68–71]. With the addition of the CP, we see that there are shifts to the peak location and the peak width as shown in a selection of representative samples in **Figure 9.7**. As seen in **Figure 9.7**, the addition of the semicrystalline conjugated polymer (RRe-P3HT) causes a sizable shift towards low-Q, indicating a growing distance between segregated blocks, and a widening of the peak as the content of CP is increased. Also notable is the abrupt peak shift and peak widening that is observed in samples containing RRe-P3HT additives between concentrations of 6.7 wt% and 10.7 wt%. In contrast, when the amorphous RRa-P3HT is added (**Figure 9.7d**), we observe a different trend. There are no visibly large changes in either the peak location or the peak width as a function of RRa-P3HT additive concentration.

To quantify these observations, we fit all the data with a broad peak model. During fitting, we fix the Porod exponent to 4, which fits the data and is appropriate for smooth interfaces between domains. Phase-separated polymer blends typically form sharp interfaces[67] and initial unconstrained fits show the Porod exponent trending towards 4 in agreement with literature. All other parameters are allowed to vary within reasonable ranges and the primary parameters of interest are the peak location and the Lorentzian length, which describes the peak width. The fits for the peak location and Lorentzian length are plotted against weight percent with error bars determined by standard deviation from three or more replicate samples at the same weight percent of additive. Horizontal error bars represent fluctuations between the target CP concentration in preparation, and the actual concentration as determined from UV-Vis measurements. The peak location for the semi-crystalline blends drops in Q rapidly (suggesting a rise in the repeat spacing) before leveling out past 10 weight percent. The RRa-P3HT blend, which is amorphous, shows a very small growth in repeat spacing with the addition of a small amount of conjugated polymer, but little or no further increase with increasing weight percent. The Lorentzian length is related to the extent of order in the matrix polymer with shorter lengths indicating wider peaks and a more disordered phase structure. We see the peak widths for semi-crystalline RRe-P3HT blends fluctuate

initially and even seem to sharpen until the 10 wt% RRe-P3HT blend sample before dropping considerably for the highest weight percent samples. In the case of RRa-P3HT blends, the Lorentzian length drops slightly, relative to the neat PS-PI-PS matrix, with the addition of conjugated polymer, but remains relatively constant with the addition of increasing weight percentages.

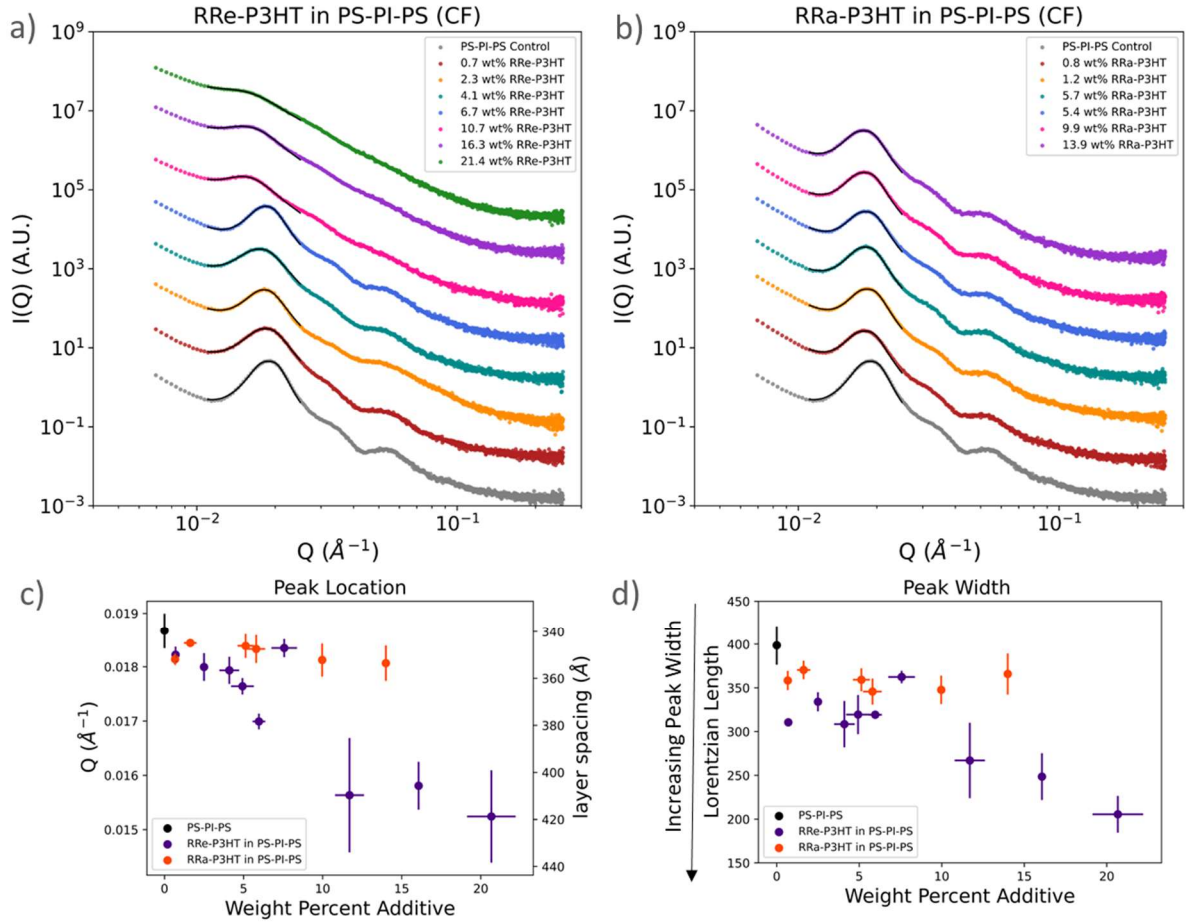

Figure 9.7: SAXS regime plots with broad peak fits of(a) Regio-regular P3HT and PS-PI-PS blends from 0-20 weight percent of conjugated polymer and b) Regio-random P3HT and PS-PI-PS blends from 0 – 15 weight percent of conjugated polymer. Parameter plots of c) peak location and d) peak width are plotted with both conjugated polymer series.

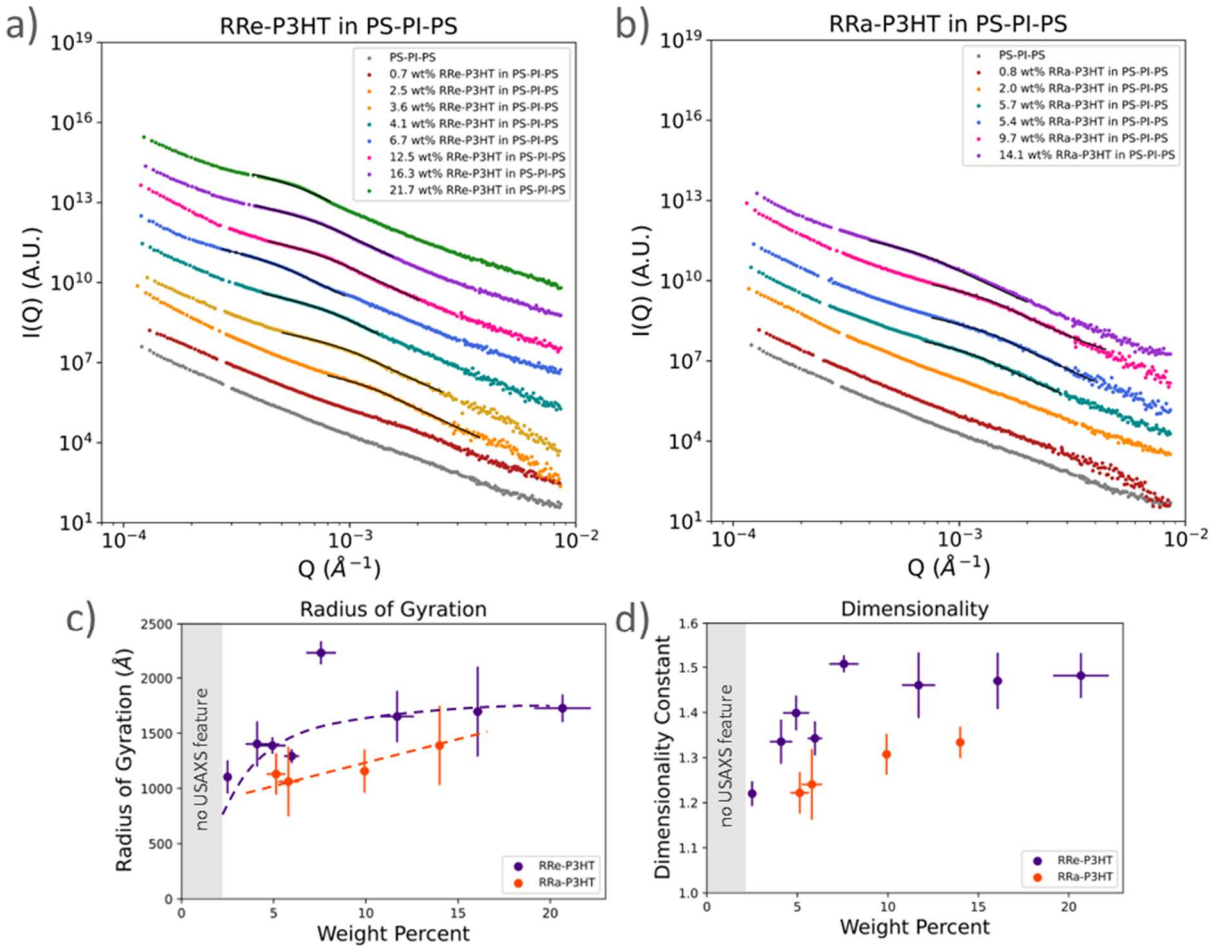

Figure 9.8: USAXS regime plots with Guinier-Porod fits of a) Regio-regular P3HT and PS-PI-PS blends from 0-20 weight percent of conjugated polymer and b) Regio-random P3HT and PS-PI-PS blends from 0 – 15 weight percent of conjugated polymer. Parameter plots of c) radius of gyration and d) dimensionality coefficient is plotted with both conjugated polymer series.

Changes are also observed in the low-Q feature that is observed in the USAXS regime for blend samples. All data shown in the USAXS dataset was collected at APS 9-ID USAXS beamline. As seen in **Figure 9.8a**, the control does not display any features in this length scale, but the addition of semi-crystalline RRe-P3HT at concentrations of 2.5 wt% or greater creates a prominent feature that is indicative of large-scale phase separation. As the CP concentration is increased, the feature shifts further towards lower Q, indicating that the characteristic length scale is growing. At and above 12.5 wt% of RRe-P3HT loading, there is a noticeable shift towards high-Q before shifting again towards low-Q with increasing CP loading. Interestingly, this shift corresponds to the loss of order and significant shift in the matrix lamellar spacing that is observed in the SAXS

regime (**Figure 9.7a**). This suggests that there is a large-scale phase-separation process that begins with the addition of RRe-P3HT, growing steadily until a shift occurs at ~10 wt%. This USAXS feature is also observed in amorphous CP additions (**Figure 9.8d**) although higher weight percentages of CP are needed to form the feature. As increasing amounts of RRa-P3HT are added, the feature again shifts towards low-Q, but there is no 'transition' towards high-Q observed in the loading range that was measured. This phase separation feature has also been observed for CP blends with PS homopolymers[67].

The USAXS feature fits well with a Guinier-Porod model, allowing for the quantitative extraction of parameters of interest. As before, the Porod exponent is fixed to 4, which is typical for sharp interfaces and was also found to be appropriate for the data. The radius of gyration, which is a general metric of domain size, and the dimensionality coefficient, which is as a metric of shape, are obtained and plotted against the loading of CP in **Figure 9.8**. We see similar trends in both domain size and shape, for both conjugated polymers we worked with. As seen in **Figure 9.8b**, the radius of gyration for the RRe-P3HT features, which is in the range of 100's of nanometers, grows rapidly before peaking around 7.5 wt%, dropping and leveling out for the highest weight percent samples. The RRa-P3HT samples grow steadily in an almost linear fashion. For both polymers, lines are added to guide the eye, not as a fit.

In **Figure 9.8c**, we see similar trends for the shape or dimensionality parameter 's'. The dimensionality variable describes the shape characteristics of the feature and ranges from 1 (rods) to 2 (plates). For both types of CPs, the phase-separated domains tend from more one-dimensional to a more two-dimensional or 'platelike' shape. However, the dimensionality parameter for RRe-P3HT increases more rapidly with increased loading before leveling out at s ~ 1.5 at the highest concentrations.

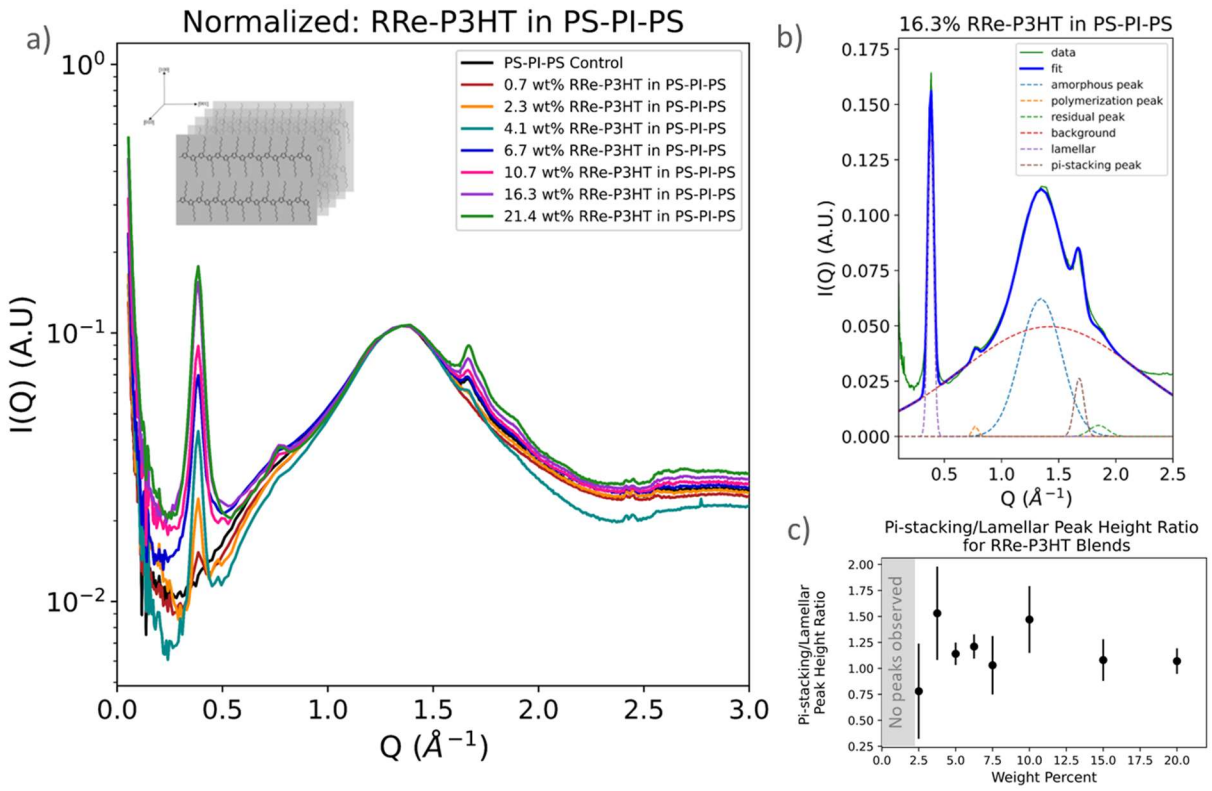

Figure 9.9: WAXS data collected of a) Regio-regular P3HT and PS-PI-PS blends from 0-20 weight percent of conjugated polymer normalized to the amorphous peak. Inset shows P3HT crystal structure. Each WAXS signal was fit with six gaussian curves, as seen in representative plot b). The ratio of the peak heights of the π-stacking and lamellar peaks is plotted for the RRe-P3HT blend series c).

Finally, at very high-Q, we analyze WAXS data from APS 12-ID-C SAXS beamline. This region allows for analysis of variations in the extent of crystallinity of the conjugated polymer component within the blends. The data is normalized to the amorphous peak at 1.4 $Å^{-1}$, and the peaks of interest for the P3HT are the lamellar peak at ~0.4 $Å^{-1}$ and the π-stacking peak at ~1.7 $Å^{-1}$. The RRa-P3HT data is not shown as no lamellar or π-stacking peaks are present due to the lack of crystallinity in a fully amorphous blend. Fits are performed using six simultaneously fit gaussian functions as shown in **Figure 9.9b**, with the intensities being extracted for the two primary peaks of interest. The ratio of these peaks, which is related to the relative crystallization in the lamellar vs. π-stacking directions, is plotted against weight percent loading of P3HT to assess changes in the crystallization within the blends. Notably, the ratio of the two peaks does not change considerably with the addition of more conjugated polymer.

9.3.3.2 Discussion

X-ray scattering shows that the addition of a conjugated polymer additive changes the structure of the template as summarized in **Figure 9.10**. Samples of pure elastomer show clear structure that is, as determined in Chapter 4, hexagonally packed cylinders (SAXS region) and no evidence of large-scale phase-segregation (USAXS region), which was maintained through multiple samples. When P3HT is added to form the composite blend, there are signs of an expanding cylinder spacing (SAXS). This suggests that some or all the RRe-P3HT conjugated polymer additive is incorporated into the block copolymer elastomer template structure, pushing the cylinders apart, which results in the expansion of the periodic structure. As the concentration of RRe-P3HT is increased, the semi-crystalline P3HT causes gradual swelling of the layers up to loadings of ~10 wt%, where there is a more abrupt large increase in template spacing that coincides with a significant loss of order. The widening peak suggests that there is increased variability in the characteristic domain size with the addition of the P3HT. From the high temperature samples in chapter 5, we anticipate this also includes phase changes to a more mixed phase. This leads us to believe that there is a loss of integrity in the PS-PI-PS matrix when enough P3HT has been added into the mixture. Perhaps a saturation point has been reached, and past that point, there is a steady formation of phase-separated P3HT-enriched domains that form outside of the lamellar template structure. The phase-separated domains emerge with the addition of between 1 and 2.5 weight percent conjugated polymer and continue to grow as more P3HT is added to the blend until a maximum size is reached around 7.5 weight percent. Around the same inflection point between 7.5 and 10 weight percent we see a plateau of size for these domains. When more than 10 weight percent of conjugated polymer is added, there is no longer an increase in size or dimensionality of the PS-PI-PS matrix repeat structure. This suggests that with higher loadings of P3HT, the most favorable state for the material is to be phase separated without a strict ordering of the phases. This loss of ordering in the phases may be seen both in a decrease regularity of the repeat space, an increase in the directions the cylinders are oriented in, or the formation of large swaths of disordered but phase separated regions.

Amorphous P3HT displays different trends. With the addition of any RRa-P3HT, we see a slight increase in the layer spacing and peak width, but there is not a significant change in either property with increasing amounts of conjugated polymer. With this in mind, we do not believe that the amorphous P3HT is incorporated in the PS-PI-PS elastomer in the same way as the stiff semi-

crystalline polymer. Instead, the P3HT is segregating with itself, outside of the structure of the template. A small amount of self-associated globular aggregates may incorporate within the structure of the template, but that amount is constant and increasing the weight percent of conjugated polymer does not increase the amount of globular RRa-P3HT aggregates within the template. Instead, the additional polymer begins to form large amorphous domains that steadily increase in size and appear as features in the USAXS region. These large aggregates require a slightly higher weight percent to form than they do in the semi-crystalline blends but show a steady increase in the size without an apparent plateau in the range measured.

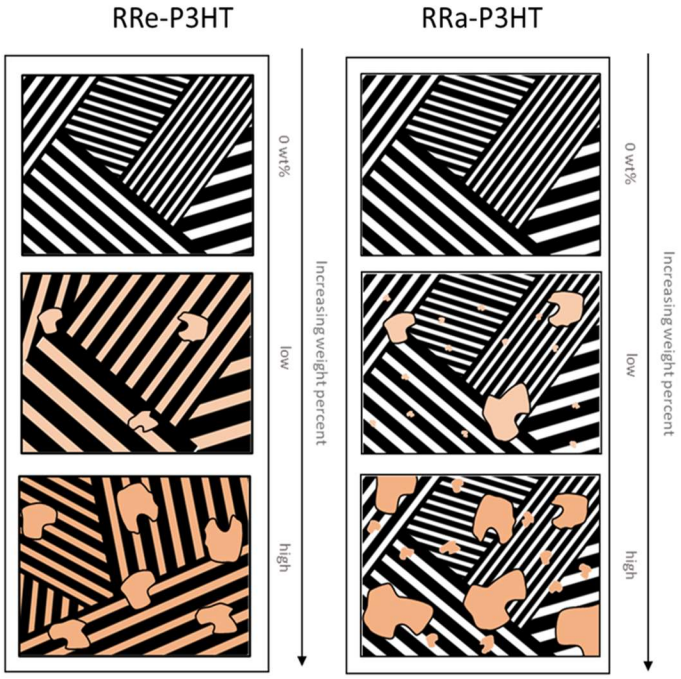

Figure 9.10: Initial schematic of morphological changes of a PS-PI-PS template with the addition of increasing weight percents of a) RRe-P3HT or b) RRa-P3HT

9.3.4 Next Steps

A series of experiments were conducted to check possible variables that may have changed the behavior between the APS triplicate set and later samples. These variables include P3HT lot (Chapter 4), pressing temperature (Chapter 4), pressing time (Chapter 5), solvent (Chapter 5), vacuum off-gassing (Chapter 5), post processing exposure to cold or hot temperatures (Chapter 5), remakes of selected samples using remaining triplicate P3HT, as well as redissolving and recasting selected triplicate samples. The recasts from the same samples showed vastly different physical properties and structure to any of the sample sets, most likely due to age and oxidation from air

exposure. The remakes showed similar trends as the other non-triplicate set with no drastic peak shifts. At this time there is no clear understanding of why the triplicate set had this trend whereas the others did not. Possible factors that have not been investigated may be related to their data collection at APS or changes due to steps taken during that process. The samples were made on campus at the University of Washington and no data/aliquots were taken from the process before they were packed, shipped, and flown to APS where they were run remotely during covid on high throughput 3d printed cartridges, packed, and shipped back to the UW where any subsequent data collection occurred.

Determining the cause of why this triplet set of RRe-P3HT samples have different trends than subsequent sample sets would be key to understanding and utilizing this data. From morphological considerations, there seems to be increased incorporation of the P3HT into the structure of the PS-PI-PS and with enough crystallization of the RRe-P3HT, there can be clear avenues of charge transfer along these channels/structures. Even without a conductivity motivation, there is a repeatable (within set) change that displays different properties from identically produced samples, and in order to better understand these complex systems, identifying processing, material, or environmental effects can better flesh out the design space.

9.4 References

1. World Health Organization. *World Malaria Report 2018*. (World Health Organization).
2. Dagan-Wiener, A. *et al.* Bitter or not? BitterPredict, a tool for predicting taste from chemical structure OPEN. doi:10.1038/s41598-017-12359-7.
3. Drugs, I. of M. (US) C. on the E. of A., Arrow, K. J., Panosian, C. & Gelband, H. A Brief History of Malaria. (2004).
4. World Health Organization. World Health Organization Essential Medicine List 23rd List (2023). (2023).
5. Baguley, D., Lim, E., Bevan, A., Pallet, A. & Faust, S. N. Prescribing for children - taste and palatability affect adherence to antibiotics: a review. *Arch Dis Child* **97**, 293–297 (2012).
6. World Health Organization. *World malaria report 2022*. https://www.who.int/teams/global-malaria-programme (2022).
7. Orubu, E. S. F. & Tuleu, C. Medicines for children: flexible solid oral formulations. *Bull World Health Organ* **95**, 238 (2017).
8. Ali, A. A., Charoo, N. A. & Abdallah, D. B. Pediatric drug development: formulation considerations. *Drug Dev Ind Pharm* **40**, 1283–1299 (2014).
9. Valeur, K. S., Holst, H. & Allegaert, K. Excipients in Neonatal Medicinal Products: Never Prescribed, Commonly Administered. *Pharmaceut Med* **32**, 251–258 (2018).
10. Bafna, A. A. FORMULATION AND EVALUATION OF TASTE MASKED ORAL SUSPENSION OF CHLOROQUINE PHOSPHATE. *Journal of Drug Delivery and Therapeutics* **4**, (2014).
11. Guimarães, T. F. *et al.* Investigation of Chloroquine Resinate Feasibility and In Vitro Taste Masking Evaluation for Pediatric Formulations. *AAPS PharmSciTech* **23**, 1–12 (2022).
12. Woertz, K., Tissen, C., Kleinebudde, P. & Breitkreutz, J. Rational development of taste masked oral liquids guided by an electronic tongue. *Int J Pharm* **400**, 114–123 (2010).

13. Kayitare, E. *et al.* Taste-masked quinine pamoate tablets for treatment of children with uncomplicated Plasmodium falciparum malaria. *Int J Pharm* **392**, 29–34 (2010).
14. Kayumba, P. C. *et al.* Quinine sulphate pellets for flexible pediatric drug dosing: Formulation development and evaluation of taste-masking efficiency using the electronic tongue. *European Journal of Pharmaceutics and Biopharmaceutics* **66**, 460–465 (2007).
15. Vaziri, A. & Warburton, B. Slow release of chloroquine phosphate from multiple taste-masked W/O/W multiple emulsions. *J Microencapsul* **11**, 641–648 (1994).
16. AL-Japairai, K. *et al.* A review on taste masked multiparticulate dosage forms for paediatric. *Int J Pharm* **632**, 122571 (2023).
17. Pittman, D. W. *et al.* The Palatability of Lopinavir and Ritonavir Delivered by an Innovative Freeze-Dried Fast-Dissolving Tablet Formulation. *AIDS Res Treat* **2018**, (2018).
18. Smith, E. L., Abbott, A. P. & Ryder, K. S. Deep Eutectic Solvents (DESs) and Their Applications. *Chem Rev* **114**, 11060–11082 (2014).
19. Zhang, Q., De Oliveira Vigier, K., Royer, S. & Jérôme, F. Deep eutectic solvents: syntheses, properties and applications. *Chem Soc Rev* **41**, 7108–7146 (2012).
20. Liu, Y. *et al.* Natural Deep Eutectic Solvents: Properties, Applications, and Perspectives. *J Nat Prod* **81**, 679–690 (2018).
21. Hikmawanti, N. P. E., Ramadon, D., Jantan, I. & Mun'im, A. Natural Deep Eutectic Solvents (NADES): Phytochemical Extraction Performance Enhancer for Pharmaceutical and Nutraceutical Product Development. *Plants* **10**, (2021).
22. Craveiro, R. *et al.* Properties and thermal behavior of natural deep eutectic solvents. *J Mol Liq* **215**, 534–540 (2016).
23. Tian, Y. *et al.* The Formation, Stabilization and Separation of Oil–Water Emulsions: A Review. *Processes 2022, Vol. 10, Page 738* **10**, 738 (2022).
24. Jiao, Y. *et al.* Enhancing the Formation and Stability of Oil-In-Water Emulsions Prepared by Microchannels Using Mixed Protein Emulsifiers. *Front Nutr* **9**, 822053 (2022).
25. Kumar, N. & Mandal, A. Surfactant Stabilized Oil-in-Water Nanoemulsion: Stability, Interfacial Tension, and Rheology Study for Enhanced Oil Recovery Application. *Energy and Fuels* **32**, 6452–6466 (2018).
26. Macritchie, F. Barrier to Coalescence in Stabilized Emulsions. *Nature 1967 215:5106* **215**, 1159–1160 (1967).
27. Baret, J. C., Kleinschmidt, F., Harrak, A. El & Griffiths, A. D. Kinetic aspects of emulsion stabilization by surfactants: A microfluidic analysis. *Langmuir* **25**, 6088–6093 (2009).
28. Dandagi, P. M., Rath, S. P., Gadad, A. P. & Mastiholimath, V. S. Taste Masked Quinine Sulphate Loaded Solid Lipid Nanoparticles for Flexible Paediatric Dosing. *Indian Journal of Pharmaceutical Education and Research* **48**, 93–99 (2014).
29. Rodriguez, J. *et al.* PhasIR: An Instrumentation and Analysis Software for High-throughput Phase Transition Temperature Measurements. *Journal of Open Hardware* **5**, (2021).
30. Akash, M. S. H. & Rehman, K. Differential Thermal Analysis. *Essentials of Pharmaceutical Analysis* 207–213 (2020) doi:10.1007/978-981-15-1547-7_18.
31. Giron, D. Applications of Thermal Analysis and Coupled Techniques in Pharmaceutical Industry. *J Therm Anal Calorim* **68**, 335–357 (2004).
32. Veluchamy, A. *et al.* Thermal analysis of LixCoO2 cathode material of lithium-ion battery. *J Power Sources* **189**, 855–858 (2009).
33. Zheng, S., Wang, L., Feng, X. & He, X. Probing the heat sources during thermal runaway process by thermal analysis of different battery chemistries. *J Power Sources* **378**, 527–536 (2018).
34. Lu, Z., Yang, L. & Guo, Y. Thermal behavior and decomposition kinetics of six electrolyte salts by thermal analysis. *J Power Sources* **156**, 555–559 (2006).
35. Frick, A. & Rochman, A. Characterization of TPU-elastomers by thermal analysis (DSC). *Polym Test* **23**, 413–417 (2004).

36. Cafiero, L., Fabbri, D., Trinca, E., Tuffi, R. & Vecchio Ciprioti, S. Thermal and spectroscopic (TG/DSC-FTIR) characterization of mixed plastics for materials and energy recovery under pyrolytic conditions. *J Therm Anal Calorim* **121**, 1111–1119 (2015).
37. Saxena, P., Shukla, P. & Gaur, M. S. Thermal analysis of polymer blends and double layer by DSC. *Polymers and Polymer Composites* **29**, S11–S18 (2021).
38. Zheng, H. *et al.* Thermal Analysis of Four Insect Waxes Based on Differential Scanning Calorimetry (DSC). *Procedia Eng* **18**, 101–106 (2011).
39. Roos, Y. H. Thermal analysis, state transitions and food quality. *J Therm Anal Calorim* **71**, 197–203 (2004).
40. Grujić, R. & Savanović, D. THERMAL ANALYSIS OF FOOD PRODUCTS USING DIFFERENTIAL SCANNING CALORIMETRY (DSC). *Contemp Mater* **10**, (2019).
41. Bhadeshiva, D. H. Thermal Analysis Techniques.
42. Janet, J. P., Ramesh, S., Duan, C. & Kulik, H. J. Accurate Multiobjective Design in a Space of Millions of Transition Metal Complexes with Neural-Network-Driven Efficient Global Optimization. *ACS Cent Sci* **22**, 0 (2020).
43. Deshmukh, S. *et al.* A Novel High-Throughput Viscometer. *ACS Comb Sci* **18**, 405–414 (2016).
44. Whitacre, J. F. *et al.* An Autonomous Electrochemical Test Stand for Machine Learning Informed Electrolyte Optimization. *J Electrochem Soc* **166**, A4181–A4187 (2019).
45. Mennen, S. M. *et al.* The Evolution of High-Throughput Experimentation in Pharmaceutical Development and Perspectives on the Future. *Org Process Res Dev* **23**, 1213–1242 (2019).
46. McCullough, K., Williams, T., Mingle, K., Jamshidi, P. & Lauterbach, J. High-throughput experimentation meets artificial intelligence: a new pathway to catalyst discovery. *Physical Chemistry Chemical Physics* **22**, 11174–11196 (2020).
47. Kawakami, K. Parallel thermal analysis technology using an infrared camera for high-throughput evaluation of active pharmaceutical ingredients: A case study of melting point determination. *AAPS PharmSciTech* **11**, 1202–1205 (2010).
48. Hou, S., Huo, R. & Su, M. High throughput integrated thermal characterization with non-contact optical calorimetry. *Review of Scientific Instruments* **88**, 104902 (2017).
49. Kheirlb. https://github.com/Kheirlb/purethermal1-uvc-capture.
50. Sigma-Aldrich. Candelilla Waxs, SDS.
51. Sigma-Aldrich. Dodecanoic Acid, SDS.
52. Sigma-Aldrich. 3-Phenylpropionic Acid, SDS.
53. Sigma-Aldrich. Phenylacetic Acid, SDS.
54. Roesing, M., Howell, J. & Boucher, D. Solubility Characteristics of Poly(3-hexylthiophene). *J. Polym. Sci., Part B: Polym. Phys* **55**, 1075–1087 (2017).
55. Teresa García, M., Gracia, I., Duque, G., de Lucas, A. & Francisco Rodríguez, J. Study of the solubility and stability of polystyrene wastes in a dissolution recycling process. (2009) doi: 10.1016/j.wasman.2009.01.001.
56. Yamazaki, H., Nagasawa, T., Choi, W. & Endo, T. Transformation of vulcanized natural rubber into lower molecular weight polymers and their application to grafted copolymer synthesis with some vinyl monomers. *J Appl Polym Sci* **101**, 4003–4010 (2006).
57. Ilavsky, J. *et al.* Development of combined microstructure and structure characterization facility for in situ and operando studies at the Advanced Photon Source. *urn: issn:1600-5767* **51**, 867–882 (2018).
58. Thing files for USAXS 48 Solid Film Holder by dpozzo - Thingiverse. https://www.thingiverse.com/thing:4639006/files.
59. Ilavsky, J. & IUCr. Nika: software for two-dimensional data reduction. *urn: issn:0021-8898* **45**, 324–328 (2012).
60. Kline, S. R. & IUCr. Reduction and analysis of SANS and USANS data using IGOR Pro. *urn: issn:0021-8898* **39**, 895–900 (2006).
61. Doucet, M. *et al.* SasView. Preprint at (2022).
62. Doucet, M. *et al.* Sasmodels. Preprint at (2020).

63. Kienzle, P. A. (Unviversity of M. C. P., Krycka, J., Patel, N. & Sahin, I. Bumps. Preprint at (2011).
64. Hammouda, B. & IUCr. A new Guinier–Porod model. *urn: issn:0021-8898* **43**, 716–719 (2010).
65. broad_peak — SasView 5.0.5 documentation. https://www.sasview.org/docs/user/models/broad_peak.html.
66. Balko, J., Lohwasser, R. H., Sommer, M., Thelakkat, M. & Thurn-Albrecht, T. Determination of the Crystallinity of Semicrystalline Poly(3-hexylthiophene) by Means of Wide-Angle X-ray Scattering. **21**, 38 (2023).
67. Wolf, C. M. *et al.* Blend Morphology in Polythiophene−Polystyrene Composites from Neutron and X-ray Scattering. doi: 10.1021/acs.macromol.0c02512.
68. Pedemonte, E., Turturro, A., Bianchi, U. & Devetta, P. The cubic structure of a SIS three block copolymer. *Polymer (Guildf)* **14**, 145–150 (1973).
69. Laurer, J. H. *et al.* Microstructural analysis of a cubic bicontinuous morphology in a neat SIS triblock copolymer. *Macromolecules* **30**, 3938–3941 (1997).
70. Widin, J. M., Schmitt, A. K., Schmitt, A. L., Im, K. & Mahanthappa, M. K. Unexpected consequences of block polydispersity on the self-assembly of ABA triblock copolymers. *J Am Chem Soc* **134**, 3834–3844 (2012).
71. Hadziioannou, G. & Skoulios, A. Molecular Weight Dependence of Lamellar Structure in Styrene/Isoprene Two-and Three-Block Copolymers. *Separation Methods in Biochemistry* **131**, 533 (1970).
72. Olsen, B. D., Shah, M., Ganesan, V. & Segalman, R. A. Universalization of the phase diagram for a model rod-coil diblock copolymer. *Macromolecules* **41**, 6809–6817 (2008).
73. Lim, H., Chao, C.-Y. & Su, W.-F. Modulating Crystallinity of Poly(3-hexylthiophene) via Microphase Separation of Poly(3-hexylthiophene) −Polyisoprene Block Copolymers. (2015) doi:10.1021/ma502417w.
74. Lin, S. H., Wu, S. J., Ho, C. C. & Su, W. F. Rational design of versatile self-assembly morphology of rod-coil block copolymer. *Macromolecules* **46**, 2725–2732 (2013).
75. Emerson, J. A., Toolan, D. T. W., Howse, J. R., Furst, E. M. & Epps, T. H. Determination of Solvent–Polymer and Polymer–Polymer Flory–Huggins Interaction Parameters for Poly(3-hexylthiophene) via Solvent Vapor Swelling. *Macromolecules* **46**, 6533–6540 (2013).

Acknowledgements

Primary support for this work was provided by the Department of Energy Office of Basic Energy Sciences under award number DE-SC0019911, which directly supported the research participation of all authors and the procurement of materials.

The use of the Xenocs Xuess 3 in Chapter 4, 5, and 9 is made possible by the use of facilities and instrumentation supported by the U.S. National Science Foundation through the Major Research Instrumentation (MRI) program (DMR-2116265) and the UW Molecular Engineering Materials Center (MEM-C), a Materials Research Science and Engineering Center (DMR-1719797).

Neutron data presented in Chapter 3 and 9 was made possible through the use of resources at the NIST Center for Neutron Research on the VSANS, NG-30 SANS, and USANS instruments. We thank the beamline scientists Yun Lui and Yimin Mao for their aid during preparation and collection of the data for this work.

Work in Chapter 4, 5, and 9 was heavily informed by data run at the Advanced Photon Source, a U.S. Department of Energy (DOE) Office of Science User Facility operated for the DOE Office of Science by Argonne National Laboratory under contract no. DE-AC02-06CH11357. We thank the beamline scientists Jan Ilavsky and Ivan Kuzmenko at 9-ID for their contributions during preparation and remote collection of preliminary data for this experiment.

This research uses the resources of the Australian Nuclear Science and Technology Organisation in Chapters 6 and 7 supported through ANSTO beamline award 15580 on Quokka Small Angle Neutron Scattering Instrument.

This work benefited from the use of the SasView application, originally developed under NSF award DMR-0520547. SasView contains a code developed with funding from the European Union's Horizon 2020 research and innovation program under the SINE2020 project, grant agreement no. 654000.